

Verificatie van het gedrag van gesegmenteerde tunnelbekledingen
met behulp van rek- en ovalisatiemetingen

Verification of the Performance of Segmental Tunnel Linings
Using Strain and Ovalisation Monitoring

Ken Schotte

Promotoren: prof. dr. ir. H. De Backer, ereprof. dr. ir. P. Van Bogaert
Proefschrift ingediend tot het behalen van de graad van
Doctor in de Ingenieurswetenschappen: Bouwkunde

Vakgroep Civiele Techniek
Voorzitter: prof. dr. ir. P. Troch
Faculteit Ingenieurswetenschappen en Architectuur
Academiejaar 2015 - 2016



ISBN 978-90-8578-893-5
NUR 956
Wettelijk depot: D/2016/10.500/25

Supervisors:

prof. dr. ir. Hans De Backer
ereprof. dr. ir. Philippe Van Bogaert

Examination board:

Chair:

prof. dr. ir. Luc Taerwe

Universiteit Gent - EA14

Faculty reading committee:

prof. dr. ir. Adam Bezuijen

Universiteit Gent - EA15

prof. dr. ir. Rui Calçada

Universidade do Porto - Portugal

prof. dr. ir. Alain De Wulf

Universiteit Gent - WE12

Other members:

prof. dr. ir. Robby Caspeepe (secretary)

Universiteit Gent - EA14

prof. dr. ir. Tom De Mulder

Universiteit Gent - EA15



Universiteit Gent

Faculteit Ingenieurswetenschappen en Architectuur

Vakgroep Civiele Techniek

Afdeling Weg- en Waterbouwkunde

Technologiepark 904

9052 Zwijnaarde

België

Tel.: +32 9 264 54 89

Fax.: +32 9 264 58 37

Dankwoord

Bij het tot stand komen van dit doctoraat hebben vele mensen een steentje bijgedragen, bewust of onbewust. Ik wil dan ook graag van de gelegenheid gebruik maken om hen te bedanken voor hun steun en vertrouwen.

Allereerst zou ik een woord van dank willen richten aan mijn beide promotoren, prof. dr. ir. Philippe Van Bogaert en prof. dr. ir. Hans De Backer. Zij hebben mij de mogelijkheid gegeven om mij te verdiepen in dit intrigerende onderwerp, met de nodige vrijheid en zelfstandigheid. Daarnaast stonden ze telkens klaar met veel inzicht en wijze raad om bij te sturen waar nodig. Ook zou ik alle leden van de examencommissie willen bedanken voor hun feedback en constructieve opmerkingen over dit werk.

Het verzamelen van de vele meetgegevens zou niet mogelijk geweest zijn zonder de medewerking van verschillende personen. Bedankt aan Prof. dr. ir. Alain De Wulf, dr. Timothy Nuttens en hun team voor de vlotte samenwerking tijdens de tunnelprojecten. Ook bedankt aan het personeel van THV Dialink, LocoBouw en LocoRail voor de logistieke ondersteuning en medewerking, en aan TUC RAIL en Pierre Detry voor de bijkomende metingen onder de Schelde. Voor de hulp bij de interpretatie van de meetgegevens wens ik graag Prof. dr. ir. Julien De Rouck en ir. Jan Verstraelen te bedanken.

Verder gaat mijn appreciatie uiteraard uit naar het personeel van onze afdeling. Hartelijk dank aan Sam, Dave, Tom en Herman voor de uitgebreide voorbereidingen en de vele uren die zij samen met mij in de tunnels hebben doorgebracht, op de meest onmogelijke tijdstippen. Bedankt aan alle collega's van AWW door de jaren heen voor de leuke contacten en dynamische werkomgeving. In het bijzonder aan Dries en Wim, voor hun ideeën en de vele leuke gesprekken, die gezorgd hebben voor de beste werksfeer die iemand zichzelf kan wensen.

Daarnaast wil ik ook al mijn vrienden bedanken voor de steun en het luisterend oor dat zij mij geboden hebben gedurende al die jaren. Hoewel hun voorstel

“A bridge too far, a tunnel too deep” als titel van dit werk het uiteindelijk nipt niet heeft gehaald, hebben zij toch meer bijgedragen aan dit doctoraat dan zij zelf zouden kunnen vermoeden. Ongelofelijk bedankt voor alle ontspannende momenten, en bedankt aan Conoscenza om mij mentaal scherp te houden gedurende de hele periode.

Tot slot zou ik mijn hele familie willen bedanken, met enkele bijzondere mensen op kop. Mama, papa en Freja, bedankt voor alles wat jullie de voorbije jaren voor mij gedaan hebben. Bedankt voor de onvoorwaardelijke steun, voor de praktische tegemoetkomingen, voor alle momenten waarop ik even mijn hart kon luchten, voor het medeleven en voor zoveel meer.

Eindelijk is het er gekomen, dat veelbesproken doctoraat. Maar het was nooit gelukt zonder de steun van jullie allemaal. Waarvoor mijn oprechte dank.

Ken Schotte, mei 2016

*Live each day as if it were your last,
learn as if you might live forever.*

Summary

Underground construction is more and more focused on the use of mechanised tunnelling techniques such as closed-shield tunnelling. Large variations in applications notwithstanding, the use of shield tunnels offers several advantages in comparison with classic methods, such as ‘cut-and-cover’. This is especially true for the impact on existing structures, noise, vibrations and often financial costs. While new transportation and utility tunnels are created underground, the surface above the tunnel alignment remains mostly undisturbed. Closed-shield tunnelling is primarily used in soft ground conditions, which implies that the use of a segmental tunnel lining as primary or solitary load-bearing component becomes necessary. This type of lining consists of reinforced concrete segments, constructed in a prefabrication plant using very precise tolerances. A tunnel boring machine (TBM) is used to excavate the soil, after which the tunnel lining is constructed by assembling the individual concrete segments one by one into a tunnel ring, under protection of the TBM shield. The positioning of the segments is done using hydraulic equipment, controlled by a human operator, so small misalignments are possible.

During the execution of this doctoral research, several tunnelling projects have been launched to extend the Belgian railway network. Among them, an improved connection to Brussels Airport, known as the Diabolo project, and a new freight connection in the Port of Antwerp, called the Liefkenshoek rail link. This has been an excellent opportunity to accompany the boring process with an experimental monitoring programme including both strain gauge measurements and ovalisation measurements using laser scanning. After the first experiences in the Diabolo tunnel, an improved monitoring technique was developed and implemented in the Liefkenshoek tunnel. The results from these measurements form the backbone for this doctoral research. The measurement data obtained in the Liefkenshoek tunnels allow for assessing the real-time behaviour of the concrete segments under various loading conditions.

The measurement data immediately allows for a number of observations. It can be seen that the loads acting on the tunnel segments during the construction process have a substantial influence on the sectional forces in the tunnel lining. The acting loads during these initial hours after ring erection can be identified as the thrust force of the shield jacks, possible pressure caused by contact with the tail seals and of course the pressure of the tail grouting. All these loads have to be considered as equally important as long-term loads caused by soil and water pressures. In any case, it is deemed logical that the construction loads have a dominant role in the segmental loading. In addition, the deformation pattern of the tunnel cross-section does not always comply with the classical expectations of tunnel lining deformations in soft soil. In general, an ellipsoidal deformation would be expected, where the horizontal tunnel diameter exceeds the vertical diameter, causing a horizontal ovalisation or so-called “pumpkin” shape. Nonetheless, situations where the vertical tunnel diameter exceeds the horizontal one are found just as regularly. Furthermore, evaluation of the strain results shows that, the impact of the passage of the second TBM on the stresses in the tunnel lining can be measured. It proves that the excavation of the adjacent tunnel shaft causes a minor horizontal ovalisation of the segmental lining in the leading tunnel. These observations illustrate the accuracy of the strain monitoring, since the ovalisation measurements did not notice significant changes during this phase. In addition, significant structural changes to the tunnel lining, such as the creation of a cross-passage, can lead to important stress variations, on the short and long term, so they should be an important aspect of the design as well. It further illustrates that a design based solely on soil parameters might not suffice if the early construction stages are not taken into account. Concluding, both strain and ovalisation measurements have proven their value in the accurate monitoring of shield-driven tunnels. Ovalisation results ensure a detailed and easy interpretable view on the cross-sectional deformations of the tunnel lining. However, strain measurements are essential in the continuous observation of the stress behaviour, which remains outside the perceptibility of the laser scanning. Their combined application proves an important advantage in the interpretation of the results.

Based on the observations of the experimental monitoring program, two main focus points were selected for further investigation as part of this dissertation: the importance of installation imperfections and the tidal influence on the tunnel lining.

Firstly, all monitoring results indicate the significant influence of the construction process on the behaviour of the segmental tunnel lining. One of the

important aspects during construction is the presence of installation imperfections between tunnel segments, which can be perceived in the ovalisation results. An advanced 3D finite element (FE) model was developed in order to study the behaviour of the segmental tunnel lining under various load conditions. Multiple tunnel sections were modelled using SAMCEF Field, a commercially available FE-analysis software. This model surpasses the current state of the art because all joints between segments are modelled using contact conditions with friction. This allows all relative displacements and rotations between segments to occur similar to actual tunnel lining behaviour. Additionally, it becomes possible to model geometrical imperfections at the joints. The FE-model with installation imperfections displayed an irregular deformation pattern which bore good resemblance to the real deformations of the tunnel. Due to the imperfect contact in the segment joints in case of an inaccurate installation, sectional forces are transferred to the neighbouring rings via friction. As a result, the maximum tangential normal forces and the bending moments around the tunnel axis increase considerably in the adjacent rings. Consequently the concrete stresses might exceed allowed stress levels, affecting the durability of the segmental lining. On other locations, lower normal forces in the imperfect ring possibly influence the waterproofness of the structure.

Secondly, the presence of a tidal river along the trajectory of the Liefkenshoek tunnel has a continuous impact on the tunnel lining. Apart from a constant fluctuation of lining stresses, an oscillating displacement of the tunnel is observed in response to the river tides. As virtually no information is available in literature on such a behaviour, a detailed investigation of the impact of the river tides is carried out. First, a clear identification of the tidal effect is pursued, after which several hypotheses are investigated to determine the origin of the tunnel movements. Levelling measurements prove that the Liefkenshoek tunnel follows the elastic movements of the Boom clay layer by the exact same magnitude. A maximum vertical displacement of 14 mm is to be expected for large variations of the water level in River Scheldt. No noticeable deformations of the cross-section occur during this vertical translation according to 3D FE-calculations, which corresponds with results from ovalisation measurements. Comparison of calculated and monitored strains proves that the segmental lining experiences the tidal variation of the water pressures along its entire circumference. An increase in uniform compression is observed with rising water levels.

The presented research proves the importance of a detailed insight into the behaviour of segmental tunnel linings, both during and after construction.

Samenvatting

Ondergrondse constructiewijzen maken meer en meer gebruik van gemechaniseerde tunnelbouwtechnieken, zoals geboorde tunnels met gesloten boorfront. Hoewel er een zeer grote variatie bestaat in de mogelijke toepassingen, biedt het gebruik van boortunnels verschillende voordelen in vergelijking met klassieke constructiemethoden, zoals diegene in open bouwput. Dit geldt met name voor de invloed van de aanleg op reeds bestaande structuren, mogelijke geluidsoverlast, optredende trillingen en vaak ook voor het financiële plaatje. Terwijl nieuwe transport- en nutstunnels ondergronds worden gebouwd, is er vrijwel geen enkele verstoring van het maaiveld noodzakelijk. De tunnelbouwtechniek met gesloten boorfront worden voornamelijk gebruikt bij terreinomstandigheden gekenmerkt door een zachte, niet-samenhangende ondergrond, wat impliceert dat het gebruik van een gesegmenteerde tunnelbekleding als primaire of enige dragende component noodzakelijk is. Dit type tunnelbekleding bestaat uit gewapende, geprefabriceerde betonsegmenten, vervaardigd met inachtneming van zeer nauwkeurige toleranties. Een TBM (tunnelboormachine) wordt gebruikt om de grond voor de machine weg te graven, waarna de tunnelbekleding geconstrueerd wordt door de afzonderlijke betonsegmenten een voor een in een tunnelring samen te voegen, onder bescherming van het schild van de boormachine. De segmenten worden gepositioneerd met behulp van een hydraulische arm, manueel bestuurd door een operator, zodat steeds kleine afwijkingen mogelijk zijn.

Tijdens de uitvoering van dit doctoraatsonderzoek zijn verscheidene tunnelprojecten gestart om het Belgische spoorwegennetwerk uit te breiden. Het gaat hier onder andere om een verbeterde aansluiting naar de luchthaven van Zaventem, bekend als het Diabolo-project, en een nieuwe vrachtverbinding in de haven van Antwerpen, de Liefkenshoek spoorverbinding genaamd. Dit vormde een uitstekende gelegenheid om tijdens het boorproces een experimenteel programma op te zetten, gebruik makend van zowel spannings- als ovalisatiemetin-

gen met behulp van rekstroken en een laser scanner. Na de eerste ervaringen bij de Diabolo tunnel, werd een verbeterde monitoringtechniek ontwikkeld en in de Liefkenshoektunnel geïmplementeerd. De resultaten van deze metingen vormen de ruggengraat van dit doctoraatsonderzoek. De bij de aanleg van de Liefkenshoektunnels verkregen meetgegevens laten toe om het real-time gedrag van de betonnen segmenten onder verschillende belastingssituaties te bestuderen.

De studie van de meetgegevens brengt snel enkele zaken aan het licht. Het kan overduidelijk vastgesteld worden dat de belastingen, die op de tunnelsegmenten uitgeoefend worden tijdens het bouwproces, een grote invloed hebben op de snedekrachten in de tunnelwand. De waargenomen belastingen tijdens de eerste uren na de constructie van een tunnelring omvatten onder andere de stuwkracht van de boorschildvijzels, de mogelijke druk veroorzaakt door contact met de dichtingen van het tunnelschild en natuurlijk de druk van de schildstaartinjectie. Al deze belastingen kunnen belangrijker worden dan de klassieke lange-termijnbelastingen ten gevolge van grond- en waterdrukken en zullen dus een dominante rol moet spelen bij het ontwerp van een gesegmenteerde tunnelbekleding. Daarnaast blijkt het vervormingspatroon van de tunneldoorsnede niet altijd te voldoen aan de verwachtingen voor tunnelvervormingen in zachte grond. Over het algemeen zou een ellipsoïdale vervorming worden verwacht, waarbij de horizontale tunneldiameter groter is dan de verticale diameter, waardoor een horizontale ovalisatie of zogenaamde “pompoen”-vervorming optreedt. Desalniettemin blijken er even veel situaties te voor te komen waarin de verticale tunneldiameter de horizontale overschrijdt. Als volgende punt blijkt uit de evaluatie van de meetresultaten dat de invloed van de passage van de tweede tunnelboormachine op de spanningen in de tunnelbekleding kan worden opgemeten. Het bewijst dat de aanleg van de aangrenzende tunnelbuis een kleine horizontale ovalisatie van de gesegmenteerde tunnelbekleding veroorzaakt in de naastliggende tunnel. Deze waarnemingen tonen de nauwkeurigheid van de uitgevoerde rekmetingen aan, aangezien de ovalisatiemetingen geen significante wijzigingen registreerden tijdens deze fase. Samenvattend onderlijnt dit alles dat belangrijke structurele veranderingen in de tunnelbekleding, zoals het maken van een dwarsverbinding tussen de tunnelbuizen, een belangrijke spanningsvariatie op zowel de korte als de lange termijn kan veroorzaken. Het illustreert verder dat het ontwerp van tunnelbekleding niet uitsluitend gebaseerd mag worden op bodemgerelateerde parameters. Voor een correct ontwerp moeten ook de belastingen tijdens alle bouwfasen in aanmerking genomen worden. Concluderend hebben zowel de rek- als ovalisatiemetingen hun waarde bewezen in dit monitoringproject. Ovalisatiemetingen

met een laserscanner leveren een gedetailleerd en gemakkelijk interpreteerbaar beeld op van de vervormingen in een dwarsdoorsnede van de tunnel. Rekmetingen zijn daarentegen essentieel omdat ze toelaten de spanningsopbouw continu op te volgen, met een precisie die buiten het meetbereik van laserscanning blijft. Een gecombineerde toepassing maakt het mogelijk de resultaten makkelijker te interpreteren.

Op basis van de vaststellingen van het experimentele monitoringprogramma, werden twee belangrijke aandachtspunten geselecteerd voor verder onderzoek binnen dit proefschrift: het belang van geometrische imperfecties ten gevolge van de installatie en de invloed van het getij op de tunnelwand.

Uit alle meetresultaten van het monitoringsprogramma blijkt de significante invloed van het constructieproces op het gedrag van de gesegmenteerde tunnelbekleding. Een van de belangrijke aspecten tijdens de bouw is de aanwezigheid van imperfecties ter plaatse van de voeg tussen tunnelsegmenten bij de installatie, die door de ovalisatiemetingen kunnen opgemeten worden. Een geavanceerd 3D eindige-elementen model werd ontwikkeld om het gedrag van de gesegmenteerde tunnelbekleding onder verschillende belastingstoestanden te bestuderen. Meerdere tunnelsecties werden gemodelleerd met de “SAMCEF Field”-software, een in de handel verkrijgbaar eindige-elementen softwarepakket. Dit model onderscheidt zich doordat alle voegen gemodelleerd worden met behulp van contactvoorwaarden, inclusief wrijving tussen de segmenten. Hierdoor kunnen alle relatieve verplaatsingen en rotaties, die tussen de segmenten optreden, gemodelleerd worden en vormt het model een nauwkeurige benadering van het gedrag van de tunnelbekleding. Bovendien wordt het hierdoor mogelijk om geometrische imperfecties te modelleren in de voegen. Bij gebruik van het eindige-elementenmodel, inclusief geometrische imperfecties, verschijnt een onregelmatig vervormingspatroon dat een goede gelijkenis vertoont met de echte vervormingen van de tunnel. Door het onvolmaakte contact tussen de elementen in de voegen ten gevolge van een onnauwkeurige installatie worden bijkomende snedekrachten overgebracht naar de aangrenzende tunnelringen via wrijving. Daardoor kunnen de maximale normaalkrachten en buigmomenten in de nabije tunnelringen aanzienlijk verhogen. Derhalve dreigen de overeenkomstige betonspanningen de toegelaten waarden te overschrijden, waardoor de duurzaamheid van de tunnelbekleding in het gedrang komt. Op andere locaties daarentegen resulteert dit in een lagere normaalkracht, wat de waterdichtheid van de constructie eventueel kan beïnvloeden.

Als tweede aandachtspunt wordt bestudeerd of de aanwezigheid van een getijdenrivier langs het traject van de Liefkenshoek tunnel een aanhoudend ef-

fect op de tunnelwand heeft. Afgezien van een constante fluctuatie van de spanningen, wordt eveneens een oscillerende verplaatsing van de tunnelsectie waargenomen en dit als reactie op de getijdewerking van de Schelde. Omdat vrijwel geen informatie beschikbaar is in de literatuur over een dergelijk gedrag, is een diepgaand onderzoek uitgevoerd. Eerst wordt een duidelijke identificatie van de getijdenwerking nagestreefd, waarna verschillende hypothesen onderzocht worden om de oorsprong van de tunnelbewegingen te bepalen. Metingen met een waterpastoestel bewijzen dat de Liefkenshoektunnel de elastische vervorming van de Boomse klei volgt en dat de grootte van de verplaatsingen identiek is. Een maximale verticale verplaatsing van 14 mm wordt teruggevonden voor de extreme waarden van het waterpeil in de Schelde. Tijdens deze verticale verplaatsing treedt geen merkbare vervorming van de tunnelsectie op, wat zowel blijkt uit verificatie met het eindige-elementenmodel als uit de ovalisatiemetingen. De vergelijking van de berekende en gemeten waarden toont aan dat de gesegmenteerde tunnelbekleding de getijdevariatie ervaart als een variatie van de waterdruk langs de gehele omtrek. Een toename in uniform compressie treedt op bij stijgende waterstanden.

Concluderend kan gesteld worden dat het onderzoek wijst op het grote belang van een gedetailleerd inzicht in het gedrag van gesegmenteerde tunnelbekledingen, zowel tijdens als na de constructiefase.

Contents

| | |
|--|-----------|
| Summary | i |
| Samenvatting | v |
| List of symbols and abbreviations | xv |
| 1 Introduction | 1 |
| 1.1 Segmental tunnel linings | 1 |
| 1.1.1 Application | 1 |
| 1.1.2 Construction methodology | 1 |
| 1.1.3 Design approach | 3 |
| 1.1.4 Frequent damage mechanisms | 6 |
| 1.2 Monitoring techniques | 6 |
| 1.2.1 Tunnel monitoring | 6 |
| 1.2.2 Strain measurements | 8 |
| 1.2.3 Deformation measurements | 10 |
| 1.3 Research objectives | 12 |
| 1.4 Structure of the dissertation | 13 |
| 2 Monitoring program: subject background | 15 |
| 2.1 Shield tunnelling projects in Belgium | 15 |
| 2.2 Diabolo project (Brussels Airport) | 15 |
| 2.2.1 Outline of the project | 15 |
| 2.2.2 Shield-driven tunnels | 16 |
| 2.2.3 Passage below hangar 117 | 18 |
| 2.3 Liefkenshoek project (Port of Antwerp) | 18 |
| 2.3.1 Outline of the project | 18 |
| 2.3.2 Shield-driven tunnels | 20 |
| 2.3.3 Crossing of River Scheldt and Port Canal | 22 |

| | | |
|----------|--|-----------|
| 3 | Monitoring program: methodology | 25 |
| 3.1 | Selected cross-sections | 25 |
| 3.1.1 | Diabolo tunnels | 25 |
| 3.1.2 | Liefkenshoek tunnels | 25 |
| 3.2 | Strain monitoring | 27 |
| 3.2.1 | Practical implementation of the strain gauges | 27 |
| 3.2.2 | Wireless strain gauge measurement system | 30 |
| 3.2.3 | USB strain gauge measurement system | 36 |
| 3.2.4 | Strain monitoring program | 37 |
| 3.3 | Ovalisation monitoring using laser scanning | 40 |
| 3.3.1 | Introduction | 40 |
| 3.3.2 | Laser scanning technique | 41 |
| 3.3.3 | Measurement methodology | 43 |
| 3.3.4 | Processing of the point cloud | 47 |
| 3.3.5 | Evaluation of ovalisation results | 50 |
| 4 | Monitoring program: results and observations | 53 |
| 4.1 | Noteworthy monitoring results | 53 |
| 4.1.1 | Initial stage after ring assembly | 53 |
| 4.1.2 | Stabilisation phase | 58 |
| 4.1.3 | Passage of the second TBM | 60 |
| 4.1.4 | Construction of cross-passages & evacuation shafts | 64 |
| 4.1.5 | Tidal influence of River Scheldt | 66 |
| 4.2 | Important observations | 68 |
| 4.2.1 | Governing construction phase | 68 |
| 4.2.2 | Local effects on lining behaviour | 70 |
| 4.2.3 | Complementary aspect of strain & ovalisation monitoring | 74 |
| 4.3 | Research subjects | 75 |
| 5 | Installation imperfections: monitoring results | 77 |
| 5.1 | Global cross-sectional deformations | 77 |
| 5.1.1 | Statistical approach of monitoring results | 77 |
| 5.1.2 | Reference measurement | 78 |
| 5.1.3 | First control measurement | 80 |
| 5.1.4 | Last control measurement | 80 |
| 5.1.5 | Evolution of tunnel radius | 82 |
| 5.2 | Segmental behaviour | 83 |

| | | |
|----------|---|------------|
| 5.2.1 | Joint imperfections | 83 |
| 5.2.2 | Segment rotations | 84 |
| 5.2.3 | Conclusion | 84 |
| 6 | Three-dimensional finite element model | 87 |
| 6.1 | SAMCEF Field | 87 |
| 6.2 | Composition of the FE-model | 89 |
| 6.2.1 | Choice of volume model | 89 |
| 6.2.2 | Geometry | 89 |
| 6.2.3 | Material properties | 96 |
| 6.2.4 | Contact joints | 96 |
| 6.2.5 | Loads | 99 |
| 6.2.6 | Boundary conditions | 103 |
| 6.2.7 | Computation of sectional forces | 106 |
| 6.2.8 | Mesh | 107 |
| 6.2.9 | Type of analysis | 108 |
| 6.3 | Results of the FE-model | 110 |
| 6.4 | Impact of the mesh size | 113 |
| 6.4.1 | Applied mesh configurations | 113 |
| 6.4.2 | Models using design geometry | 113 |
| 6.4.3 | Models including installation imperfections | 118 |
| 6.4.4 | Selection of the mesh size | 123 |
| 6.5 | Impact of the joint friction | 124 |
| 6.5.1 | Applied coefficients of friction | 124 |
| 6.5.2 | Models using design geometry | 124 |
| 6.5.3 | Models including installation imperfections | 125 |
| 6.5.4 | Selection of the coefficient of friction | 129 |
| 7 | Installation imperfections: effect on lining behaviour | 131 |
| 7.1 | Introduction | 131 |
| 7.2 | Tunnel section S2726 | 131 |
| 7.2.1 | Composition of the FE-model | 131 |
| 7.2.2 | Results of FE-calculations | 132 |
| 7.2.3 | Discussion | 138 |
| 7.2.4 | Selection of the coefficient of friction | 140 |
| 7.3 | Theoretical installation imperfections | 140 |
| 7.3.1 | Applied joint imperfection | 140 |
| 7.3.2 | Imperfect installation of 1 segment | 141 |

| | | |
|----------|---|------------|
| 7.3.3 | Imperfect installation of 1 joint | 146 |
| 7.3.4 | Imperfect installation of multiple segments | 146 |
| 7.3.5 | Conclusion | 153 |
| 8 | Observation of the tidal influence | 155 |
| 8.1 | Introduction | 155 |
| 8.2 | Tidal characteristics of River Scheldt | 156 |
| 8.3 | Description of the measurement set-up | 158 |
| 8.3.1 | Introduction | 158 |
| 8.3.2 | Strain measurements | 160 |
| 8.3.3 | Ovalisation measurements | 160 |
| 8.3.4 | Levelling measurements | 161 |
| 8.4 | Monitoring results of tidal influence | 162 |
| 8.4.1 | Levelling measurements | 163 |
| 8.4.2 | Ovalisation measurements | 166 |
| 8.4.3 | Strain measurements | 166 |
| 8.5 | Discussion | 171 |
| 9 | Clarification of the tidal movements | 175 |
| 9.1 | Introduction | 175 |
| 9.2 | Impermeability of Boom clay | 175 |
| 9.2.1 | Influence depth of tidal changes | 175 |
| 9.2.2 | Tidal effect on Boom clay | 178 |
| 9.3 | One-dimensional FE beam model | 182 |
| 9.3.1 | Characteristics of the beam model | 182 |
| 9.3.2 | Calculation results of the 1D FE beam model | 186 |
| 9.4 | Analytical calculation of settlements in Boom clay layer | 188 |
| 9.4.1 | Hydrodynamic theory of Terzaghi | 188 |
| 9.4.2 | Immediate elastic response calculation using E_0 | 190 |
| 9.5 | Discussion | 196 |
| 9.6 | 3D FE-model of tunnel cross-section | 198 |
| 9.6.1 | Composition of the 3D FE-model | 198 |
| 9.6.2 | Results of 3D FE-calculations | 199 |
| 9.7 | Conclusion | 204 |

| | |
|--|------------|
| 10 Conclusions | 207 |
| 10.1 Research conclusions | 207 |
| 10.1.1 Combined monitoring of segmental tunnel linings | 207 |
| 10.1.2 Early-stage behaviour | 208 |
| 10.1.3 Presence of installation imperfections | 208 |
| 10.1.4 FE-modelling using contact definitions | 209 |
| 10.1.5 Influence of installation imperfections | 209 |
| 10.1.6 Tidal influence | 210 |
| 10.2 Future research prospects | 212 |
| 10.2.1 Strain monitoring | 212 |
| 10.2.2 Ovalisation monitoring | 212 |
| 10.2.3 Design of segmental tunnel linings | 213 |
| 10.2.4 Tidal influence | 216 |
| Bibliography | 217 |
| A Keystone orientation in the monitored sections | 231 |
| B Passage of second tunnel drive: additional results | 241 |
| C Impact of the mesh size: additional results | 245 |
| D Impact of the joint friction: additional results | 251 |

List of symbols and abbreviations

Latin symbols:

| | |
|-------------|--|
| A | constant in empirical relation for G_0 |
| b | width of a tunnel ring |
| B | combined width of one segment, ring joint and kaubit strip |
| c_v | coefficient of consolidation |
| c' | effective cohesion |
| C | modulus of compressibility |
| C_1 | constant in best linear fit equation |
| d_e | concrete cover at the extrados |
| d_i | concrete cover at the intrados |
| D_{in} | inner tunnel diameter |
| D_{out} | outer tunnel diameter |
| e | void ratio |
| E_0 | small strain modulus of elasticity |
| E_c | Young's modulus of elasticity for concrete |
| E_{oed} | oedometer modulus |
| EI | bending stiffness |
| f_{ctm} | concrete tensile strength |
| F_f | frictional force |
| F_{grout} | resulting force of grout pressures |
| F_n | normal force in Coulomb friction formula |
| F_s | resulting force of soil pressures |
| F_w | resulting force of water pressures |
| g | standard gravity |
| G_0 | small strain shear modulus |

| | |
|--------------|---|
| h | vertical distance between top of tunnel and point on tunnel circumference (Chapter 6) |
| h | thickness of soil layer (Chapter 9) |
| h_{av} | long term mean water level in river |
| i | counter in reference to tunnel section |
| j | counter in reference to ovalisation measurement |
| k | permeability coefficient of soil |
| k_r | radial spring stiffness |
| k_v | vertical component of spring stiffness |
| K_0 | lateral earth pressure coefficient at rest |
| K_{rot} | rotational spring stiffness |
| $K_{v,down}$ | total vertical spring stiffness in downward direction |
| $K_{v,up}$ | total vertical spring stiffness in upward direction |
| L | wavelength of tidal wave |
| m | number of angular values for which a monitored radius is available |
| m_v | coefficient of volume compressibility |
| M_z | bending moment around the longitudinal z-axis |
| n | number of tunnel sections (Chapter 5) |
| n | number of observations (Chapter 8) |
| n | stress exponent reflecting the effect of the consolidation stress (Chapter 9) |
| N | tangential normal force |
| N_{max} | maximum tangential normal force |
| p_a | reference stress |
| q_c | cone resistance in a CPT |
| r | monitored radius value |
| r' | deviation of monitored radius r from inner tunnel radius R_{in} |
| r'_0 | r' for reference measurement |
| r'_1 | r' for first control measurement |
| \bar{r}' | mean deviation of monitored tunnel radius |
| R' | average deviation of inner tunnel radius for a single measurement |
| R'_i | average deviation of inner tunnel radius for one section |
| R_{in} | inner tunnel radius |
| R_{out} | outer tunnel radius |
| s | standard deviation |
| s_c | experimental standard deviation for control measurement |
| s'_c | experimental standard deviation for additional control measure- |

| | |
|------------|--|
| | ment after fire-resistant spaying |
| s_r | experimental standard deviation for reference measurement |
| s_t | settlement at time t |
| s_∞ | final settlement |
| SE | standard error |
| t | thickness of the tunnel lining (Chapter 2) |
| t | time (Chapter 9) |
| t_{slab} | slab thickness |
| t_{void} | thickness of the void between tunnel lining and soil |
| T | tidal wave period |
| T_v | time factor |
| u | joint irregularity (Chapter 5) |
| u | pore water pressure (Chapter 9) |
| \bar{u} | average joint irregularity |
| u_0 | pore water pressure at top of clay layer |
| U | degree of consolidation |
| x | random unknown (Chapter 3) |
| x | horizontal position (Chapter 9) |
| z | vertical distance below surface level |
| z' | vertical distance in clay layer |
| z_{top} | depth of tunnel top below surface level |
| z_w | vertical distance of the water level below the surface level |

Greek symbols:

| | |
|--------------------|---|
| Δh_w | water level variation in river |
| $\Delta h_{w,av}$ | average water level variation in river |
| $\Delta h_{w,max}$ | maximum water level variation in river |
| $\Delta h_{w,min}$ | minimum water level variation in river |
| Δr_{0-1} | variation of inner tunnel radius between reference measurement and first control measurement |
| Δu | variation of joint irregularity u |
| Δz | height of soil layer |
| $\Delta \epsilon$ | variation of strain |
| $\Delta \gamma$ | variation of angular rotation γ |
| $\Delta \sigma'$ | effective soil stress variation |
| γ | angular rotation of tunnel segment |
| $\bar{\gamma}$ | average value of angular rotations of tunnel segments |
| γ' | effective unit weight of soil |

| | |
|----------------------|--|
| γ_c | unit weight of concrete |
| γ_d | dry unit weight of soil |
| γ_{grout} | unit weight of liquid grout |
| γ_s | saturated unit weight of soil |
| γ_w | specific gravity of water |
| φ' | effective angle of internal friction |
| μ | population mean (Chapter 5) |
| μ | coefficient of friction (Chapters 6 to 10) |
| μ_0 | population mean for reference measurement |
| μ_{0-1} | population mean for difference between reference measurement and first control measurement |
| μ_1 | population mean for first control measurement |
| $\mu_{R'}$ | population mean for R' |
| μ_u | population mean for joint irregularity u |
| $\mu_{\Delta u}$ | population mean for variation of joint irregularity Δu |
| $\mu_{\Delta\gamma}$ | population mean for variation of angular rotation $\Delta\gamma$ |
| $\mu\epsilon$ | microstrain (unit of strain) |
| μ_γ | population mean for angular rotation γ |
| ν | Poisson's ratio |
| ν_c | Poisson's ratio for concrete |
| ρ_c | mass density of concrete |
| ρ_w | specific mass of water |
| σ | population standard deviation |
| σ_{grout} | radial grout pressure |
| σ_w | radial water pressure |
| σ' | consolidation stress |
| σ'_h | effective horizontal soil pressure |
| σ'_r | effective radial soil pressure |
| σ'_t | effective tangential soil pressure |
| σ'_v | effective vertical soil pressure |
| θ | tunnel angle with respect to vertical axis (clockwise direction) |

Abbreviations:

| | |
|-----|-----------------------|
| 1D | one-dimensional |
| 2D | two-dimensional |
| 3D | three-dimensional |
| CAD | computer-aided design |
| CI | confidence interval |

| | |
|-------|--------------------------------|
| CM | control measurement |
| CP | cross-passage |
| CPT | cone penetration test |
| ES | evacuation shaft |
| FBG | fibre Bragg grating |
| FE | finite element |
| LDC | low duty cycle |
| LM | levelling measurement |
| MB | megabyte |
| NATM | new Austrian tunnelling method |
| RC | resistor-capacitator |
| RMSE | root mean squared error |
| rebar | reinforcement bar |
| SE | standard error |
| TAW | tweede algemene waterpassing |
| TBM | tunnel boring machine |
| VW | vibrating wire |

Chapter 1

Introduction

1.1 Segmental tunnel linings

1.1.1 Application

An important part of the underground construction industry is based on the use of mechanised tunnelling techniques such as closed-shield tunnelling. Although their application depends on specific project parameters, the use of shield tunnels offers several advantages in comparison with classic methods, such as ‘cut-and-cover’, regarding impact on existing structures, noise, vibrations and often financial costs. While new transportation and utility tunnels are created underground, the surface above the tunnel alignment remains mostly undisturbed, apart from the launch and arrival shafts. In addition, an increasing number of tunnels is planned beneath various obstacles that leave no alternative construction method but shield tunnelling. Whether due to severe restrictions toward settlements in highly urbanized areas or as a result of large groundwater pressures, an extensive number of projects benefits from the closed-shield tunnelling technique to overcome the boundaries that once seemed ‘a bridge too far’. One can think of several examples, such as excavating the subsoil of large metropolitan areas, tunnelling beneath airport infrastructures, or crossing busy waterways.

1.1.2 Construction methodology

Closed-shield tunnelling is most often used in soft ground, such as sands and clays. In these cases, it implies the use of a segmental tunnel lining as primary

or solitary load-bearing component. A segmental lining consists of precast concrete segments, constructed in a prefabrication plant using very precise tolerances, up to 0.2 mm (Harding & Chappell, 2014). The segments are equipped with a steel cage of traditional reinforcement bars (rebars) in the majority of the projects, although recently steel fibres are used in an increasing number of projects in addition to or in replacement of the rebars (Tiberti & Plizzari, 2014).

The soil is excavated using a tunnel boring machine (TBM). The tunnel lining is constructed by assembling the individual concrete segments one by one into a tunnel ring close to the excavation face, under protection of the TBM shield. The positioning of the segments is done using a vacuum erector, a hydraulic crane that is controlled by an operator, based on observations and indications by the crew. This procedure is therefore prone to human error, resulting in small installation imperfections of the circular tunnel rings that are an inevitable part of segmental lining construction (Rossler *et al.*, 2012). The TBM uses hydraulic jacks to push itself off from the last installed ring, until sufficient soil has been excavated and the next tunnel ring can be erected. Usual practice is to apply a staggering joint configuration (joints between segments in one tunnel ring coincide with the middle of the segments in the adjacent rings) in order to increase the tunnel's bending stiffness (Jones, 2015a). The void between the tunnel lining and the soil is filled with grout at the tail of the TBM shield. Figure 1.1 gives a visual representation of the construction method.

Longitudinal joints are present between segments in a single tunnel ring. At these locations, the concrete segments are often in plain contact over a part of their thickness, without packing materials. Between adjacent tunnel rings, circumferential joints are present. Again there is contact between the concrete segments, but these joints are generally supplied with packing materials of small thickness (around 2 mm)(Arnau & Molins, 2012), such as plywood plates (Ring & da Fonseca, 2014), plastic plates (Arnau & Molins, 2015) or kaubit strips (a bituminous material). To limit deformation differences between adjacent rings, a coupling system is often used in the circumferential ring joints, e.g. cam and socket (Arnau & Molins, 2012) or bicones (Ring & da Fonseca, 2014).

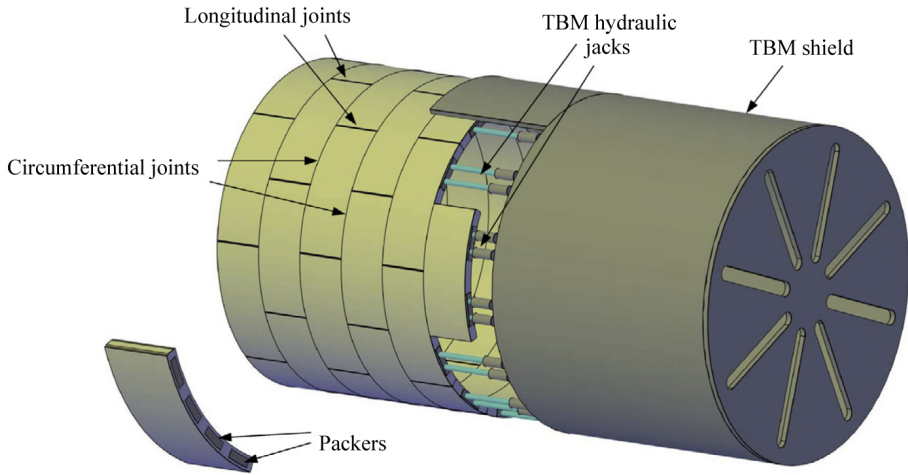


Figure 1.1. Installation of lining segments in a TBM (Arnau & Molins, 2015).

1.1.3 Design approach

Load states

For many years, various theoretical models have been used to design segmental tunnel linings. In general, a correct identification of the loads acting on the reinforced concrete segments is an essential step in the design process of the tunnel lining. Defining these loads however is one of the most challenging aspects of underground projects (Grübl, 2012; Ishimura *et al.*, 2013). Due to the complex nature of the mechanised tunnelling procedure, shield tunnelling requires consideration of the loads during construction of the segmental lining (Mashimo & Ishimura, 2006; Jones, 2015a). Determination of the loads during ring erection, advance of the TBM, building-up of earth pressure and bedding of the articulated ring is quite complicated (Grübl, 2012). As a result, the assembly of the lining is generally neglected in the design stage, and an ideal situation is assumed as initial condition for the calculations, which is probably not realistic (Bakker & Bezuijen, 2009b). However, as very few measurement results of actual tunnel lining behaviour at an early stage are available, estimating the accuracy of the theoretical model output in comparison with the in situ material behaviour remains very difficult.

Naturally, tunnel linings are designed with respect to the soil and groundwater pressures, acting along the tunnel profile, together with possible overburden loads on the surface level. The soil pressures on the lining are assumed to be equal to the primary stresses in undisturbed soil, prior to excavation. All

these loads can mostly be considered constant in the applied design methods (Duddeck & Erdmann, 1985; ITA Working Group on General Approaches to the Design of Tunnels, 1988). However, numerous other load conditions occur during and after construction which have to be taken into account when designing the tunnel lining, in order to ensure the long-term durability of the underground structure (Blom, 2002). These include jack forces, tail grouting pressures, traffic loads and accidental loads such as fires or earthquakes (Working Group No. 2 International Tunnelling Association, 2000). In addition, for tunnels located below a sea or a tidal river, the water pressure continuously varies in accordance with the tidal fluctuations. In these cases, the influence of the changing tide should be taken into consideration in tunnel lining design (Lin *et al.*, 2015).

The design is generally reduced to a (semi-)two-dimensional approach for the most critical cross-sections (Jones, 2015a; Do *et al.*, 2013). It is assumed that the erection of a ring results in a perfectly circular tunnel ring. Multiple approaches can be applied to calculate the sectional forces in the tunnel lining.

Analytical calculations

Analytical calculations use a simplified representation of the tunnel cross-section and are often used in the preliminary design. Most of these models assume plane-strain conditions for the lining and the ground. In the elastic equations method, a uniform bending rigidity is assumed for a single lining ring and the soil is viewed as a continuum (Lin *et al.*, 2015). Member forces are calculated using elastic equations available in literature (JSCE, 2007; Working Group No. 2 International Tunnelling Association, 2000). Another widely adopted approach is the beam-spring method, which is based on the work of Duddeck (1980) and applies the following principles (Bakhshi & Nasri, 2014):

- Segments are modelled as beam elements;
- Soil loading is modelled as active loading, while soil support is modelled by linear translational springs in radial, tangential and longitudinal directions. The elasticity of the springs might be reduced at the top of the lining in case of limited soil cover;
- The presence of the longitudinal joints is either neglected, by assuming a solid ring with full bending rigidity, or averaged out, by assuming a solid ring with reduced bending rigidity (Muir Wood, 1975), or modelled using hinges, with or without rotational stiffness. In the latter case,

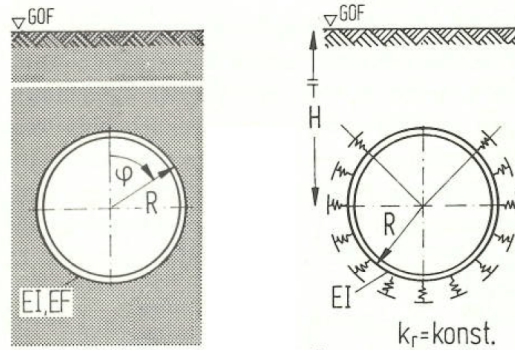


Figure 1.2. Common types of analytical models for tunnel design: continuum model (left); bedded beam model (right) (Erdmann & Duddeck, 1983).

the determination of the non-linear stiffness of the rotational springs is derived from the theory developed by Janssen (1983);

- Ring interaction in the circumferential joints is either neglected (resulting in a 2D model) or modelled using shear springs. In the latter case, a so-called two-and-a-half-dimensional model is applied where multiple rings are considered to take into account the effect of the staggering joint configuration. The coupling springs are radially orientated and account for the behaviour of the coupling system and the friction of the concrete and packing materials.

Examples of both types of calculation models are shown in Figure 1.2.

Finite element calculations

For the final design of the tunnel lining, finite element (FE) models are applied. A distinction can be made between continuum models and bedded ring models. The former primarily focus on the behaviour of the soil, which is considered as a continuous medium, and account for full or partial bonding between the lining and the soil (Zhang *et al.*, 2015). In general, only a two-dimensional approach is used (Bakhshi & Nasri, 2014). The bedded ring approach models the soil support using radial and tangential springs (Arnau & Molins, 2015), similar to the analytical beam-spring method. In most of these models, the two-dimensional approach of the lining design is expanded by modelling multiple adjacent rings, to account for coupling of the rings (Arnau & Molins, 2015). The lining can be modelled using beam, shell or volume elements (Arnau &

Molins, 2015; Ring & da Fonseca, 2014; Tajima *et al.*, 2006). Finally, additional FE-models might be developed for a detailed study of the impact of the jacking forces (Bakhshi & Nasri, 2014), the presence of cross passages (Della Valle *et al.*, 2014), etc. Examples of the various types of FE-models are shown in Figure 1.3.

In all FE-models, the joints between the tunnel segments represent a simplification of reality, similar to the analytical approaches. As a consequence, convergence of the FE-models can easily be obtained without any problems and calculation times are kept within limits (Do *et al.*, 2013). However, the question remains whether these simplifications do not lead to overdimensioning in some areas and underestimation of some influences in other areas.

1.1.4 Frequent damage mechanisms

During construction of a segmental tunnel lining, various situations occur that cause stress concentrations in the lining segments. As the construction phase is not adequately covered in the current models, these large stresses are not predicted in the design. As a result, damage to the lining is often observed during the installation stage, which influences the structural durability on the long term. Observations show that virtually all the significant damage occurs during ring installation and initial advance of the TBM in the first three to four, at most ten, rings after the TBM (Grübl, 2006). The most frequent types of damage to the lining segments are: longitudinal cracks due to radial eccentricities in the jacking loads or uneven support in the circumferential joint (Jones, 2015b), spalling of the segment edges (Tiberti & Plizzari, 2014) and chipping of the segment corner (Cavalaro *et al.*, 2011). The majority of this damage is caused by contact deficiencies in the segment joints. Therefore, accurate ring assembly is of major importance in the prevention of damage to the tunnel lining.

1.2 Monitoring techniques

1.2.1 Tunnel monitoring

Instrumentation and monitoring are an essential part of current tunnelling practice. They can provide valuable information for safe and economical tunnelling in sensitive environments. The main objectives of tunnel monitoring are (The British Tunnelling Society and The Institution of Civil Engineers, 2004):

- to obtain information on the ground response to tunnelling;

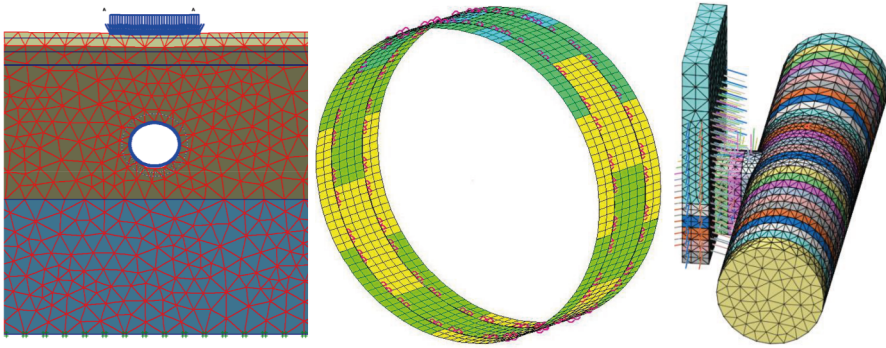


Figure 1.3. Various types of FE-models for tunnel design: continuum model (left); bedded ring model (centre); volume model studying the presence of an evacuation shaft (right) (Bakhshi & Nasri, 2014; Ring & da Fonseca, 2014).

- to provide construction control;
- to verify design parameters and models;
- to measure the performance of the tunnel lining during and after construction;
- to monitor impact on the surrounding environment, such as surface settlement and groundwater regime.

The main purpose lies in the optimisation of the design and execution of safe tunnelling works. The required degree of effort and expense employed for instrumentation and monitoring depends on the nature of the project, perceived hazards and the level of risk. In high-risk environments, such as shallow tunnels in variable soil conditions, the benefits of monitoring are even more important. Therefore, structural monitoring should be viewed as an integral part of the construction process (AITES/ITA WG2-Research, 2011).

When monitoring a tunnel structure, there is an important distinction to be made between monitoring the impact of the tunnel construction on the surface level and surrounding infrastructure, and monitoring the behaviour of the tunnel itself. In shield tunnelling, the monitoring program generally incorporates the registration of various geotechnical parameters, such as surface settlements, piezometric levels and borehole displacements. In addition, structural parameters can be monitored as well, such as the deformations and stresses of the lining. As a result, typical tunnel monitoring sections might include

instrumentation to measure stresses, strains, relative and/or absolute displacements and changes in lining curvature. Common types of instrumentation are extensometers, pressure sensors, strain gauges, load cells, tape extensometers and piezometers (AITES/ITA WG2-Research, 2011).

Over the decades, monitoring techniques have been considerably improved, resulting in accurate instrumentation devices. In this research, the main focus lies on the combined monitoring of strains in the concrete lining and deformations of the tunnel cross-section. The variety of available techniques for these purposes are presented in the next sections.

1.2.2 Strain measurements

Different types of strain gauges

While there are several methods of measuring strains, the most common is with a strain gauge (Figure 1.4). The most widely used gauge is the bonded metallic strain gauge. The working principle of this type of strain gauge is based on the variation of electrical resistance in proportion to the amount of strain (Hoffmann, 2012). To accurately measure these small changes in resistance, additional signal conditioning is necessary, often in the form of a Wheatstone bridge resistance network. In order to transfer the strain of the object under investigation to the strain gauge without any losses, a close bond is required between both. The use of an adhesive is the most significant method to ensure a perfect bond, although spot welding and fixing with ceramic materials is also used. This type of strain gauges was developed more than 50 years ago, making them technically mature today and available in many shapes and sizes. They provide a high accuracy for measuring local strains in a single point. As a result, metallic strain gauges are implemented in numerous applications.

Another common type of strain gauges are vibrating wire (VW) strain gauges, which are often applied in geotechnical applications (Sharma *et al.*, 2000). They are designed to be welded to or embedded in various structures. A VW strain gauge essentially consists of a steel wire tensioned between two supports at a predetermined distance. Variation of this distance alters the natural frequency of vibration of the wire, which allows to determine the change in strain causing it (Lee & Park, 2013). The main advantages of this type of strain gauges are that their frequency output is immune to electrical noise and their ability to tolerate wet wiring (The British Tunnelling Society and The Institution of Civil Engineers, 2004).

Finally, fibre optic sensors have become increasingly popular recently. Their

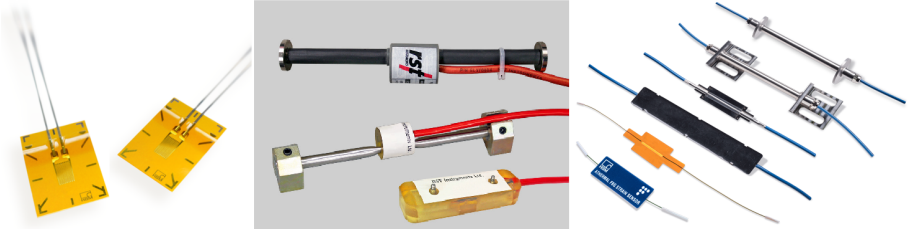


Figure 1.4. Various types of strain gauges: metallic strain gauges (left); vibrating wire strain gauges (centre); fibre optic strain gauges (right) (Hottinger Baldwin Messtechnik GmbH, 2016a,b; RST Instruments, 2016).

principle is mainly based on the fibre Bragg grating (FBG) technology, where a glass optical fibre is modified in order to measure the effect of strains on the reflected wavelength of light in the fibre (Majumder *et al.*, 2008). Multiple sensors can be chained along a single optical fibre, which can be embedded or mounted on a structure. FBG optical strain sensors provide an advantage in applications that are exposed to harsh environments and require long-range, long-term deployments. Additionally, they are immune to electromagnetic interference. This is ideal for applications requiring sensor measurements in close proximity to noise sources such as power transformers, electric motors, etc (The British Tunnelling Society and The Institution of Civil Engineers, 2004).

Strain monitoring in tunnelling applications

Monitoring the strains in a segmental lining during the whole construction process and later, during the lifetime of a tunnel, is useful to gain a deeper knowledge of its real performance. Due to the harsh conditions in tunnelling applications, vibrating wire strain gauges are commonly used (Lin *et al.*, 2015; Bilotta *et al.*, 2005; Bilotta & Russo, 2012), as they are easily embedded in the concrete lining. Additionally, fibre optic sensors are more and more applied (Huang *et al.*, 2013), allowing the implementation of multiple sensors using a single wire. In literature, almost no examples are found where common metallic strain gauges are used to monitor strains in a tunnel lining. Nonetheless, classic strain gauges are a well-established technology, providing a familiar and cost-effective solution (National Instruments, 2016). They can be installed at various locations on the reinforcement bars or concrete surface of the tunnel segments. Consequently, they were chosen for application in the experimental monitoring program presented in this research.

1.2.3 Deformation measurements

Techniques for tunnel deformation monitoring

Various techniques for tunnel convergence monitoring can be used or combined, whether installed on the tunnel surface or operated from within the tunnel. Tunnel convergence can be measured using tape extensometers (contact method) or using a total station (non-contact method). Applying metal tape extensometers to measure distances between fixed points on the tunnel surface can result in an accuracy of around 0.2 mm to 0.5 mm (Clarke, 1996; Kavvadas, 2003; Kontogianni & Stiros, 2005). To measure deformations of the tunnel surface in three dimensions, a total station can be used to monitor prism reflectors fixed to the tunnel surface. In this case, only a limited number of points can be measured in a fixed time frame (Clarke, 1996; Alba *et al.*, 2006). When using motorised high precision total stations in combination with automatic target recognition, the tunnel convergence can continuously be measured and results can be transferred to a computer, giving a warning when predefined thresholds are reached (Henriques & Casaca, 2006). Using conventional techniques such as total station measurements to obtain the necessary number of points for a detailed profile of the tunnel is very time consuming and not feasible during the construction works on site (Huang *et al.*, 2010).

A first alternative to cover more points on the tunnel surface is the use of so-called ‘tunnel profile scanners’ or profilometers, with an achievable accuracy of around 5 mm. These instruments are based on the photogrammetric principle of recording stereographic images with two cameras mounted on a fixed frame. However, because sufficient overlap between the stereographic images and minimum lighting conditions are needed, this technique can often not be applied in tunnel monitoring projects. High resolution laser scanning is another method which allows covering a larger part of the tunnel structure with a dense point grid, either from a static set-up or from a mobile platform (Qingwu & Wanlin, 2012; Yoon *et al.*, 2009). Because laser scanning is an active measurement technique, restrictions for lighting conditions are not to be considered. Previous experiments using laser scanning data to detect tunnel deformations resulted in an accuracy of about 2 to 5 mm (Yoon *et al.*, 2009). Moreover, laser scanning results in a dense and detailed point cloud of a larger part of the tunnel than just a single cross-section. This is illustrated in Figure 1.5. Because of this large amount of information, the measured point cloud of the tunnel structure can also be used for further processing, such as 2D or 3D individual segment monitoring, checking the piping infrastructure or installed railway facilities,

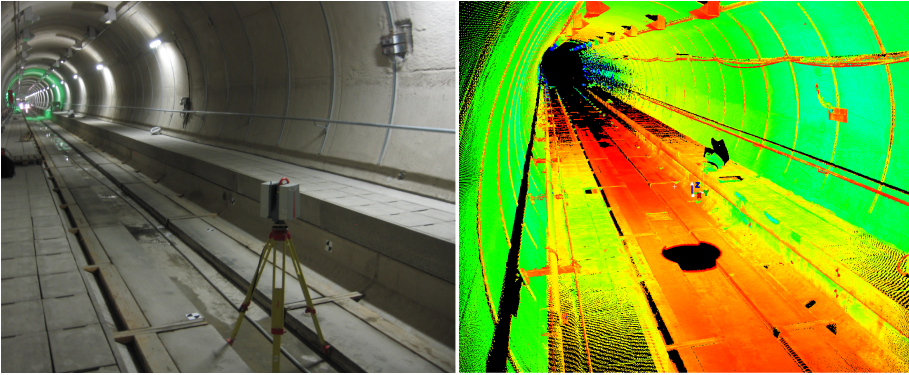


Figure 1.5. Actual tunnel interior (left) and corresponding point cloud resulting from laser scanning (right).

etc. However, the cost of the equipment and the relatively limited amount of available automated processing algorithms for huge 3D point clouds have been important barriers for a practical implementation of laser scanning in a wide range of projects (Hesse & Stramm, 2004; Iyer *et al.*, 2005; Rahayem *et al.*, 2012; Sternberg & Kersten, 2007; Walsh *et al.*, 2013).

Laser scanning in tunnelling applications

Based on the recent advances in 3D measurement techniques and the need for detailed 3D information in tunnelling applications, the laser scanning technique is being applied in this research for deformation monitoring of segmental tunnel linings. It allows to overcome several restrictions, such as the available time on site and the accessibility, whereas traditional surveying techniques often fail to meet such project requirements (Nuttens, 2014). Using laser scanning, a large amount of points can be measured in a very short time frame (up to one million points per second) with a detailed accuracy (millimeter-level) (Boehler & Marbs, 2003; Lichti *et al.*, 2000; Rioux, 1994). Examples indicate detectable damage, cracks or deformations of 2 mm or larger (Yoon *et al.*, 2009). Furthermore, a large part of a tunnel structure is recorded, without limiting the measurements to specific points or dimensions of the structure. The high resolution point set is available for further processing, allowing the identification of individual tunnel segments and joints and possible changes in position caused by the deformation of the tunnel structure.

1.3 Research objectives

The main objectives of this research are:

- Development of an experimental monitoring program for the structural verification of segmental tunnel linings, combining strain and ovalisation measurements for an accurate identification of the tunnel lining behaviour, during construction as well as after completion;
- Determining whether strain and ovalisation measurements provide a complementary data set, where results of both techniques are in good agreement and supplement each other, or if they might show contradictions in the combined results. Find out if one monitoring method is more representative than the other and could suffice for a detailed assessment of the structural behaviour;
- Verifying whether various loads during the early stage of construction have a substantial impact on the stresses and deformations of the tunnel lining, and might be governing in the design of shield-driven tunnels;
- Development of a detailed FE-approach, surpassing the current state of the art, in order to simulate the complicated three-dimensional deformation state in the initial period after ring assembly and the corresponding stresses in the lining segments;
- Determining the magnitude of installation imperfections due to inaccurate assembly of the lining segments, mainly in the longitudinal lining joints;
- Providing the ability to implement these installation imperfections in the FE-model, in order to evaluate their impact on the structural behaviour of the segmental lining.
- Formulating possible improvements to the design models of segmental tunnel linings, in order to enhance their safety and durability, based on the results of FE-analysis and structural monitoring;
- Clarifying the structural response of the tunnel lining in reaction to tidal fluctuations of the water level, by combining results of strain, ovalisation and levelling measurements;
- Identifying the origin of vertical movements of the tunnel lining, attributed to the oscillating water level in the river, by investigating the effect of the river tides on the tunnel lining and surrounding soil layers.

1.4 Structure of the dissertation

The previous sections provided the general context and the objectives of this research. In the following chapters, a detailed description is given of the various stages of the research in search for the correct answer to the research questions.

In the first part of the research, an experimental monitoring program was developed in order to verify the behaviour of segmental tunnel linings during and after construction. First, Chapter 2 will provide some background on the tunnelling projects that formed the main subject of the monitoring program. In Chapter 3, the main methodology will be discussed of the extensive strain measurements and laser scanning measurements that were performed in these tunnels. Next, Chapter 4 will show some of the most important monitoring results and observations that were made during and after tunnel construction. Based on these observations of the experimental monitoring program, two main focus points will be selected for further investigation in this dissertation. Firstly, the impact of installation imperfections during the assembly of the tunnel lining will be studied. For this purpose, the results of the laser scanning measurements are analysed in detail in Chapter 5. In the following chapter, an advanced 3D finite element model is developed using SAMCEF Field, modelling all joints between the individual tunnel segments using contact conditions. In Chapter 7, this model will be applied to determine the impact of the installation imperfections on the sectional forces and deformations of the tunnel lining. In the last part of this dissertation, the influence of the presence of a tidal river along the trajectory of the Liefkenshoek tunnel will be investigated. First, a clear identification of the structural response to the tidal effect is pursued in Chapter 8, combining the results of strain, ovalisation and levelling measurements. Next, in Chapter 9, several hypotheses will be studied in order to determine the origin of the tunnel response to the tidal fluctuation of the water level in River Scheldt. Finally, Chapter 10 summarizes all conclusions of the presented research and offers some possible future research tracks.

Chapter 2

Monitoring program: subject background

2.1 Shield tunnelling projects in Belgium

In Belgium, several tunnelling projects have been launched in the last decade in order to extend the Belgian railway network. Among them are the Antwerp north-south link tunnel, located along the international high-speed railway lines (Van Bogaert & Vereerstraeten, 2005), an improved connection to Brussels Airport, known as the Diabolo project (Van Bogaert & De Pauw, 2008), and a new freight connection in the Port of Antwerp, called the Liefkenshoek rail link (Van Bogaert, 2008, 2009). The start of recent tunnel works has been an excellent opportunity to accompany the boring process with an experimental monitoring programme. After the first experiences with strain gauge measurements and ovalisation measurements in the Diabolo tunnel, an improved monitoring programme was pursued in the Liefkenshoek tunnel.

2.2 Diabolo project (Brussels Airport)

2.2.1 Outline of the project

Brussels Airport is located at less than 8 km from the city centre, thus offering easy connections to all passengers travelling to various activities at the heart of Europe. However, up until a few years ago, this short distance to the city caused many problems for reaching the airport, especially by road congestion.

As for public transportation, the airport was easily reached by train, but not for passengers travelling from the north of the country, since the airport connections necessarily went via one of the Brussels stations. This situation has inspired authorities to improve the railway and road connection to the airport. The largest part of the ambitious project was concerned with establishing a direct railway link between the existing underground dead-end station and a new line between Brussels and Mechelen, located at the central reservation of the motorway between these cities.

Figure 2.1 shows the project area of the airport. In the centre, the airport facilities are shown, as well as the existing underground station, which was extended by some 300 m. The new railway link then runs to the north-west, down the main runway and taxi-lanes, leaving the airside below the industrial area of companies involved in handling goods or airway-related industry. Subsequently, the line is split by switches and joins the new tracks in the central reservation of the motorway in both directions of Brussels and Mechelen. Because of the triangular plan view of tracks near the motorway, which is also found to the south side at the connection to the renewed railway line from Brussels to Louvain, the project received its name after the resembling diabolo toy.

Obviously, the airport traffic could not be interrupted for a longer period. Hence, apart from the station, the crossing below these facilities was constructed by a twin bored tunnel. The remaining parts could be built by various ‘cut-and-cover’ methods.

2.2.2 Shield-driven tunnels

The bored tunnel section has a length of 1080 m and crosses below the air side. It consists of two shield-driven circular sections of 7.30 m inner diameter. The tunnel lining consists of precast concrete elements in C50/60 concrete quality, which are assembled into a sequence of tunnel rings as the excavation progresses. Each ring is 1.50 m wide and consists of seven concrete segments and a smaller keystone, with a thickness of 0.35 m. The TBM is of the mix shield type and has a diameter of 8.20 m. The geometry of the tunnel lining is shown in Figure 2.2. It should be noted that the orientation of the keystone (‘K’) varies for every tunnel ring, as a staggering joint configuration is applied.

Figure 2.3 shows the longitudinal profile of the shield-driven tunnel section. The soil conditions encountered along the trajectory are quite favourable, since the substratum consists of tertiary medium sand, which also contains soft sand-



Figure 2.1. Overview of the Diabolo project: A. present extended railway station; B. shield-driven tunnels below runway; C. northern connection to Brussels; D. connection to Mechelen; E. eastern connection to Brussels; F. connection to Louvain.

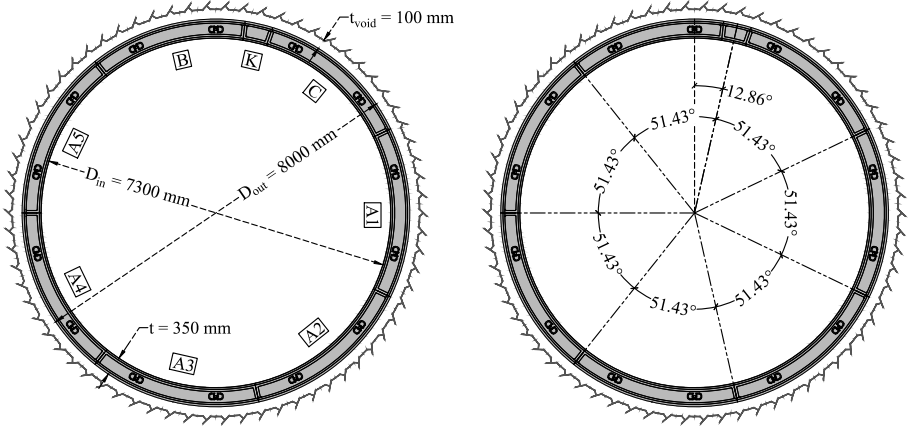


Figure 2.2. Geometry of the Diabolo tunnels.

stone horizons. In some areas, the sandstone has become decalcified and cavities appear below the stone layers. This caused some minor problems during the excavation process, as suspension and injection materials were suddenly lost through the cavities. The sand continues to 35 m depth and is followed

by soft tertiary clay. As the project does not reach this depth, excavation or building in clay can be avoided. The ground water level is about 2 m higher than the tube crown and slightly rises towards the station. Initially, excavation on the first tunnel tube (tunnel B) started in April 2009 from the north side and reached the arrival shaft by the end of June. The second drive (tunnel A) then started in September and was executed in an identical direction as the first one, keeping the soil and materials installations operational at the same location. Late October 2009, breakthrough of the second tube was realized.

Safety of passengers in railway tunnels is an important issue, especially in sensitive locations such as near airports. Hence, cross-passages between both tunnels have been foreseen, as well as a central escape route. The latter connects both tubes to a vertical shaft and staircase and a smaller tunnel, which ends on the existing airport service road. Both the cross-passages and evacuation shaft must be built without ground water lowering, to prevent large settlement of the airport facilities. Consequently, the cross-passages are to be built by freezing of the soil and subsequent excavation using the New Austrian Tunnelling Method (NATM) with sprayed concrete.

2.2.3 Passage below hangar 117

An important obstacle close to the departure location of the tunnels was hangar number 117, used by Brussels Airlines for maintenance of smaller aircraft. As this building is just 60 m away from the entrance shaft, the crossing was considered critical. The hangar has a foundation of precast concrete piles and, at some locations, the tunnel crown is at 2 m distance from the pile base. This can be observed in Figure 2.3, and is illustrated more in detail in Figure 2.4. There was a risk that, while boring the tunnels, causing destabilization of the surrounding soil mass, the piles would suddenly collapse. Reinforcement of the piles by passive jet grouting was considered to provide sufficient strength, nonetheless the crossing of hangar 117 remained a critical section in the construction process.

2.3 Liefkenshoek project (Port of Antwerp)

2.3.1 Outline of the project

The Liefkenshoek project, completed in 2014, is one of the largest infrastructural projects in Belgium in the last decade. Due to the intensive traffic in

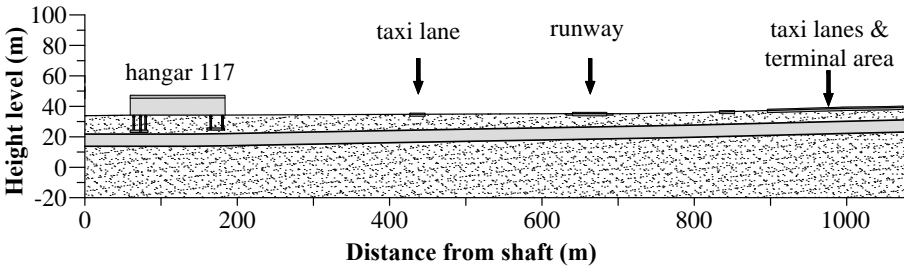


Figure 2.3. Longitudinal profile of the Diabolo tunnel.

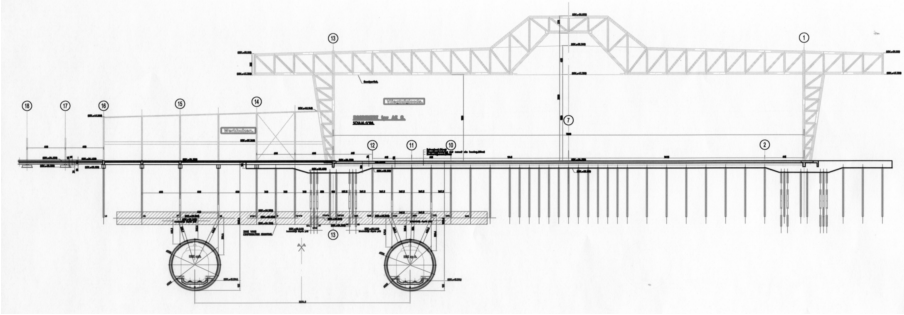


Figure 2.4. Critical tunnel excavation below hangar 117.

the Port of Antwerp, a considerable increase of goods transportation by train is being expected. While the main railway hub is located on the right bank of River Scheldt, a new tidal dock, called ‘Deurganckdok’, is completed on the left bank, having a future annual capacity of 7.5 million containers. The location of both is shown in Figure 2.5. As soon as the new dock will be in full operation, the traffic expectancy between both river banks will exceed 100 freight trains a day, weighing up to 2000 tons instead of the previous 700 tons. The existing harbour facilities showed only one rail link below the river, namely the Kennedy tunnel, which already suffered from traffic congestion. As a solution to this capacity shortage, the Liefkenshoek project established a new railway connection for freight traffic between the left and right bank section of the Port of Antwerp, enabling the circulation of freight trains without having to leave the port area. As a result, operational costs are lowered considerably as the distance by rail between both banks is reduced to 22 km instead of 47 km. The new rail link has a total length of approximately 16 km.

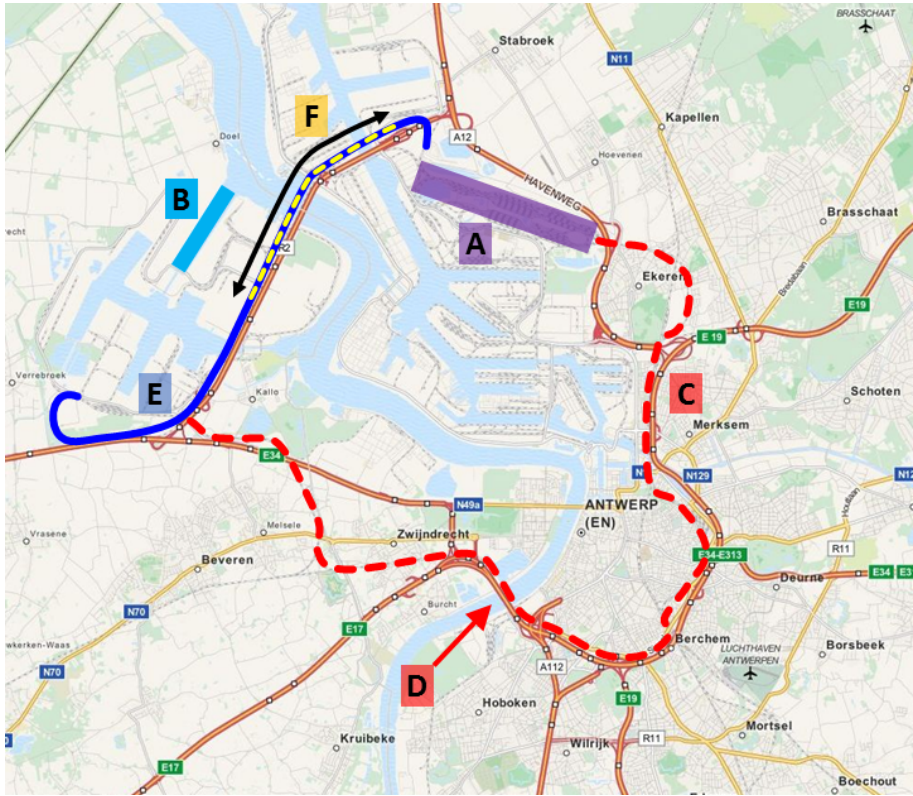


Figure 2.5. Overview of the Liefkenshoek project: A. main railway hub; B. Deurganckdok; C. existing railway link; D. existing Kennedy tunnel; E. Liefkenshoek project; F. shield-driven tunnel section.

2.3.2 Shield-driven tunnels

A section of six kilometres was constructed as a twin bored tunnel by two shield-driven TBMs using the mix shield method (Boxheimer & Mignon, 2009). The parallel tunnels were labelled as tunnel north and south, based on their location. Both single-track tunnels were excavated below River Scheldt and the Port Canal. The geometry shows a lot of similarities with the Diabolo project. Again, an internal diameter of 7.30 m is present and seven concrete segments and a smaller keystone in C50/60 concrete quality are used in each ring. However, in this project, each tunnel ring is 1.80 m wide. Furthermore, due to the large water pressures below the river, a lining thickness of 0.40 m was chosen, resulting in an outer diameter of 8.10 m. The total diameter of the TBM shield equalled 8.39 m. Consequently, an annular tail void of

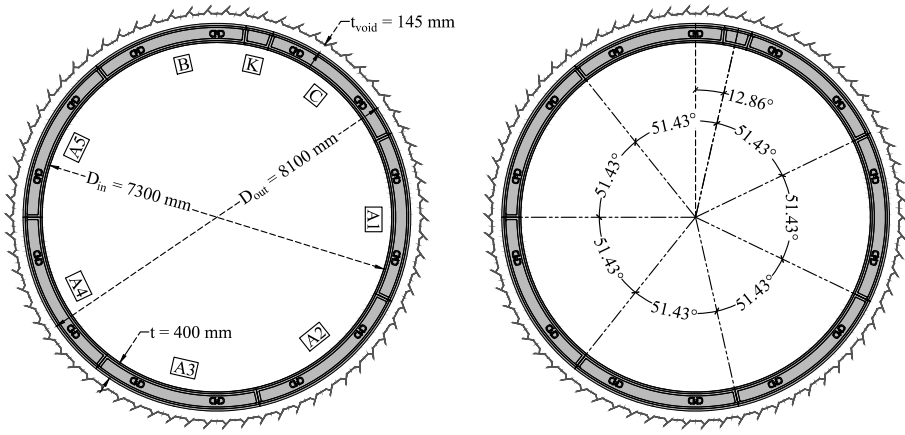


Figure 2.6. Geometry of the Liefkenshoek tunnels.

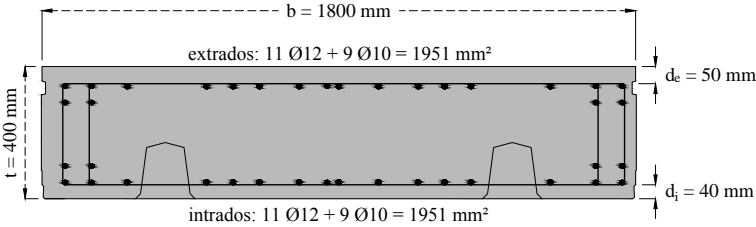


Figure 2.7. Cross-section of a tunnel segment and positioning of reinforcement bars.

approximately 15 cm had to be filled with a grout mixture. The geometry of the tunnel rings is shown in Figure 2.6. Again, a staggering joint configuration is applied, resulting in a variable position of the keystone. Figure 2.7 shows the arrangement of the steel reinforcement bars (rebars) in the segment cross-section. An identical reinforcement section of 1951 mm^2 is found at the inner and outer side.

Figure 2.8 gives an overview of the tunnel alignment and geology. Soil investigations showed a rather variable composition along the tunnel axis (Van Bogaert, 2009). The stratum at the project site comprises a total of eleven layers (DOV, 2015; Laga *et al.*, 2001), governed by a general downward slope from the west towards the east. The left bank of the River Scheldt consists of sandy surface layers, below which quaternary soil is found as soft clay. At larger depth the soil composition is mainly governed by fine sands of the tertiary era, which contain silt and lenses of clay. On the right bank of the river, all these sandy layers are significantly thicker compared to the left bank. The soil at a greater depth consists of Boom clay, a rigid and overconsolidated tertiary

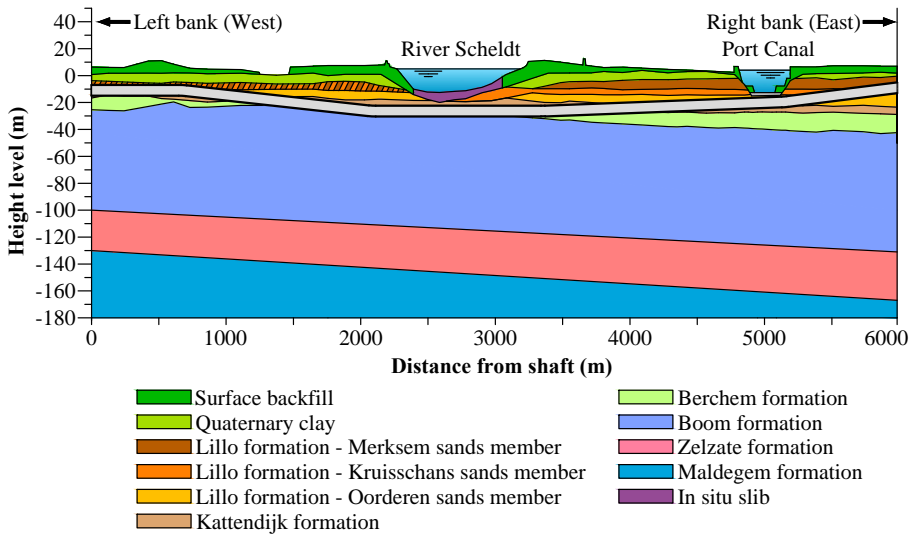


Figure 2.8. Longitudinal profile of the Liefkenshoek tunnel with soil composition.

clay, the thickness of which exceeds 80 m. This layer is saturated with water and behaves as impermeable soil. Tables 2.1 and 2.2 give an overview of the properties for each layer as determined by the soil investigations. The tunnel alignment is mainly located in the tertiary sands. However, at its deepest point below the river, the Boom clay ranges up to 40% of the tunnel cross-section.

In January 2010, the first TBM started drilling on tunnel north, followed by the second TBM of tunnel south in March 2010. The two TBMs reached the arrival shaft respectively in August and May 2011. The first TBM was overtaken by the second, due to parallel construction works on the cross-passages and evacuation shafts. For safety reasons, 13 cross-passages (CP) and 8 connections with evacuation shafts (ES) were built at an average distance of 300 m. Since some of these passages are located below the maritime fairways, they had to be built under important water pressure after freezing of the surrounding soil. The principle of their construction is based on the New Austrian method.

2.3.3 Crossing of River Scheldt and Port Canal

The crossing of the River Scheldt and the Port Canal required special attention, due to the shallow overburden above the tunnel. Adequate measures were taken to prevent boring face destabilization at these critical sections (Boxheimer & Mignon, 2011). As shown in Figure 2.8, the River Scheldt crossing was characterized by a minimal overburden of 9.7 m (Brux, 2013) and a river-

Table 2.1. Overview of soil layers for the Liefkenshoek project.

| Layer | Name | Composition |
|-------|-------------------------------------|---|
| 1 | In situ slib | sedimentary silt deposits |
| 2 | Surface backfill | sand |
| 3 | Quaternary clay | soft clay, containing vases & peats |
| 4 | Lillo formation - Merksem sands | tertiary fine sand, containing silt & mixture of fine sand & clay |
| 5 | Lillo formation - Kruisschans sands | tertiary fine sand, containing silt & mixture of fine sand & clay |
| 6 | Lillo formation - Oorderen sands | tertiary fine sand, containing silt & lenses of clay |
| 7 | Kattendijk formation | tertiary fine sand, containing silt & lenses of clay |
| 8 | Berchem formation | tertiary fine sand, containing large fractions of glauconite |
| 9 | Boom formation | rigid & overconsolidated tertiary clay |
| 10 | Zelzate formation | mixture of tertiary fine sands & clay |
| 11 | Maldegem formation | mixture of tertiary fine sands & clay |

Table 2.2. Overview of soil properties for the Liefkenshoek project.

| Layer | Thickness (m) | Depth (m) | γ_d (kN/m ³) | γ_s (kN/m ³) | φ' (°) | K_0 (-) | c' (kPa) | E_{oed} (MPa) |
|-------|------------------|--------------|------------------------------------|------------------------------------|-------------------|--------------|---------------|--------------------|
| 1 | 4 - 8 | 0 - 8 | 13 | 17 | 20.0 | 0.66 | 2 | 1 |
| 2 | 0.5 - 13 | 0 - 13 | 17 | 20 | 27.5 | 0.54 | 2 | - |
| 3 | 3 - 9 | 0 - 20 | 16 | 19 | 25.0 | 0.58 | 5 | 5 |
| 4 | 3 - 10 | 5 - 22 | 16 | 20 | 32.0 | 0.47 | 0 | 30 |
| 5 | 3 - 8 | 6 - 26 | 16 | 19 | 25.0 | 0.58 | 10 | 30 |
| 6 | 4.5 - 10 | 10 - 30 | 16 | 20 | 37.5 | 0.39 | 0 | 50 |
| 7 | 2 - 10 | 16 - 37 | 16 | 20 | 37.5 | 0.39 | 0 | 50 |
| 8 | 0 - 15 | 20 - 50 | 16 | 20 | 32.0 | 0.47 | 0 | 40 |
| 9 | 75 - 88 | 23 - 138 | 19 | 19 | 25.0 | 0.58 | 20 | 20 |
| 10 | 30 - 36 | 106 - 174 | - | - | - | - | - | - |
| 11 | 53 - 60 | 136 - 234 | - | - | - | - | - | - |

Notes: γ_d is the dry unit weight; γ_s is the saturated unit weight; φ' is the effective angle of internal friction; K_0 is the lateral earth pressure coefficient at rest; c' is the effective cohesion; E_{oed} is the oedometer modulus.

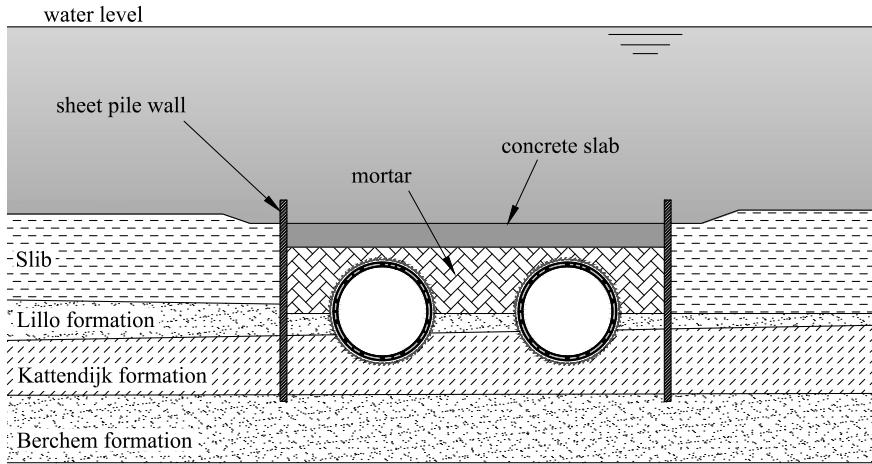


Figure 2.9. Critical passage below the Port Canal.

bed containing silt sedimentation and thick layers of disturbed sediment soil. In combination with the high water pressure, this led to a very small range between the minimum slurry confinement pressure and the blow-up pressure. Furthermore, during the drilling process, the water level variation of the river, linked to the tides of the North Sea, had to be taken into account. As a consequence of the small range between the decisive pressure levels and the quick change of water pressure, the slurry confinement pressure to support the front face had to be adjusted by the TBM operators at a high frequency. Moreover, the influence of the river tides was not limited to the construction stage, since tidal fluctuations continue to affect the tunnel structure as the results of the monitoring program presented in Chapter 8 will show.

The passage of the TBMs below the Port Canal was even more critical. Regarding the extremely shallow overburden of less than 2 m, increasing safety conditions to an acceptable value would have required filling the Port Canal by 7 m of sand. Since it must be kept free for large ships, such a measure was not acceptable for the port authority. After consideration of several alternatives, the problem was solved by producing a roughly 250 m long and 35 m wide pile wall excavation pit, in which the silt on the bottom of the canal was replaced by a low-strength mortar. The mortar was then covered by a reinforced concrete slab of 2 m thickness, which also serves as anchor protection and formed shelter during TBM boring. During passage of the TBMs, the slab was temporarily covered with an additional sand bed of 2 m, which was removed after tunnel boring. Figure 2.9 shows the resulting situation below the Port Canal.

Chapter 3

Monitoring program: methodology

3.1 Selected cross-sections

3.1.1 Diabolo tunnels

Since large settlements of the airport infrastructure or neighbouring hangars had to be avoided or at least detected in an early stage, six cross-sections of the tunnel lining were selected in each tunnel tube for the concentration of the measurement program. These sections include the ones located below the runway and just in front of hangar 117 as described in Chapter 2. These crossings were considered critical, as the excavation works below the airport runway, taxi-lanes and several buildings were executed without shutting down any airport activity. At each monitored section, both strain and ovalisation measurements were carried out. The location of the measurement sections is indicated in Figure 3.1. Table 3.1 shows the exact ring numbers of each section.

3.1.2 Liefkenshoek tunnels

To verify the structural behaviour of the newly constructed tunnel lining, 28 measurement sections were initially included in the Liefkenshoek project. At a later stage, two additional cross-sections were selected in each tunnel tube. Two main methods were used for the monitoring of these tunnel rings: strain measurements and laser scanning. Strain gauges embedded in the concrete lining segments allowed for verification of the real-time stresses in the tunnel

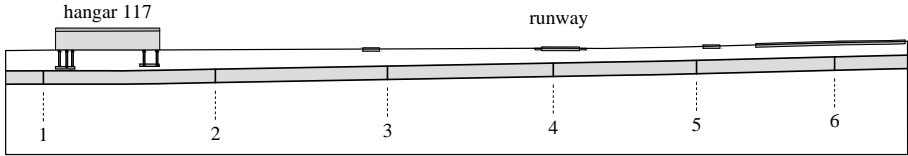


Figure 3.1. Location of the measurement sections in the Diabolo tunnels.

Table 3.1. Overview of measurement sections in the Diabolo project.

| section | ring number | | distance from shaft (m) | | laser scanning | strain monitoring |
|---------|-------------|----------|-------------------------|----------|-------------------|----------------------|
| | tunnel B | tunnel A | tunnel B | tunnel A | | |
| 1 | B30 | A30 | 398 | 410 | ✓ | ✓ |
| 2 | B167 | A167 | 700 | 702 | ✓ | ✓ |
| 3 | B305 | A304 | 1242 | 1242 | ✓ | ✓ |
| 4 | B443 | A436 | 1337 | 1339 | ✓ | ✓ |
| 5 | B550 | A550 | 1618 | 1611 | ✓ | ✓ |
| 6 | B660 | A660 | 2144 | 2142 | ✓ | ✓ |

lining, while laser scanning was used to monitor deformations and ovalisation of the corresponding cross-sections. Eight sections in each tunnel tube were monitored using both strain gauges and laser scanning, while six additional cross-sections in each tube were monitored using ovalisation measurements only. The locations of these monitored cross-sections were carefully chosen in order to investigate the effect of several local influences on the tunnel lining, such as the presence of an evacuation shaft, the largest overburden, the crossing of the River Scheldt and the Port Canal, etc. The exact locations of the measurement sections along the tunnel alignment are indicated in Figure 3.2. Table 3.2 shows the exact ring numbers of each section and the type of measurements that were performed at that location. Sections indicated in blue in Figure 3.2 were monitored using combined strain and ovalisation measurements, while the ones in black were only monitored using laser scanning. The two sections in red were the ones that were added at a later stage, where only strain measurements on the inner concrete lining were performed.

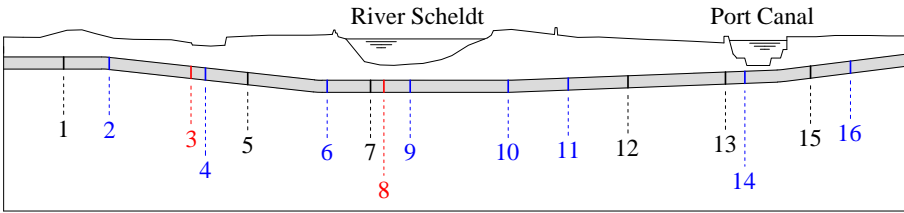


Figure 3.2. Location of the measurement sections in the Liefkenshoek tunnels.

Table 3.2. Overview of measurement sections in the Liefkenshoek project.

| section | ring number | | distance from shaft (m) | | laser scanning | strain monitoring |
|---------|-------------|-------|-------------------------|-------|-------------------|----------------------|
| | north | south | north | south | | |
| 1 | N221 | S228 | 398 | 410 | ✓ | |
| 2 | N389 | S390 | 700 | 702 | ✓ | ✓ |
| 3 | N690 | S690 | 1242 | 1242 | | ✓ |
| 4 | N743 | S744 | 1337 | 1339 | ✓ | ✓ |
| 5 | N899 | S895 | 1618 | 1611 | ✓ | |
| 6 | N1191 | S1190 | 2144 | 2142 | ✓ | ✓ |
| 7 | N1351 | S1351 | 2432 | 2432 | ✓ | |
| 8 | N1400 | S1400 | 2520 | 2520 | | ✓ |
| 9 | N1497 | S1500 | 2695 | 2700 | ✓ | ✓ |
| 10 | N1858 | S1850 | 3344 | 3330 | ✓ | ✓ |
| 11 | N2079 | S2076 | 3742 | 3737 | ✓ | ✓ |
| 12 | N2299 | S2319 | 4138 | 4174 | ✓ | |
| 13 | N2658 | S2671 | 4784 | 4808 | ✓ | |
| 14 | N2729 | S2726 | 4912 | 4907 | ✓ | ✓ |
| 15 | N2971 | S2978 | 5348 | 5360 | ✓ | |
| 16 | N3118 | S3115 | 5612 | 5607 | ✓ | ✓ |

3.2 Strain monitoring

3.2.1 Practical implementation of the strain gauges

Each initial cross-section that included strain monitoring consists of a tunnel ring equipped with several strain gauges, distributed across the ring perimeter. Prior to concrete casting in the prefabrication plant, all segments of a measurement ring, except for the smaller keystone, were equipped with two internal strain gauges attached to the inner and outer reinforcement bars in the circumferential direction, as shown in Figure 3.3.

The strain gauges used for this embedded application are T rosette strain gauges with two orthogonal measuring grids. This type was chosen to allow for an accurate installation of a Wheatstone half-bridge configuration for each strain gauge. The carrier and protection layer of the strain gauges consists of a thin polyimide layer, while the measuring grid is a constantan foil. The main advantages of this type of strain gauge are their ease of use, sturdiness and flexibility. In addition, the thermal expansion coefficient of $10.8 \times 10^{-6} / \text{K}$ matches the temperature response of the reinforcement steel and surrounding concrete. The size of the strain gauges is 11.5 by 7.3 mm, while the active grids measure only 3 by 3 mm. This size is well adapted to this specific application and allows for a smooth installation of the strain gauges and a correct determination of the strains in the reinforcement bars of 12 mm nominal diameter. The resistance of the internal strain gauges was selected as 350 Ω , instead of the more common 120 Ω . The former corresponds to less specific heat generation because of the lower measurement current. The soldering islands are chosen to be independent from the carrier in order to facilitate the alignment of the strain gauges along the reinforcement bars and provide strain relief for the strain gauge connections, as shown in Figure 3.4. The solder terminals consist of nickel-plated copper on a polyimide carrier.

In order to allow for a full attachment of the strain gauges, the oxidation layer of the reinforcement bars was first locally removed and the bars were smoothed mechanically by removing the ribs. Attention was given that this smoothing was executed without reducing the nominal cross-section of the reinforcement steel, as illustrated in Figure 3.4. The contact surface was degreased and pH-neutralised using an effective degreasing solvent and water-based acidic and alkaline surface cleaners. The strain gauges were then glued to the steel surface using a fast-drying, easily applicable and creep-free cyanoacrylate glue. This adhesive hardens in one minute, under thumb pressure, followed by a minimum two-minute delay before the cable connections can be soldered. However, the performance of the adhesive can be degraded by humidity conditions or moisture absorption. Hence, all strain gauges were protected from moisture using a covering agent consisting of aluminium foil coated with a 3 mm-thick kneading compound. The cables for data transfer were guided to a small plastic ‘waiting box’, attached to the reinforcement cage with the exact thickness of the concrete cover, in order to protect the cables during concrete casting and to be able to connect them to the data logger at a later stage. This entire procedure was completed in the prefabrication plant.

The equipped segments were subsequently precast, consolidated in a normal

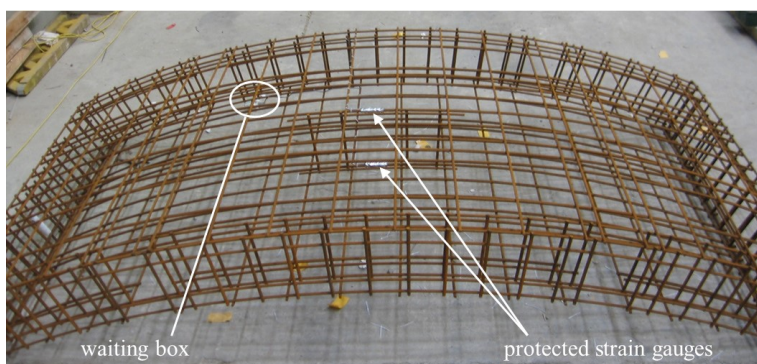


Figure 3.3. Reinforcement cage equipped with strain gauges.

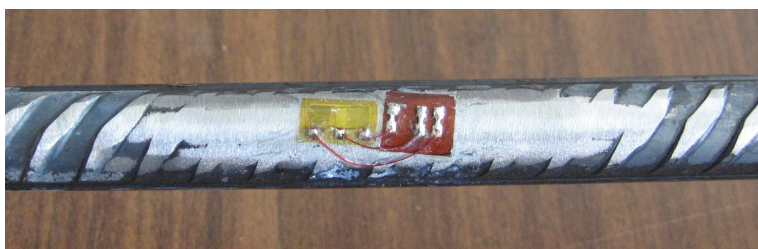


Figure 3.4. Strain gauge installation on reinforcement bar.

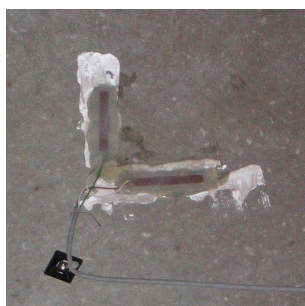


Figure 3.5. Strain gauge installation on internal concrete surface.

manner and transported to the construction site. Immediately after installation of the segments in the tunnel, before the excavation process was restarted, each segment was provided with a third strain gauge glued to the inner concrete surface of the tunnel lining. The additional strain gauges were installed at the centre of the concrete segment surface and strains were measured in the circumferential direction, corresponding to the internal strain gauges. The installation of these strain gauges could not be done before completion of the

ring erection due to the application of the vacuum segment erector, which creates a vacuum area on the concrete surface to lift and place the segments into position.

The strain gauges used for the surface application are standard, unidirectional strain gauges, yet each time installed as an orthogonal couple to ensure the Wheatstone half-bridge configuration for every measurement location, as shown in Figure 3.5. Identical characteristics for the surface strain gauges apply as for the embedded strain gauges. However, the inhomogeneous structure of concrete requires strain gauges with longer measuring grids for mean value calculation. Therefore, the size of the strain gauges on the concrete surface is 63.6 by 8.2 mm, while the active grid measures 50 by 0.8 mm. This grid length exceeds two times the grain size of the concrete and allows for correct identification and sufficient accuracy of the strains at the concrete surface. Unlike the internal strain gauges, the resistance of the surface strain gauges was chosen as 120 Ω , due to the relative insensitivity to variations in insulation resistance, for example caused by effects of humidity.

The bonding surface was degreased and the strain gauges were glued to the concrete surface using a methyl metacrylate two-component adhesive paste, which is a strong pore-filling adhesive that bonds reliably even if residual moisture is still present. The strain gauges can be installed using thumb pressure and the adhesive hardens in a few minutes, depending on the temperature. After soldering of the cable connections, all strain gauges were protected from moisture using a thick silicone layer with a neutral pH to minimise interference.

Since the cables leading to the lowest segment would be damaged by the advancing TBM's work train, the installation of strain gauges in this segment was omitted. Consequently, the process resulted in a total of 18 wired strain gauges, the locations of which are illustrated in Figure 3.6.

3.2.2 Wireless strain gauge measurement system

Specifications

Immediately after installation of the precast segments in the tunnel under construction, the waiting boxes were cut open and the cables for data transfer of the embedded strain gauges were connected to the measurement system. Simultaneously, the additional strain gauges on the concrete surface were installed as described and directly connected to the measurement set-up. The result of this stage is depicted in Figure 3.7.

The applied measurement system is a commercially available wireless data

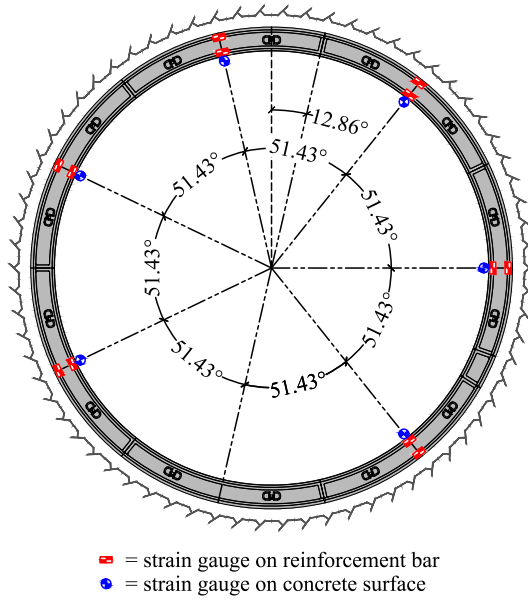


Figure 3.6. Strain gauge locations in the tunnel cross-section.

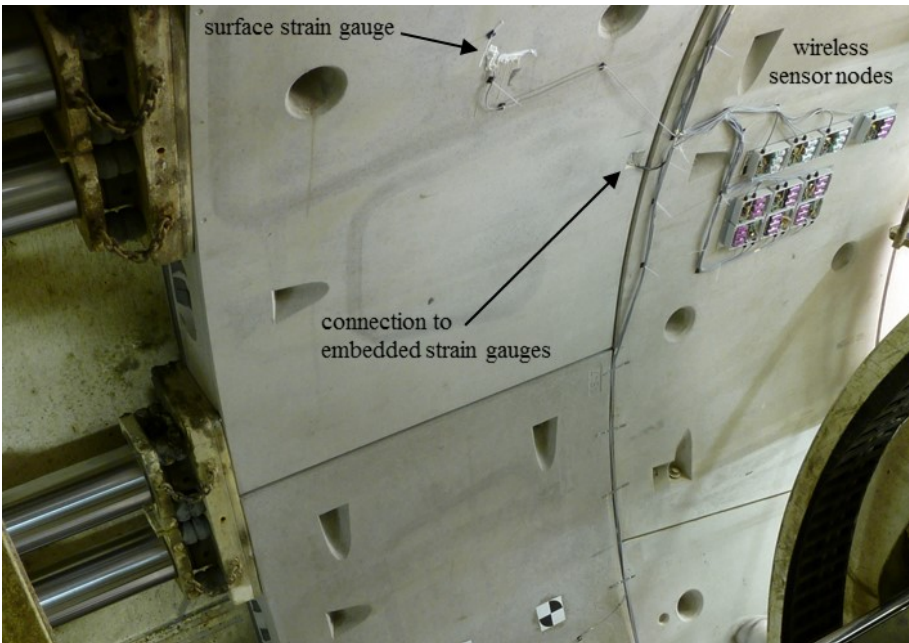


Figure 3.7. Strain measurement set-up after ring assembly.

acquisition system, which comprises three main components: wireless sensor nodes, which acquire and transmit strain data; USB base stations, which receive and pass the data to a host (laptop); and a Windows-based software package, which operates the system. Each sensor node provides four differential input channels (strain channels) for 350 Ω strain gauges or, due to issues of power consumption, only two input channels for strain gauges of 120 Ω resistance. This implies that six individual sensor nodes were required to monitor the strain data in each measurement ring. The layout of a wireless sensor node is depicted in Figure 3.8. Every sensor node employs a 12-bit A/D converter to digitise the voltage on the differential input. The digital data is passed to the on-board microprocessor, processed with the embedded algorithm and saved to the 2 MB on-board flash memory for later wireless download using the base stations. Furthermore, the integrated circuit of the nodes (Figure 3.8 - A) includes Wheatstone bridge completion resistors for each channel and internal resistors for wireless shunt calibration. One entire unit is powered by three lithium-ion D-cell batteries of 3.6 V each (Figure 3.8 - C) and the circuitry is built into an IP65 polycarbonate enclosure (Figure 3.8 - D) for protection against dirt and moisture. Figure 3.8 also shows the internal on-off switch (B) and cable glands (E).

Host computer software enables downloading and recording of the data to a file and erasing the on-board flash memory of the nodes. Furthermore, it allows the user to configure and actuate the system and to perform a wireless shunt calibration of each strain channel. The data acquisition system has a measurement resolution of only 1 $\mu\epsilon$ with an accuracy of $\pm 0.1\%$. The high flexibility of the system combined with the accuracy of the resulting strains makes it the appropriate measurement system for this specific application.

After the first experiences with the measurement set-up in the Diabolo tunnel, both strengths and weaknesses of the wireless measurement system became clear and some important improvements were completed to the advantage of the monitoring programme in the Liefkenshoek tunnel. In the following paragraphs, some of these issues are discussed.

Wheatstone bridge completion

Basically, all strain results should be rectified with a temperature correction, based on calibration graphs supplied by the manufacturer of the strain gauges. These graphs indicate the correction in $\mu\epsilon$ that should be applied for given temperature fluctuations, due to differences in expansion or contraction of the

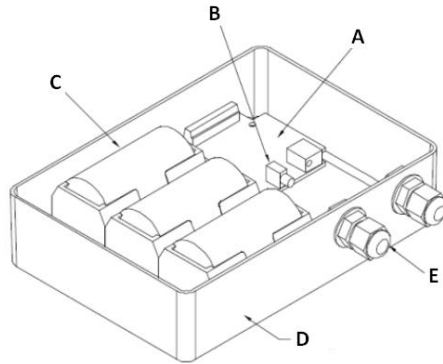


Figure 3.8. Wireless sensor nodes (see text for explanation of letters).

strain gauges compared to the base material. For temperature variations of about 20°C , the correction equals 5 to $10\ \mu\epsilon$. However, it is not always practical to apply the temperature correction to all strain measurements for several reasons. Most importantly, monitored temperature data concern only the surrounding air inside the tunnel. As the strain gauges attached to the reinforcement are embedded in concrete, the assumption that they adopt the same temperature as the air inside the tunnel would lead to excessive and improper corrections of the monitored strains. The same applies to the strain gauges attached to the concrete surface and covered by a protective layer of silicone.

Hence, the described temperature correction does not appeal for practical application. The alternative is to change the Wheatstone bridge completion. The quarter-bridge system was used in the Diabolo project, whereas in the measurements of the Liefkenshoek project the more stable half-bridge configuration is applied. Briefly stated, this involves a change in the electrical circuit of resistors, with a reference gauge built in together with the actual measuring strain gauge in the half-bridge system, as shown in Figure 3.9. In the quarter-bridge configuration, an equivalent reference resistor would be located in the internal electric circuitry of the sensor nodes. One of the main advantages of the half-bridge completion is that the reference resistor is now subject to the same surrounding conditions as the measuring gauge and is consequently subjected to identical temperature changes and ageing. In addition, as each strain gauge is connected to the measuring system by means of three separate cables to complete the half-bridge circuit, in this set-up it becomes possible to filter the influence of the leadwires on the resistance. This should result in a nearly complete elimination of deviations due to the aforementioned effects,

automatically corrected temperature variations and more stable measurement results in general.

Measurement frequency

If the data logging sampling method used in the Diabolo project is applied, the measurement system can be configured to sample data as fast as 2048 Hz on each channel or to decrease the frequency down to 32 Hz. The lowest sampling frequency of 32 Hz already resulted in a very short measurement period of less than five hours and excessively detailed strain data. In this method, downloading of the stored data took about eight minutes for each node and was required before the next data logging session could be initiated. Taking into account the number of sensor nodes used in each measurement ring, wireless transfer of the stored data became a labour-intensive process.

Implementation of a low duty cycle (LDC) mode allowed configuration of sampling frequencies from one sample per hour up to 500 Hz per channel. Activation of this LDC mode in the Liefkenshoek project made it possible to significantly lower the measurement frequency, resulting in a longer monitoring period and fewer download sessions. At a frequency of one sample every 10 s, sufficient accuracy of the monitored strains in the first weeks after ring erection was ensured. In addition, wireless transfer of the stored data was reduced to a maximum of one and a half minutes for each sensor node. For long-term monitoring, the frequency was reduced to one sample every 30 s, as a result of which strain data needed to be downloaded every three weeks only. Later in the project, further reduction of the sampling frequency to one sample every two minutes was applied, requiring a download every three months.

As a positive side-effect of the lowered frequency, internal heating of the strain gauges at the start of each measurement period was no longer a problem. Strain data in previous applications clearly showed a temperature drift at the start of each monitoring period, due to the sudden initiation of high-frequency measurements and strong electric current through the strain gauges. Since the measurements in LDC mode run over an extended time lapse and should not normally be interrupted for longer than the duration of a single download, this start-up phenomenon disappeared. Hence, the actual internal heating of strain gauges was considerably smaller thanks to the reduced measurement frequency and the adequate selection of the strain gauge types.

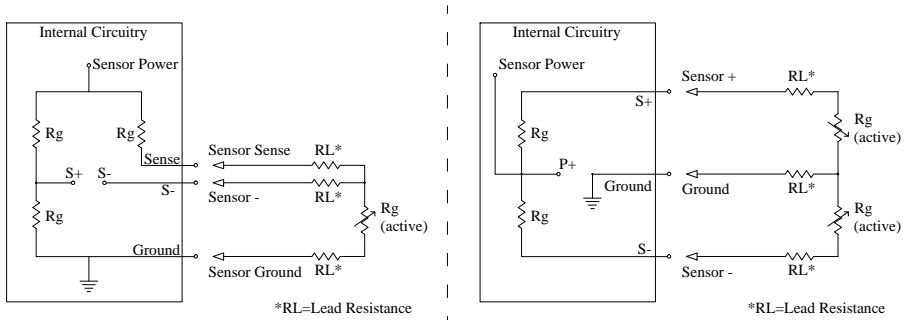


Figure 3.9. Wheatstone bridge completion: quarter-bridge (left); half-bridge (right).

Further issues

In previous paragraphs, several issues were mentioned together with improvement of the measurement method. However, some minor flaws still remained in the data logger set-up.

First, the wireless range of the sensor nodes is inadequate for wide application of the measurement system. Theoretically, the sensor nodes allow communication up to a range of 70 m line-of-sight. However, on the construction site this is reduced to about 12 m. As the internal diameter of the monitored tunnels equals 7.3 m, this range is sufficient for tunnel measurements. In addition, in the current state of development, downloading data in LDC mode requires manual switching off and reconnection of the sensor nodes to interrupt ongoing measurements. This implies that all sensors have to be installed within reach, which renders the wireless function of the measurement system practically unprofitable.

Secondly, the sensor nodes obviously require a power supply. Due to the installation procedure and passage of the TBM's work train in the first week after assembly, a fixed power cable connection was not practically feasible. To assure the independence of the measurement system and the continuation of the monitoring process in case of power failure, each sensor node is powered by three D-cell batteries. In LDC mode, the lifetime of these batteries equals approximately five months. As a result, long-term measurements also require accessibility of the sensor nodes to replace batteries when needed.

Finally, the sensor nodes make use of an integrated clock of the RC type to handle time stamping in LDC mode. The stability of this clock according to product specifications and on-site experience equals $\pm 10\%$, which is insufficient for accurate use. For example, a single measurement period of three weeks

in LDC mode with one sample every 30 seconds corresponds to a possible deviation of two days. Experience shows that accuracy should be maintained by calculating each time stamp based on the start and end time of the monitoring period and the total number of enclosed measurement samples.

3.2.3 USB strain gauge measurement system

Due to the remaining issues with the wireless sensor nodes, the data logging set-up was further upgraded to a new measurement system after several years of monitoring in the Liefkenshoek project. This new system is a robust data acquisition unit, commercially available in two models, depending on the required number of input channels. The smaller model is able to measure five strain channels in its standard configuration, while the advanced model provides 16 input channels. However, the capacity of both can be increased using multiple expansion modules, adding 20 channels at a time up to a total of 100 (smaller model) or 320 channels (advanced model). Each channel is able to measure strain gauges of 120 Ω or 350 Ω in a quarter, half or full bridge configuration. As a result, only one system unit was required to monitor the strain data in each measurement section. The data acquisition system has a measurement resolution of less than 1 $\mu\epsilon$, with an accuracy of $\pm 0.15\%$ at 5°C to 40°C and $\pm 0.45\%$ at -45°C to 70°C. Figure 3.10 shows the advanced model of the new measurement system.

At the moment of the upgrade, the tunnel had already been equipped with various power circuits for lighting, safety installations and other railway-related facilities. Therefore, it was possible to install a fixed power supply to the measurement units, removing the need for expensive batteries. Nonetheless, each data logger is equipped with a fixed, internal, rechargeable lead acid battery with a capacity of 1.2 Ah (smaller model) or 4 Ah (advanced model), guaranteeing an independence of several days in case of power failure. In addition, a protective earth connection was incorporated, providing a safe discharge path for large electrical currents which may occur due to electrical faults in the tunnel railway infrastructure. The on-board flash memory of 128 MB provides a much larger internal storage capacity, compared to the wireless measurement system. As a result, a measurement cycle of one year without intermediate data collection was now possible, significantly reducing the required number of download interventions. This proved extremely useful, since it was no longer allowed to freely access the tunnel interior once the railway traffic was fully operational. Furthermore, the collected data is easily accessible for download



Figure 3.10. Advanced model of the USB measurement system.

by USB memory stick. Finally, each data logging unit is equipped with a real-time clock, with an accuracy of ± 1 min/year at 0°C to 40°C and ± 4 min/year at -40°C to 70°C . This largely exceeds the clock precision of the wireless measurement system, solving all remaining issues of the latter.

3.2.4 Strain monitoring program

Immediately after installation of the lining segments in the tunnel under construction and connection of all data cables to the wireless measurement system, monitoring of the 18 strain gauges in each measurement section was initiated. The excavation works of the TBM were only resumed after the start of the measurements. At an initial sampling frequency of one sample every 10 s on each channel, strains were registered during the various steps in the boring process following the erection of the measurement section. Monitored data include the reaction of the tunnel lining to the tail grout injection, thrust force of the hydraulic shield jacks and transfer of soil and water pressures onto the concrete elements. After this initial stage, generally corresponding to the first week after installation, the measurement frequency was lowered to one sample per 30 s and in a later stage to one sample every two minutes. The saved data were downloaded on a regular basis for a continuous period of several years and allow assessment of the real-time behaviour of the tunnel lining under various load states.

Figures 3.11 and 3.12 show a scheme of the measurement cycles for all monitored sections. The dots represent the download sessions on which the monitored data were collected for processing. Each measurement cycle started at the moment of ring installation at a sampling frequency of one measurement every 10 s (red section), after which the frequency was lowered to one meas-

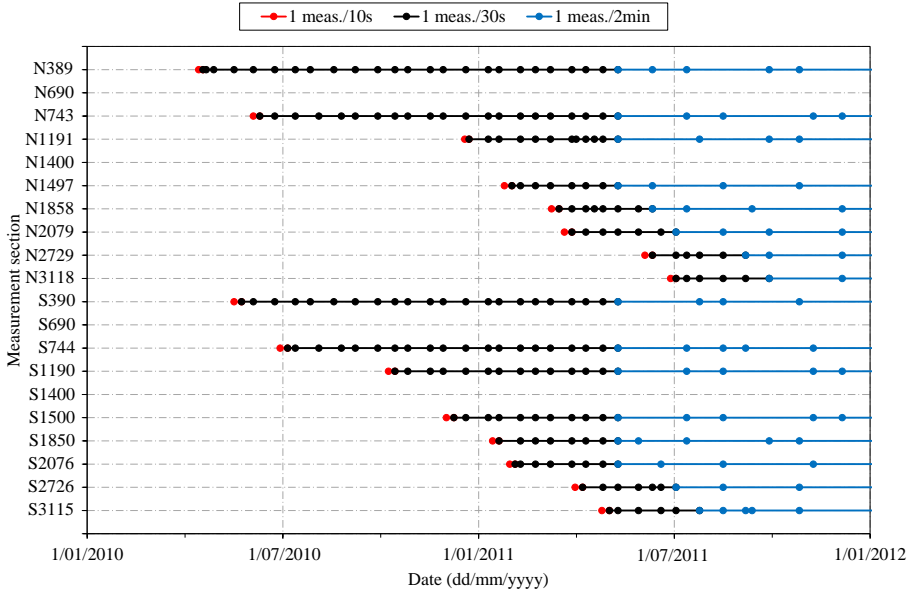


Figure 3.11. Overview of measurement cycles and data collection instants for the wireless measurement system (part 1).

urement per 30 s (black section). This frequency was maintained until at least three months after installation, up to one year for the tunnel sections that were installed first in the excavation process. Due to the high sampling frequency and the limited flash memory of the wireless sensor nodes, a lot of download interventions were needed during this period. After that, the sampling frequency was lowered to one measurement every two minutes (blue section), requiring less frequent data collection. This period lasted approximately one year.

At this time in the construction phase, a fire-resistant coating was sprayed onto the inner surface of the tunnel lining. As a result, the measurement cycles were interrupted, as all measurement systems were temporarily removed to avoid damage due to the high-pressure spraying technique. Data cables were protected for the same reason behind steel plates attached to the concrete lining. After the application of the fire-resistant coating, the wireless sensor nodes were reinstalled and strain monitoring was initiated once again at a frequency of one measurement every two minutes for a period of about one year (green section in Figure 3.12). However, for some sections (N1191, S1850, S3115), no new measurements were started. This was due to errors by the tunnel construction crew, as a result of which data cables were inaccessible or got damaged, notwithstanding the protective measures.

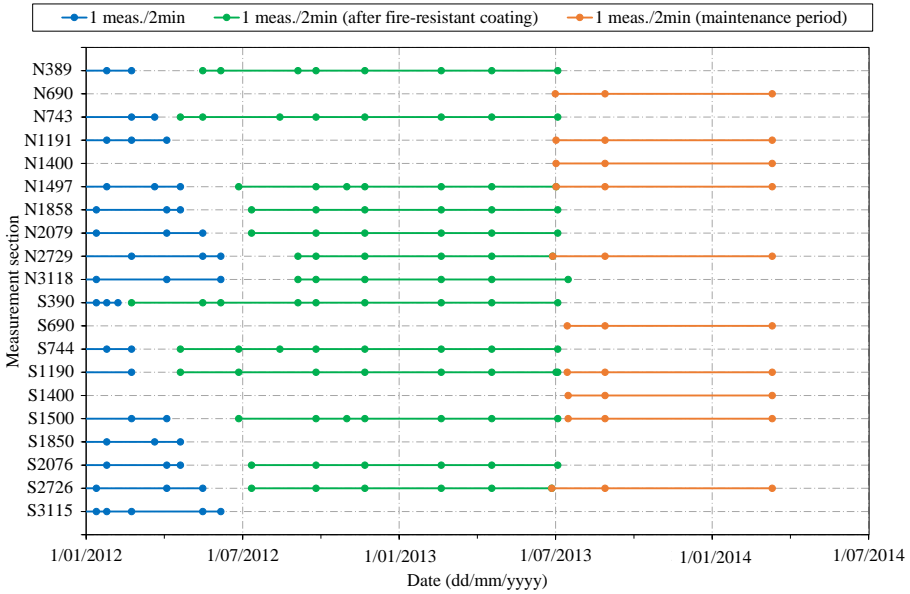


Figure 3.12. Overview of measurement cycles and data collection instants for the wireless measurement system (part 2).

By the summer of 2013, all major construction works on the tunnel project were finished. It was decided to permanently cease the strain monitoring programme in a majority of the tunnel sections. Nonetheless, strain measurements were still considered valuable for the continued verification of the structural behaviour in the long term during the maintenance period of the tunnels. However, the focus was shifted to a smaller number of 10 tunnel sections: six of the initial monitoring sections (N1191, N1497, N2729, S1190, S1500, S2726) and four new ones (N690, N1400, S690, S1400). In the existing sections, all original strain gauges that were still intact at this time after installation were again monitored. In addition, defective strain gauges at the inner concrete lining were repaired or reinstalled by locally removing the fire-resistant coating, in order to access the precast concrete lining. An identical procedure was applied to install strain gauges on the inner concrete surface of the new measurement sections. Only those strain gauges were monitored in the new sections, as it was impossible to attach additional strain gauges to the reinforcement bars at this time. The repair and installation of new strain gauges was conducted according to the specifications described in section 3.2.1. Finally, all ten monitoring sections were activated once again at a frequency of one measurement every two minutes for a period of about eight months (orange

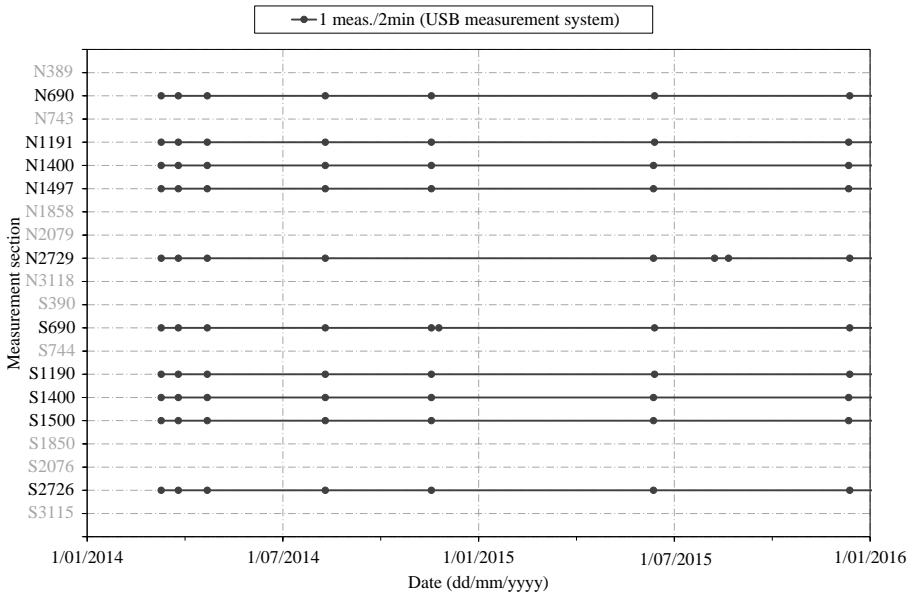


Figure 3.13. Overview of measurement cycles and data collection instants for the USB measurement system.

section in Figure 3.12).

After this, an update of the measurement system was performed at the beginning of 2014. Following the conversion of all ten monitoring sections to the new type of data loggers of section 3.2.3, strain monitoring was once again initiated at a frequency of one measurement every two minutes. Figure 3.13 shows a scheme of the measurement cycles for the remaining monitoring sections. It can be observed that, after an initial period for verification of the correct operation of the new measurement system, a lot less download sessions for the collection of the monitored data were needed, compared to the wireless sensor nodes. At the start of 2016, this measurement program was still fully operational in the Liefkenshoek tunnels, in order to continuously monitor the structural condition of the segmental lining for many years to come.

3.3 Ovalisation monitoring using laser scanning

3.3.1 Introduction

In the Diabolo project, the use of laser scanning for ovalisation monitoring of tunnel cross-sections was tested and implemented by the Department of Geo-

graphy of Ghent University. In the Liefkenshoek project, the workflow was optimised and the processing of the data sets further elaborated. This subject was the main focus of the PhD thesis of Timothy Nuttens. This section discusses the resulting methodology after all optimisations, based on his research.

3.3.2 Laser scanning technique

General background

The deformations of the monitored cross-sections were measured at several points in time using a laser scanner, which is a non-contact active surveying instrument that uses an emitted beam of laser light to measure the distance between the instrument and an object (Rönnholm *et al.*, 2007). Since the laser scanning method needs no specific lighting conditions and is able to deliver millions of accurate 3D coordinates in a couple of minutes, it proved to be most suitable for detecting deformations of the concrete lining segments in the tunnel (Schäfer *et al.*, 2004; Zogg & Ingensand, 2008). With a total station, the operator can only measure a limited number of selected points, whereas a laser scanner can fully automatically measure the field of view with a specified horizontal and vertical point density, based on rotations of the range finder or a rotating mirror system (Pfeifer & Briese, 2007). The measured distance, combined with the registered horizontal and vertical angle of the instrument, results in 3D coordinates for every measured point (Abellán *et al.*, 2011; Pfeifer & Briese, 2007; Wehr & Lohr, 1999). The technique allowed for the registration of a dense and detailed point cloud in a very short time-frame, reducing the downtime of the excavation works. However, a laser scanner is a line of sight instrument, which means that only the points in the direct line of sight of the instrument can be measured. Therefore, to cover a larger area or object, multiple set-ups are often necessary.

Different types of laser scanners

Terrestrial laser scanners can be divided into different types, based on the principle of the distance measurement between the laser scanner and the object. The three most important types that can be identified are triangulation laser scanners, pulse-based laser scanners and phase-based laser scanners. Each type of laser scanner has its specific characteristics, making it more suitable for different applications.

Triangulation laser scanners are suited for high precision measurements over

very short distances, limited to a few metres. Their measurement principle is based on widening the laser beam to form a plane or pattern and to record the image of the laser pattern on the object with a built-in camera. Because the limited range of this technique, it was not applied for the tunnel deformation measurements of this research.

Pulse-based laser scanners (also called time-of-flight or pulse round trip laser scanners) are based on the emission of a short (a few nanoseconds) but powerful laser pulse. The backscatter of the laser beam is recorded by the scanner and the travelling time of the laser pulse from the scanner to the object and back is calculated (Pfeifer & Briese, 2007). As a result, the distance between the laser scanner and the object can be calculated using the known speed of the laser beam. The accuracy of the distance measurements largely depends on the accuracy of the time measurement and detection of the backscatter, typically resulting in cm-level accuracy (Pfeifer & Briese, 2007). Because the measurement principle is based on a strong laser pulse, the range of this type of laser scanners for accurate measurements can be very large, up to 1 km or more (Leica Geosystems, 2013a). The latest technical developments on the market present pulse-based laser scanners with a scanning speed up to one million points per second (Leica Geosystems, 2013b; Trimble, 2013). In the Diabolo project, two types of pulse-based laser scanners were tested: Leica ScanStation 2 and Leica C10 (High-Definition Surveying Division, Leica Geosystems AG, Heerbrugg, Switzerland).

A higher accuracy (mm-level) and larger scanning speed can be obtained by using phase-based laser scanners (Pfeifer & Briese, 2007). This type of laser scanner emits a continuous laser beam and uses the phase difference between the emitted signal and the reflected backscatter to determine the distance between scanner and object. Because of the lower power of the emitted laser signal, the achievable range of this type of laser scanners is limited. Typically, distances of up to 80-100 m can be measured, depending on the reflectivity of the object (Leica Geosystems, 2009; Trimble, 2012). In the Diabolo project, a Leica HDS6100 phase-based laser scanner was tested (High-Definition Surveying Division, Leica Geosystems AG, Heerbrugg, Switzerland).

Apart from both types of laser scanners, a robotic total station Trimble S6 2" DR300+ (Trimble Navigation Limited, Sunnyvale, USA) with automated measurement function was tested. Extensive test measurements and comparison of the different scanners during the Diabolo project indicated the phase-based Leica HDS6100 laser scanner as the most suited laser scanner for tunnel application, based on the high scanning speed (and thus shorter measurement

time on site), large field of view and achievable accuracy. More information on the comparison of the different types of scanners can be found in Nuttens *et al.* (2015).

Theoretical versus on site measurement accuracy

The term “accuracy” refers to how close the measurements are located to the real point locations in space. In order to compare the measured data with a reference geometry, a highly accurate point cloud is specifically desired (Jacobs, 2005). Possible errors in laser scanning can be divided into different categories, depending on the source. Delaloye *et al.* (2011) for example distinguish three large sources of errors: errors in the range measurement and errors in the vertical and horizontal angle measurements. Besides these three instrument dependent errors, possible other errors are the phenomenon of spurious points, errors in the laser scanner operating procedures or in the processing of the data (Delaloye *et al.*, 2011). The specifications of the applied Leica HDS6100 laser scanner mention a 5 mm position accuracy of a single measurement and a distance accuracy of less than 2-3 mm up to 25 m, depending on the reflectivity of the object. The modelled surface precision is 1-2 mm at 25 m and 2-5 mm at 50 m. However, experience shows that the actual accuracy differs from instrument to instrument. Moreover, manufacturer’s specifications are often difficult to compare and the measurement conditions on site have a large influence on the final accuracy that can be obtained (Boehler & Marbs, 2003; Jacobs, 2004; Lichti *et al.*, 2000). In the case of this research, the dusty and hard conditions of a tunnel under construction render an in situ accuracy assessment indispensable. The corresponding results are discussed in section 3.3.4.

3.3.3 Measurement methodology

Monitoring schedule

Seven moments in time were defined on which the selected tunnel sections were measured:

- A reference measurement (CM 0) immediately after construction of the tunnel section
- Control measurement 1 (CM 1): one week after installation
- Control measurement 2 (CM 2): two weeks after installation
- Control measurement 3 (CM 3): three weeks after installation

- Control measurement 4 (CM 4): one month after installation
- Control measurement 5 (CM 5): two months after installation
- Control measurement 6 (CM 6): three months after installation

The reference measurement was performed immediately after assembly of the individual tunnel segments in the head of the TBM. This means that the monitored tunnel section was still under protection of the TBM shield, as the excavation works had not yet been restarted after installation. Some of the scheduled control measurements could not be performed, due to circumstances on site or ongoing construction works that did not allow accessing the corresponding measurement sections.

Reference measurements

During the reference measurements, several restrictions had to be overcome. Because no vibrations or movements of the TBM were allowed during the measurements, the excavation works had to be stopped during each reference measurement. Of course, the downtime of the TBM during the measurements had to be minimised, so the time pressure for the preparation of the scanning positions and the measurements was significant. On average, about two hours were needed to perform the preparation and installation of the scanning positions, the scanning process itself and the strain gauge installation. Moreover, the free space in the head of the TBM was very limited, which obstructed the field of view of the laser scanner and the works of the measurement crew. Due to this limited free space, it was impossible to scan the entire tunnel section from one scanning position.

To cover the whole tunnel profile and to limit the incidence angles of the laser beam (Argüelles-Fraga *et al.*, 2013), three scanning positions were needed during the reference measurement immediately after erection of the tunnel ring. These positions are shown in Figure 3.14. In scanning positions I and II, the laser scanner was placed on a steel bracket on the tunnel surface (left and right side), as seen in Figure 3.15. From each scanning position, the full field of view was measured without placing the laser scanner in a specific direction. For position III, the scanner could be mounted on a tripod in the invert of the tunnel section.

To enable the combination of the measurements from these three scanning positions into a single point cloud, sixteen Leica black-and-white targets were attached to the tunnel surface, as shown in Figure 3.15. These targets were

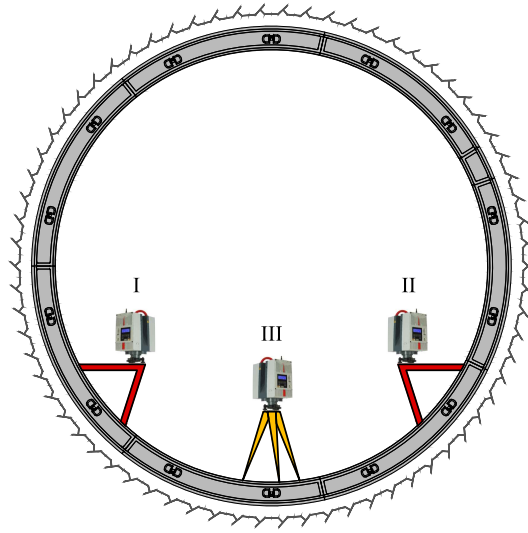


Figure 3.14. Three scanning positions during a reference measurement.

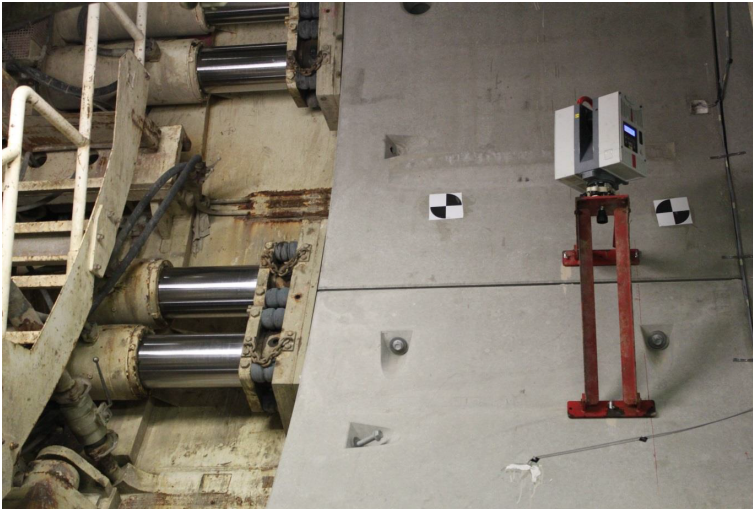


Figure 3.15. Laser scanner mounted on a bracket during the reference measurement.

printed on waterproof polyester and glued to the concrete surface with special highly adhesive glue to guarantee the further use of these targets during the following measurements. These sixteen targets were equally spread over the tunnel surface, in order that at least six to eight overlapping targets existed between two scanning positions. The exact centre of each black-and-white target is recognised by the processing software (Trimble Realworks for the

Diabolo project, Leica Cyclone for the Liefkenshoek project). Furthermore, one of these targets was indicated as the so-called “master reference target”, which determined the exact location of the cross-section for the further processing of each measurement.

Control measurements

The control measurements started one week after construction of the monitored tunnel section. By that time, generally the TBM back-up systems, which were approximately 100 m in length, had completely passed this section. To cover a maximal area of the tunnel surface, the six control measurements required one scanning position only where the laser scanner was positioned in the tunnel invert (position III in Figure 3.14). The set-up and scanning process during a control measurement took about 10 minutes. However, in the resulting point cloud, “shaded” areas without scanning data could not be avoided, due to the presence of the installed pathway, piping installations and the ventilation tube at the top of the tunnel section. Figure 3.16 shows an example of a resulting point cloud obtained during a control measurement. Areas in black represent the shaded zones that were not measured. The colours in Figure 3.16 are a visualisation of the intensity value, which is the amount of reflected radiation with respect to the emitted laser beam. This value depends on the physical characteristics of the reflecting surface, the wavelength of the incident radiation and the distance between the laser and the object (Pfeifer & Briesse, 2007).

Scanning resolution

For each scanning position, the point cloud covered the whole field of view of the Leica HDS6100 laser scanner: 360° in horizontal direction and 310° in vertical direction. However, the density of the point clouds varied, depending on the type of measurement. For a control measurement, the horizontal and vertical angle increment between two consecutive points was set at 0.036° , resulting in a data point every 4 mm at the maximum distance of about 6 m on the tunnel surface of the monitored cross-section. For a reference measurement, the selected angle increment was 0.018° , which resulted in data points every 2 mm at a maximum distance of about 6 m. Nevertheless, during processing of the point clouds from reference measurements, only one data point out of four was used for the 3D meshing (see section 3.3.4) in the processing software (one out of two both in horizontal and vertical direction). This resulted in a point cloud resolution of about 4 mm or higher. The original scanning resolution for

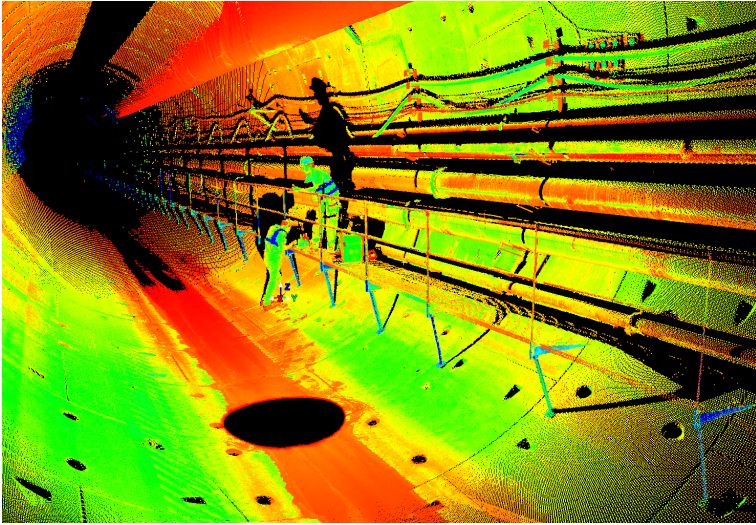


Figure 3.16. Resulting point cloud obtained during a control measurement.

reference measurements did not significantly contribute to the required level of detail or accuracy. Moreover, the overlap of the three scanning positions increased the point density to a level comparable to the control measurements, which offered sufficient detail for processing and interpretation of the point clouds.

3.3.4 Processing of the point cloud

General methodology

As laser scanning measurements register all points within the field of view, many spurious points had to be filtered at the start of the point cloud processing. For the reference measurements, a lot of data points covered the TBM, which do not contribute to the coverage of the monitored tunnel section. In a control measurement, the point cloud also contained a lot of points of adjacent tunnel sections, piping installations, the ventilation equipment and the installed pathway (Figure 3.16). Consequently, manual filtering of the point clouds was performed. However, an automated filtering algorithm was developed at a later stage as well as part of the research performed by Nuttens (2014).

After filtering of the point cloud, a best-fit cylinder with a free diameter was calculated, of which the longitudinal axis was considered to represent the tunnel axis. Next, a 3D triangulated surface (mesh) of the point cloud was calculated.

Subsequently, a cross-section perpendicular to the tunnel axis was determined through this mesh, resulting in a 2D polyline representing the measured tunnel profile. The exact intersection of the cross-section with the tunnel surface was fixed by the master reference target, which ensured an identical location of the cross-section for each consecutive measurement. Thanks to the triangulated surface, a polyline was obtained instead of a much smaller collection of individual points.

During data processing, a uniform coordinate system had to be defined. The origin was positioned on the axis of the best-fit cylinder, with the z-axis oriented along the tunnel axis, in opposite direction of the TBM drive. The coordinate system was further characterised by a horizontal x-axis and an upward y-axis, as shown in Figure 3.17. This user defined coordinate system allowed a better comparison between consecutive measurements of a tunnel section, as the original position and orientation of the laser scanner was not fixed and therefore varied for each measurement.

In the next step, a radius value from the axis of the best-fit cylinder to the polyline was determined every 0.1 gon, resulting in 4000 values or a value for every 5.7 mm on the tunnel surface. Subsequently, each radius value was smoothed by calculating the average over an interval of x gon to the left and right of this radius, in order to remove the high-frequency noise and to improve the readability of the results. Different smoothing levels were investigated in the Diabolo project to find the optimum interval, keeping sufficient detail to avoid masking correct measurement data. Finally, taking into account the accuracy requirements imposed by the client for the Liefkenshoek project, a $[x - 0.5 \text{ gon}; x + 0.5 \text{ gon}]$ smoothing interval was applied on the calculated radius values, corresponding to an interval of 57 mm on the tunnel surface. The result of the smoothing procedure is illustrated in Figure 3.18. Consequently, using smoothed data for interpretation does not significantly alter the conclusions on the deformation behaviour, but only yields clearer drawings without masking excessive measurements. In particular, the areas around the segment joints where data points were filtered are mostly larger than 2.5 gon, so the smoothing procedure does not affect the evaluation of joint irregularities.

Combination of multiple scanning set-ups

To combine the three scanning set-ups of the reference measurements into one point cloud, multiple approaches are possible. However, the highest accuracy can be obtained by applying a target-to-target registration, which was used in

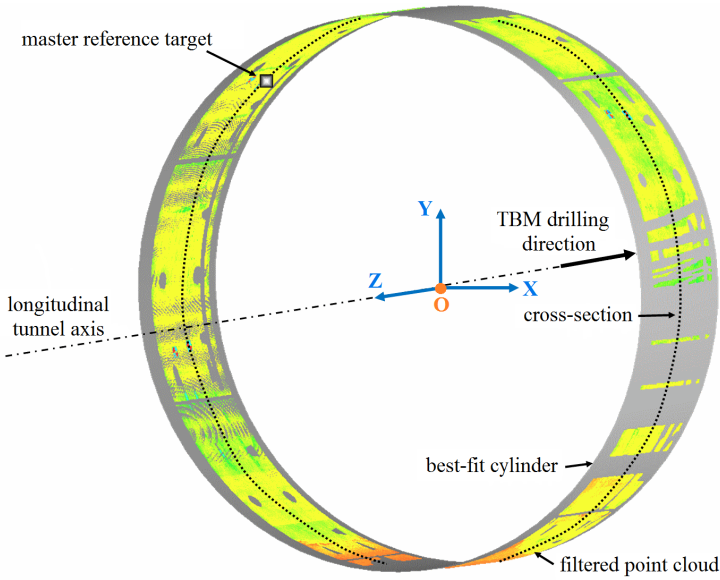


Figure 3.17. Schematic overview of the filtered point cloud, best-fit cylinder, coordinate system and cross-section.

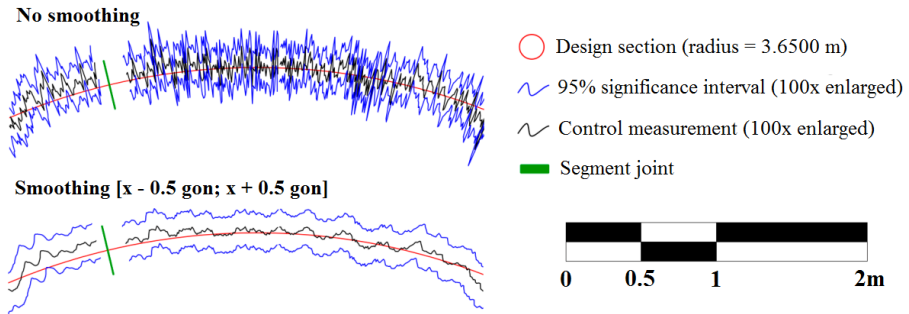


Figure 3.18. Comparison of the results without smoothing (top) and with $[x - 0.5 \text{ gon}; x + 0.5 \text{ gon}]$ smoothing interval (bottom).

this study. Based on common black-and-white targets between different point clouds, these point clouds could be combined. The large number of overlapping targets ensured a solid registration and minimisation of the target-to-target registration errors based on a least-squares optimisation. When the overlap between different point clouds is up to 30 or 40%, no artificial targets are necessary to register the point clouds, because then a cloud-to-cloud registration based on best-fit algorithms can be applied. However, the latter generally

results in a lower registration accuracy. For the control measurements, only one scanning set-up was used, so no combination of multiple point clouds was necessary.

Experimental standard deviation

The determination of the experimental standard deviation is based on a series of measurements in which a specific tunnel section was measured four times within a time frame of approximately one hour. Considering this short time frame, it can be assumed that no significant deformation of the tunnel section occurred between all measurements. A distinction was made between measurements from multiple scanning positions (reference measurement) and from a single central position on a tripod (control measurements). The experimental standard deviation was calculated based on the radius values obtained for every 0.1 gon of the four measurements, following the processing methodology above. As a result, an experimental standard deviation $s_r = 0.48$ mm was established for multiple scanning positions (reference measurement). For the control measurements using one scanning position, an experimental standard deviation $s_c = 0.38$ mm was established in actual tunnel conditions. More information on the detailed calculation of the experimental standard deviations can be found in Nuttens *et al.* (2015).

3.3.5 Evaluation of ovalisation results

After manual filtering and further processing of the point cloud obtained by laser scanning, the determined cross-section of a tunnel ring was compared to the design shape and, if applicable, to the reference measurement and the previous control measurement of that tunnel section. For each measurement, plots of the monitored cross-section were developed to visually represent the measurement results. The emphasis lies on a 2D representation to assure an easily interpretable visualisation. This type of 2D drawings gives a very quick overview of areas of the cross-section where significant deviations occur. In order to detect any significant changes, all calculated deviations are compared with the 95% confidence levels, based on the experimental standard deviations. These 95% confidence levels depend on the type of measurement data that is compared and are equal to:

- for comparison of all measurement results with the design shape:
 $2 s_r = 0.96$ mm

- for comparison of a reference measurement and a control measurement:
 $2 \sqrt{s_r^2 + s_c^2} = 1.22 \text{ mm}$
- for comparison of two control measurements:
 $2 \sqrt{s_c^2 + s_c^2} = 1.07 \text{ mm}$

For the interpretation of the results, it is important to mention that the centre of the resulting cross-section of each measurement is based on the axis of the best-fit cylinder, as previously described. As this cylinder is determined for each measurement individually, based on the filtered point cloud, small variations may occur in the orientation of this best-fit cylinder and its centre point, even if there are no deformations in the monitored section. Therefore, some caution is needed with regard to the interpretation of the results, as the measured areas are not always equally spread around the inner tunnel surface. For an accurate evaluation, the ovalisation axis and the deformation pattern should be taken into account in order to compensate for the non-measured areas. In addition, due to the fact that the measurements are not located in an absolute coordinate system, a vertical shift of the whole tunnel structure cannot be detected in the results. However, the extended analysis required to solve these issues lies outside the scope of the presented research.

Chapter 4

Monitoring program: results and observations

4.1 Noteworthy monitoring results

The measurement data obtained in the Liefkenshoek tunnels allow assessment of the real-time behaviour of the concrete segments under numerous loading conditions during construction of the tunnel lining. The following sections present some specific results to indicate important observations of the structural behaviour and demonstrate the reliability of the measurement set-up and operating procedures.

4.1.1 Initial stage after ring assembly

Strain measurements

Figure 4.1 shows a preview of the obtained results for measurement section N3118 during the first hours after ring erection. Due to the calibration and start-up of the data logging process immediately after assembly of the monitored ring, the strain measurements only relate to changes occurring after ring installation. This implies that the reaction of the tunnel ring due to its dead weight and possible assembly stresses, following the installation of the key segment and temporary bolts, is not visible in the measurement results. The various curves in the graph show the various strain gauges installed in this cross-section, each indicated by a coloured code as shown to the right of the chart. For each code, the first number refers to the measurement section, the

second one to the segment and the last number indicates the location of the strain gauge: at the outer (3) or inner (2) reinforcement or at the concrete surface (1). The orientation of the segments and the keystone can be found in Appendix A. By convention, tensile stresses correspond to positive strains and compressive stresses to negative values.

Due to the manufacturing and handling of the precast concrete segments and the rough conditions at the actual tunnel site, each measurement section inevitably includes a small fraction of defective strain gauges. This can be caused either by damaged strain gauges, for instance during concrete casting, or by damaged data cables, due to overcrossing by the wheels of the TBM or preparation works for the cross-passages. Section N3118 showed two defective strain gauges at the start of the measurements. Apart from those, we can see that the measurement system gives very good results, enabling the strain conditions to be followed very accurately. Figure 4.1 shows a clear distinction between the various steps in the construction process following the installation of the measurement ring N3118. It can be seen that drilling works restarted with the excavation of ring N3119 one and a half hours after start-up of the strain measurements. After another half hour, the progression of the TBM excavation caused the first end of the measurement ring to gradually pass the shield tail. At the end of the excavation works on ring N3119, the measurement ring was already half outside the TBM shield. At this point, ring N3119 was installed, causing a standstill of the TBM for about 30 minutes. Next, excavation continued on ring N3120, pushing the measurement ring further out of the protection of the TBM shield. After approximately three hours into the measurements, ring N3118 had completely left the shield tail. Following the excavation and assembly of ring N3120, advance was shortly interrupted due to the extension of the slurry feeding pipes. One and a half hour later, it was resumed with the excavation and erection of ring N3121.

The measurement results of Figure 4.1 allow a good observation of the gradual development of strains and corresponding stresses in the concrete segments. Evaluation of the monitored strains shows that, once the measurement ring starts to leave the shield tail, the monitored stresses gradually decrease, indicating a uniform compression of the tunnel lining. This compression continues until the ring is completely outside the TBM shield. During excavation of ring N3121 (and the following ring N3122), the strain state implies an up-right ovalisation of the tunnel lining into an “egg” shape, with the vertical ring diameter exceeding the horizontal diameter. This is particularly pronounced in tunnel segments A1 and A3. Segment A1 shows a decrease of the com-

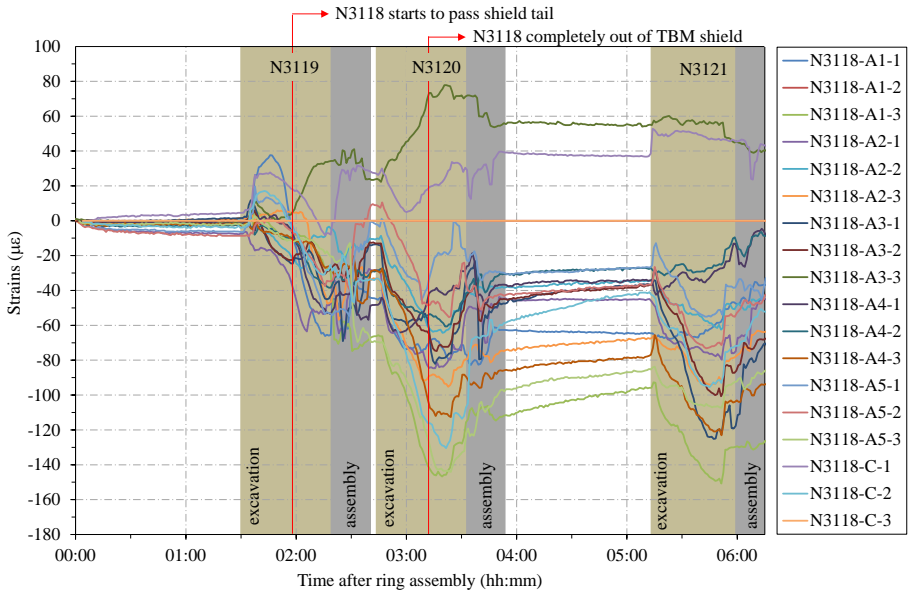


Figure 4.1. Strain results of section N3118 immediately after ring assembly.

pression forces at the inside of the tunnel lining, while segment A3 displays an increase of compression at the inner concrete surface. This corresponds to the upright ovalisation and is confirmed by the ovalisation measurements using laser scanning for this cross-section (see next section). This phenomenon may be explained by the use of larger tail grouting pressures at the sides of the tunnel section compared to the top and bottom.

Strain results of the first 24 h following the assembly of ring N3118 are shown in Figure 4.2. The results show that the start of the measurements comes with peak values in the strain development during the initial hours after ring erection. As mentioned, this is due to the thrust force of the hydraulic jacks pushing the tunnel ring out of the TBM, transferring the grout loading and soil and water pressures onto the ring. Maximum values of the monitored strains are reached within the progression of the first six rings following the measurement ring, corresponding to the first 10 h after installation, or approximately 7 h after the ring has passed the shield tail. Beyond this point, strains tend to decrease, indicating a relaxation of the measurement ring. The latter can be explained by the gradual dissipation of tail grouting pressures. After this, most large variations in the strain results remain absent, as shown in section 4.1.2. In general, the monitored strains often remain smaller than the initial values

from the first hours after ring assembly. Although Figures 4.1 and 4.2 present results from one tunnel section, identical conclusions can be drawn based on the other measurement sections.

From these results, it may be presumed that the loads acting on the tunnel segments during the construction process have a substantial influence on the sectional forces occurring in the tunnel lining. Apart from the long term soil and hydrostatic loads, the acting loads during these initial hours after ring erection can be identified as the thrust force of the shield jacks, possible pressure caused by contact with the tail seals and of course the pressure of the tail grouting. These loads may vary according to the position of the tunnel ring or the applied values of fluctuating thrust force and grout pressures. In any case it is reasonable that the construction loads have a dominant role in the segmental loading.

Ovalisation measurements

Figure 4.3 shows results of the first control measurement using laser scanning of section N3118. Both the reference measurement immediately after ring assembly (orange) and the first control measurement one week after installation (black) are displayed. The difference between both measurements is plotted against the nominal cross-section using the green line. The blue lines indicate the 95% confidence interval. All deviations that remain in between those lines are not considered to be significant, based on the achievable standard deviations. To improve the visual interpretation, all deviations are 100 times enlarged. However, the indicated numerical values represent the real deviations between both measurements. The green line shows that deformations of the tunnel lining in this cross-section have an upright ovalised shape after the first week, compared to the reference measurement. The left side shows a larger inward movement than the top and bottom of the section, causing the vertical ring diameter to exceed the horizontal diameter. This corresponds to the observations of the strain measurements in the previous section.

However, this deformation pattern does not comply with the classical expectations of tunnel lining deformations in soft soil. In general, one would expect an ellipsoidal deformation where the horizontal tunnel diameter exceeds the vertical diameter, causing a horizontal ovalisation or so-called “pumpkin” shape. Nonetheless, the latter is still observed in a large number of tunnel sections. Figure 4.4 for example shows the results of the first control measurement of section S390, clearly indicating a horizontal ovalisation of the cross-section.

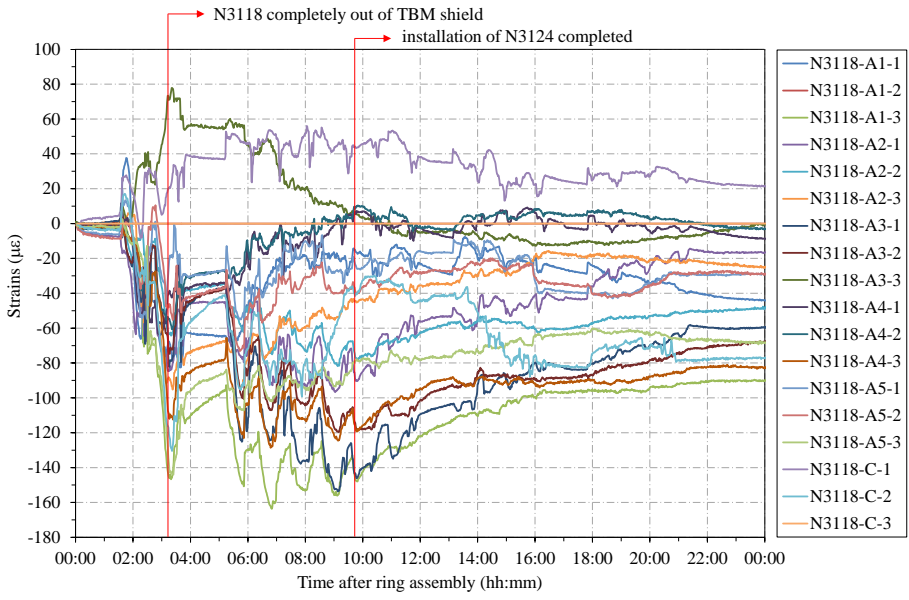


Figure 4.2. Strain results of section N3118 in the first day after ring assembly.

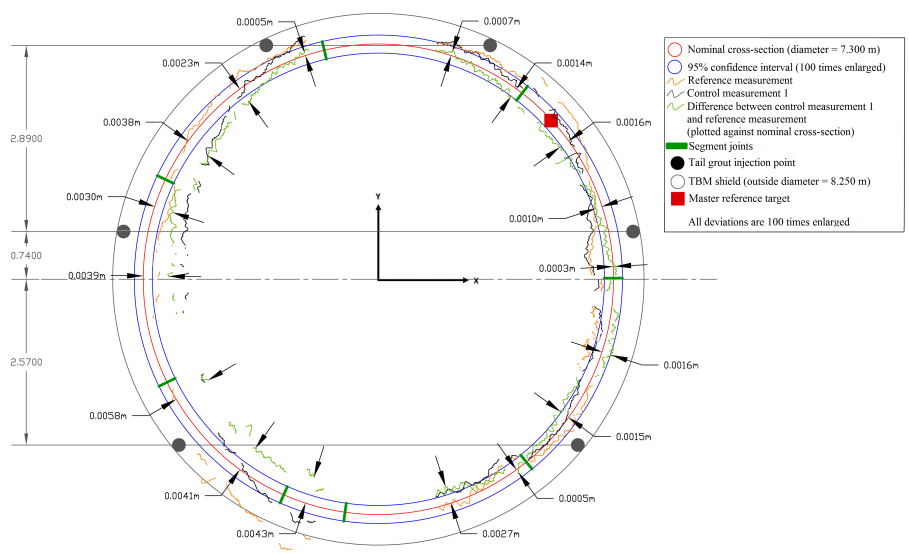


Figure 4.3. Results of first control measurement in section N3118.

A similar deformation pattern is found in about half of the monitored sections. The other half is divided between sections showing the mentioned egg deformation, and others, experiencing only a uniform compression of the lining. These results demonstrate the diverse deformation pattern of the tunnel lining, which will be further discussed in Chapter 5.

4.1.2 Stabilisation phase

Strain measurements

As discussed in section 4.1.1, most large variations in the strain results of the monitored sections remain absent after a progression of about six to seven tunnel rings. This is illustrated in Figure 4.5, which again presents strain results of measurement section N3118, this time during the first two weeks after installation. Some minor fluctuations still occur as the measurement ring is still supporting the TBM back-up train. These are particularly present in the results of segment C, which is located at the bottom of the tunnel section and directly encounters the loads of the back-up installations. Nonetheless, once the monitored section has left the TBM back-up train, the measurement results almost fully stabilise. In addition, the monitored strains often remain smaller than the initial values from the first hours after ring assembly.

Such a stabilisation after the initial installation phase can be observed for all monitored sections. As an example, Figure 4.6 shows strain data in the third month after erection of ring S390. While no permanent changes occur in the monitored data of all strain gauges, it can be noticed that the ones attached to the inner concrete surface (1) seem to show more daily fluctuations than the internal gauges attached to the reinforcement (2 and 3). This is due to the lower modulus of elasticity for concrete compared to reinforcement steel, making small fluctuations in the lining forces more visible in the strain data. After conversion of the monitored strains to stresses, the concrete of the inner tunnel surface shows equivalent fluctuations as the rebars. These remain rather insignificant and are mostly due to external influences such as temperature variations. They do not affect the conclusion that a clear stabilisation occurs on the long term.

Ovalisation measurements

Analysing the laser scanning results of all monitored cross-sections, it can be concluded that significant changes in ring ovalisation always occur during the

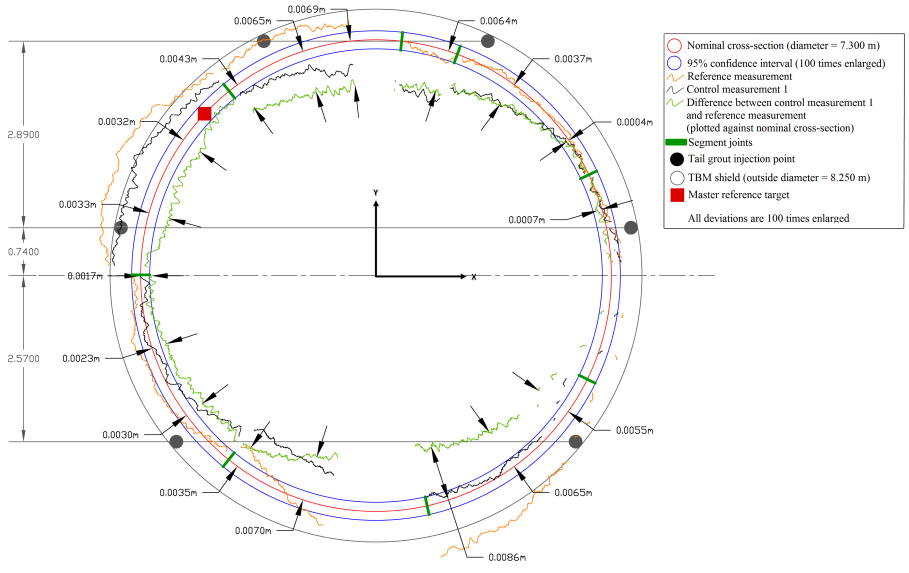


Figure 4.4. Results of first control measurement in section S390.

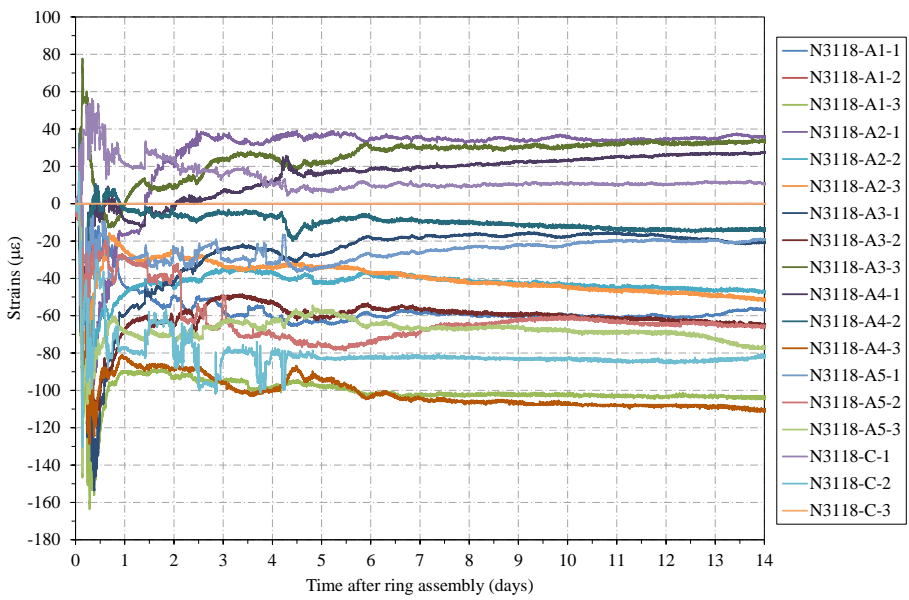


Figure 4.5. Strain results of section N3118 in the first two weeks after ring assembly.

first week after construction of the monitored tunnel sections. After that, no significant changes whatsoever are observed, not even on the long term. Corresponding deformations can be perceived in the results of the first control measurement, which is compared to the reference measurement immediately after ring assembly. All following control measurements indicate no additional deformations of the tunnel sections in respect to that first control measurement. The 95% confidence levels can be taken into account as the threshold for this determination. Figure 4.7 shows an example of the second control measurement in section S390. Comparison of this measurement to the previous control measurement (green line) demonstrates that all deviations stay perfectly within the blue 95% confidence levels, indicating that no significant deformations occurred between both measurements. Identical observations are made for the following control measurements, and this for all monitored cross-sections.

4.1.3 Passage of the second TBM

Strain measurements

Despite the fact that TBM south was initially launched seven weeks after the northern tunnel drive, it overtook TBM north before the crossing of River Scheldt due to parallel works on the cross-passages in tunnel north. After thorough maintenance works prior to the river crossing, TBM north followed the leading tunnel drive with a delay of approximately two months (Boxheimer & Mignon, 2011). The lead of one tunnel drive on the other allowed monitoring strains and ovalisation in the lining of the first tunnel during passage of the second TBM, at a distance of approximately 8 m. Table 4.1 shows the installation dates of the measurement sections in both tunnel tubes. From these dates, the initial head start and overtaking of the northern tunnel drive between the second and third monitoring section in each tunnel can be observed. As a result, the effect of the passage of the second TBM was registered in the continuous strain results of measurement sections N389 and N743 in tunnel north and the six remaining sections in tunnel south.

For the first four measurement sections (N389, N743, S1190, S1500), no significant effect of the passage of the second tunnel drive was monitored. However, the other four sections (S1850, S2076, S2726, S3115) clearly experienced a change in the strain results, as shown in Figure 4.8 for section S3115. Identical graphs for sections S1850, S2076 and S2726 can be found in Appendix B. The passage of the second TBM can be observed distinctly in the stabilised strain results of completed tunnel sections. For section S3115, the effect already

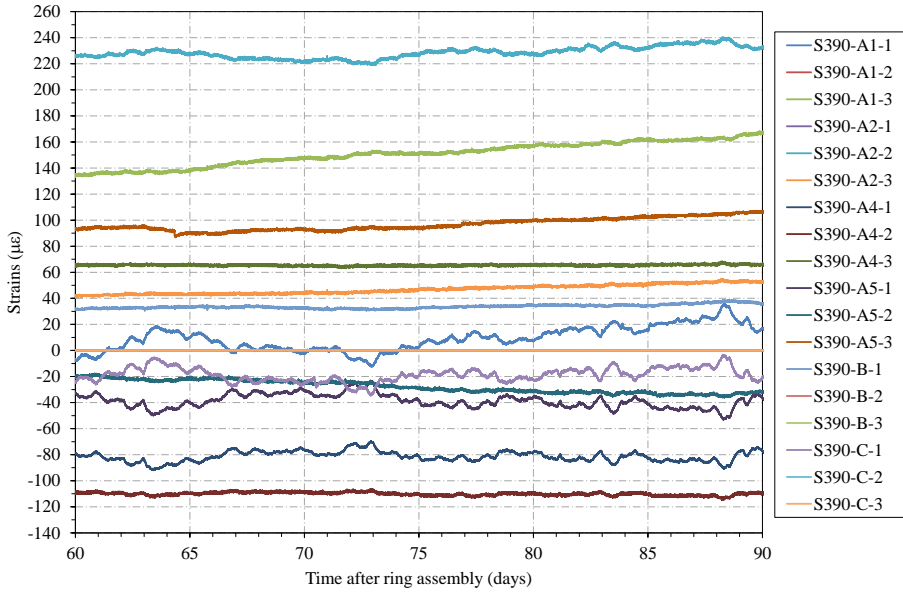


Figure 4.6. Strain results of section S390 in the third month after ring assembly.

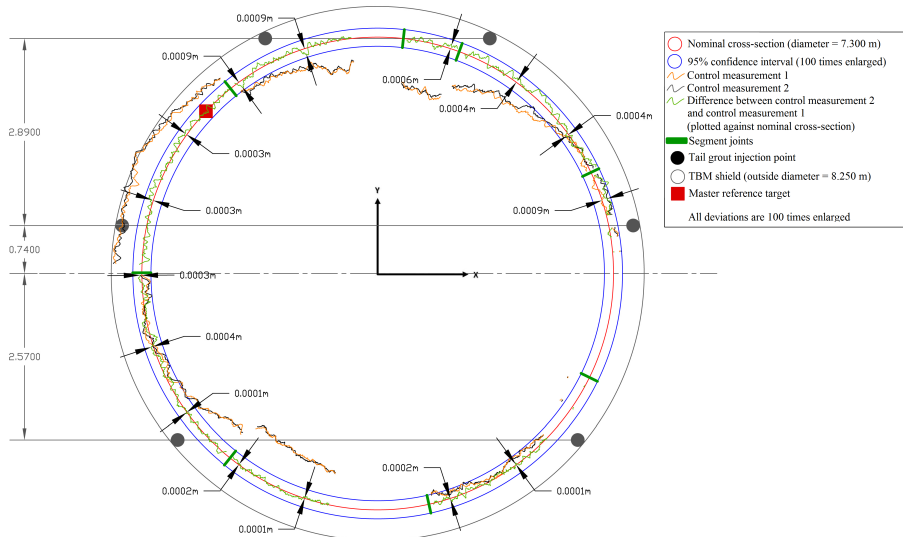


Figure 4.7. Results of second control measurement in section S390.

Table 4.1. Installation dates of the measurement sections in the Liefkenshoek project.

| tunnel north | | tunnel south | | difference (days) |
|--------------|--------------|--------------|--------------|----------------------|
| section | installation | section | installation | |
| N389 | 15/04/2010 | S390 | 18/05/2010 | -33 |
| N743 | 05/06/2010 | S744 | 30/06/2010 | -25 |
| N1191 | 19/12/2010 | S1190 | 09/10/2010 | 71 |
| N1497 | 25/01/2011 | S1500 | 02/12/2010 | 54 |
| N1858 | 10/03/2011 | S1850 | 14/01/2011 | 55 |
| N2079 | 22/03/2011 | S2076 | 30/01/2011 | 51 |
| N2729 | 05/06/2011 | S2726 | 01/04/2011 | 65 |
| N3118 | 29/06/2011 | S3115 | 26/04/2011 | 64 |

appears before the passage of the cutterhead, when the tunnel face is at a longitudinal distance of approximately 18 m from the measurement section (see Figure 4.9 for clarification). It still continues for a short period after the shield tail has passed the equivalent position of the measurement section. The strain results stabilise once the shield tail is at a distance of about 20 m. The latter is confirmed by the other three measurement sections: the influence of the passage generally dissolves once the shield tail has passed by about 22-24 m, corresponding to time spans of 10 to 17 hours. However, the instant when the influence of the second tunnel drive starts to become noticeable occurs much later for the other measurement sections, compared to section S3115. On average, the front face is already at a short distance of only a few meters before the effect is monitored in the adjacent tunnel.

Evaluation of the strain results shows that, in general, the impact of the passage of the second tunnel drive on the stresses in the tunnel lining is limited to about 1-4 N/mm². At the top and bottom of the tunnel section, an increase in tension forces is found for the inner reinforcement and concrete surface, while a rise in compression forces is observed for the outer reinforcement. At the sides of the tunnel section, the opposite effect is detected, with increasing compression at the inside of the lining and tension at the outer part. This proves that the excavation of the adjacent tunnel shaft causes a minor horizontal ovalisation of the segmental lining in the leading tunnel. These observations demonstrate the achieved accuracy of the continuous strain monitoring programme, as the simultaneous ovalisation measurements using laser scanning (discussed in the next section) did not notice significant alterations during this phase.

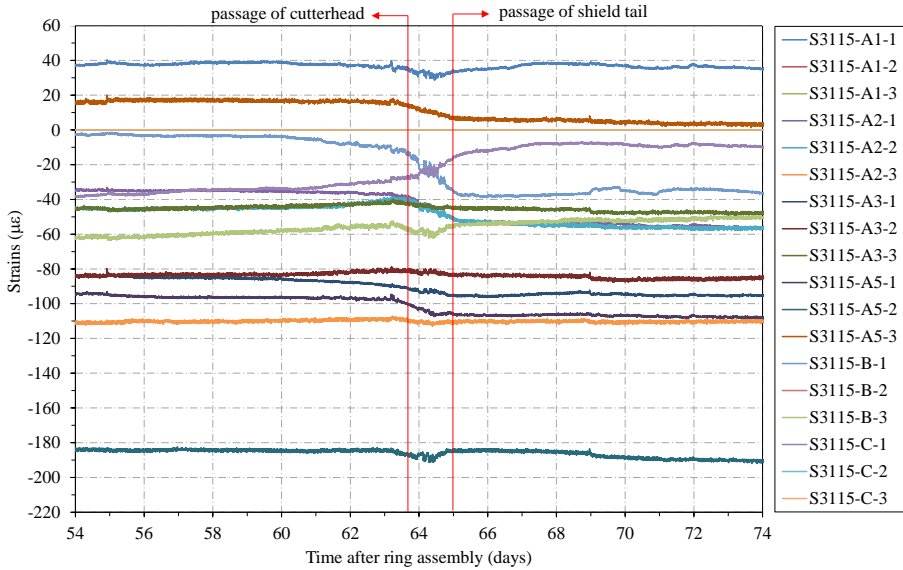


Figure 4.8. Strain results in section S3115 during passage of second tunnel drive.

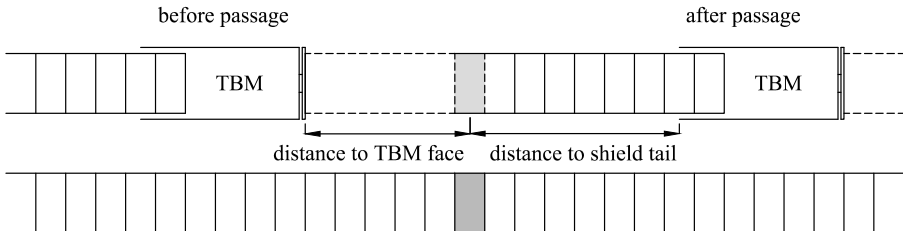


Figure 4.9. Passage of second tunnel drive.

Ovalisation measurements

In general, the frequency of the control measurements using laser scanning did not allow a detailed study of the passage of the second TBM on the deformations of the leading tunnel. Therefore, additional control measurements were executed to monitor the deformations of section S2726 in tunnel south. They were performed at regular intervals during the approach of the second tunnel drive to the neighbouring section in tunnel north (N2729), until several days after the TBM had passed the corresponding ring. Tunnel north counted three tunnel rings more at the equivalent section of S2726, due to a curve in the tunnel trajectory. A first ovalisation measurement (CM P0) was performed at a rather late stage in the passage, when the tunnel face was already at a

distance of approximately 7 m from section S2726. Nonetheless, this measurement showed no significant deformations of the tunnel section compared to the previous control measurement, about one month earlier. It was taken as a reference for the following measurements. During the next six days, the tunnel section was measured approximately every hour, resulting in a large number of measurements. However, only three of them were processed:

- CM P1: when the tail seal passed section S2726;
- CM P2: when the tail seal was at an approximate distance of 15 m;
- CM P3: when the tail seal was at an approximate distance of 65 m;

The latter was executed approximately two days after construction of section N2729. However, comparison of all three measurements to the first measurement CM P0 showed no significant deformations of the tunnel section. All deviations fall within the 95% confidence intervals, indicating that no measurable changes occurred in tunnel south during the excavation of tunnel north. For illustration, corresponding results of the last measurement (CM P3) in comparison with CM P0 are given in Appendix B.

4.1.4 Construction of cross-passages & evacuation shafts

Strain measurements

As mentioned in section 2.3.2, various cross-passages (CP) were constructed within a frozen soil body. All drillings of the freezing tubes were performed from within tunnel north. After completion of the soil freezing, the construction consisted of a partial removal of the tunnel lining of tunnel north, followed by the excavation of the distance of 8 m to the adjacent tunnel. Next, the connection between both tunnels was made by creating the opening in the concrete lining of tunnel south. Temporary shotcrete was applied before a sealing membrane was installed to ensure water tightness. Finally, the highly reinforced inner shell of the CP was constructed. The intensive works corresponding with these consecutive construction phases are clearly depicted in the strain development of the concrete tunnel segments. Figure 4.10 shows strain results from one of the rings in tunnel south, which were actually cut during the construction of CP03. Even the start of the freezing process to create the frozen soil body can be noticed. After completion of the soil freezing, large and sudden jumps can be observed due to the gradual opening of the tunnel shell for the construction of the cross-passage. The variations are particularly pronounced

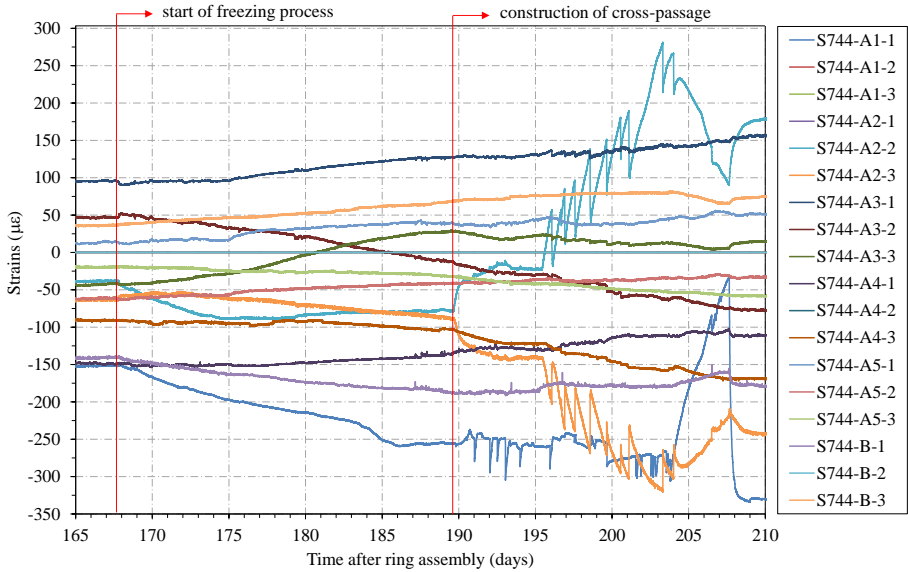


Figure 4.10. Strain results in section S744 near cross-passage CP03.

in tunnel segments A1 and A2, which are oriented to the side of the tunnel that is being cut and partly removed.

In addition, the tunnel tubes had to be connected to the evacuation shafts (ES), constructed as rectangular shafts of diaphragm walls between both tunnels. The connection galleries were mainly built within treated soil by blocks of cement-bentonite with a low strength. To construct the gallery, at first an opening had to be cut into the diaphragm walls, after which the gallery had to be excavated within the water retaining sealing block over a short distance of less than 2 m. After protection with shotcrete, the tunnel lining was cut and partly removed. Figure 4.11 shows strain results of tunnel south near ES07, around ten months after assembly of the adjacent measurement ring. Again, the impact of the opening of the tunnel shell for the construction of the connection gallery can be observed clearly in tunnel segments A4 and A5, which are oriented to the side of ES07.

Furthermore, during construction of the diaphragm walls for one of these shafts, an incident occurred where the tunnel sealing was breached. As a result, a large amount of mud entered the tunnel, which was immediately evacuated. Luckily, the situation could be stabilised rather quickly, but questions remained on the condition of the tunnel lining as a result of this breach. The incident occurred near one of the measurement sections, allowing a fast verification of

the structural integrity. It could be perceived in the strain data, but only a very small change in the monitored strain results was identified, in the order of magnitude of a few microstrains. Consequently, the incident did not significantly affect the stress and strain state of the tunnel lining. As a result, the safety of the tunnel work site could be assured and construction activities in the tunnel tubes could be resumed.

Ovalisation measurements

As can be observed in the time scale of Figures 4.10 and 4.11, all activities on the creation of the cross-passages and evacuation shafts occurred several months after construction of the monitoring sections. As a result, no control measurements using laser scanning were performed any more at this time after installation. Therefore, no additional information was available on the deformations of the tunnel lining due to the partial opening for the connection with the cross-passages and evacuation shafts.

4.1.5 Tidal influence of River Scheldt

Strain measurements

As can be observed in Figure 3.2, several measurement sections were located below River Scheldt. This is a tidal river, of which the water levels are linked to the tides of the North Sea. Measurement results have shown that the influence of the river tides is depicted in the monitored strains of all measurement sections below the river. Figure 4.12 shows the obtained strain results for section N1497, over the time frame of two weeks, around one month after ring assembly. At the top, the half-daily fluctuations of the water level of the river are plotted as well. From this graph, it can be observed that periodic half-daily fluctuations occur in the stabilised strain results, which can be directly linked to the water level. Strains tend to increase at low tide, indicating a relaxation or general decrease in compression of the tunnel rings. A larger head of water at high tide in turn causes larger compression forces in the tunnel rings. As additional levelling measurements indicated a movement of the tunnel section below the river as well, the structural behaviour of the tunnel lining in response to the river tides was further investigated in detail. The results of this study will be discussed in Chapter 8.

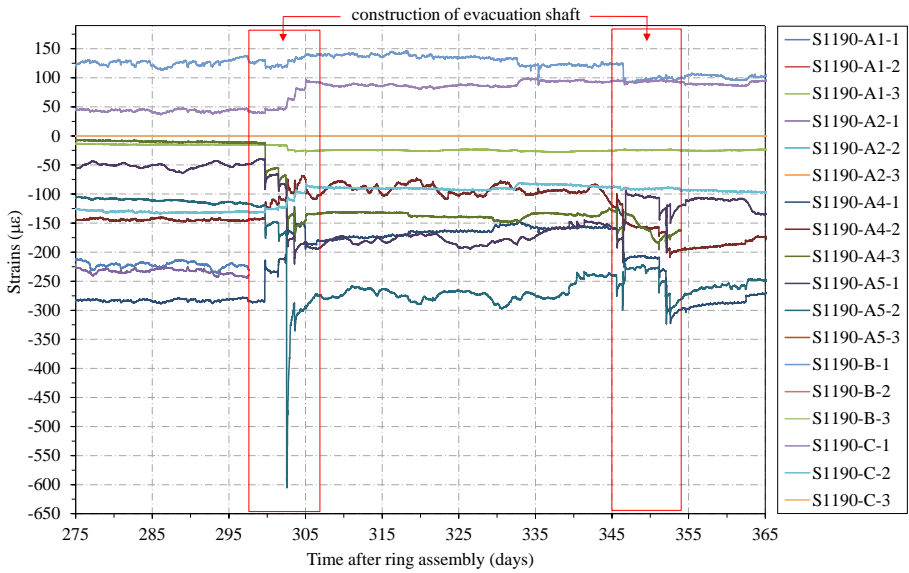


Figure 4.11. Strain results in tunnel south near evacuation shaft ES07.

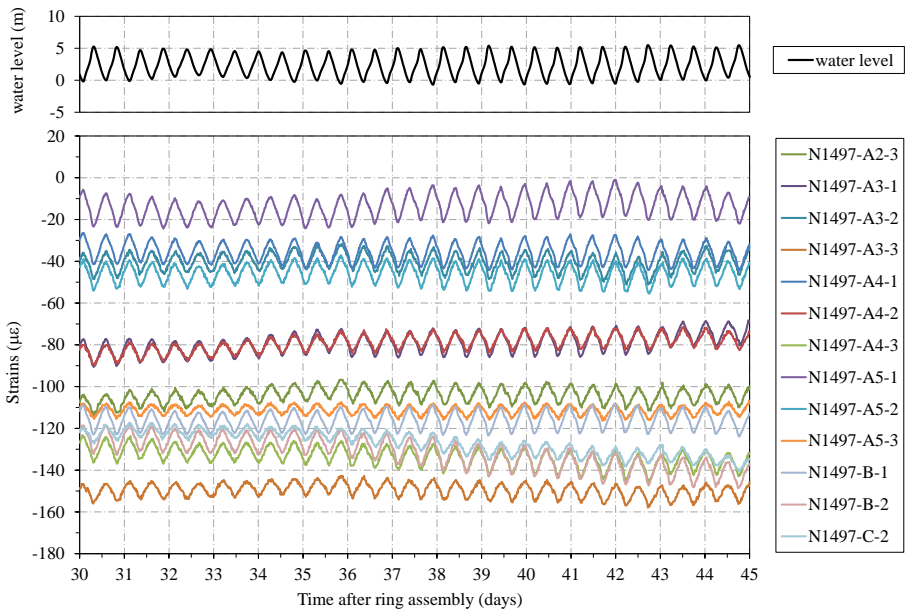


Figure 4.12. Tidal fluctuation of strain results below River Scheldt.

Ovalisation measurements

The time interval between two ovalisation measurements of the tunnel lining is either one week or one month, as discussed in section 3.3.3. As a consequence, standard ovalisation results should not be applied for an evaluation of the half-daily impact of the river tides on the deformations of the tunnel lining. Therefore, additional control measurements using laser scanning were performed as part of the extensive study of the tidal influence. The corresponding results played a substantial role in the accurate identification of the deformation behaviour of the tunnel lining below River Scheldt. They are discussed in detail in Chapter 8.

4.2 Important observations

4.2.1 Governing construction phase

The results of section 4.1.1 showed that the initial stage after ring assembly comes with peak values in the strain development, due to various loads acting on the tunnel segments during the construction process. The thrust forces of the hydraulic jacks push the tunnel rings passed the shield tail, after which grout pressures and long term soil and water loads are transferred onto the tunnel lining. Maximum values of the monitored strains were reached during this phase, which corresponds to a progression of about six rings following the measurement ring. Afterwards, advance of the excavation front moves the TBM further away and the grout filling the tail void starts to consolidate, causing strains to gradually decrease and stabilise around a lower value. After this, most large variations in the strain results remain absent. In general, the monitored strains often remain smaller than the initial values from the first hours after ring assembly. In addition, laser scanning results showed that significant deformations always occur during the first week after construction of the monitored tunnel sections. After that, no significant changes are observed.

From these results, it would appear as if the initial hours after assembly are critical for the design of the tunnel lining. Since this tendency can be observed for all monitored sections, it was investigated if every single strain gauge reaches its extreme values within this initial time frame. For this purpose, all strain results were analysed, from the start of the measurements until the installation of the fire-protective coating. This corresponds with the red, black and blue zones in Figures 3.11 and 3.12. For each strain gauge, it was verified at what

Table 4.2. Occurrence of extreme strain values.

| Time after installation | Maximum compression ¹ | Maximum tension ¹ | Defective sensors ² |
|-------------------------|----------------------------------|------------------------------|--------------------------------|
| Within 24h | 48% | 76% | 22% |
| Within 48h | 50% | 77% | 24% |
| Within 7d | 53% | 81% | 27% |

Notes: ¹The percentage relates to total number of non-defective strain gauges;

²The percentage relates to total number of installed strain gauges.

time after installation it reached its minimum or maximum strain value. Since compressive stresses correspond to negative strains, minimum strain values are linked to compression and maximum values to tension. The results are given in Table 4.2. This table shows that over a monitored period of almost two years, around half of the total amount of installed strain gauges encounters maximum compression during the first 48 hours after the installation of the corresponding measurement section. The number of strain gauges reaching maximum tension within the initial phase after installation even amounts up to 80%. These values refer to non-defective sensors only. In general, strain gauges that provided erroneous results within the first month after installation, were not incorporated in the data analysis.

Table 4.2 shows a relatively large number of strain gauges that was considered defective within the first days of monitoring. The amount ranges up to a quarter of the installed sensors and can generally be ascribed to two different causes. Due to the manufacturing and handling of the precast concrete segments, various strain gauges were already damaged before the start of the measurements, for instance during concrete casting, which mostly explains the 22% of faulty sensors after the first 24 hours. The loss of measurement data can also be caused by damaged cables for data transfer, due to overcrossing by wheels of the TBM during the initial hours of advance. Apart from the data cables that were damaged within the first day, an additional 5% was lost in the first week after installation, due to the passage of the TBM back-up train and corresponding operations. Construction traffic in the tunnel and rough site conditions lead to a further increase in the number of defective strain channels during the measurement period.

Results of Table 4.2 prove that the initial phase of the first few days after installation might be governing for a significant majority of strain gauges, showing a strain development comparable to Figure 4.2. Construction loads cause

the existence of unfavourable tensile stresses in this short time frame, which are governing for the majority of the measurement points. Around 50% also experiences compressive stresses immediately after construction that are not exceeded at a later stage. However, a reasonable amount of measurement points reaches its extreme values at some time after construction of the tunnel section. This can be due to long term stabilization effects of the tunnel structure and surrounding soil bedding, or as a result of on-going construction works in the tunnel. For example, section 4.1.4 showed that the intense activities corresponding with the construction of cross-passages and evacuation shafts have a distinct effect on the forces in the tunnel lining.

The figures of Table 4.2 show that the construction loads have a dominant role in the segmental loading. Yet due to the absence of the segmental erection phase in the monitoring results, there is a resulting lack of knowledge regarding the assembly stresses present in the concrete elements at the start of the measurements. Therefore, reliable statements on the absolute values of compressive or tensile stresses in the lining segments remain difficult. However, it should be clear that if unfavourable tensile stresses are present in the concrete tunnel lining somewhere during its lifetime, the chances of them occurring during the construction phase immediately after installation of the tunnel ring are very high. Indeed, around 80% of the sensors reach their maximum value during this initial installation phase. Significant structural changes to the tunnel lining, such as the creation of a cross-passage, can lead to governing phases at a later stage and naturally require special attention in the design. However, since half of the monitored sensors also experience maximum compressive forces during the initial stage after installation, it is absolutely clear that the construction phase should form an integral part of the design process of the precast concrete tunnel lining. A design based solely on soil parameters or obvious points of particular interest, such as cross-passages or evacuation shafts, might not suffice if the early construction stages are not taken into account.

4.2.2 Local effects on lining behaviour

In general, the design loads on the segmental tunnel lining are considered to be the soil and water pressures, which vary gradually along the tunnel trajectory. If they were the main governing loads on the concrete segments, then neighbouring cross-sections in both tunnel tubes should show nearly identical stress and deformation behaviour, as they are located at the same position along the tunnel axis. However, measurement results have shown that this is not true in

many cases. The comparison of adjacent measurement sections in both tunnel tubes shows but partial resemblance in the monitored strains. Although the local environment and hence the general loading on the tunnel lining are the same, still different strain results are often found for such adjacent cross-sections. This is illustrated in Figures 4.13 and 4.14, which show strain results during the first 48 h after ring assembly of neighbouring sections N1497 and S1500. Section N1497 shows tensile strains in one of the surface gauges during the initial hours after installation, followed by compression behaviour in all strain gauges, with strain values reaching $-160 \mu\epsilon$. In section S1500, strain values are much higher, up to almost $400 \mu\epsilon$ both in compression and tension. No uniform compression state is found, as several strain results remain in the positive tensile range, long after the tunnel ring has left the shield tail.

The ovalisation measurements confirm the observation that neighbouring measurement sections not always show identical behaviour. A different deformation pattern is found in sections N1497 and S1500, but in other neighbouring sections as well. For example, Figures 4.15 and 4.16 present the results of the first control measurement in sections N2971 and S2978. While section S2978 shows the classical pumpkin deformation shape of the tunnel lining in the first week after installation, section N2971 experiences a vertical ovalisation or egg-shape. Furthermore, initial deviations of the theoretical tunnel radius already existed immediately after installation of the tunnel sections, as visible in the results of the reference measurements. This inaccurate installation of the individual segments during ring assembly causes imperfections in the joints between segments. The results of the first control measurement show that these imperfections remain present in the deformed tunnel lining. Although the final cross-sectional deformation of the monitored sections can generally be identified as an elliptical shape (pumpkin or egg), deviations of the perfect ellips obviously still exist. They are different for each measurement section and mostly due to the initial imperfections of individual segments in the erected ring.

Both observations from strain and ovalisation measurements confirm the supposition that local effects, other than the general loading conditions, play an important role in the stress and deformation state of each individual section. Such local influences might be the variable tail grouting pressures on the segmental lining, or the shifting orientation of the keystone. But most importantly, the imperfect installation of the individual segments during ring assembly can lead to unequal supports in joints. These installation imperfections influence the force transfer between segments of the same ring or adjoining rings, causing

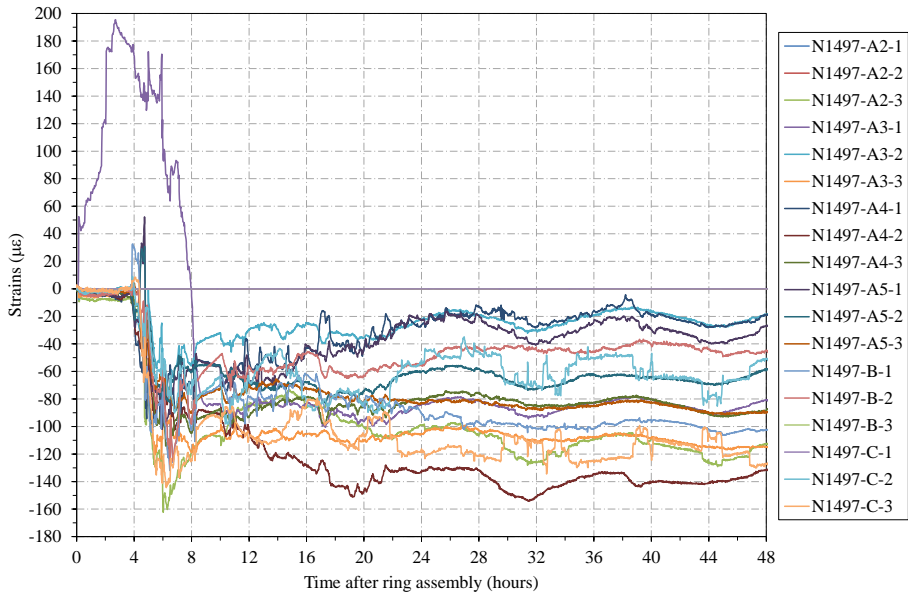


Figure 4.13. Strain results of section N1497 in the first two days after ring assembly.

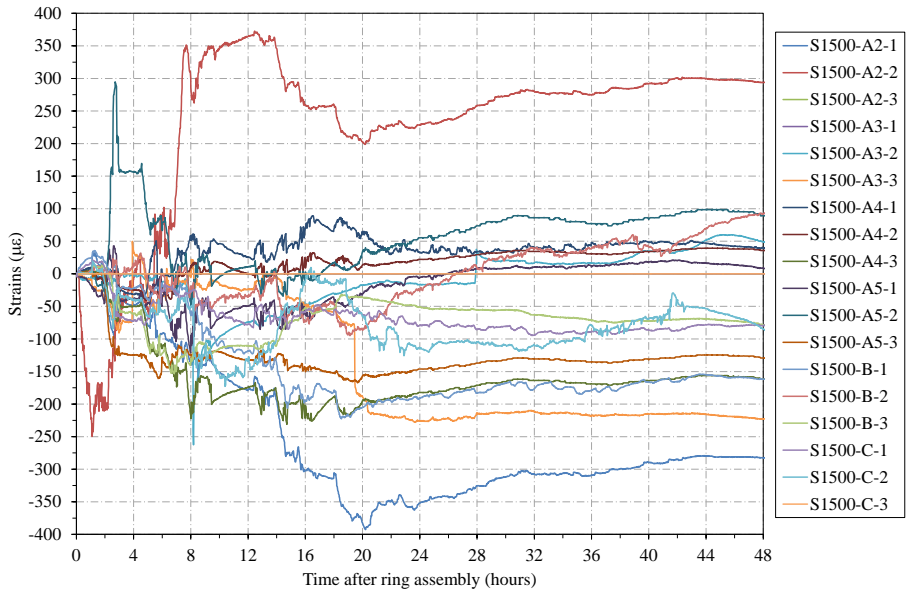


Figure 4.14. Strain results of section S1500 in the first two days after ring assembly.

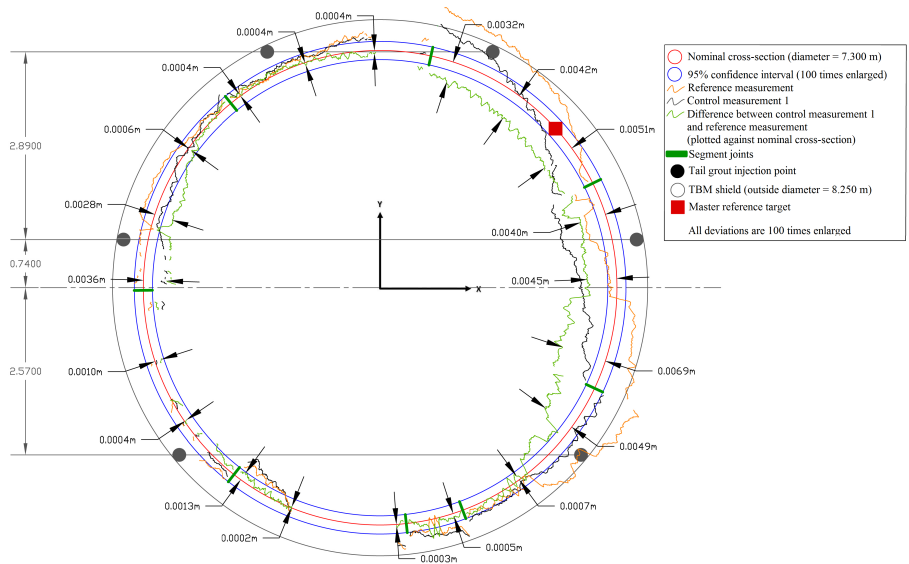


Figure 4.15. Results of first control measurement in section N2971.

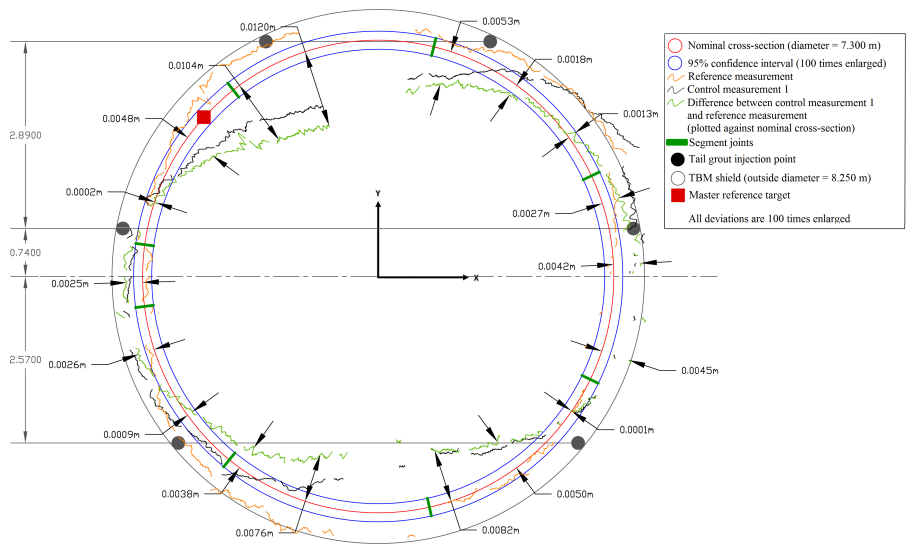


Figure 4.16. Results of first control measurement in section S2978.

deviations from the normal stress patterns in the concrete lining. The presence of these installation inaccuracies remains visible after deformation of the tunnel sections, indicating a permanent disruption of the theoretical segmental lining behaviour.

4.2.3 Complementary aspect of strain & ovalisation monitoring

In literature, very few simultaneous strain and laser scanning measurements of actual tunnel lining behaviour are available. Therefore, the question remained how well both data sets agree and how they can be integrated for better insights in segmental lining behaviour. The obtained monitoring results give the unique opportunity to assess both measurement techniques and the contribution of their integration to tunnel monitoring.

Due to the segmental composition of the tunnel lining, the global deformation of a tunnel cross-section is the result of deformations of the individual concrete elements and displacements and/or rotations in the joints between adjacent segments. Thanks to their high accuracy level, the ovalisation measurements are able to measure the global deformation pattern as well as the joint behaviour of the segmental lining. Compression of the sealing gaskets in the segment joints and rotations of adjacent segments relative to each other are likely to occur due to normal forces and bending moments in the tunnel lining. This joint behaviour can cause displacements of the tunnel segments that are not always easily identified by the strain results. On the other hand, the standard deviation of the laser scanning set-up is not small enough to be able to detect actual deformations in the individual concrete segments. Results of the strain monitoring program have shown that the occurring strains in the concrete lining equal deformations of sub-millimetre level that are not likely to be registered by the ovalisation measurements. Therefore strain measurements are required to study the stresses introduced into the lining segments during and after construction. As a result, in order to obtain a full image of the cross-sectional deformations, both aforementioned monitoring techniques need to be applied to acquire a complementary set of measurement data.

In general, the results of strain and ovalisation measurements are in good agreement. Monitored strains in the individual segments are in correspondence with the cross-sectional deformations as registered using laser scanning. Both techniques have indicated that the most important changes in the tunnel lining occur in the initial period after ring assembly. However, ovalisation meas-

urements are not able to specify critical moments in the construction stage in detail. Due to the presence of the TBM installations and back-up train, no intermediate laser scanning measurements can be executed during the first week after ring assembly. The continuous aspect of the strain measurements allows monitoring the response of the tunnel lining more closely in each step of the construction process. Also after the initial assembly stage, a detailed evaluation of the lining behaviour is possible, as indicated by various results in this chapter. For example, the passage of the second tunnel drive could be identified in the strain results, whereas the ovalisation measurements were not able to perceive any significant deformations. Furthermore, the influence of the river tides was observed in the continuous fluctuation of the strain data. If only laser scanning was included in the monitoring program, this tidal effect would have remained unnoticed. Nonetheless, the ovalisation measurements had a substantial role in the identification of the tunnel lining behaviour in response to the river tides (see Chapter 8).

In conclusion, both strain and ovalisation measurements have proven their value in the accurate monitoring of shield-driven tunnels. On the one hand, ovalisation results ensure a detailed and easy interpretable view on the cross-sectional deformations of the tunnel lining. On the other hand, strain measurements are essential in the continuous observation of the stress behaviour in the lining segments, which mostly remains outside the perceptibility of the laser scanning technique. Ultimately, their combined application proves an important advantage in the structural assessment of segmental tunnel linings.

4.3 Research subjects

In this chapter, some important observations of the experimental monitoring program have been discussed. They gave rise to two main focus points that were selected for further investigation as part of this dissertation.

Firstly, all monitoring results indicate the significant influence of the construction process on the behaviour of the segmental tunnel lining. Apparently, this behaviour is not only determined by the general loading conditions, such as soil and water pressures, but by several other effects as well. One of the important aspects during construction is the presence of installation imperfections between tunnel segments, which can be perceived in the ovalisation results. Therefore, the following chapter will determine the magnitude of these imperfections. Next, using FE-modelling, their impact on the deformations and sectional forces in the tunnel lining will be evaluated.

Secondly, the presence of a tidal river along the trajectory of the Liefkenshoek tunnel has a continuous impact on the tunnel lining. Apart from a constant fluctuation of lining stresses, an oscillating displacement of the tunnel was observed in response to the river tides. As virtually no information is available in literature on such a behaviour, a detailed investigation of the impact of the river tides is carried out. First, a clear identification of the tidal effect is pursued, after which several hypotheses are investigated to determine the origin of the tunnel movements.

Chapter 5

Installation imperfections: monitoring results

5.1 Global cross-sectional deformations

5.1.1 Statistical approach of monitoring results

As 28 tunnel sections were monitored using laser scanning, conclusions on the deformational behaviour of the tunnel lining can be drawn from the average ovalisation results. For each control measurement or reference measurement, a radius value r was found for 4000 values of the angle θ in each monitored tunnel ring. The definition of θ is specified in Figure 5.1 and is not affected by the variable segment orientation in the various measurement sections. The nonconformity of the values r with respect to the inner design radius $R_{in} = 3650$ mm are noted as r' . A positive value of r' corresponds to the measured radius being larger than the design radius, as depicted in Figure 5.1.

Combining the results of all the measured tunnel sections for each individual value of θ , a mean radius value \bar{r}' can be found for each θ using equation 5.1. In this equation, n denotes the number of sections for which a measured radius value is available for the considered value of θ . Since n is quite large, the sample mean \bar{r}' obtained by equation 5.1 for n measurement rings is a good estimation of the population mean μ for all tunnel rings (based on a normal distribution). The standard deviation s can be determined using equation 5.2. A 95% confidence interval for the values of r' then equals $\bar{r}' \pm 1.96s$, implying that only 5% of the monitored values fall outside this interval.

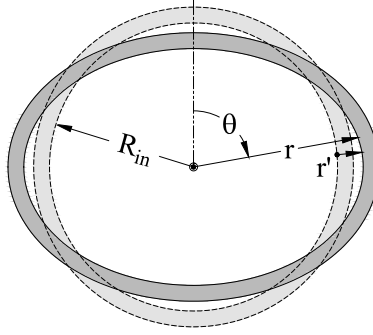


Figure 5.1. Definition of radial values r and r' .

$$\bar{r}' = \frac{\sum r'}{n} \quad (5.1)$$

$$s = \sqrt{\frac{\sum (r' - \bar{r}')^2}{n - 1}} \quad (5.2)$$

According to the central limit theorem (Moore *et al.*, 2009), the distribution of the sample mean \bar{r}' is approximately normal with mean μ and standard deviation σ/\sqrt{n} , with σ being the population standard deviation for all tunnel rings. This value is not known but can be estimated with the sample standard deviation s . In that case, the standard deviation of \bar{r}' can be estimated by the standard error SE , given by equation 5.3. Finally, the interval $\bar{r}' \pm t_{n-1;0.975}SE$ is an appropriate 95% confidence interval for μ , with $t_{n-1;0.975}$ being the inverse of the Student's t-distribution with a 97.5% chance and $n-1$ degrees of freedom (Moore *et al.*, 2009).

$$SE = \frac{s}{\sqrt{n}} \quad (5.3)$$

5.1.2 Reference measurement

Figure 5.2 shows the results obtained from the ovalisation monitoring for the reference measurement immediately after installation (CM 0), using the data processing method described above. Due to the manually operated installation of the segments, a tunnel ring is never installed perfectly circular. Figure 5.2 shows that a significant spread is present in the measured deviations r' of the theoretical tunnel radius, as can be seen by the 95% confidence interval (CI) for r' . It can be observed that deviations from the theoretical design profile

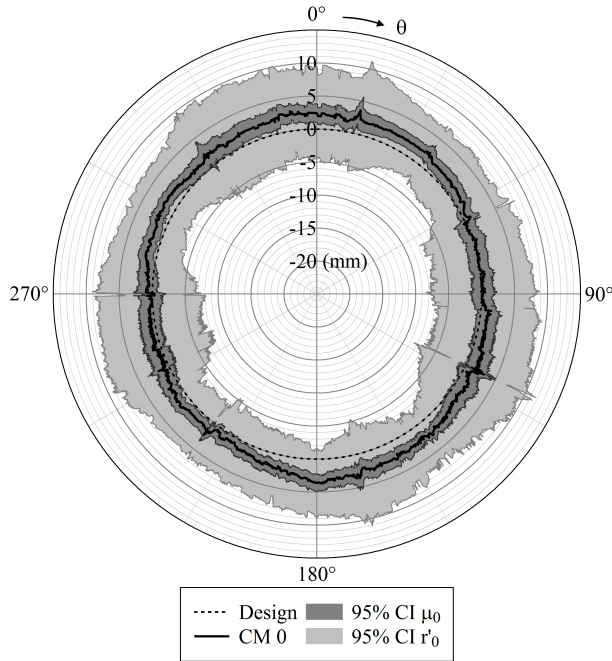


Figure 5.2. Deviation of inner tunnel radius from theoretical radius for CM 0.

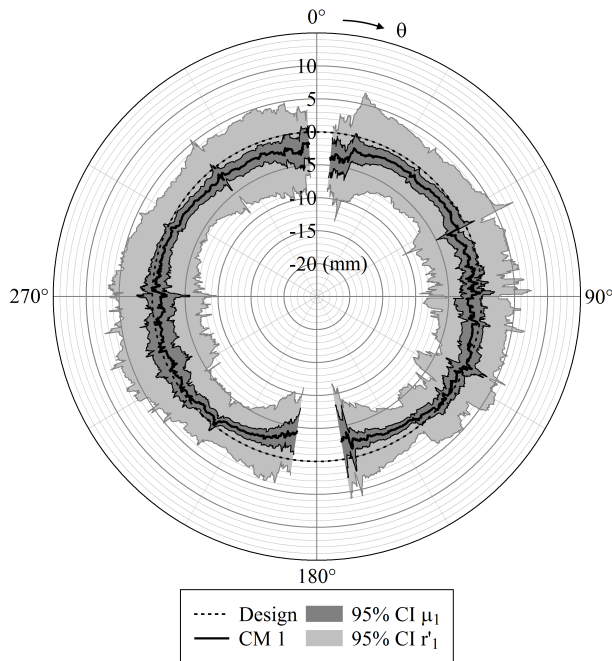


Figure 5.3. Deviation of inner tunnel radius from theoretical radius for CM 1.

range up to 11 mm. Nonetheless it can be concluded that on average the installed ring profile is egg-shaped: the vertical ring diameter is larger than the horizontal diameter and exceeds the design tunnel diameter. This conclusion can be stated with a good reliability for the entire tunnel lining, since the 95% confidence interval for the mean μ is restricted to a few millimetres and therefore does not affect the validity of the conclusion.

5.1.3 First control measurement

Figure 5.3 shows the results for the first control measurement (CM 1) one week after installation. After interaction with the tail grouting pressures and the soil and water loads, a scattered deformation pattern can be identified for the monitored sections, as reflected in the 95% confidence interval for r' . This is due to the distribution of the monitored locations along the tunnel trajectory. Every section interacts with the local environment, which often influences various parameters of the shield tunnelling process as well. Nonetheless conclusions can be drawn from the combined measurement results. In particular, the global average displacements obtained by CM 1 shows an elliptical deformation of the tunnel sections, where the horizontal tunnel diameter exceeds the vertical diameter. This horizontal ovalisation of the tunnel cross-section complies with the classical expectations of a pumpkin-shaped deformation for circular tunnels in soft soil (Blom, 2002; Schulze & Duddeck, 1964; Duddeck, 1980; Duddeck & Erdmann, 1985). The consequential deformations between ring installation (CM 0) and the first control measurement are in correspondence with these observations. They are plotted in Figure 5.4. The top and invert show an average inward displacement of 5 mm, which is larger than the deformation at the sides. This again applies to the entire tunnel lining, given the relatively narrow 95% confidence intervals for the mean value μ .

5.1.4 Last control measurement

In Figures 5.3 and 5.4, one could observe openings in the measurement data at the crown and invert of the cross-sections. This is due to the blind spots of the laser scanner, caused by the ventilation tube at the top and the tripod used to support the measurement device at the bottom of the section. Similar openings due to the same reasons are present in Figure 5.5 as well. The latter shows the deformations between the first control measurement (CM 1) and the last one (CM 6) executed three months after installation. It can be observed that basically no significant deformations occur after the first control measurement,

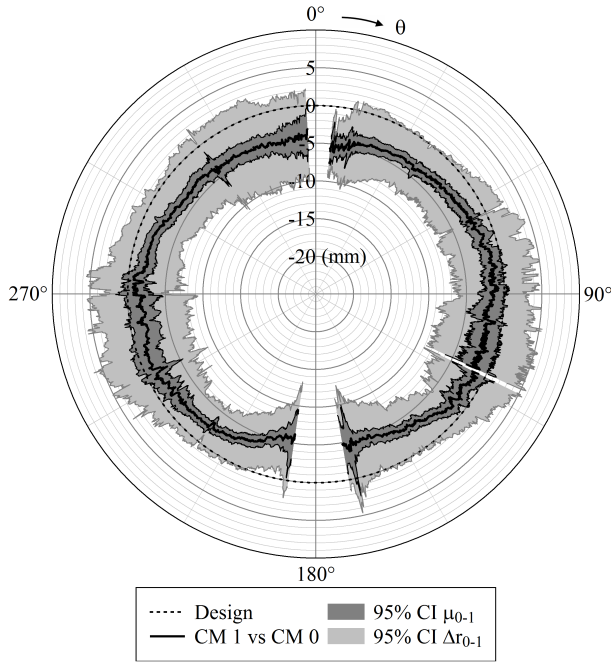


Figure 5.4. Variation of inner tunnel radius between CM 0 and CM 1.

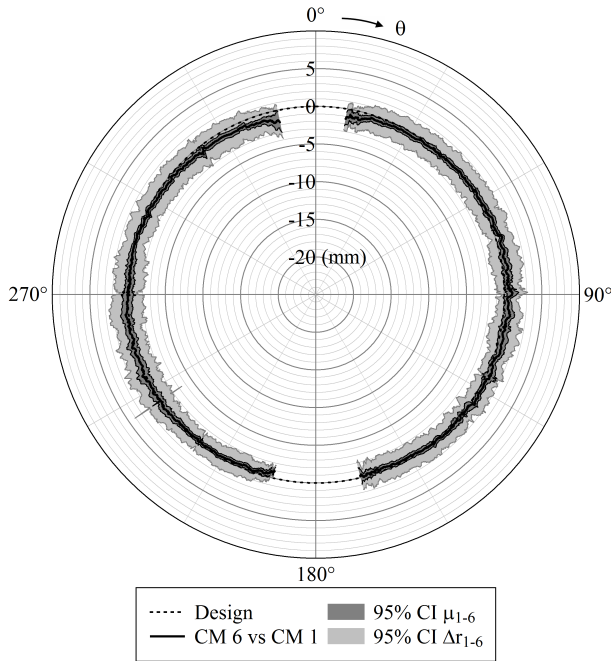


Figure 5.5. Variation of inner tunnel radius between CM 1 and CM 6.

as the 95% confidence interval for the tunnel mean value μ almost perfectly coincides with the zero reference line. Therefore it can be concluded that all noteworthy deformations of the tunnel lining occur during the first week after installation. Most probably they mainly occur in the short period following the exit of the tunnel rings out of the tail shield of the TBM. However, due to equipment of the TBM blocking the sight at this time, no additional ovalisation measurements can be performed to verify this supposition.

5.1.5 Evolution of tunnel radius

Finally, the same conclusions can be derived from the calculation of the average monitored tunnel radius. For each measurement, an average deviation R'_i of the theoretical tunnel radius R_{in} can be calculated for every measurement section i using equation 5.4. In this equation, m equals the number of angular values of θ for which a monitored radius value is available. Subsequently the average deviation R' of the theoretical tunnel radius for each measurement can be calculated by averaging over the n monitored tunnel sections using equation 5.5.

$$R'_i = \frac{\sum r'}{m} \quad (5.4)$$

$$R' = \frac{\sum R'_i}{n} \quad (5.5)$$

Figure 5.6 shows the resulting variation in time of the average tunnel radius with respect to the theoretical radius. As can be seen from this figure, the initial radius of the installed tunnel ring (CM 0 at 0 days after installation) is always larger than the design radius, due to the manually operated assembly of the segments. By CM 1 (7 days after installation), the tunnel radius is reduced by an average of 3 mm and is now smaller than the theoretical value. The corresponding change in tunnel circumference equals around 19 mm. Afterwards no significant changes can be observed in the results, which complies with the earlier observations regarding the cross-sectional deformations in time. Once again, a restricted 95% confidence interval of less than ± 0.3 mm is obtained for μ , providing the reliability to make this conclusion generally applicable to the entire tunnel lining.

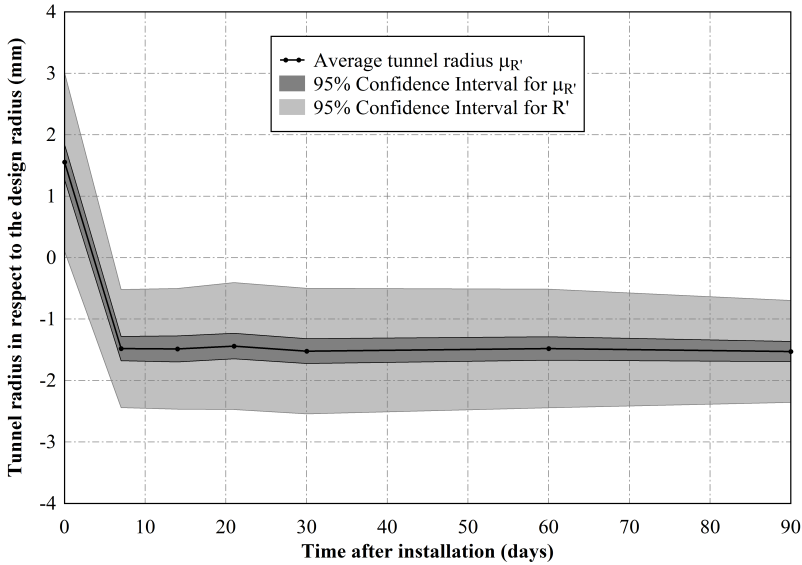


Figure 5.6. Variation of average tunnel radius.

5.2 Segmental behaviour

5.2.1 Joint imperfections

Apart from the global deformation pattern of the tunnel sections, the ovalisation measurements give insight in the behaviour of the joints between adjacent lining segments. Due to inaccurate installation, small irregularities of the inner tunnel surface are present at the location of the joints. Figure 5.7 shows the joint between two segments of a tunnel ring in the theoretical configuration and with a (visually exaggerated) joint irregularity u . The value of u is calculated as the difference between the measured radius values r immediately left and right of the joint. Detailed analysis using Student's t-tests indicates that no significant distinction in the magnitude of u can be determined between the different joint types. For example, this means that the joint irregularities around the keystone, which is installed last, are not consistently larger (or smaller) than the irregularities for the segments that are installed at the beginning of the ring building procedure. Hence the average value \bar{u} of all joints in the 28 monitored sections can be calculated for every ovalisation measurement, which forms an accurate representation of the average joint irregularity μ_u for all joints in the tunnel lining. A 95% confidence interval was calculated in similar fashion to the approach used in the previous sections.

Figure 5.8 shows the variation of this average joint dislocation in time. In general, the initial joint imperfections due to installation range between 2.0 and 2.5 mm, with an occasional maximum of about 6 mm (not shown). It can be seen that μ_u remains virtually constant over the three months between installation and the last control measurement.

The relative displacement $\Delta u = |u_{j+1} - u_j|$ of the individual joints between subsequent measurements j and $j+1$ can be calculated as well. The average value for Δu is again shown in Figure 5.8. It can be observed that in the period between installation and CM 1, the segment joints show the largest displacements. However, these relative changes have no significant effect on the general magnitude of the joint imperfections. Afterwards, only minor disruptions in the joints are registered. Consequently, we can conclude that after CM 1 no significant displacements occur in the joints, parallel to the observations for the general cross-sectional deformations.

5.2.2 Segment rotations

Very similar to the joint behaviour, the angular orientation of the individual segments can be evaluated. Using the monitoring results at both ends of a segment, the angular rotation γ with respect to the design orientation can be derived for each element, as shown in Figure 5.9. For every ovalisation measurement, the average value $\bar{\gamma}$ of all segments in the 28 monitored sections can be calculated, which forms an accurate representation of the average segment orientation μ_γ for all segments in the tunnel lining.

Figure 5.10 shows the fluctuation of the average segment orientation in time, together with the average variation $\Delta\gamma$ of individual segment orientations between subsequent measurements. Similar to the joint behaviour, the angular orientation of the segments relative to the design orientation changes the most in the first week after installation. Again, this has a negligible effect on the overall magnitude of the angular deviation from the design. After the first week, almost no significant change of segment orientations can be detected between subsequent measurements. Therefore, Figures 5.8 and 5.10 confirm the conclusions of the previous section, i.e. all noteworthy lining deformations occur during the first week after erection.

5.2.3 Conclusion

These results of the segmental behaviour lead to the observation that the initial joint inaccuracies which are present after installation of the segments, remain

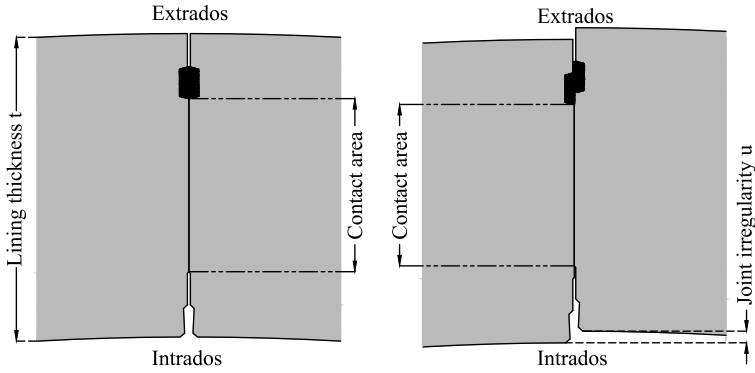


Figure 5.7. Segment joint: perfect installation (left) and irregular joint (right).

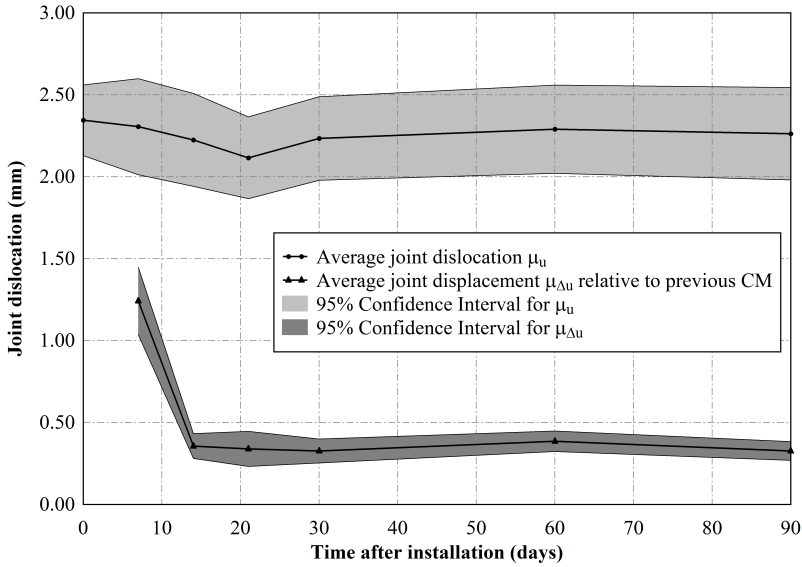


Figure 5.8. Variation of average joint irregularity.

visible in the remaining lifetime of the structure. Their order of magnitude is not reduced after the soil and water pressures act upon the tunnel lining. Therefore it is highly probable that the joint dislocations influence the deformation behaviour and stress distribution in the concrete segments. To investigate this effect more in detail, FE-modelling is applied in chapter 7.

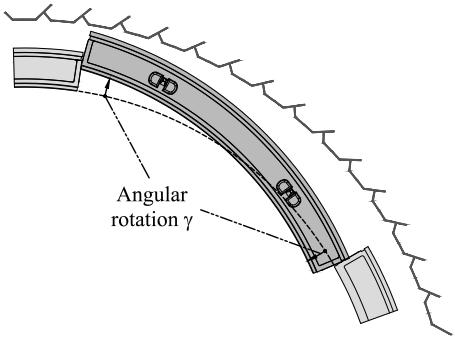


Figure 5.9. Definition of angular rotation of individual segments.

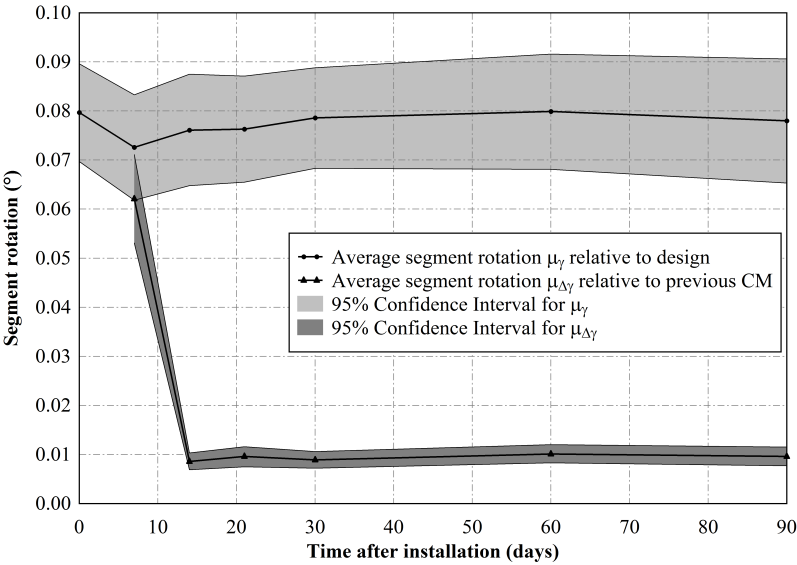


Figure 5.10. Variation of average segment rotation.

Chapter 6

Three-dimensional finite element model

An advanced 3D finite element model was developed in order to study the behaviour of the segmental tunnel lining under various load conditions. Multiple tunnel sections were modelled using SAMCEF Field (Siemens PLM Software, 2014), a commercially available finite element analysis software. This chapter describes in detail the composition of the general FE-model and the outcome of several parameter investigations into the behaviour of the modelled tunnel lining.

6.1 SAMCEF Field

The FE-model is created using SAMCEF Field, which is a commercially available finite element analysis software currently licensed by Siemens PLM Software. It is designed to provide the complete environment for performing a finite element analysis using a graphical interface. SAMCEF Field is based on the regular SAMCEF software package, originally developed in 1965 by the University of Liège in close collaboration with the industry. It is a general-purpose finite element software for structural and heat transfer analysis. Its applications are in widespread use in the mechanical, electrical, aeronautic, nuclear and naval engineering industries as well as in the fields of transport, civil and offshore engineering. The analysis capabilities of SAMCEF enable the user to tackle problems in statics and dynamics, stability, linear or non-linear.

The SAMCEF Field software consists of five main modules to guide the user through each of the logical stages required to complete a successful FE-analysis. First, a geometrical model of the structure under investigation can be created, edited or imported in the “Modeller” module. Models can be created in a parametric fashion, meaning that the dimensions and proportions can be easily modified. The quality of geometries imported from Computer-Aided Design (CAD) software packages can be checked and repaired if necessary. In the “Analysis data” module, loads, physical constraints, material properties and engineering characteristics can be assigned to the modelled geometry using numerous predefined types. Next, different means of generating a finite elements mesh are provided in the “Mesh” module. SAMCEF Field will generate the mesh for a specific model or component using a default set of conditions, which determine the type of mesh elements to be created, the meshing method and the density and distribution of the mesh. Subsequently, the “Solver” module is responsible for the computation of the FE-analysis, based on the defined analysis data and the meshes. A number of finite elements solvers are provided, allowing several types of analysis to be performed (linear, non-linear, thermal, buckling, etc.). Finally, the “Results” module is used for post processing of the data that is generated during the calculations performed in the “Solver” module. A large range of results can be obtained and viewed for easy interpretation. All the analysis data is managed through a structured data tree and saved as a coherent data set.

The SAMCEF Field software has many advantages to model the complex behaviour of segmental tunnel linings. In addition to the traditional finite elements, a very complete library of utility elements is available. Furthermore, macro-operators allow a simple definition of the boundary conditions and an efficient application of the loads. Commonly used with non-linear analysis, contact and friction conditions can also be applied to linear statics for small displacement analysis. However, some shortcomings are present in the SAMCEF Field software as well. As a result, additional pre- and post-processing had to be performed in the regular SAMCEF software package, using command language instead of a graphical input. Nevertheless, this had no negative impact on the obtained results.

6.2 Composition of the FE-model

6.2.1 Choice of volume model

In order to be able to model the joints between adjacent segments using contact definitions (see section 6.2.4), it was chosen to represent the tunnel lining using volume elements, instead of beam or shell elements. By developing a full 3D volume model, the detailed incorporation of the contact area in the segment joints is possible. Furthermore, the advanced ability to model installation imperfections is created (see Chapter 7). When using a 2D beam representation for the tunnel rings, such implementations would not have been possible due to the large amount of simplifications required in the beam approach. In a similar way, the representation of the concrete segments using shell elements would not have allowed modelling the complex joint behaviour of the segmental tunnel lining that is aimed for in this research. As a result, a full three-dimensional FE-model was developed, requiring the input of a detailed geometry of the individual tunnel segments.

6.2.2 Geometry

In order to allow for a comparison between the FE-results and the monitored data in actual tunnel conditions, the Liefkenshoek tunnel is used as reference for the geometry of the FE-model. Based on the available construction drawings, a solid 3D representation of each individual segment is developed in a CAD software package. Four different types of segments are modelled, corresponding to the segment configuration presented in Figure 2.6: a rectangular segment ‘A’, a keystone ‘K’ and segments ‘B’ and ‘C’ adjacent to the keystone. Figures 6.1 to 6.3 show the many details present in the real geometry of the precast concrete segments (the rubber gaskets are not included in these figures). Due to this level of detail, some simplifications are made:

- The conical shape of the tunnel rings is neglected. In order to allow for curves in the tunnel trajectory, the width of each tunnel ring varies along its circumference, with a maximum deviation of 15 mm in respect to the nominal width of 1.80 m. However, in the FE-model, each tunnel ring is assumed to have a constant width of 1.80 m, enabling to model the lining geometry in a straightforward way.
- The application of connection bolts in the longitudinal and circumferential joints is ignored. The bolts result in local pre-stressing of the sealing

gaskets, which helps to avoid leakage in case the axial forces should be shortly reduced during construction. A secondary function of the bolts is to provide security against falling of a segment when the jack force on the segment is released. Since all bolts only have a temporary function and are removed once the tail grout has hardened, their presence is neglected in the FE-analysis.

- The presence of the bolt sockets and holes for the centre cones of the vacuum erector is ignored. These details are likely to generate areas of stress concentrations in the final results (Tiberti & Plizzari, 2014) and should therefore not be neglected in detailed investigations into cracking mechanisms of the concrete lining. However, as the presented research is mainly focussed on the general forces and deformations of the tunnel lining, this simplification can be made without major consequences.
- The presence of the reserved spaces for the plastic guiding rods in the longitudinal joints of the keystone and the adjacent segments B and C (visible in Figures 6.2 and 6.3) is neglected. These cylindrical guiding rods help to install the keystone as the last segment in the ring assembly procedure. It is assumed that their presence does not influence the force transfer and deformation behaviour of the corresponding joints in a significant way, due to their round shape and solid material. Therefore, their neglect is considered justified.
- The presence of the rubber gaskets is neglected in the structural behaviour of the tunnel lining, as it is believed that they do not contribute to a significant force transfer in the segment joints.
- The geometry of the longitudinal and circumferential joints consists of many small-scale grooves, notches and rounded corners (see Figures 6.1 to 6.3), which complicate the generation of accurate mesh elements at these locations. Consequently, some simplifications are made in the joint geometry at several locations, as shown in Figures 6.4 to 6.7. Nonetheless, attention is given that these simplifications are not able to significantly influence the deformation behaviour of the joints.

The resulting geometry of the modelled segments is illustrated in Figures 6.1 to 6.7. They still present an accurate representation of the actual lining segments. All main dimensions of each segment are in accordance with reality. The effective contact area in both longitudinal and circumferential joints is taken into account (shaded in red in Figures 6.6 and 6.7), as well as the presence of the

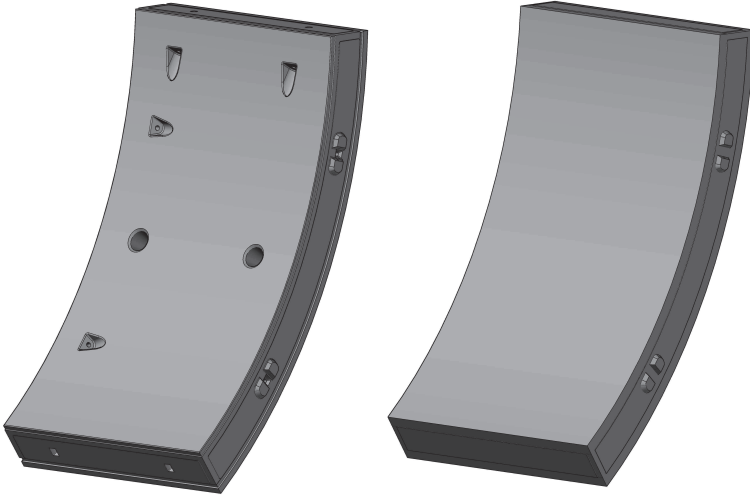


Figure 6.1. 3D-view of a tunnel segment of type A: real geometry (left) and simplified geometry used in the FE-model (right).

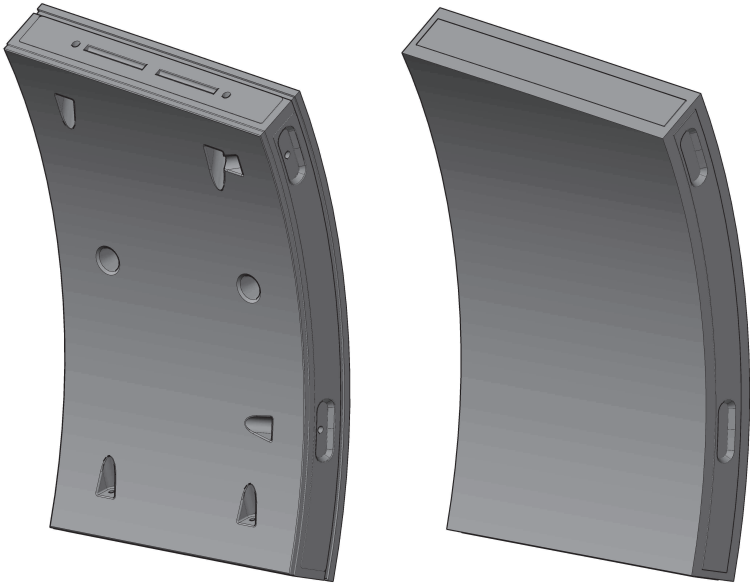


Figure 6.2. 3D-view of a tunnel segment of type B: real geometry (left) and simplified geometry used in the FE-model (right).

dowel and socket coupling system in the circumferential joints (Figure 6.5). The keystone K and both adjacent segments B and C are modelled realistically using inclined longitudinal joints, activating the three-dimensional nature of

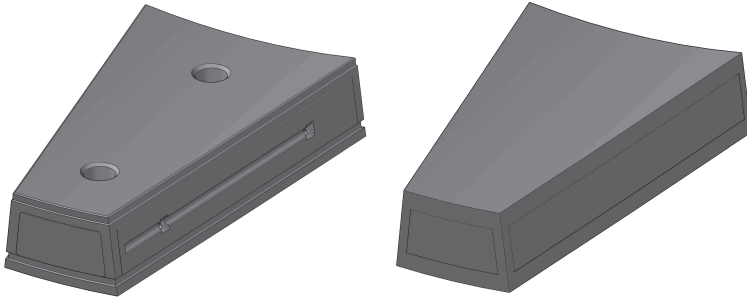


Figure 6.3. 3D-view of a tunnel segment of type K: real geometry (left) and simplified geometry used in the FE-model (right).

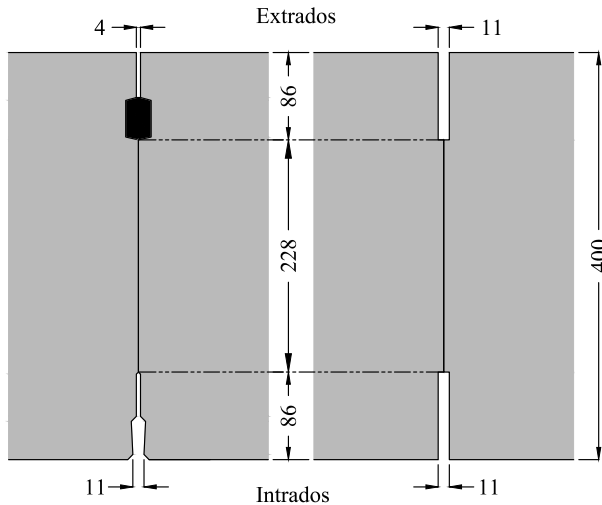


Figure 6.4. Cross-section of the circumferential joint: real geometry (left) and simplified geometry used in the FE-model (right).

the ring behaviour, despite its rather two-dimensional orientation.

All modelled segments are imported into SAMCEF Field from the CAD software. As a result, it is not possible to create a parametric model, which implies that the dimensions and proportions of the model are not easily modified. The individual segments are placed into a ring formation according to the configuration presented in Figure 2.6. In order to be able to compute the sectional forces in the lining at the end of the FE-analysis, predefined cross-sections of the tunnel segments have to be made. The reason for this is explained in section 6.2.7. For this purpose, the entire tunnel ring is subdivided in 56 sections corresponding to an angle of $360^\circ/56$, equally distributed along the circumfer-

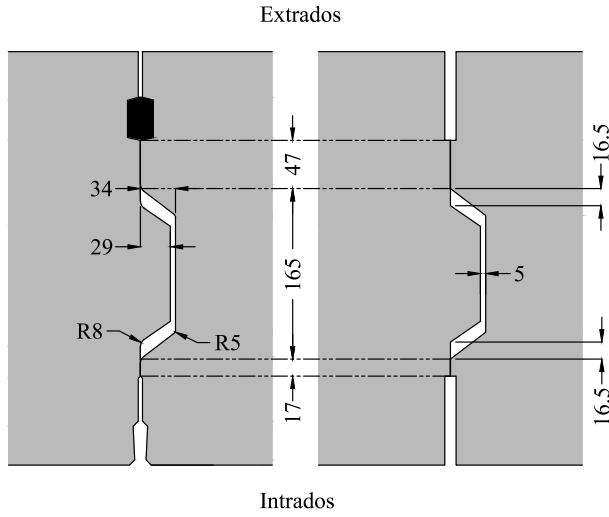


Figure 6.5. Cross-section of the circumferential joint at the position of the coupling system: real geometry (left) and simplified geometry used in the FE-model (right).

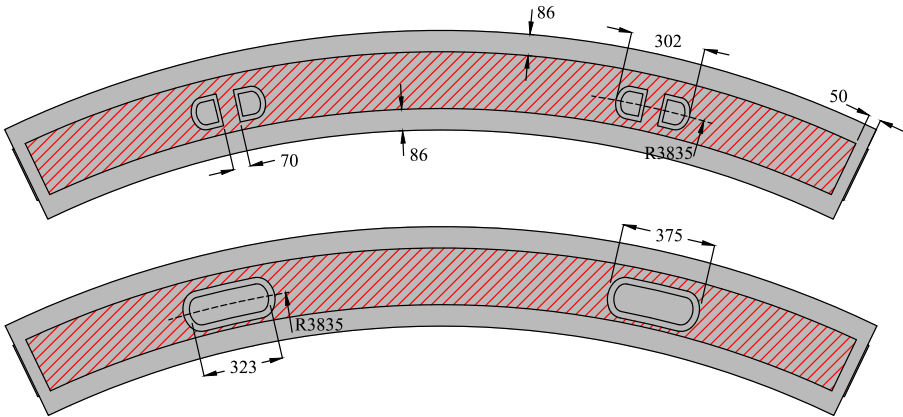


Figure 6.6. Perpendicular view of the circumferential joint geometry used in the FE-model: side away from TBM (top) and TBM side (bottom).

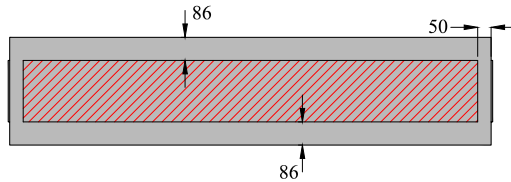


Figure 6.7. Perpendicular view of the longitudinal joint geometry used in the FE-model.

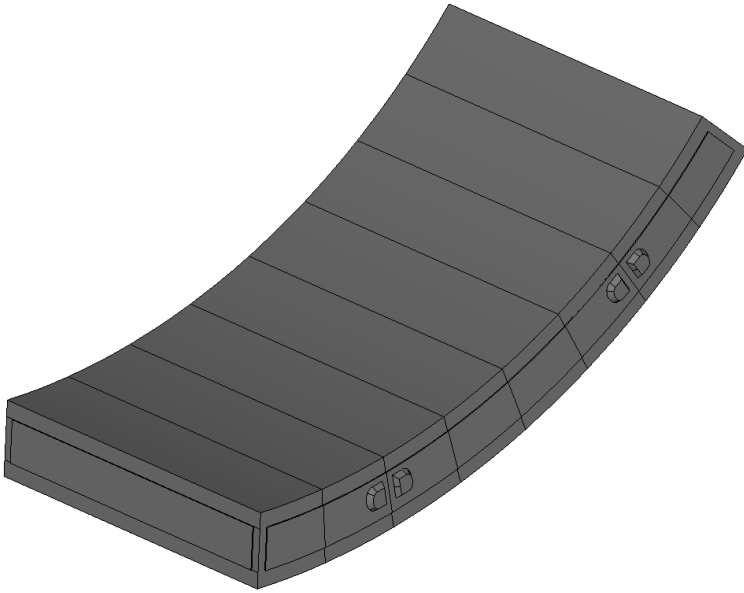


Figure 6.8. FE-model geometry of a tunnel segment of type A including subdivisions.

ence. As a result, each regular segment (A1-A5) is subdivided into eight parts, as illustrated in Figure 6.8. A simplification is made at the location of the inclined joints alongside the keystone, as shown in Figure 6.9. Consequently, segments B and C consist of seven parts, while the keystone only counts two parts. All parts of each segment are glued together in the FE-software, resulting in a single shape for each segment.

Finally, for each FE-analysis, three adjacent tunnel rings are modelled, in order to account for the coupling of the rings in the circumferential joints. For that purpose, the assembled tunnel ring is duplicated two times and rotated around the longitudinal tunnel axis over an angle of $360^\circ/14$, corresponding to half a tunnel segment, to obtain a staggering joint configuration. The resulting geometry is visualised in Figure 6.10, where the three tunnel rings are labelled as ‘ring -1’, ‘ring 0’ and ‘ring +1’. In this figure, one can also observe that an additional subdivision is made on the extrados of the tunnel segments. The outer surface of each ring is split in half along its width, to allow the definition of an external load on only one half of the tunnel ring if necessary. As this subdivision is made for other reasons than the one described above, it does not apply to the full thickness of the tunnel lining, but only to the outer surface.

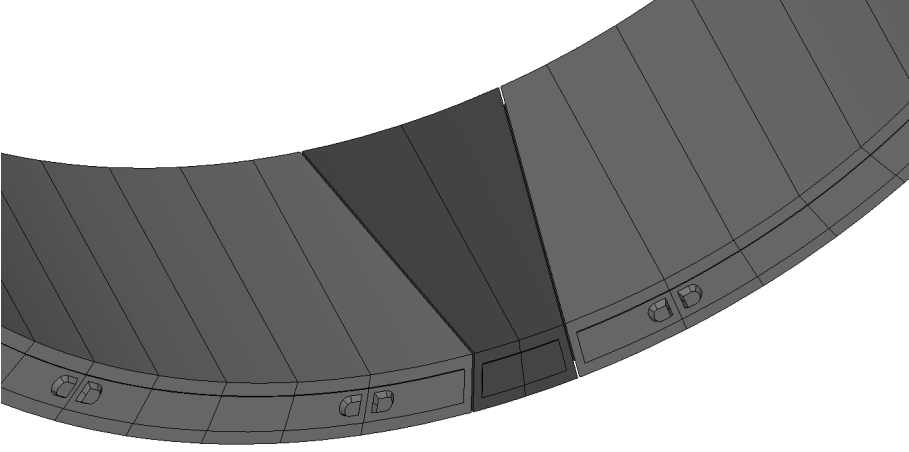


Figure 6.9. FE-model geometry of keystone and adjacent segments including subdivisions.

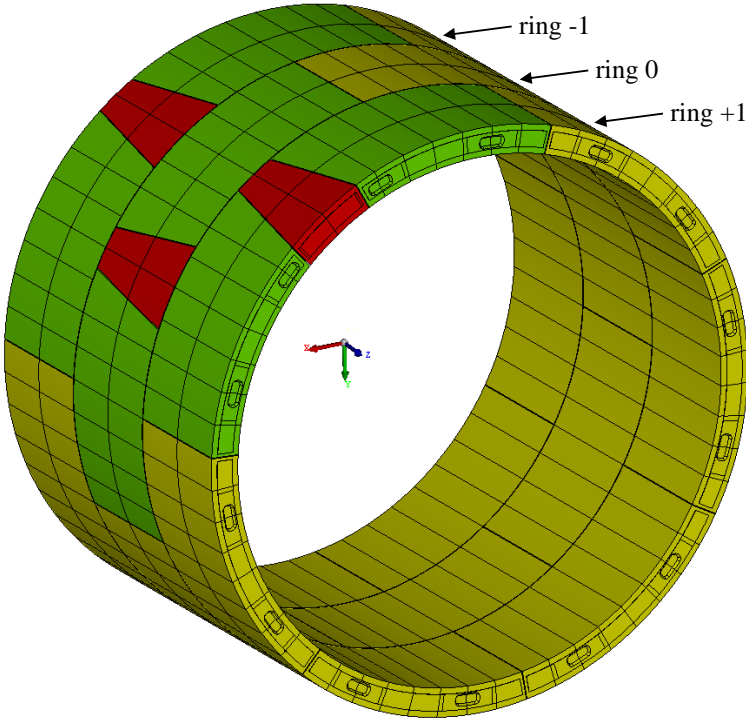


Figure 6.10. 3D-view of the modelled geometry in the FE-model.

6.2.3 Material properties

The precast segments of the Liefkenshoek tunnel consist of reinforced concrete of C50/60 concrete quality. In the FE-model, a simplified linear elastic material behaviour is assumed, characterised by a Young's modulus of elasticity $E_c = 37000 \text{ N/mm}^2$, a Poisson ratio $\nu_c = 0.2$ and a mass density $\rho_c = 2450 \text{ kg/m}^3$. The non-linear behaviour of concrete, including cracking in tension and crushing in compression, is not taken into account. Furthermore, the presence of the reinforcement bars is neglected in the FE-model, as well as the yielding phenomenon of these steel rebars.

As a consequence, caution is advised when interpreting stress results directly generated by the FE-model. Alternatively, the performance of the tunnel lining is evaluated by computing the sectional forces at predefined cross-sections (see section 6.2.7), after which the corresponding stresses in the concrete and steel rebars can be calculated manually, based on the concrete and steel areas depicted in Figure 2.7.

6.2.4 Contact joints

As mentioned in the state of the art, all present analytical and finite element models for segmental tunnel linings use a simplified interpretation of the joint behaviour. As a result, the design models are not able to accurately predict the actual behaviour in the longitudinal and circumferential joints. For example, relative displacements between adjacent segments cannot occur in the longitudinal joints. Consequently, all current models assume a perfectly circular tunnel ring, without any installation imperfections. In the FE-model developed in this research, all joints are modelled using contact conditions with friction between the segments. This allows all relative displacements and rotations between segments to occur similar to actual tunnel lining behaviour. Additionally, it becomes possible to model geometrical imperfections at the joints due to human errors/inaccuracies in the ring building procedure (see Chapter 7).

No packing materials are present in either the longitudinal or the circumferential joints of the tunnel lining at the Liefkenshoek project. Only in the sockets of the coupling system between adjacent tunnel rings, small bituminous strips (kaubit) were attached, as shown in Figure 6.11. However, the dimensions of the dowel and socket do not allow contact between both parts in normal loading conditions, which can be observed in Figure 6.5. In addition, the relative displacements in radial direction, required to cause contact between the concrete dowel and socket, never occur in the FE-results presented in this re-



Figure 6.11. Two kaubit strips attached to the sockets in the circumferential joint.

search. Therefore, these areas are not included in the modelled contact area of the circumferential joints. Furthermore, contact between the rubber gaskets is not taken into account. Due to the lower stiffness of the gasket material in comparison with the concrete of the lining segments, no significant contribution to the force transfer or friction resistance in the joints is believed to occur. The resulting parts of both joint types for which contact is considered, are shaded in red in Figures 6.6 and 6.7. All contact in the segment joints is assumed to occur between two concrete surfaces.

SAMCEF Field allows a detailed definition of contact conditions between two entities using a macro command. This command creates contact between a set of nodes on the first surface (“slave nodes”) and a group of facets on the second surface (“master facets”). The contact problem is analysed in several steps. First, the software searches for the closest facet for each slave node. This topology search can be made once, at the beginning of the analysis, or it can be performed at each iteration or the beginning of a new time step (non-linear analysis). Due to an inconsistency with the command to compute the sectional forces in the predefined cross-sections (see section 6.2.7), only the first option is available in this research. This implies that during the analysis, each slave node can only slide on one corresponding master facet, which is correct as long as the relative displacements between the faces in contact are small. Secondly, the normal distance is computed, in order to define when contact appears. By default, contact starts when the normal distance between the node and the face is equal to zero. However, the option exists to change this zero value by the initial distance between the node and the face. So as soon as the slave node moves in the direction of the face, contact appears. This is useful when there are small imperfections in the nodal coordinates and when it is known that the contact surfaces are close together. This is the case in the theoretical situation where the tunnel segments have been installed flawlessly, making

perfect contact at the segment joints. In the final step, the contact algorithm is selected. In this research, the coupled iterations method proved to be the most appropriate. In that case the contact is treated as a non-linearity. A contact condition is created causing a kinematic constraint that is active when contact occurs and is inactive when the contact does not occur. According to the SAMCEF Field software, this method should be used when there is friction and when the parts are in contact at the beginning of the analysis, which is the case in this research. However, it is only available in a non-linear analysis.

As briefly mentioned, friction is taken into account at the contact faces by introducing a coefficient of friction μ . In this research, the classical Coulomb friction formula is applied: $F_f = \mu F_n$. No relative displacement occurs until the frictional force F_f exceeds the normal force F_n multiplied by the coefficient of friction μ . The linear friction law is applied in the two orthogonal directions. Regarding the coefficient of friction to be applied for concrete-to-concrete contact, a lot of uncertainty exists at the moment. The values presented in literature are characterized by a large range of values and have generally been determined for other types of structures. Table 6.1 shows the documented mean values of μ for multiple surface classifications. Due to the particularly small tolerances applied in segment prefabrication, a very smooth concrete surface is obtained for the precast concrete segments used in shield tunnelling. As a result, a coefficient of friction $\mu = 0.4$ is initially assumed in this research. However, the impact of the applied value for μ on the results of the FE-analysis is studied as well. Results of this investigation are presented in section 6.5.

Table 6.1. Overview of coefficients of friction for concrete-to-concrete contact from literature (Fib, 2013; Precast/Prestressed Concrete Institute, 2010; British Standards Institution, 2008; Bloemhof, 2001).

| | fib (2013) | PCI (2010) | BSI (2008) | Bloemhof (2001) |
|----------------------|------------|------------|------------|-----------------|
| smooth interface | 0.5-0.7 | 0.6 | | |
| rough interface | 0.7-1.0 | 1.0 | 0.4 | 0.4 |
| very rough interface | 1.0-1.4 | 1.4 | | |

6.2.5 Loads

Dead load

The dead load of all modelled elements is taken into consideration in the FE-analysis, using the correct mass density of concrete as mentioned in section 6.2.3. It is practically implemented in the software by applying an acceleration of 9.81 m/s^2 along the vertical axis.

Soil and water pressures

Each FE-analysis is performed using the representative soil and water pressures according to the corresponding location of the investigated cross-section in the Liefkenshoek project. For that purpose, the position and characteristics of the various soil layers, shown in Figure 2.8, are taken into account. For the acting soil pressures on the tunnel lining, the undisturbed situation prior to the excavation process is assumed. In that case, the effective vertical soil pressure at a depth z_{top} below the surface level, corresponding to the top of the tunnel, is given by equation 6.1:

$$\sigma'_{v,top} = \sum_{z=0}^{z_w} \gamma_{s,i} \Delta z_i + \sum_{z=z_w}^{z_{top}} \gamma'_i \Delta z_i \quad (6.1)$$

where z equals the vertical distance below the surface level, z_w is the vertical distance of the (ground)water level below the surface level, Δz_i is the height of soil layer i , $\gamma_{s,i}$ is the saturated unit weight of soil layer i and γ'_i is the effective unit weight of soil layer i . The effective vertical soil pressure at an angle θ of the tunnel's external surface is:

$$\sigma'_v(\theta) = \sigma'_{v,top} + \sum_{z=z_{top}}^{z(\theta)} \gamma'_i \Delta z_i \quad (6.2)$$

In equation 6.2, $z(\theta)$ is the depth below the surface level of the point at an angle θ along the tunnel's external circumference, which equals:

$$z(\theta) = z_{top} + h(\theta) = z_{top} + R_{out}(1 - \cos \theta) \quad (6.3)$$

where R_{out} is the outer radius of the tunnel lining, equal to 4.05 m. The effective horizontal soil pressures can be calculated in a similar way, using the lateral earth pressure coefficient at rest K_0 of the corresponding soil layer:

$$\sigma'_h(\theta) = K_0 \sigma'_v(\theta) \quad (6.4)$$

The vertical and horizontal soil pressures can be translated into radial and tangential ones:

$$\sigma'_r(\theta) = \sigma'_v(\theta) \cos^2 \theta + \sigma'_h(\theta) \sin^2 \theta \quad (6.5)$$

$$\sigma'_t(\theta) = -\sigma'_v(\theta) \cos \theta \sin \theta + \sigma'_h(\theta) \cos \theta \sin \theta \quad (6.6)$$

The hydrostatic water pressures are omnidirectional, so the radial water pressure acting in a point at an angle θ along the tunnel's external circumference is directly given by:

$$\sigma_w(\theta) = \gamma_w(z(\theta) - z_w) \quad (6.7)$$

where γ_w is the specific gravity of water.

The tangential soil stresses are neglected in this FE-analysis, corresponding with the classic assumption of tangential slip between soft soil and the lining in segmental tunnel design (Chaipannna *et al.*, 2012; Anheuser, 1981; Groeneweg, 2007). The radial soil and water pressures of equations 6.5 and 6.7 are given as a function of the angle θ . However, the SAMCEF Field software does not allow to implement a pressure that constantly changes in amplitude and direction. As illustrated in Figure 6.12, the soil and water pressures are applied as individual resultant forces on the 56 parts of each tunnel ring, discussed in section 6.2.2. For that purpose, the resulting forces on part j are calculated by integrating the pressures along the corresponding part of the outer tunnel circumference:

$$F_{s,j} = b \int_{\theta_j}^{\theta_{j+1}} \sigma'_r(\theta) R_{out} d\theta \quad (6.8)$$

$$F_{w,j} = b \int_{\theta_j}^{\theta_{j+1}} \sigma_w(\theta) R_{out} d\theta \quad (6.9)$$

In these equations, $b = 1.80$ m is the width of a tunnel ring. The angles θ_j and θ_{j+1} are clarified in Figure 6.13.

Tail grouting pressures

The soil and water pressures calculated in the previous section can be applied in the normal loading situation of the tunnel lining, when the grout filling the tail void has already hardened. However, it might be useful sometimes to consider the situation immediately after the tunnel section has left the protection of the TBM shield. In that case, the tail grout is still in a liquid state and

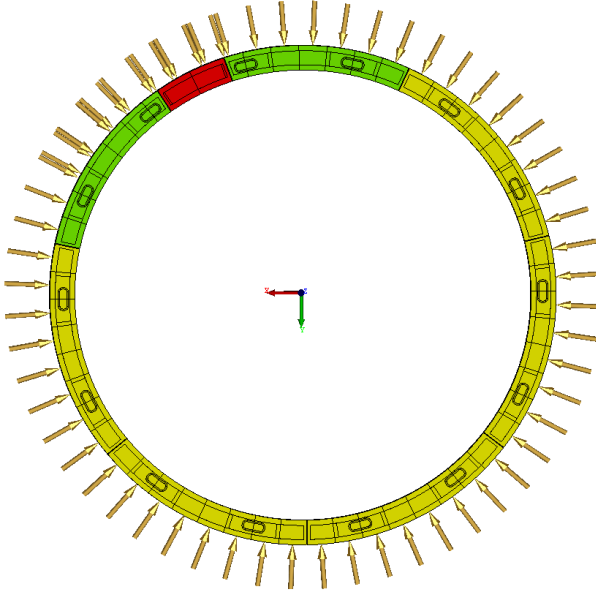


Figure 6.12. Soil and water loads acting on the FE-model.

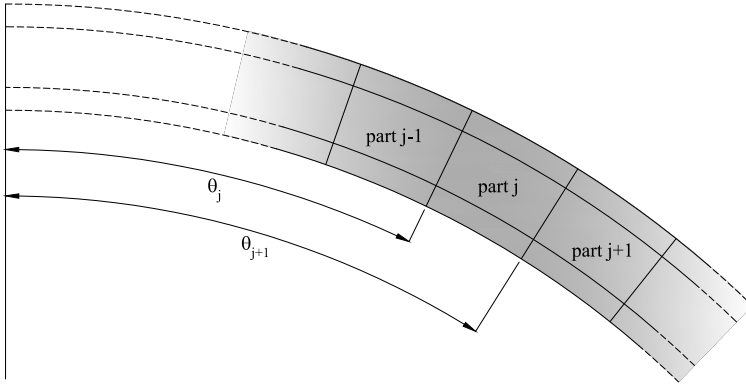


Figure 6.13. Definition of angles θ_j and θ_{j+1} in equations 6.8 and 6.9.

corresponding grout pressures apply on the outer tunnel surface. The resulting loads can be calculated in a similar way as the soil and water loads in the previous section. An assumption has to be made considering the magnitude of the grout pressures. According to Haring (2002) and Bloemhof (2001), the grout pressures at the top of the tunnel are assumed to be 10% larger than the governing groundwater pressures at that location:

$$\sigma_{grout,top} = 1.1\sigma_{w,top} = 1.1\gamma_w(z_{top} - z_w) \quad (6.10)$$

An even distribution of the grout along the tunnel perimeter is assumed, resulting in a hydrostatic pressure distribution (Luttikholt, 2007; Blom & van Oosterhout, 1997):

$$\sigma_{grout}(\theta) = \sigma_{grout,top} + \gamma_{grout}h(\theta) \quad (6.11)$$

In equation 6.11, γ_{grout} is the unit weight of the liquid grout, equal to 22 kN/m³. The resulting force on part j of a tunnel ring is calculated by integrating the grout pressure along the corresponding part of the outer tunnel circumference:

$$F_{grout,j} = b \int_{\theta_j}^{\theta_{j+1}} \sigma_{grout}(\theta) R_{out} d\theta \quad (6.12)$$

However, several uncertainties still remain with regard to the correct magnitude of the initial grout pressures. The latter depend on a multitude of parameters, which are related to the composition of the grout mixture, the soil properties, distribution of the injection ports at the shield tail, applied injection pressures, etc. (Bakker & Bezuijen, 2009a; Shirlaw *et al.*, 2004; Talmon & Bezuijen, 2005; Ummenthun, 2001). In situ measurements of grout pressures in literature have indicated larger values than the ones assumed in the approach mentioned above (Bezuijen & Talmon, 2004). Furthermore, resulting vertical pressure gradients have been observed that are considerably lower than the hydrostatic gradient (Bezuijen *et al.*, 2004). Therefore, in order to model a realistic grout loading in the FE-analysis, real-time monitoring data of the initial grout pressures on the actual tunnel lining of the Liefkenshoek project should have been obtained. Yet, no such information is available at this point. As a result, the presented research will mainly focus on the response of the tunnel lining to the classic soil and water pressures, as determined in the previous section. The implementation of realistic tail grouting pressures in the FE-analysis will be the subject of future research.

Surface loads

As the major part of the tunnel trajectory is located below the maritime fairways and no large structures are present immediately above the tunnel, no additional surface loads are taken into account in the FE-analysis. Only for the cross-sections located below the Port Canal, the presence of the concrete

slab (see section 2.3.3) is accounted for in the horizontal and vertical soil pressures. In that case, equation 6.1 needs to be substituted by equation 6.13:

$$\sigma'_{v,top} = \sigma'_{v,surcharge} + \sum_{z=0}^{z_w} \gamma_{s,i} \Delta z_i + \sum_{z=z_w}^{z_{top}} \gamma'_i \Delta z_i \quad (6.13)$$

For the concrete slab, located below the water level, the surcharge load can be easily calculated using the slab thickness t_{slab} and the unit weight of concrete γ_c :

$$\sigma'_{v,surcharge} = t_{slab}(\gamma_c - \gamma_w) \quad (6.14)$$

Longitudinal (thrust) forces

At one end of the FE-model, corresponding with the side of the TBM, longitudinal forces are introduced to account for the axial pressure in the tunnel lining originating from the TBM thrust forces. They are implemented as resultant forces, acting on the free contact surface of the outermost circumferential joint, as shown in Figure 6.14. A total longitudinal force of 14,000 kN is assumed to be equally spread along the tunnel perimeter. As a result, each individual segment is loaded with a force proportional to its cross-sectional area in the circumferential plane.

6.2.6 Boundary conditions

Radial soil springs

To model the soil interaction, radial soil springs are used along the entire tunnel circumference, as can be seen in Figure 6.15. The spring stiffness k_r is defined as a non-linear function. In case of inward displacements away from the surrounding soil, k_r equals zero and no interaction occurs. In case of outward displacements towards the soil, a compression stiffness according to equation 6.15 is applied, based on the recommendations of Duddeck (1980):

$$k_r = \frac{E_{oed}}{R_{out}} \quad (6.15)$$

In equation 6.15, E_{oed} represents the oedometer modulus of the surrounding soil layer. The resulting shape of the stiffness function is shown in Figure 6.16. In the software, a radial spring is defined for each of the 56 faces along the tunnel perimeter, as shown in Figure 6.15. For that purpose, the stiffness

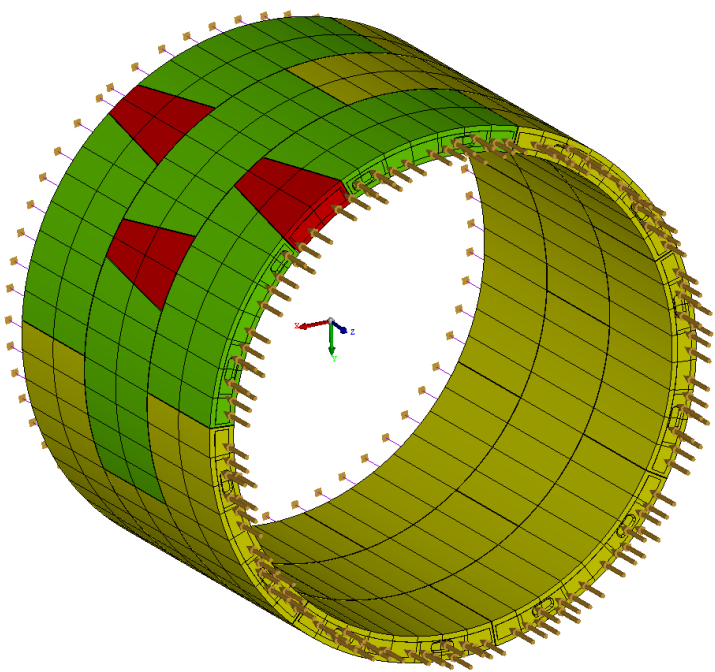


Figure 6.14. Illustration of longitudinal forces and support on the FE-model.

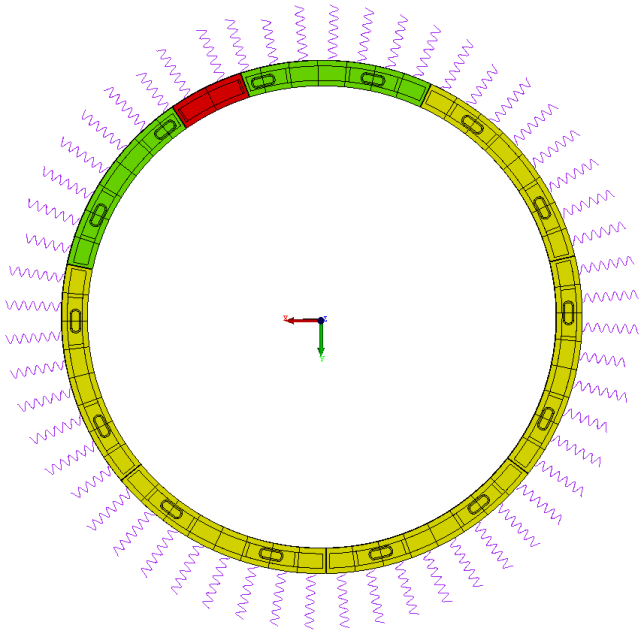


Figure 6.15. Illustration of radial soil springs on the FE-model.

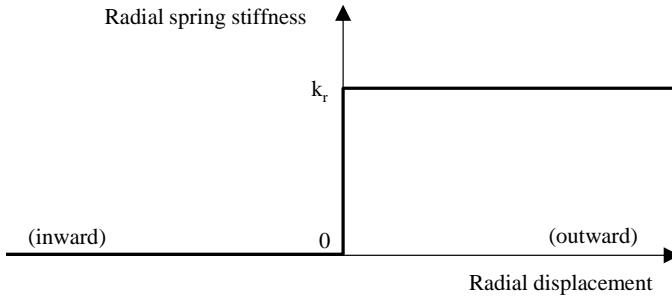


Figure 6.16. Stiffness function of the radial soil springs.

k_r has to be multiplied with the outer surface area of each part. Similar to the soil pressures, no tangential springs are applied in this FE-analysis, which corresponds with many approaches in literature (Duddeck, 1980; The British Tunnelling Society and The Institution of Civil Engineers, 2004; van der Horst, 1999, 1998; Ahrens *et al.*, 1982).

Longitudinal support

In order to account for the presence of the earlier installed tunnel sections, a surface support is modelled at one end of the FE-model, corresponding with the side away from the TBM. That way, the longitudinal forces in the tunnel lining can be sustained. The surface support is assigned to the free contact surface of the outermost circumferential joint, at the opposite end of where the longitudinal forces are introduced, as shown in Figure 6.14. This stiff support fully constrains the displacement of the corresponding segment edges in the direction of the tunnel axis.

Additional translational and rotational support

In order to provide some computational stability to the FE-model, additional supports are introduced to limit excessive horizontal and vertical displacements and rotations along the longitudinal axis. This is required to obtain convergence of the FE-analysis. The supports are defined using a ‘mean assembly’ in the software, of which the principle is shown in Figure 6.17. The mean displacement and rotation of a set of master nodes is given by a slave node N1. There are 6 kinematic constraints, no matter how many master nodes there are. Such a mean assembly is defined at both ends of the FE-model: each group of master nodes consists of all nodes on the free contact surface of the outer

circumferential joint. These are the same sections of the model where the longitudinal thrust forces and longitudinal surface support are applied. Next, the displacements perpendicular to the tunnel axis and the rotations around the tunnel axis are restrained for both slave nodes of the defined mean assemblies. As a result, cross-sectional deformations are still allowed at the end faces, but a general shift or rolling movement of the entire tunnel model is prevented. This is done to account for the presence of the adjacent tunnel sections that were not included in the model. As the input of this type of supports has to be done using command language instead of a graphical input, a visualisation of their application in the FE-model is not readily available.

6.2.7 Computation of sectional forces

As previously mentioned, caution is advised when evaluating the stress results generated by this FE-analysis, due to the linear elastic material behaviour that is assumed for the reinforced concrete. It is preferred to assess the tunnel behaviour by calculating the sectional forces in the lining. Since this is not a standard output for a volume model, the sectional forces have to be computed using a specific macro-command of the SAMCEF Field software. This command writes a reaction element which measures the total reaction forces and the total moments between two parts of the structure. The principle of the command is visualised in Figure 6.18. The separation between both parts (an imaginary cut) is defined by a group of faces. The resultant forces and moments in the three orthogonal directions of the coordinate system are computed at a master node, which is defined at the centre of gravity of the cut in this research. The position of this master node is important for the accurate calculation of the resultant moments. In order to be able to make the imaginary cut through the whole thickness of the segment, all faces of the group need to be in one plane. The best way to do this, is to prepare the cut before meshing of the model by creating a glueing of the geometry. For that purpose, it is chosen to divide the entire tunnel ring into 56 sections, as described in section 6.2.2, after which all parts of each segment are glued together in the FE-software. As a result, a predefined cross-section is created at the location of each glueing, where all faces of the mesh will be in the same cross-sectional plane, allowing the accurate computation of the sectional forces.

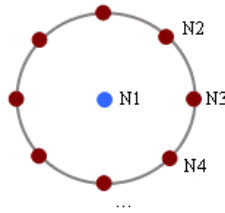


Figure 6.17. Principle of a mean assembly in SAMCEF Field.

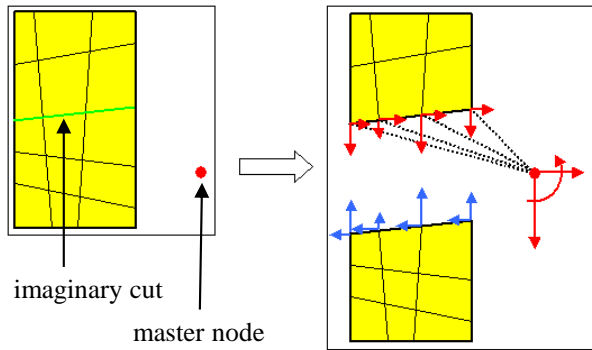


Figure 6.18. Principle of macro-command to compute sectional forces in SAMCEF Field.

6.2.8 Mesh

After all data has been assigned to the geometry, the FE-model can be meshed. Due to the various details and complex geometry, the GHS3D tetrahedral free-mesher of the SAMCEF Field software is applied. This is an automatic tetrahedral mesher based on the Voronoi-Delaunay method which makes it possible to process any three-dimensional domain. First, a 2D triangular mesh is created on the surface of each object, after which the mesher generates a 3D mesh made up of tetrahedrons. More specific, four-node linear tetrahedral (T4) elements are used, which are triangular pyramid shaped elements as illustrated in Figure 6.19. The mesh size can be specified by defining an average distance that will be set between nodes. When selecting an average mesh size of 100 mm, the resulting FE-model consists of a total of around 500,000 tetrahedral volume elements, as shown in Figure 6.20. The mesh quality was verified using the incorporated check of the SAMCEF Field software. Section 6.4 will show the impact of the mesh size on the calculation times and results of the FE-analysis.

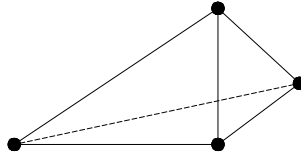


Figure 6.19. Four-node linear tetrahedral (T_4) mesh elements.

6.2.9 Type of analysis

As mentioned in section 6.2.4, the selected contact algorithm is only available in a non-linear analysis. Consequently, this type of analysis is performed, which at the same time provides the ability to make the loads on the model time-dependent. In order to be able to investigate the influence of each loading condition separately, it is chosen to introduce the various loads at a different time in the analysis, as shown in Figure 6.21. A total time interval of 5 s is selected for the simulation, representing five arbitrary steps in the load introduction. At the beginning of the analysis, only the longitudinal forces are introduced on the model, to provide stability to the lining segments. Next, the dead load is activated. Afterwards, the external pressures on all three modelled tunnel rings are activated, one ring at a time. This allows to verify the impact of the loading of a tunnel ring on the adjacent ring(s). Nonetheless, the results of the final situation are identical to the case where all tunnel rings are loaded at the same time. The choice of the time interval has no effect on the obtained results. Furthermore, an automatic time step selection is preferred, enabling the solver to choose the time step depending on the rate of convergence. However, imposed time values are defined at 1 s, 2 s, 3 s, 4 s and 5 s in order to obtain intermediate results at these precise instants in the computation.

In normal situations, a static response is selected for the FE-analysis, which takes stiffness effects into account. However, when installation imperfections are implemented in the model (see Chapter 7), convergence problems arise for this type of response. This is due to the imperfect contact in the joints and the small displacements that occur as a result of that. Consequently, a dynamic analysis has to be selected, taking inertia effects into account. Finally, in order to obtain computational stability when installation imperfections are modelled, some advanced computation parameters need to be adjusted as well. This allows to overcome convergence problems during some intermediate time steps of the calculation, without influencing the final balance of the structural model.

Calculations are performed on a 64-bit Windows 7 PC, with an Intel Core

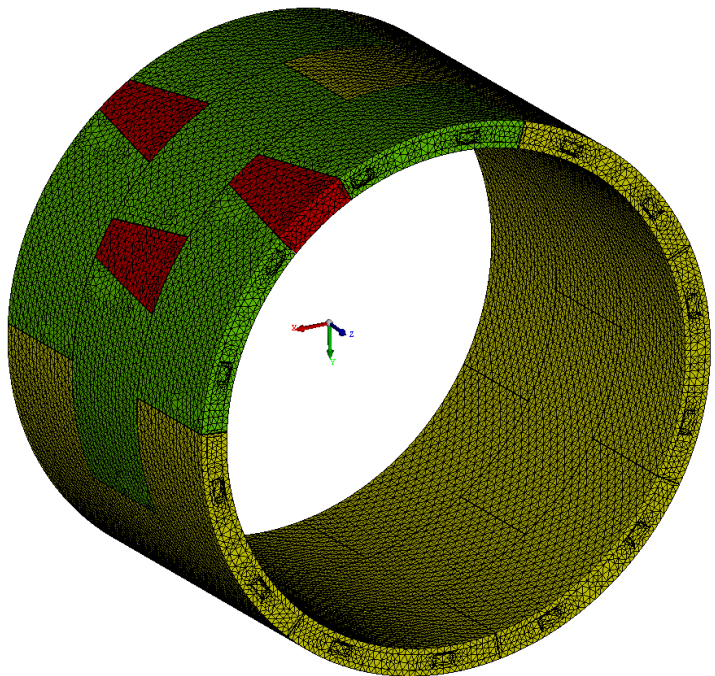


Figure 6.20. 3D-view of the meshed FE-model.

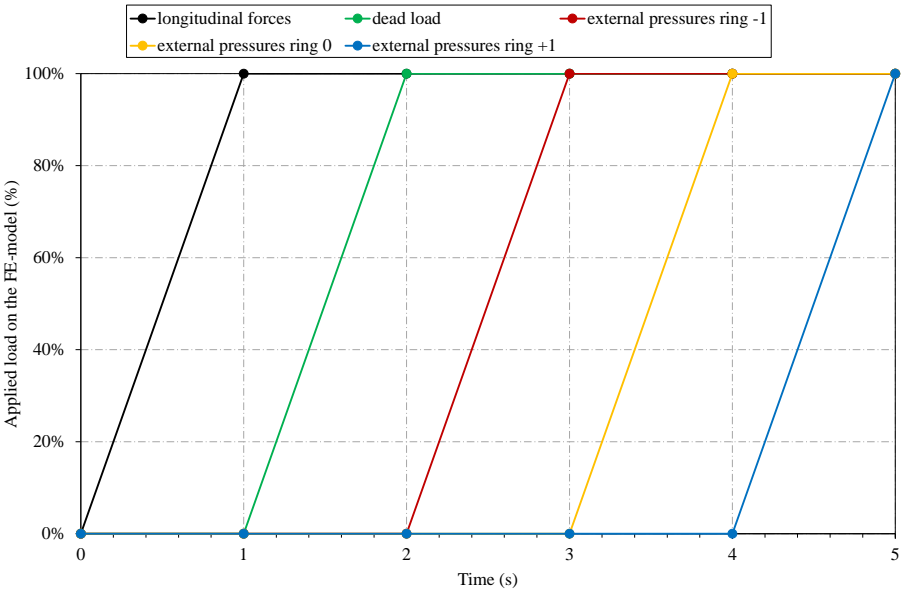


Figure 6.21. Introduction of loads on the FE-model at different time steps.

i7-3770 3.40 GHz processor and 12 Gb RAM memory.

6.3 Results of the FE-model

Figure 6.22 shows an example of the absolute deformations (in mm) of the FE-model, as calculated using the methodology described above. These results allow a detailed observation of the response of the tunnel section to the applied loads. A horizontal ovalisation can be observed, corresponding to the classical pumpkin-shaped deformation pattern for tunnel linings in soft soil. The tunnel invert moves upward by about 3.25 mm, while the top of the lining shows an inward displacement of almost identical magnitude. The sides move outward by approximately 2 mm. A smooth transition of the deformations over the entire model can be noticed, indicating the good cooperation between adjacent segments and tunnel rings via contact in the longitudinal and circumferential joints. Although the 3D-visualisation of Figure 6.22 proves very useful for the verification of the model deformations, only 2D cross-sections of these results will be presented further in the text. This will allow for a straightforward comparison between the results of different calculations and monitoring results of the ovalisation measurements.

Figures 6.23 and 6.24 present the tangential normal forces and the bending moments around the longitudinal z-axis in all three tunnel rings of the model. These distributions were calculated from the 56 predefined cuts in each ring, as explained in section 6.2.7. The higher normal forces at the bottom of the tunnel section ($\theta = 180^\circ$) for ring 0 can be contributed to the increased depth, which generates higher soil loads and water pressures at this location. For rings -1 and +1, this effect is somewhat levelled out by the presence of the additional supports at the outer ends. Nonetheless, the average normal force is the same for all three tunnel rings. The bending moments show a confirmation of the pumpkin-shaped ovalisation of the tunnel lining. Maximum positive bending moments are found at the top and bottom of the tunnel cross-section, while negative bending moments of equal absolute value are found at the sides. Minor variations exist between the distribution for ring 0 and the adjacent rings, due to the staggering joint configuration and the corresponding difference in the specific location of the longitudinal joints.

These results are very similar to the ones obtained by applying a simplified load distribution, where soil and water pressures are assumed constant along the entire tunnel height. This approach is often found in literature (Duddeck, 1980; Ahrens *et al.*, 1982; ITA Working Group on General Approaches to the

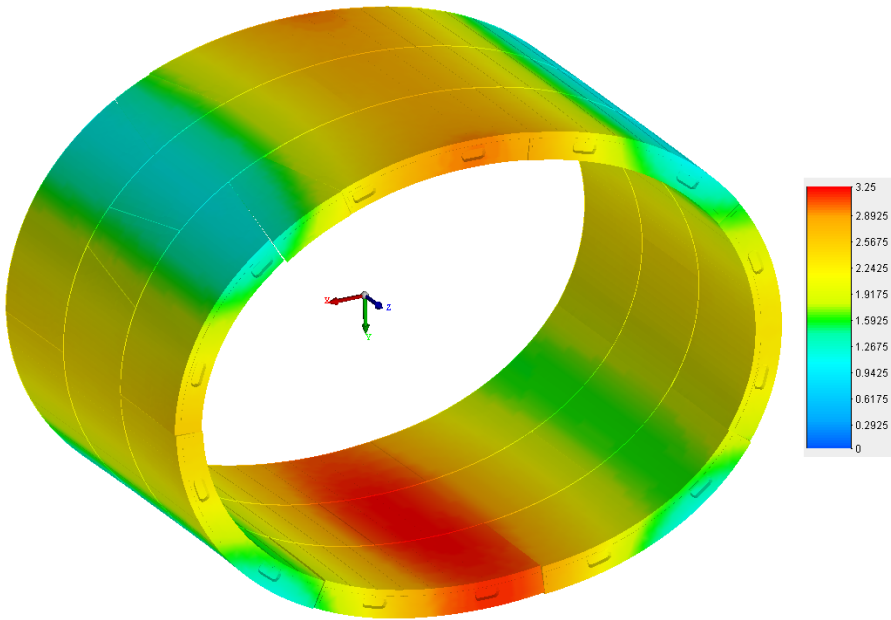


Figure 6.22. Deformations calculated using the FE-model (scale in mm).

Design of Tunnels, 1988; Möller & Vermeer, 2005), where it is used in order to obtain vertical equilibrium. Comparison shows that such a simplified load state, combined with a release of the vertical translational supports described in section 6.2.6, results in identical cross-sectional deformations and distribution of bending moments in the tunnel lining as the main approach used in this FE-analysis. Furthermore, the magnitude of the normal forces is constant along the entire tunnel circumference for the simplified approach, and corresponds to the mean value of the normal force distribution shown in Figure 6.23. As a result, the presented research allows to establish clear parallels with the simplified tunnel design models from literature.

Due to the radial loading of the tunnel rings and the absence of localised loads, all other sectional forces, such as shear forces and bending moments around the x- and y-axis, remain negligibly small, compared to the normal forces and bending moments around the z-axis. Therefore, they are not mentioned explicitly in the results. Nonetheless, they are taken into account in the determination of concrete and steel stresses based on the FE-results, as applied further in the research.

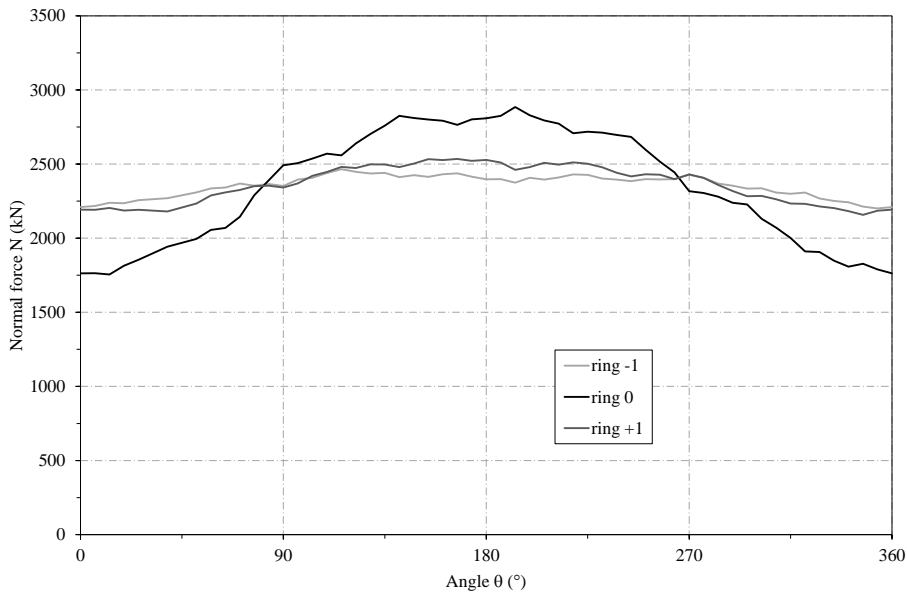


Figure 6.23. Normal force N calculated using results from FE-model.

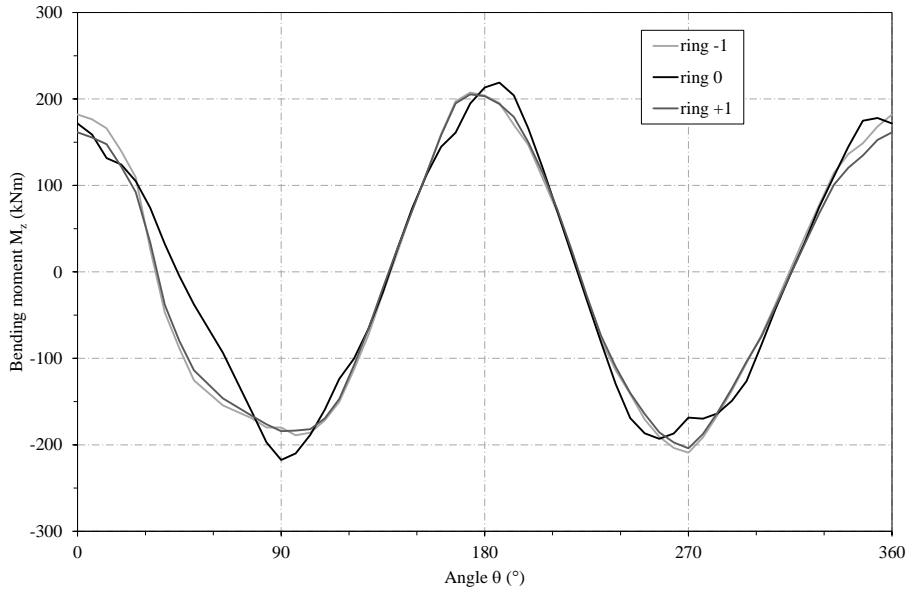


Figure 6.24. Bending moment M_z calculated using results from FE-model.

6.4 Impact of the mesh size

6.4.1 Applied mesh configurations

In order to investigate the impact of the mesh size on the results and computation times of the FE-analysis, multiple mesh configurations were considered. A distinction was made between the mesh size of the middle tunnel ring (ring 0) and the adjacent rings (ring -1 and ring +1). As the focus of attention in most of the performed FE-calculations lies on the middle tunnel ring, an equal or smaller mesh size for ring 0 in respect to the adjacent rings was pursued. Table 6.2 shows the various mesh configurations that were considered and indicates the number of mesh elements in the corresponding FE-model. Values between brackets correspond to configurations for which no results were obtained, due to the large number of elements and the implied complexity of the model. The increasing amount of elements for smaller mesh sizes is illustrated in Figure 6.25. A strong rise in the number of mesh elements can be observed when an average mesh size of 50 mm is used, even when this is only applied to the middle ring in the model.

Table 6.2. Number of mesh elements depending on mesh size.

| mesh size rings -1/+1 (mm) | mesh size ring 0 (mm) | | | | |
|-------------------------------|-----------------------|-----------|---------|---------|---------|
| | 50 | 75 | 100 | 150 | 200 |
| 50 | (2,920,637) | - | - | - | - |
| 75 | (1,593,330) | (931,583) | - | - | - |
| 100 | (1,301,771) | 639,703 | 496,104 | - | - |
| 150 | (1,108,239) | 446,596 | 302,703 | 205,809 | - |
| 200 | (1,045,451) | 383,622 | 239,760 | 142,823 | 111,197 |

6.4.2 Models using design geometry

For FE-models using a theoretically perfect geometry of the tunnel lining, the calculation times show a considerable increase for smaller mesh sizes, as can be observed in Figure 6.26. Naturally, this graph only presents the results of the mesh configurations for which results could actually be obtained. Once the mesh size in ring 0 goes below 100 mm, a strong rise in calculation times is observed. A mesh size of 100 mm for both adjacent rings -1 and +1 also results in larger calculation times of more than seven hours. Figure 6.27 shows

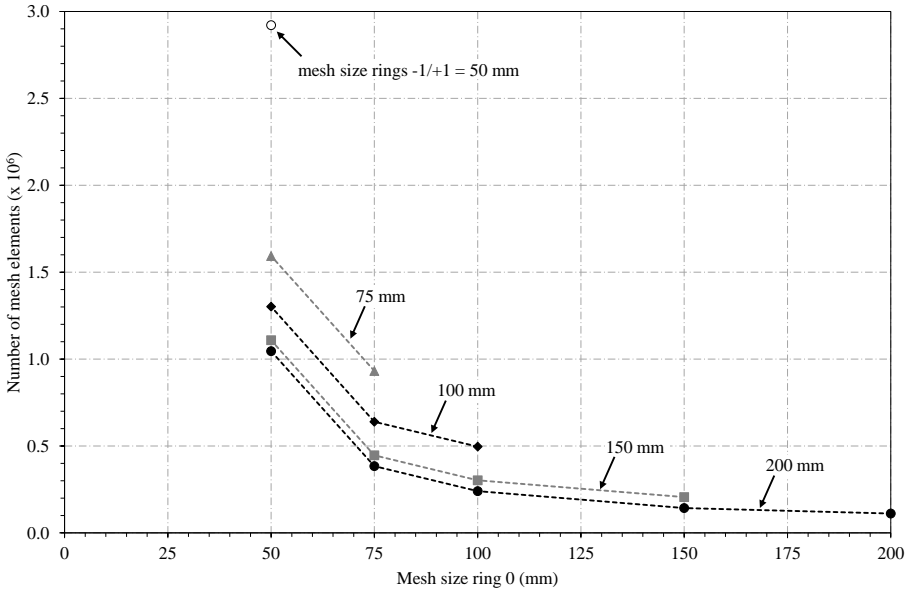


Figure 6.25. Variation of number of mesh elements with mesh size.

the variation of calculation times with the number of mesh elements. The corresponding relationship between both can be estimated using a quadratic function. The trend line indicates that for even smaller mesh sizes, of which the number of elements was given between brackets in Table 6.2, calculation times would rise up to 19 to 176 h. Consequently, the choice of the mesh size has a strong impact on the duration of the FE-calculation.

Figures 6.28 to 6.31 show the normal forces and bending moments for the various mesh configurations, for ring 0 and ring +1 respectively. The results of ring -1 are similar to those of ring +1. In the legend of all these graphs, the first number refers to the mesh size of ring 0, while the second number indicates the mesh size of the adjacent rings. All figures indicate that only minor variations in the normal forces are observed due to the variation in mesh size, which remain well below 5% between different mesh configurations. The maximum normal force encountered in a tunnel ring merely differs 1%. Only for the minimum and maximum values of the bending moments, significant changes up to 20% due to mesh size are found. The smaller the mesh size in ring 0, the smaller the absolute values of the corresponding bending moments in that ring. The same applies to rings -1 and +1. The impact of the mesh size in one ring on the obtained results for another ring in the same model can

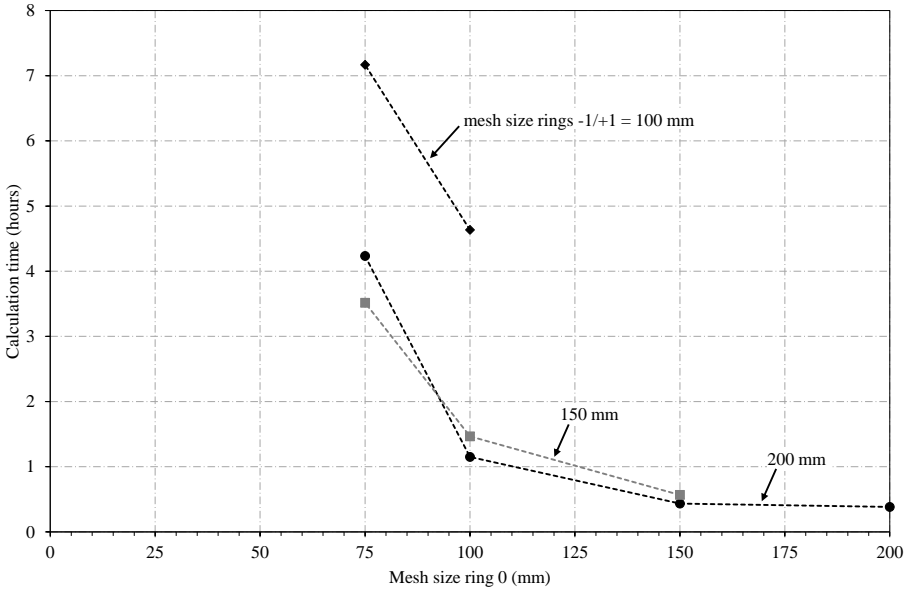


Figure 6.26. Increase of calculation times with mesh size for models using design geometry.

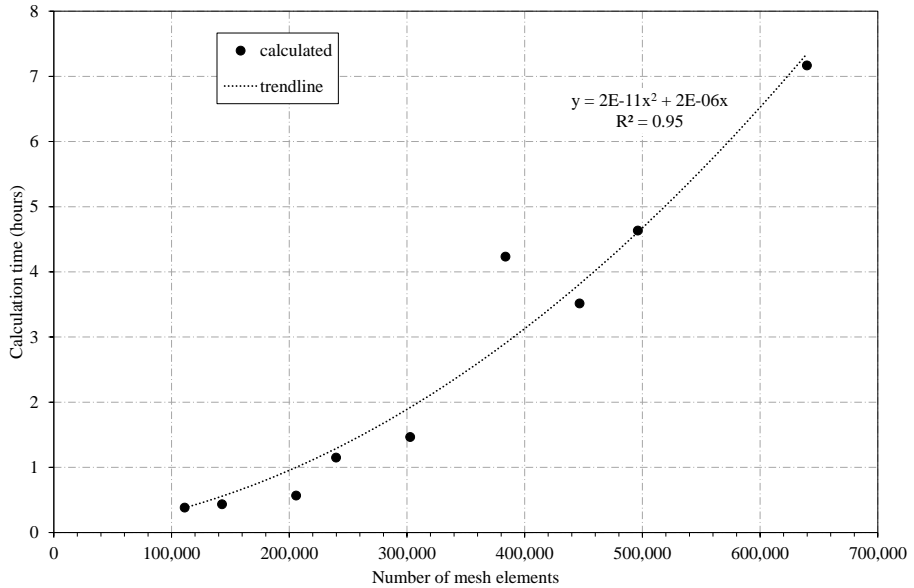


Figure 6.27. Increase of calculation times with number of mesh elements for models using design geometry.

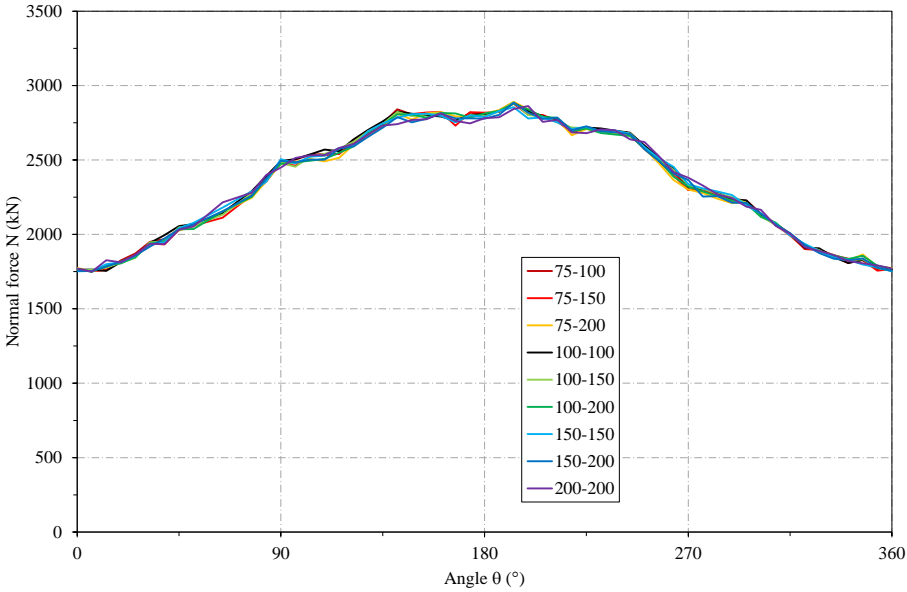


Figure 6.28. Variation of normal force N in ring 0 with mesh size for models using design geometry.

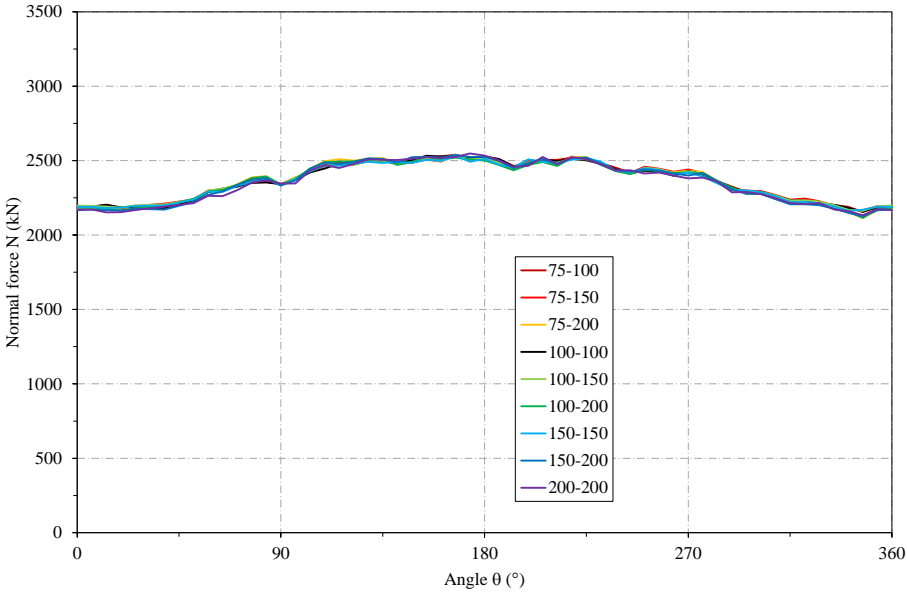


Figure 6.29. Variation of normal force N in ring +1 with mesh size for models using design geometry.

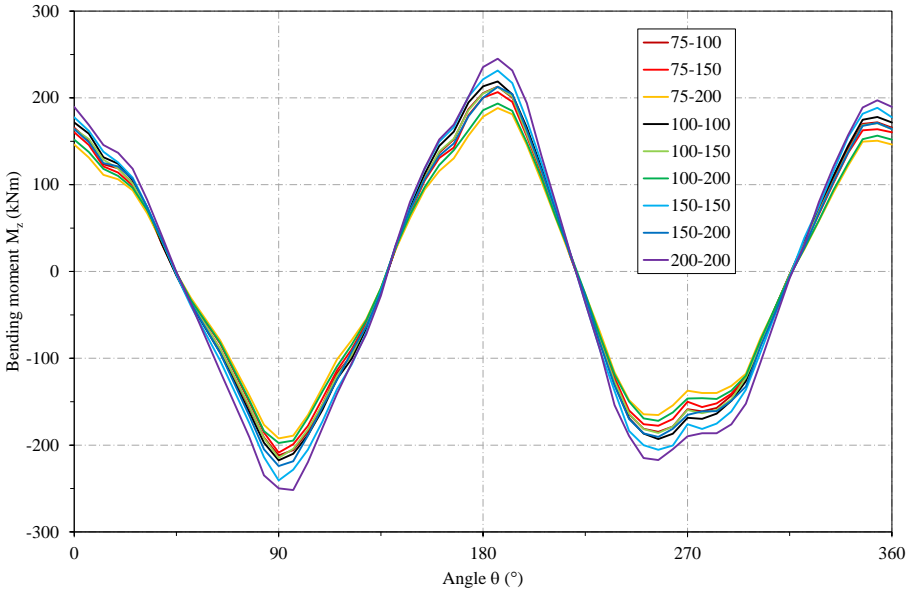


Figure 6.30. Variation of bending moment M_z in ring 0 with mesh size for models using design geometry.

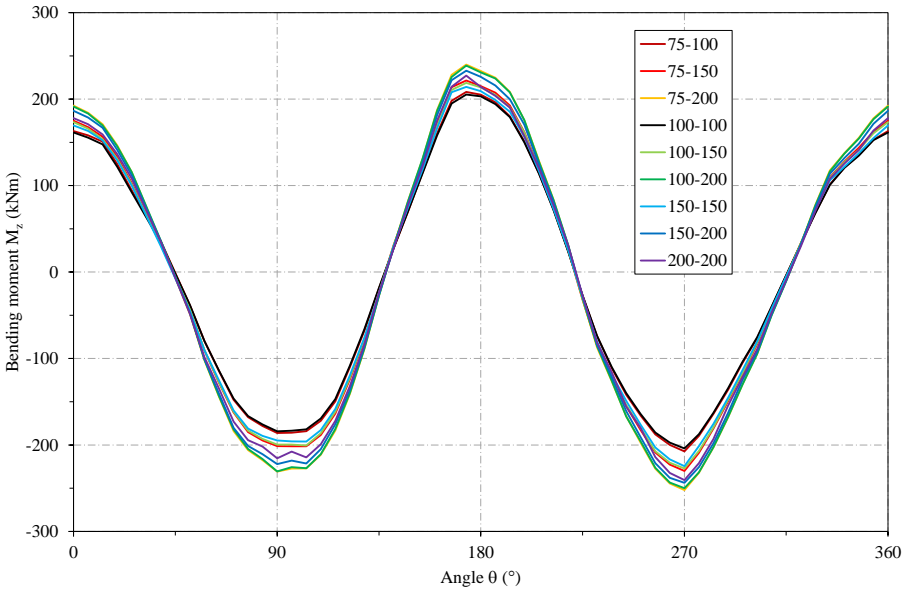


Figure 6.31. Variation of bending moment M_z in ring +1 with mesh size for models using design geometry.

reach up to 10%. All these effects can be studied in detail in the additional graphs of Appendix C, which explicitly show the impact of the mesh size on the maximum normal forces and bending moments in the tunnel rings.

Finally, the radial displacements of ring 0 are presented in Figure 6.32. Again, a significant effect of the mesh size on the obtained results is visible. This effect is largest for $\theta = 180^\circ$, corresponding to the bottom of the tunnel section. When smaller mesh sizes are applied, both in ring 0 as well as in rings -1 and +1, the absolute value of the displacements at this location in ring 0 increases. Variations between different mesh configurations can reach 15%. An explicit comparison of the displacements for $\theta = 180^\circ$ as a function of the mesh size is again presented in Appendix C. In conclusion, the application of a denser mesh has a much larger impact on the duration of the calculation than on the values of sectional forces and deformations of the modelled tunnel sections.

6.4.3 Models including installation imperfections

The calculations of the previous section used a perfect geometry of the tunnel lining. However, the FE-model allows to simulate the presence of installation imperfections in the joints between segments as well. The impact of the applied mesh size was investigated for models including such imperfections as well. More details on the implementation of installation imperfections in the model are given in the next chapter. This section only discusses the influence of the mesh configuration on the FE-results and calculation times.

When joint imperfections are modelled in ring 0, the duration of the calculation is much larger, compared to the models using the design geometry. This is illustrated in Figure 6.33. For a mesh size of 200 mm or 150 mm in rings -1 and +1, the calculation times are about two or three times the duration of the models using the design geometry. For smaller mesh sizes, a major rise can be observed, up to 76 h for an average mesh size of 75 mm in ring 0 and 100 mm in the outer rings. Figure 6.34 shows that in this case, the increase of the calculation times with the number of mesh elements can be estimated using an exponential relationship. Consequently, the final choice of the mesh configuration will be mainly determined by the impact on the models including installation imperfections, rather than the ones applying the theoretically perfect geometry.

Figures 6.35 to 6.38 again show the normal forces and bending moments for the various mesh configurations. More details on the implications of these

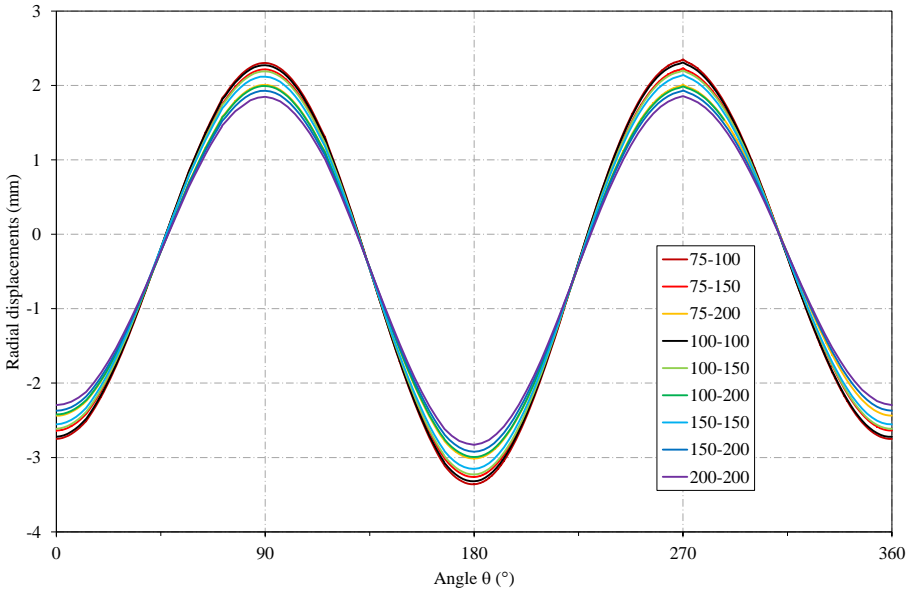


Figure 6.32. Variation of radial displacements in ring 0 with mesh size for models using design geometry.

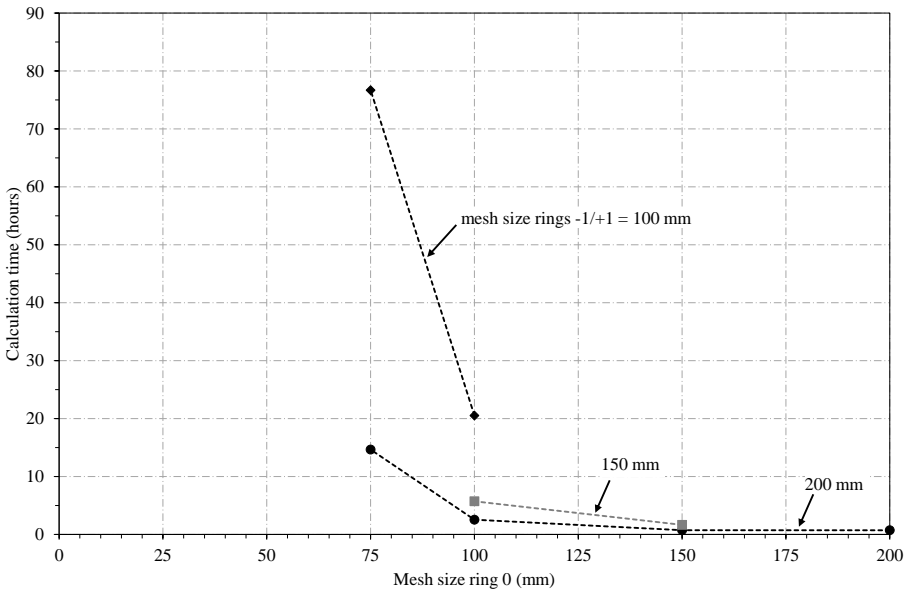


Figure 6.33. Increase of calculation times with mesh sizes for models with installation imperfections.

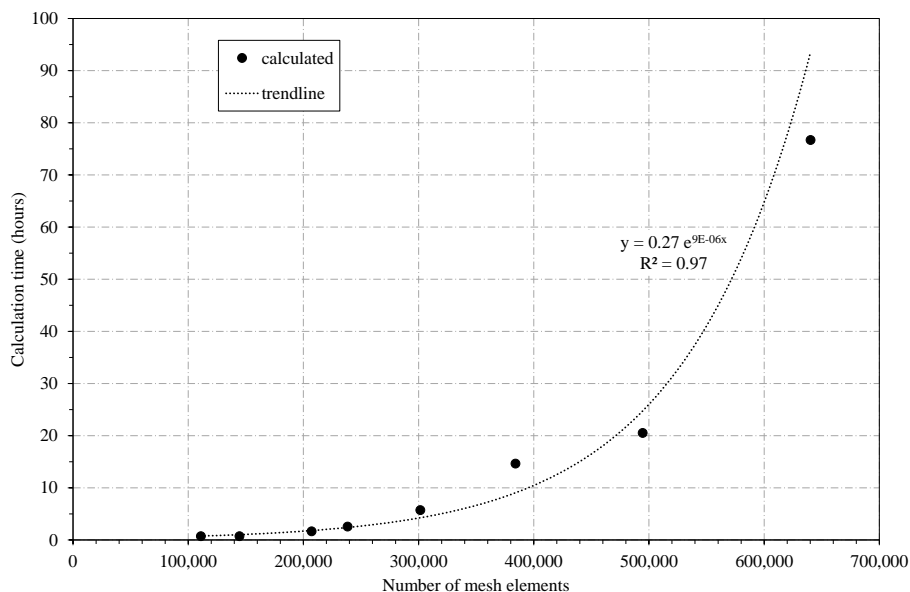


Figure 6.34. Increase of calculation times with number of mesh elements for models with installation imperfections.

results are given in the next chapter, which deals with the impact of the installation imperfections. Figures 6.35 and 6.36 again confirm that only minor variations in the normal forces are observed due to the variation in mesh size. The impact on the maximum normal forces remains well below 10%. Also for the variation in bending moments, similar observations can be made as for the models without installation imperfections, although the impact of the mesh size on the maximum values is slightly smaller.

The radial displacements of ring 0 are presented in Figure 6.39. Again, a variation in the obtained results is visible due to the impact of the mesh size. The effect is largest for $\theta = 167^\circ$, corresponding to the location of a joint at the tunnel invert. When smaller mesh sizes are applied in rings -1 and +1, the absolute value of the displacements at this location in ring 0 increases up to 15%. However, the mesh size of ring 0 itself shows no major impact on these values. An explicit comparison of the displacements for $\theta = 167^\circ$ as a function of the mesh size is presented in Appendix C, as well as the impact of the mesh size on the maximum normal forces and bending moments in the tunnel rings.

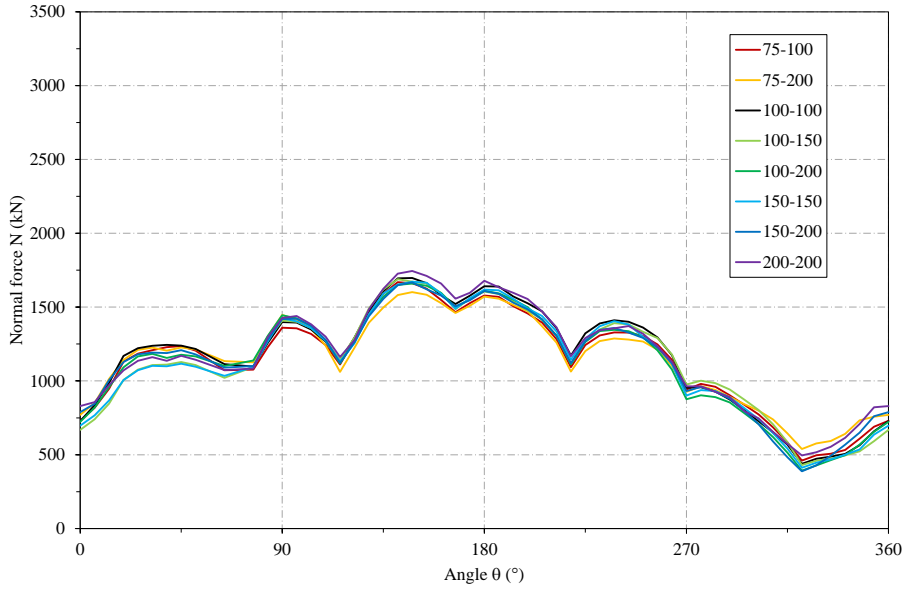


Figure 6.35. Variation of normal force N in ring 0 with mesh size for models with installation imperfections.

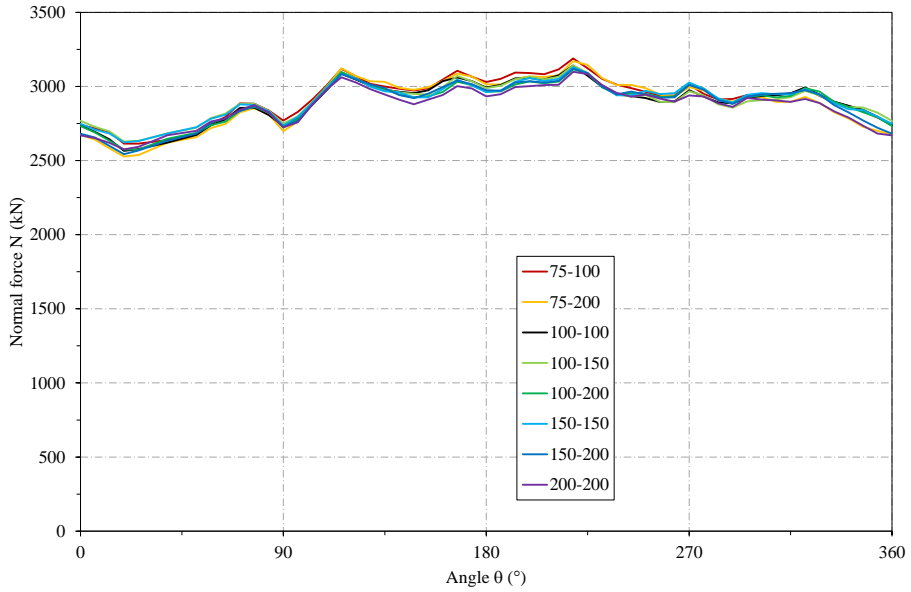


Figure 6.36. Variation of normal force N in ring +1 with mesh size for models with installation imperfections.

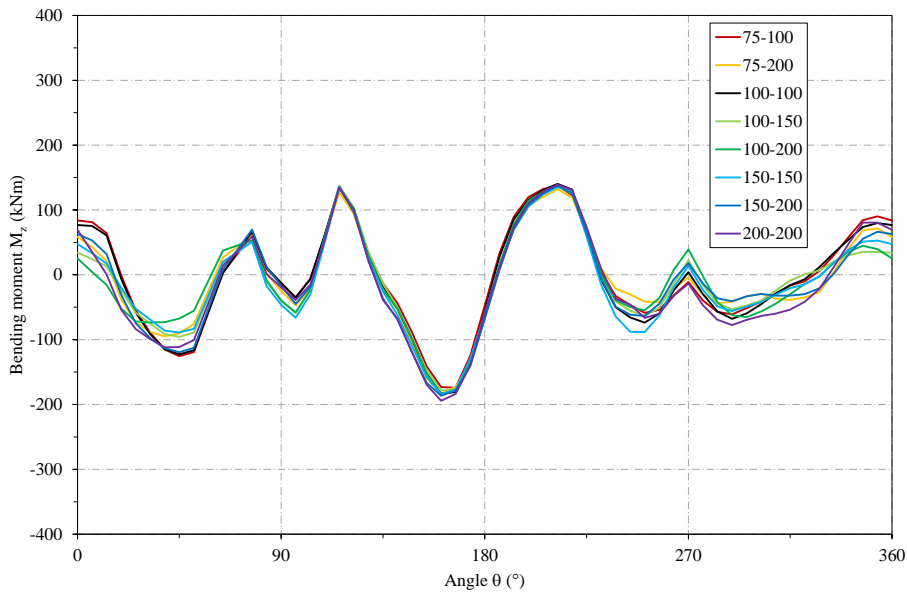


Figure 6.37. Variation of bending moment M_z in ring 0 with mesh size for models with installation imperfections.

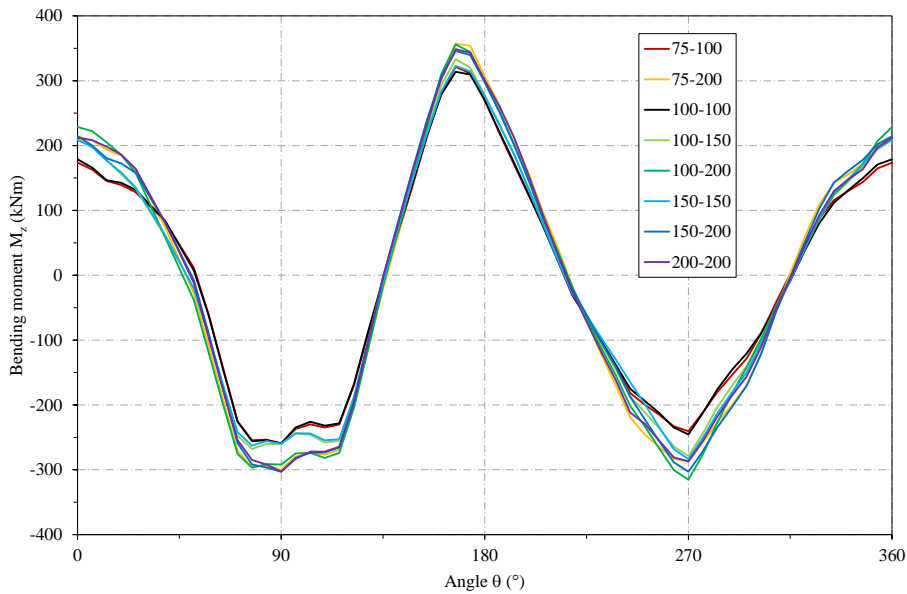


Figure 6.38. Variation of bending moment M_z in ring +1 with mesh size for models with installation imperfections.

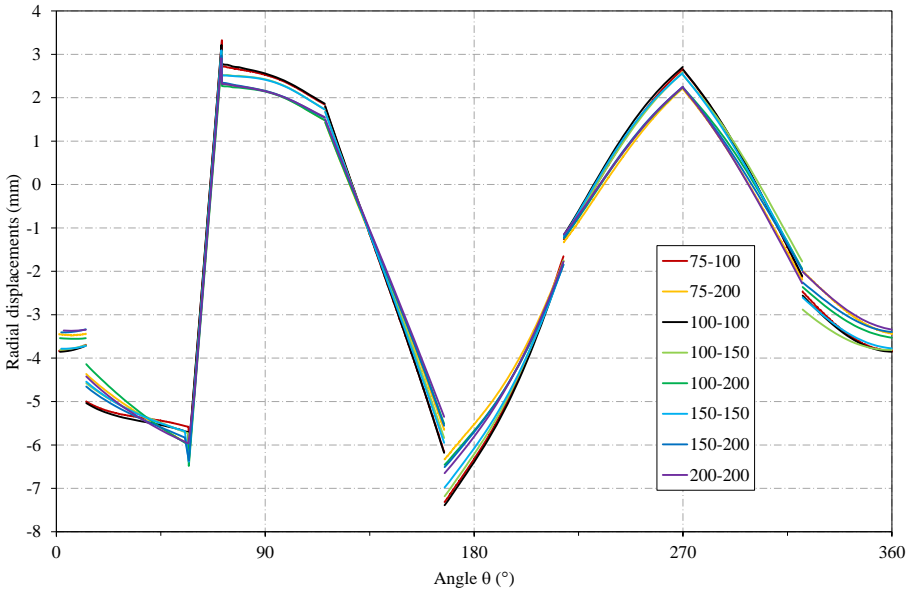


Figure 6.39. Variation of radial displacements in ring 0 with mesh size for models with installation imperfections.

6.4.4 Selection of the mesh size

For detailed analyses where the computational effort is believed to remain within acceptable limits, an average mesh size of 100 mm is used for both ring 0 as well as the adjacent rings -1 and +1. Previous sections showed that for this mesh configuration, accurate results can be obtained. The expected errors are believed to remain insignificantly small. However, the calculation times can reach up to 20 h if the model includes installation imperfections.

As a result, when multiple FE-calculations have to be performed, often a larger mesh size of 200 mm is chosen for rings -1 and +1. For ring 0, still a mesh size of 100 mm is applied. Consequently, the duration of the calculation can be kept much lower, at approximately 2.5 h for models including installation imperfections. The resulting error on the obtained sectional forces and deformations is rather limited, as illustrated in previous sections. For the normal forces in ring 0, as well as for the adjacent rings, the error is insignificant ($\pm 1\%$). Due to the larger mesh size in rings -1 and +1, the maximum bending moments in these rings are overestimated by about 10% (with installation imperfections) to 15% (for perfect geometry). Correspondingly, the bending moments in ring 0 might be underestimated by about 10%, compared to the

most dense mesh configuration. And finally, the maximum displacements of the middle ring are underestimated by approximately 10% by using the larger mesh size for the outer rings. Considering the huge reduction of the calculation times obtained for this mesh configuration, these results are believed to be very satisfactory. The corresponding errors should be taken into account in the evaluation of the results.

6.5 Impact of the joint friction

6.5.1 Applied coefficients of friction

As mentioned in section 6.2.4, a lot of uncertainty exists regarding the coefficient of friction μ to be applied for the contact conditions in the segment joints. Values for μ presented in literature generally range between 0.4 and 0.7 for concrete-to-concrete contact with a smooth interface. Due to the small tolerances applied in segment prefabrication, resulting in a very smooth concrete surface, a standard coefficient of friction $\mu = 0.4$ is initially assumed in this research. However, additional calculations were performed using $\mu = 0.5$, $\mu = 0.6$ and $\mu = 0.7$ in order to investigate the impact on the FE-results. Again, a distinction was made between models using the design geometry and others including installation imperfections. Taking into account the observations of the previous section, a mesh size of 100 mm for ring 0 and 200 mm for rings +1 and -1 was chosen for these simulations.

6.5.2 Models using design geometry

Figure 6.40 shows the impact of the applied coefficient of friction on the calculation times for the models without installation imperfections. Values of μ above 0.4 result in a significant increase in calculation times, up to almost double the required duration for $\mu = 0.4$. Figures 6.41 to 6.44 show the normal forces and bending moments for the various coefficients of friction, for ring 0 and ring +1 respectively. Virtually no impact on the sectional forces can be observed. Figure 6.45 presents the radial displacements of the middle ring. Again, no variation in the deformations can be perceived for larger values of μ . Similar to the analysis for the impact of the mesh size, an explicit comparison of the maximum normal forces, bending moments and displacements as a function of the coefficient of friction is presented in Appendix D, although Figures 6.41 to 6.45 are already very clear on the virtually non-existent impact

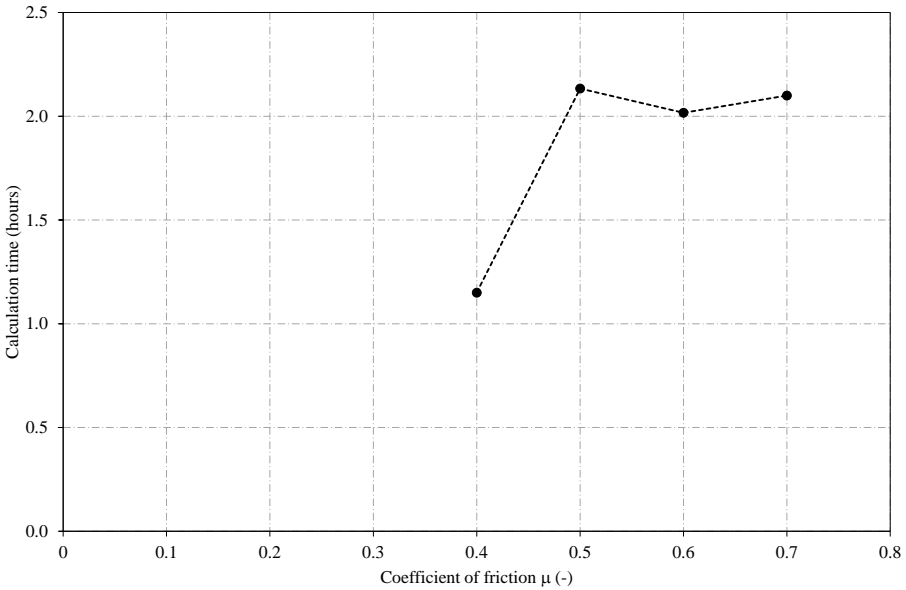


Figure 6.40. Variation of calculation times with coefficient of friction for models using design geometry.

of the coefficient of friction.

6.5.3 Models including installation imperfections

Similar calculations were performed for models including installation imperfections in the middle ring. Figure 6.46 shows the impact of the applied coefficient of friction on the calculation times for these models. Again, calculation times of more than twice the duration of the models using the design geometry are noticed. Larger values of μ result once more in larger calculation times compared to $\mu = 0.4$. The duration of the calculation for $\mu = 0.6$ is smaller than for both $\mu = 0.5$ and $\mu = 0.7$. No clear explanation for this divergent behaviour can be found.

The coefficient of friction has a substantial impact on the structural behaviour of the models including installation imperfections. Therefore, the influence of the applied value for μ on the sectional forces and deformations for this type of models is discussed in detail in the next chapter, which deals with the effect of the installation imperfections.

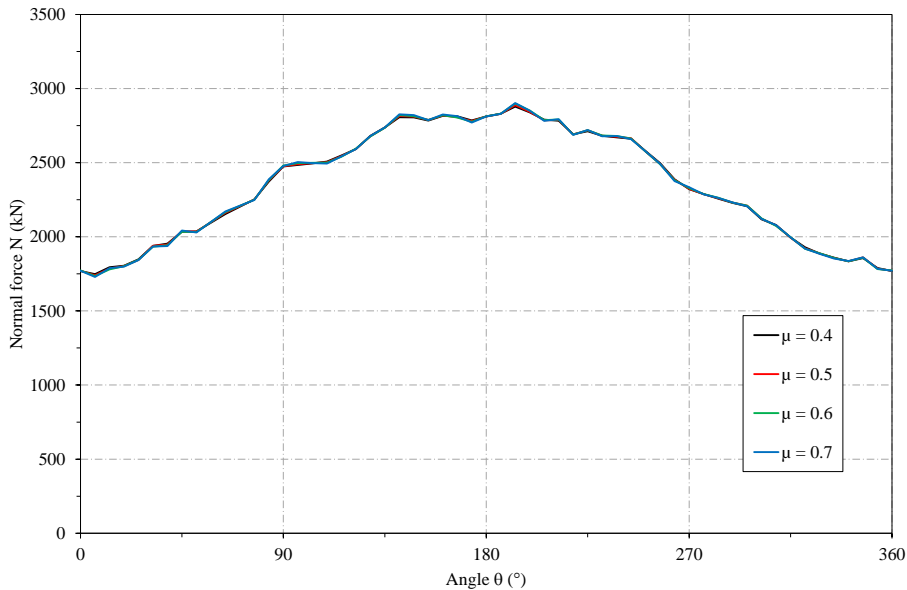


Figure 6.41. Variation of normal force N in ring 0 with coefficient of friction for models using design geometry.

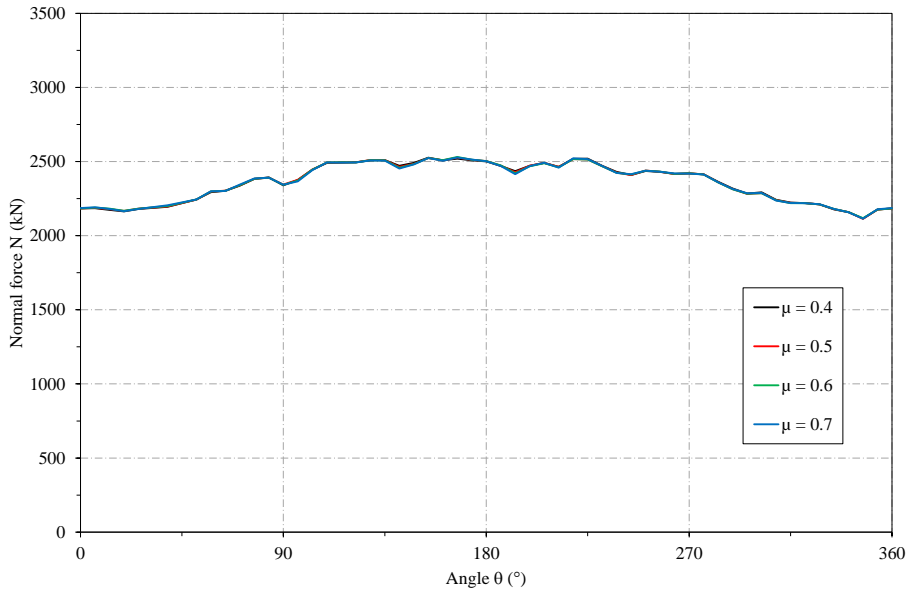


Figure 6.42. Variation of normal force N in ring +1 with coefficient of friction for models using design geometry.

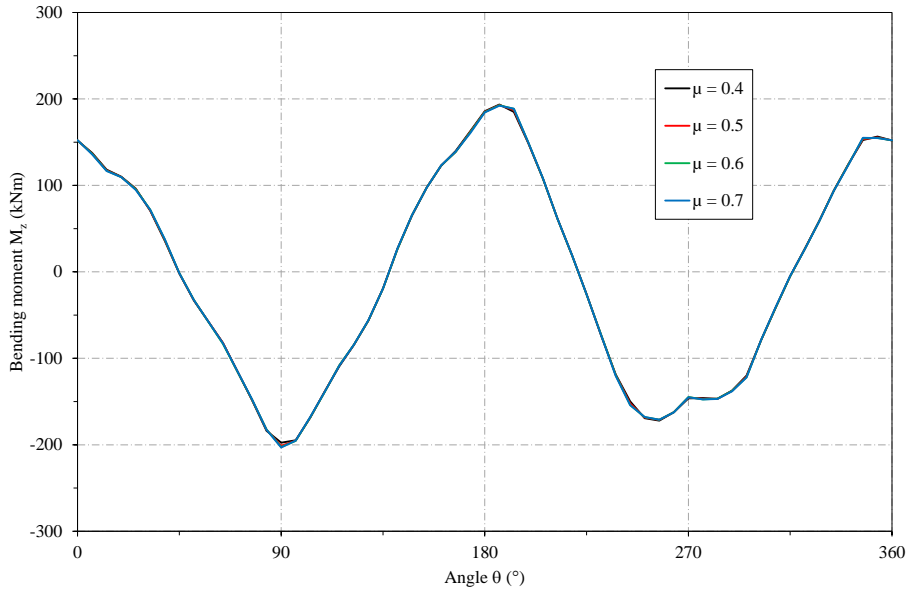


Figure 6.43. Variation of bending moment M_z in ring 0 with coefficient of friction for models using design geometry.

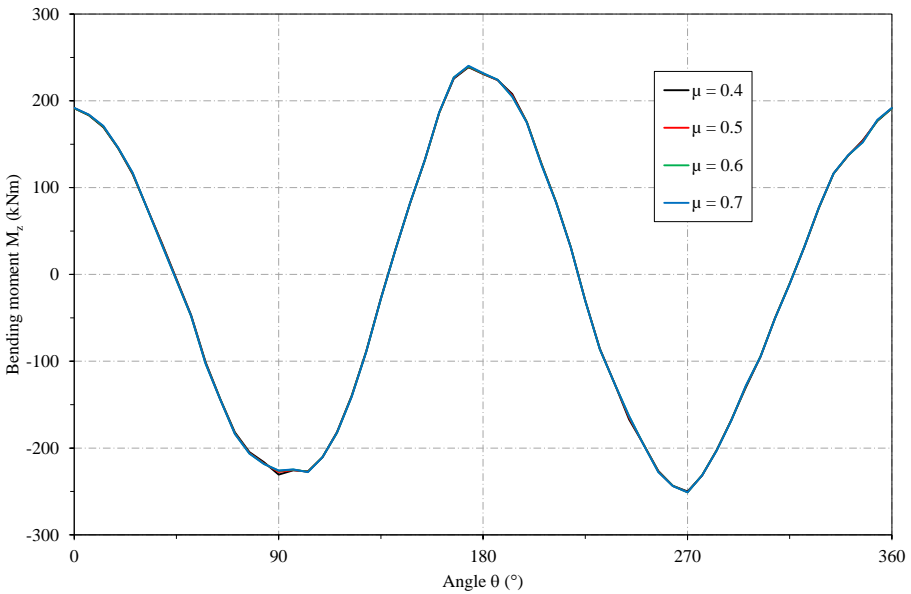


Figure 6.44. Variation of bending moment M_z in ring +1 with coefficient of friction for models using design geometry.

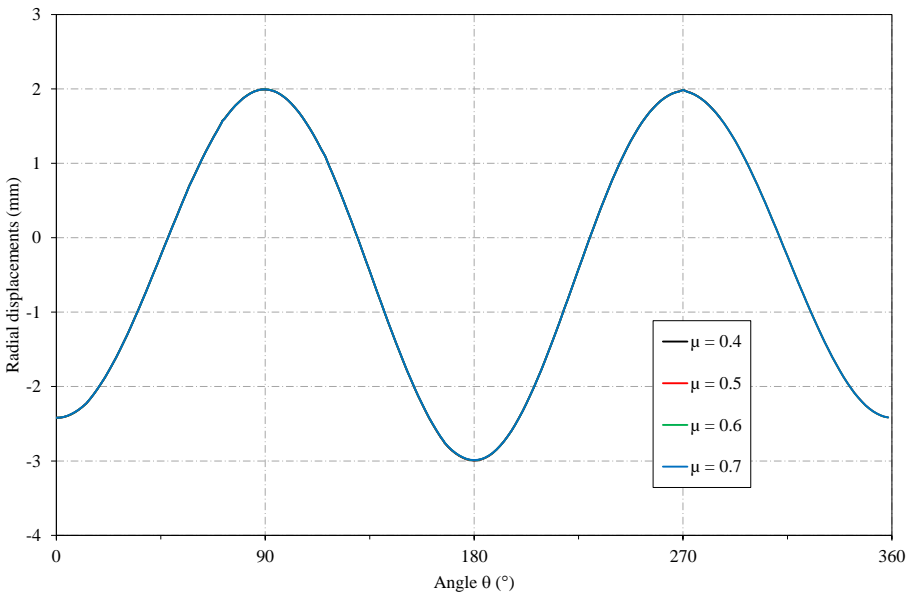


Figure 6.45. Variation of radial displacements in ring 0 with coefficient of friction for models using design geometry.

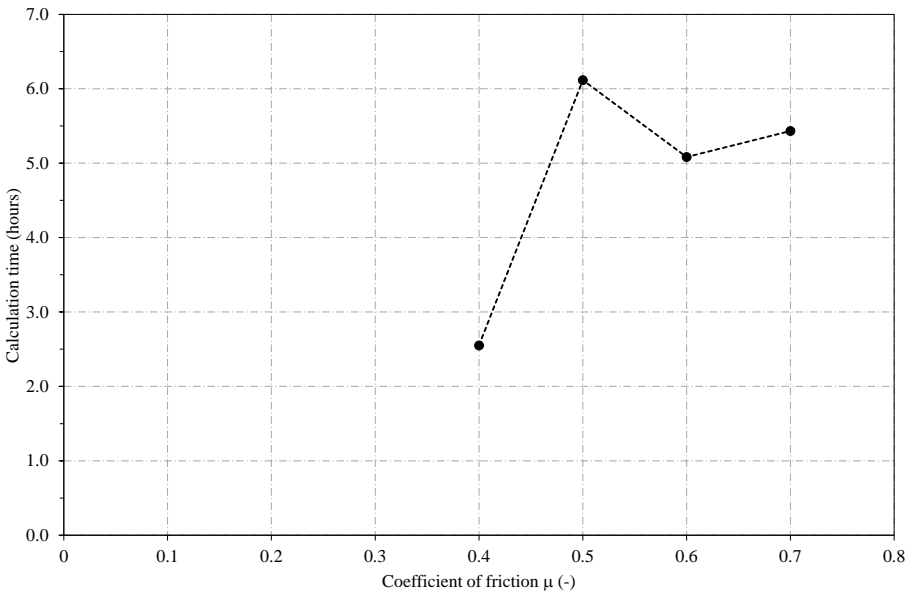


Figure 6.46. Variation of calculation times with coefficient of friction for models with installation imperfections.

6.5.4 Selection of the coefficient of friction

For models using a theoretically perfect geometry, no impact of the coefficient of friction is observed. Therefore, the results are not influenced by the choice for a specific value of μ . In these cases, it is chosen to apply $\mu = 0.4$, considering the significant profit in calculation times for the FE-analysis. When the FE-model includes installation imperfections, the selection of an adequate coefficient of friction for the application in the contact joints proves no easy task. This is discussed in Chapter 7.

Chapter 7

Installation imperfections: effect on lining behaviour

7.1 Introduction

As mentioned many times earlier in the text, during construction of the Liefkenshoek tunnel, in situ deformations of the tunnel lining were monitored using laser scanning. The results of early-stage conditions after assembly of a tunnel ring allowed for quantifying the inaccuracies during segment installation, as previously discussed in Chapter 5. These imperfections are now used as input for a numerical verification model using FE-modelling. The FE-model aims to assess the impact of the installation imperfections on the sectional forces.

7.2 Tunnel section S2726

7.2.1 Composition of the FE-model

Based on the results of the ovalisation monitoring, a specific tunnel section is selected which showed the most interesting results regarding joint behaviour and overall deformations. This proves to be ring S2726 in tunnel south, located below the Port Canal. This section is modelled according to the methodology of Chapter 6. Two separate models are developed: the first one using perfectly circular tunnel sections according to the theoretical design, and a second model where the middle ring was modelled with installation inaccuracies. From here on, they will be referred to as model 1 and model 2 respectively. The specific

laser scanning results of the reference measurement immediately after installation of ring S2726 are used as input for the joint irregularities and segment orientations in the FE-software for model 2. Figure 7.1 shows the imperfect ring geometry as was modelled for the middle tunnel ring of model 2.

For both models, a mesh size of 100 mm is selected for ring 0 and 200 mm for rings -1 and +1. For model 1 using the theoretically perfect geometry, a single coefficient of friction $\mu = 0.4$ is applied, as the previous chapter showed that the results for this type of model are not influenced by the choice for a specific value of μ . For model 2 including installation imperfections however, the coefficient of friction has a considerable impact on the obtained results. Therefore, the simulations of this model are performed for four different values of μ , similar to section 6.5.

7.2.2 Results of FE-calculations

Deformations

Both FE-models are calculated using the characteristic soil and water pressures according to the corresponding location of the section in the tunnel project. The calculated results show a strong distinction between model 1 (without installation inaccuracies) and model 2 (with joint imperfections and angular rotations). Figure 7.2 displays the calculated radial displacements due to the external loads for both FE-models, and for $\mu = 0.4$ to 0.7 in model 2. The results for the first model simulating a theoretically perfect ring erection show a seamlessly ellipsoidal deformation with the major axis oriented horizontally. The deformations of the second model clearly differ from this classical deformation pattern for model 1. Irregular deformations occur for multiple segments, which are caused by the installation imperfections. The results show a significant impact of μ on the radial displacements of ring 0. Naturally, for larger values of the coefficient of friction, smaller displacements are found. This is due to the interaction with the adjacent rings via friction in the ring joints. In addition, smaller dislocations in the joints of ring 0 are found as well. This is mainly visible for the joint located at $\theta = 167^\circ$. At the right side of this joint, the difference in radial displacements between $\mu = 0.7$ and $\mu = 0.4$ equals around 20%. An additional graph showing the variation of these displacements as a function of the coefficient of friction is presented in Appendix D.

The calculated results can be compared with the actual in situ deformations of the modelled section S2726 obtained by ovalisation monitoring. The latter were calculated as the difference between the reference measurement

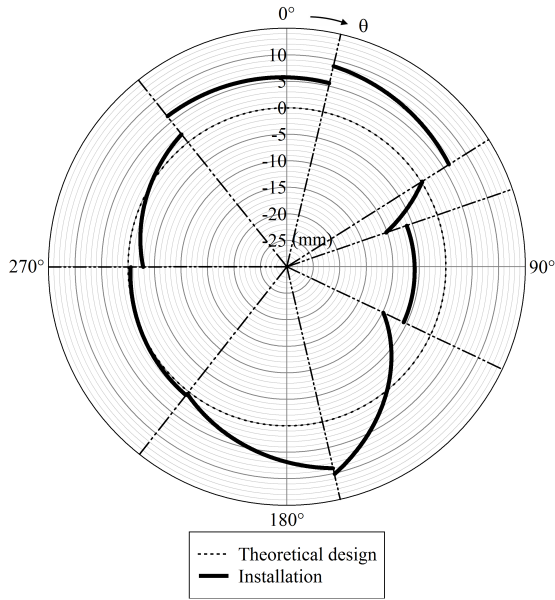


Figure 7.1. Modelled radial installation inaccuracies in the FE-model.

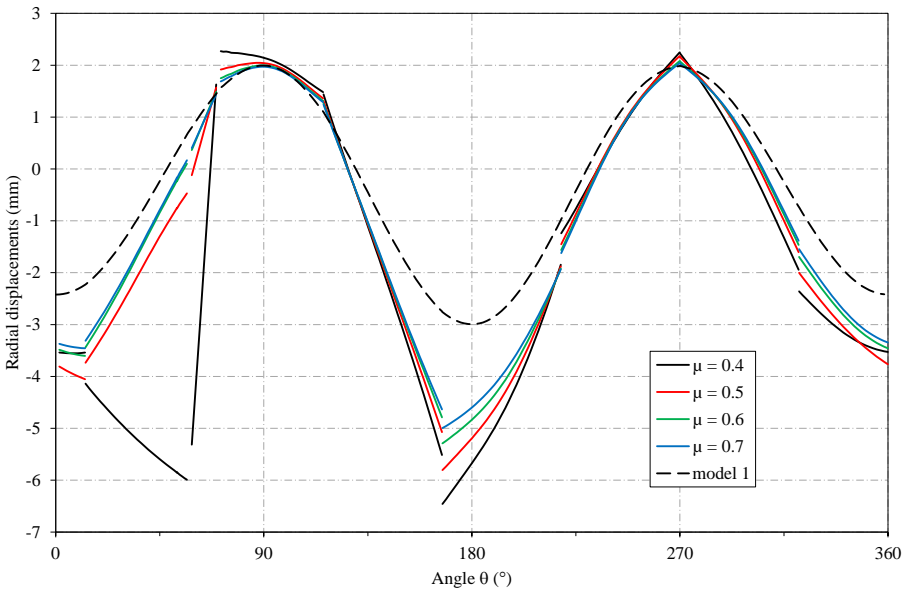


Figure 7.2. Comparison of radial displacements in ring 0 for model 1 and model 2 with various values of μ .

and control measurement 1. Such a comparison is shown in Figure 7.3, which presents the radial displacements as calculated for model 1 and for model 2 using $\mu = 0.4$. The results for $\mu = 0.5$ are shown in Figure 7.4. The results for $\mu = 0.6$ and 0.7 show a very similar profile. It can be observed that the deformations calculated with model 2 and $\mu = 0.4$ show a good resemblance to the real deformations of the tunnel section. Only for θ -values around 270° a larger difference can be found between the calculated and monitored results. This is most probably due to an excess in tail grouting pressures during tunnel construction below the Port Canal. Values of the coefficient of friction larger than 0.4 are not able to accurately simulate the deformational behaviour in the upper right corner of the tunnel section.

Tangential normal forces

The adequate resemblance between the calculated deformations from the FE-modelling ($\mu = 0.4$) and the monitored results from the actual tunnel lining allow for a quantification of the impact of the installation inaccuracies on the sectional forces in the tunnel lining. Figures 7.5 and 7.6 show the calculated tangential normal forces for the various values of the coefficients of friction in model 2, for ring 0 and ring +1 respectively. In case of a flawless installation, the middle ring and both adjacent rings of the FE-model show a distribution of normal forces according to model 1, which is given as a reference in both graphs as well. The imperfect segment installation causes a strong reduction of the normal forces in the middle ring where the installation inaccuracies are present. Due to the imperfect contact in the segment joints, the forces are transferred to the neighbouring rings via friction in the ring joints. Consequently, the normal forces in both adjacent rings, which are perfectly circular in the FE-model, increase with about half the amount of the reduction in the middle ring. As a result, the maximum normal force N_{max} in the adjacent rings increases by more than 20% for $\mu = 0.4$, while N_{max} in the imperfectly installed middle ring drops by 40%. The minimum normal force in the imperfect ring even reduces to less than a quarter of the original normal force.

Furthermore, a considerable impact of the coefficient of friction is observed. Due to the irregularities in the segment joints, individual segments experience small displacements and rotations in the search for perfect contact with adjacent segments. Naturally, for larger values of μ , these deformations are obstructed to a larger extent. As a result, more sectional forces are transferred across the ring joints via friction, influencing the normal forces in the tunnel

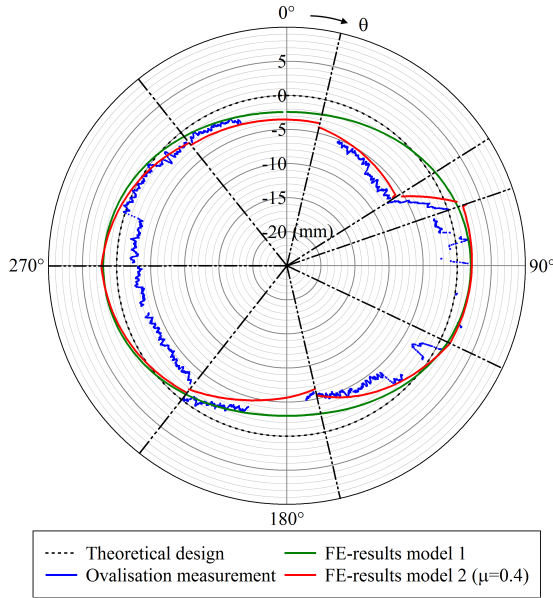


Figure 7.3. Comparison of radial displacements obtained from the FE-models and measurements.

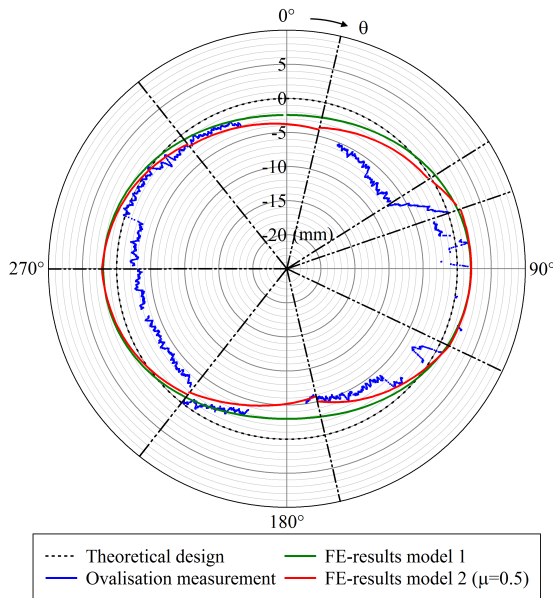


Figure 7.4. Comparison of radial displacements obtained from the FE-models and measurements.

rings considerably. For rings -1 and +1, the increase in normal force due to the imperfections in the middle ring reaches almost 50% for $\mu = 0.7$. However, for the middle ring, the impact of the applied coefficient of friction is even more drastic. At some locations, large values of μ prevent adjacent segments from establishing a good contact in the joint. As a result, no forces can be transferred directly at these longitudinal joints and the normal forces locally drop to zero.

Bending moments around longitudinal z-axis

Figures 7.7 and 7.8 show a similar comparison for the bending moments M_z around the tunnel axis. Due to the modelled imperfections in model 2, the bending moments in the ring with installation inaccuracies are greatly disturbed. The joint irregularities cause a disruption in the moment transfer between segments, due to which the adjacent tunnel rings carry a larger amount of bending moments. For ring 0, the influence of the coefficient of friction is not as straightforward as for the normal forces. For the adjacent rings -1 and +1, the rise in maximum bending moments is larger for smaller values of μ . An increase of 25% is found for $\mu = 0.7$, while for $\mu = 0.4$ this value reaches almost 50%. Additional graphs showing the comparison of the maximum normal forces and bending moments as a function of the coefficient of friction are presented in Appendix D.

Lining stresses

The observed increase of the governing normal force in the adjacent rings might fall within the safety levels provided by the partial safety factors used in the design process. Among other things, they account for small geometric imperfections with respect to the theoretical design. Of course, the safety level is now reduced by a significant amount due to the imperfect segment installation, leaving a smaller margin for other uncertainties regarding the load magnitude. On the other hand, the increase of bending moments is far more negative on the design of the concrete lining and possibly leads to excessive sectional forces in the concrete lining. In order to verify this, Table 7.1 presents the maximum circumferential stresses in the concrete and reinforcement bars, as calculated using the results for the sectional forces of model 1 and model 2 for $\mu = 0.4$.

Table 7.1 demonstrates a general increase in maximum steel and concrete stresses in the adjacent rings due to installation imperfections, both in tension and compression. This overall increase is found both at the interior and exter-

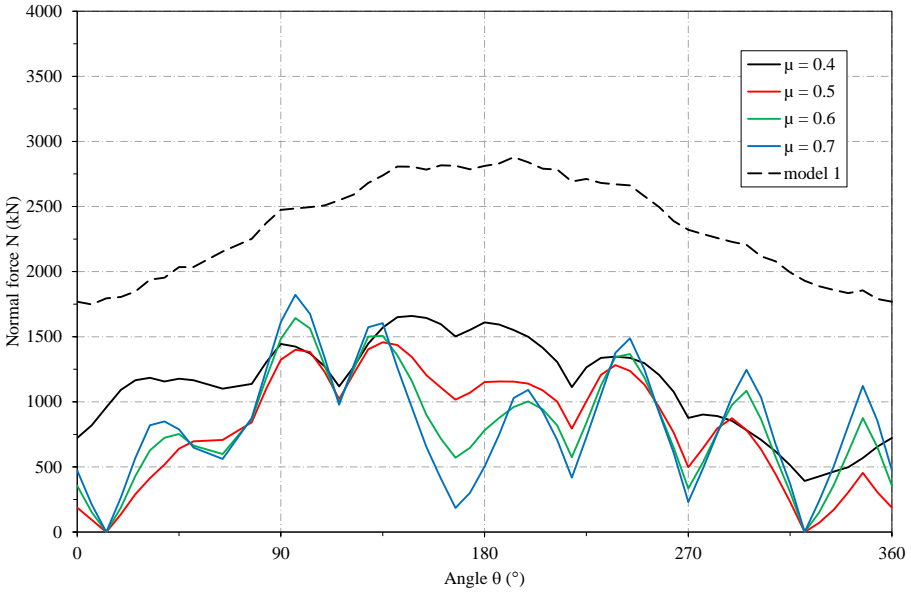


Figure 7.5. Comparison of normal force N in ring 0 with coefficient of friction for models with installation imperfections.

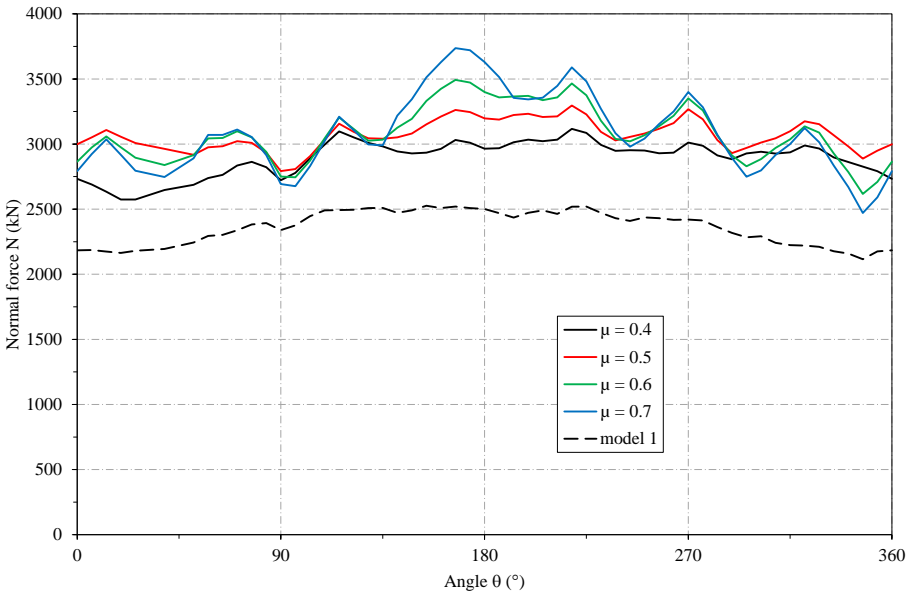


Figure 7.6. Comparison of normal force N in ring +1 with coefficient of friction for models with installation imperfections.

Table 7.1. Comparison between maximum calculated stresses (MPa) from model 1 and model 2 using $\mu = 0.4$.

| | | concrete | | | | reinforcement steel | | | |
|------------|---------|-------------|--------|-------------|--------|---------------------|--------|-------------|--------|
| | | intrados | | extrados | | inner layer | | outer layer | |
| | | tens. | compr. | tens. | compr. | tens. | compr. | tens. | compr. |
| ring 0 | model 1 | 0.94 | -7.35 | 0.70 | -7.72 | 1.49 | -35.34 | - | -36.44 |
| | model 2 | 2.63 | -6.51 | 3.32 | -4.85 | 10.21 | -29.89 | 11.44 | -21.75 |
| ring -1/+1 | model 1 | 2.06 | -8.95 | 3.09 | -8.48 | 5.43 | -41.81 | 8.56 | -38.49 |
| | model 2 | <u>6.48</u> | -12.05 | <u>4.31</u> | -12.59 | 24.70 | -56.26 | 12.22 | -55.50 |

ior of the tunnel lining. In the middle ring, the stress increase between model 1 and model 2 only occurs in tension, since the observed decrease in normal force leads to lower compressive stresses. Overall the stress levels in the reinforcement bars remain small enough not to cause any problems. However the increasing concrete stresses draw special attention. The compressive stresses in the concrete increase with 25% to 50% in model 2 (ring +1) and might exceed the allowable compressive stresses in tunnel sections with a larger overburden than cross-section S2726 under consideration. Furthermore, model 2 with installation inaccuracies shows concrete stresses exceeding the tensile strength $f_{ctm} = 4.1$ MPa in the adjacent rings (underlined values in Table 7.1). Consequently concrete cracks might develop at the intrados as well as the extrados, affecting the durability of the segmental lining. Similar observations are made for larger values of μ .

7.2.3 Discussion

These results demonstrate the considerable negative effects of inaccuracies during segment installation. Due to the imperfect contact in the segment joints, the sectional forces in the neighbouring rings show a substantial increase that might surpass the safety levels applied in the design of segmental tunnel linings. Consequently the allowed circumferential stress levels in the concrete might be exceeded in the serviceability limit state, both in tension and compression, creating undesirable cracks in the concrete lining. However, an advanced analysis using non-linear material behaviour should be performed for a detailed evaluation of concrete cracking. Finally the decrease of normal forces in the imperfect ring might give rise to problems with waterproofing of the structure,

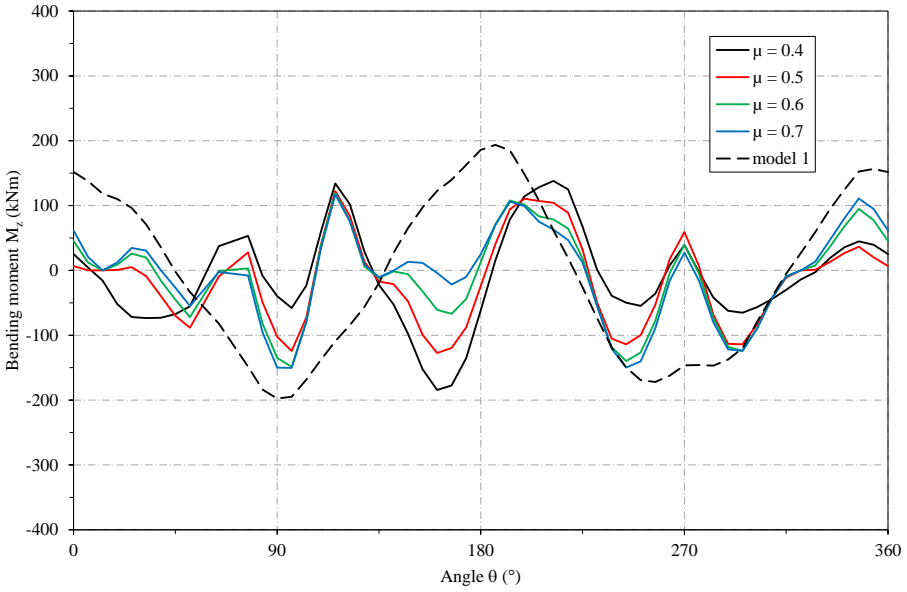


Figure 7.7. Comparison of bending moment M_z in ring 0 with coefficient of friction for models with installation imperfections.

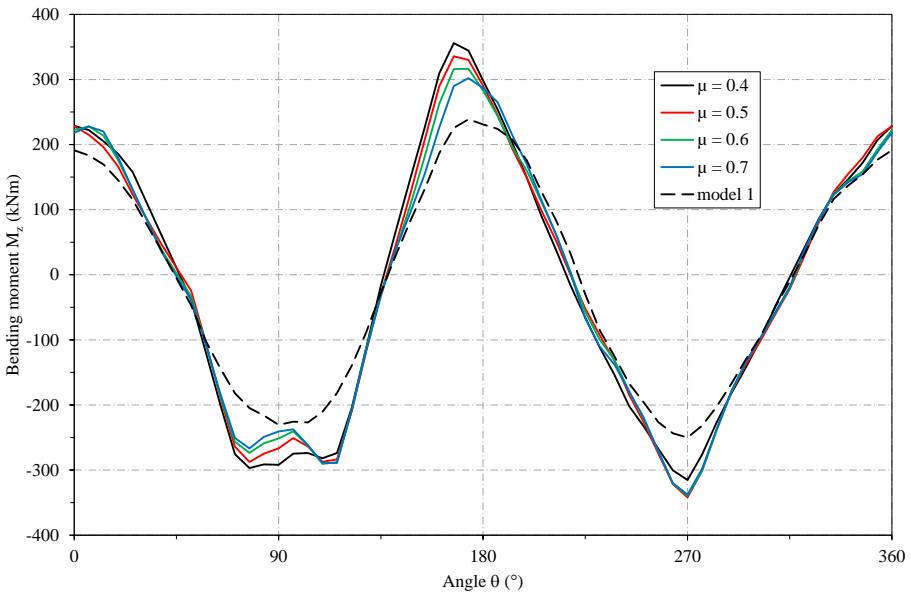


Figure 7.8. Comparison of bending moment M_z in ring +1 with coefficient of friction for models with installation imperfections.

due to a reduced compression of the sealing gaskets.

7.2.4 Selection of the coefficient of friction

When the FE-model includes installation imperfections, the selection of an adequate coefficient of friction for the application in the contact joints proves no easy task. As a result, the impact of the applied value for μ should in fact be investigated in every analysis. Nonetheless, the results of the previous section have indicated that for the Liefkenshoek tunnel, the calculated deformations using $\mu = 0.4$ show the best resemblance to the real deformations of the tunnel section, as monitored using laser scanning. Furthermore, this value corresponds to the largest increase in bending moments in the adjacent tunnel rings, which has the most negative impact on the stresses in the concrete lining. Consequently, this value for the coefficient of friction is assumed in further calculations in this chapter, where no additional study of the impact of μ is performed.

7.3 Theoretical installation imperfections

7.3.1 Applied joint imperfection

In the previous section, the monitored installation imperfections of tunnel section S2726 were used for numerical verification. As shown in Figure 7.1, almost all of the segments deviated from their position in the theoretical design, resulting in a very specific configuration of imperfections. In this section, the impact is investigated when only one segment or one single joint is inaccurately installed. For that purpose, two types of local installation imperfections are investigated in the following sections. Nonetheless, multiple other types still exist in reality. For both types under investigation, the imperfection results in an irregularity u at only one or two joints of the tunnel section, similar to Figure 5.7. The value of u that is applied in this theoretical study, is based on the analysis of the laser scanning results of Chapter 5. Evaluation of all monitored sections showed that the average joint irregularity immediately after installation equals 2.34 mm, with a standard deviation of 1.52 mm. In order to apply a representatively large value for the joint irregularity, the magnitude of u in the following sections is determined as the 97.5-percentile according to equation 7.1, meaning that only 2.5% of the irregularities exceed this value.

$$u = 2.34 + 1.96 \times 1.52 = 5.33 \text{ mm} \quad (7.1)$$

7.3.2 Imperfect installation of 1 segment

In the first type of installation imperfection, the inaccurate placement of one single segment is considered. This segment is rotated along the longitudinal axis, resulting in an equal but opposite joint irregularity u at both ends. Each segment can be rotated in a positive direction (anti-clockwise), as shown in Figure 7.9, or in a negative direction (clockwise). At the same time, all other segments are modelled in accordance with the theoretically perfect geometry.

Figure 7.10 shows the results of such a calculation in the example of a negative rotation of segment A1, located almost at the bottom of the tunnel section. In this figure, the final cross-sectional profile of the tunnel section is shown, after deformation. The result for a perfect geometry of the entire section (model 1) is given as well for comparison. It can be observed that the installation imperfection remains present after deformation of the tunnel section into the pumpkin shape, at almost its full original magnitude. This confirms the observations of the ovalisation measurements in previous chapters, where monitored installation imperfections after assembly remained visible in subsequent control measurements of the section.

As a result, the force transfer between the lining segments is permanently disrupted. Figures 7.11 and 7.12 show the normal forces and bending moments in ring 0 and ring -1, for the same imperfect installation of segment A1 in ring 0. The results of ring +1 are identical to ring -1. Due to the joint irregularities, the normal force in the middle ring is locally reduced around the edges of the dislocated segment, and transferred to the adjacent rings. Further away from the imperfect area, the results correspond to the situation of the perfect ring geometry. In the results of the bending moments, a considerable increase of the minimum and maximum values in the imperfect ring can be observed. In the adjacent rings, the effect is much less pronounced for this configuration.

An identical calculation is performed for a positive rotation of segment A1, as well as for both types of rotation of all other segments in a tunnel ring. In each case, only one segment at a time is considered to be inaccurately installed. The combined results for the normal forces and bending moments are shown in Figures 7.13 to 7.16. The results are equivalent to the ones for segment A1 mentioned above. Each individual dislocated segment causes a local transfer of normal forces to the adjacent rings. As a result, a decrease of normal forces up to 40% is observed in the middle ring around the location of the imperfection, corresponding to an increase of about 20% in the adjacent rings. The effect is most negative around the sides of the tunnel section. The

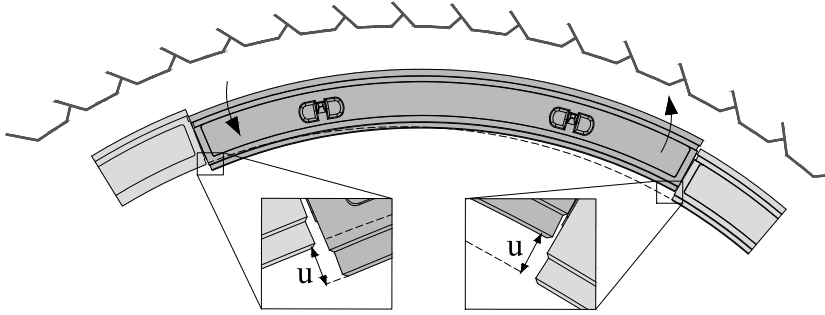


Figure 7.9. Imperfect installation of a single segment resulting in identical joint irregularities at both sides.

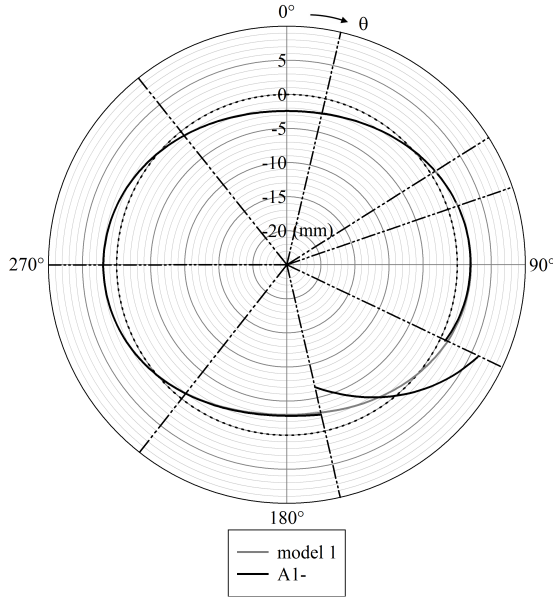


Figure 7.10. Impact of imperfect installation of segment A1 on final tunnel profile.

imperfection also causes a disruption of the bending moments in both the middle ring as well as the adjacent rings. Especially for the latter, the effect is most pronounced at both the top, bottom and sides of the section. The rise in maximum bending moments (both positive and negative) reaches 40% in the ring which includes the imperfection, and even 50% in the adjacent rings. Finally, the calculated deformations for each configuration confirms the observation made for Figure 7.10, that nearly all of the initial imperfections remain visible after deformation of the tunnel section.

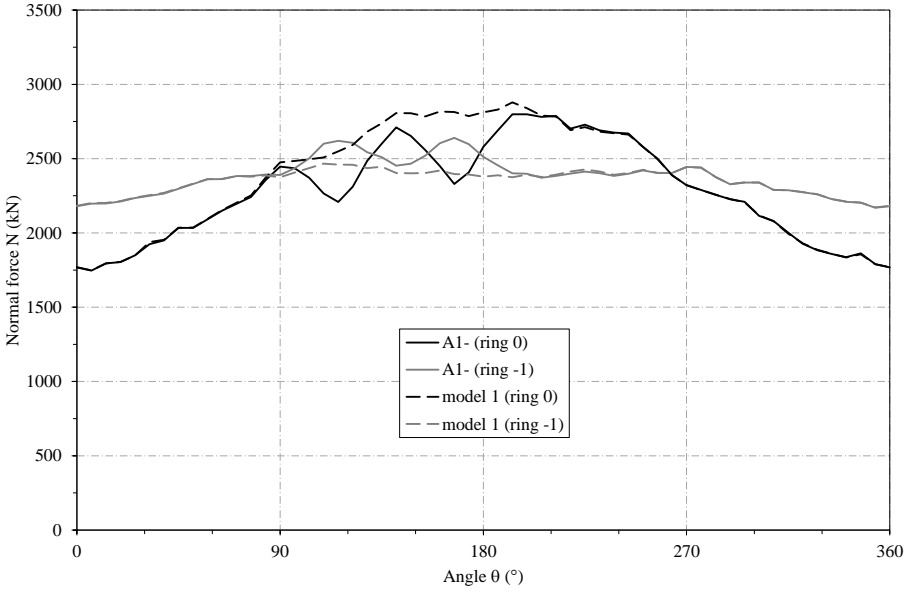


Figure 7.11. Impact of imperfect installation of segment A1 on normal force N .

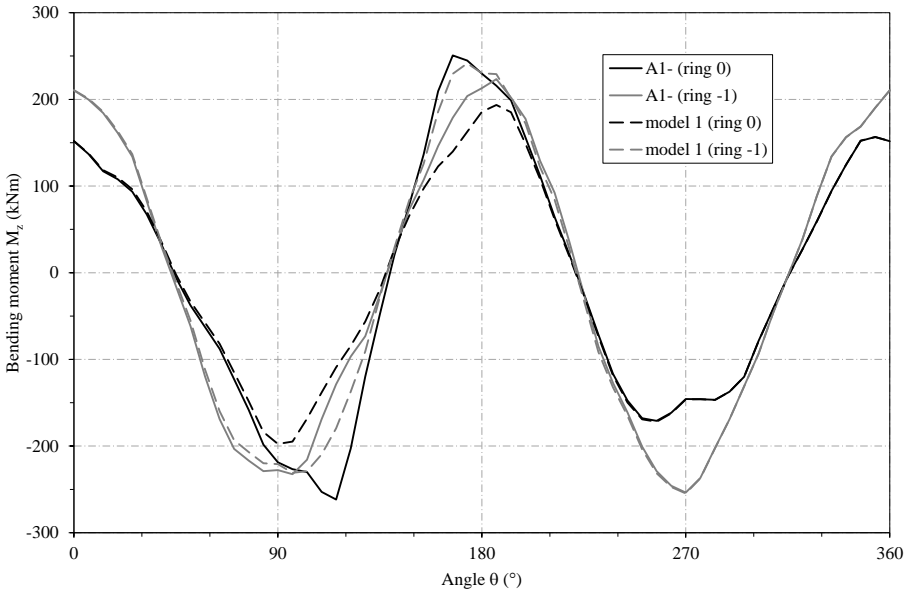


Figure 7.12. Impact of imperfect installation of segment A1 on bending moment M_z .

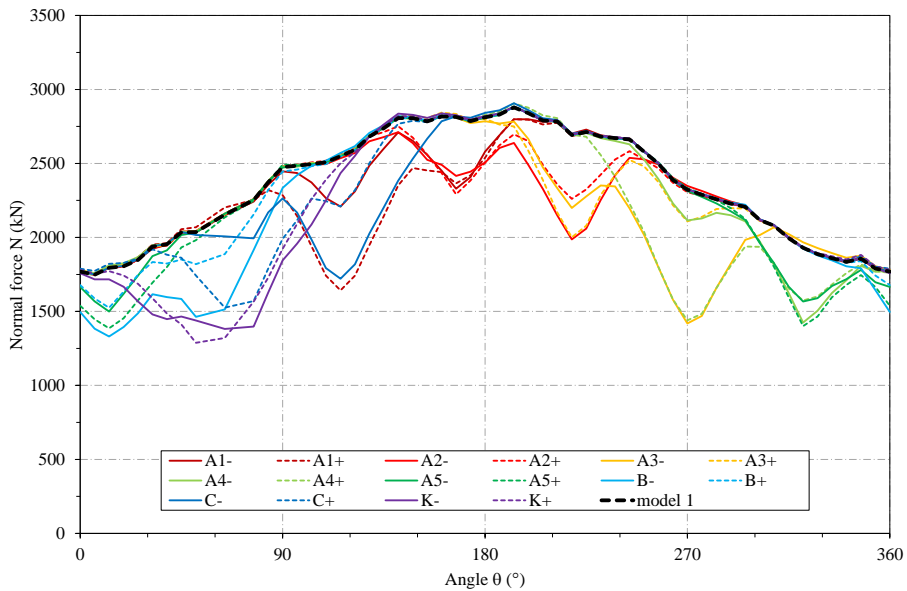


Figure 7.13. Impact of imperfect installation of segments on normal force N in ring 0.

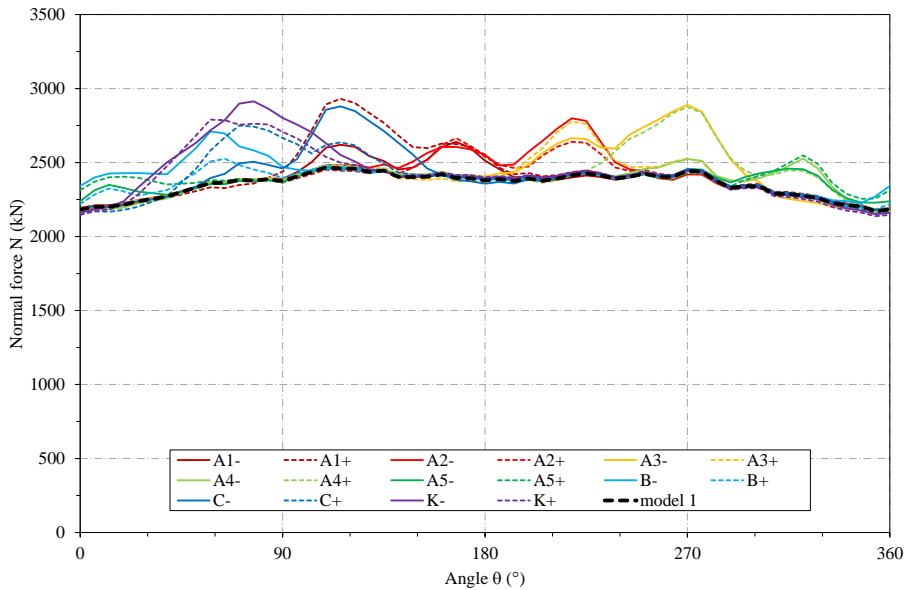


Figure 7.14. Impact of imperfect installation of segments on normal force N in ring -1.

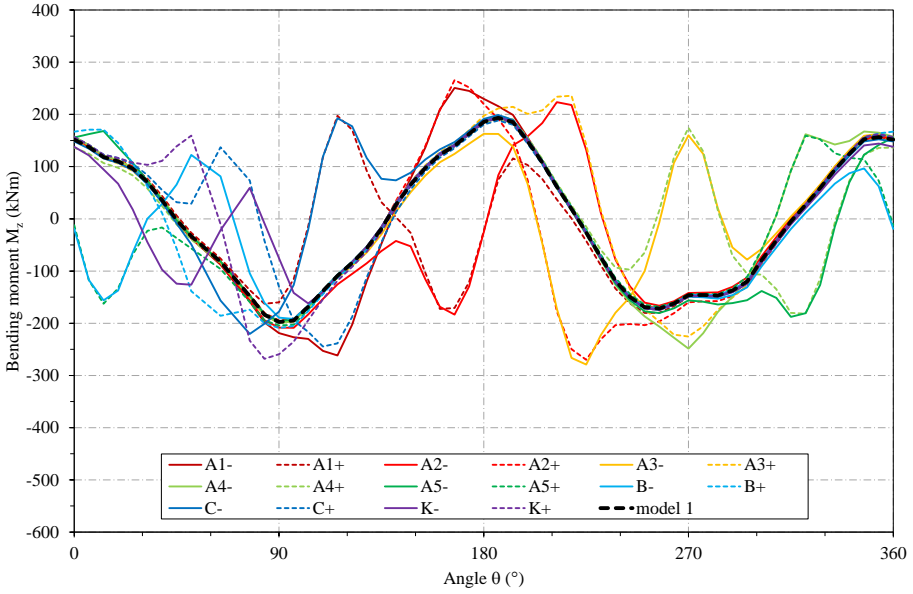


Figure 7.15. Impact of imperfect installation of segments on bending moment M_z in ring 0.

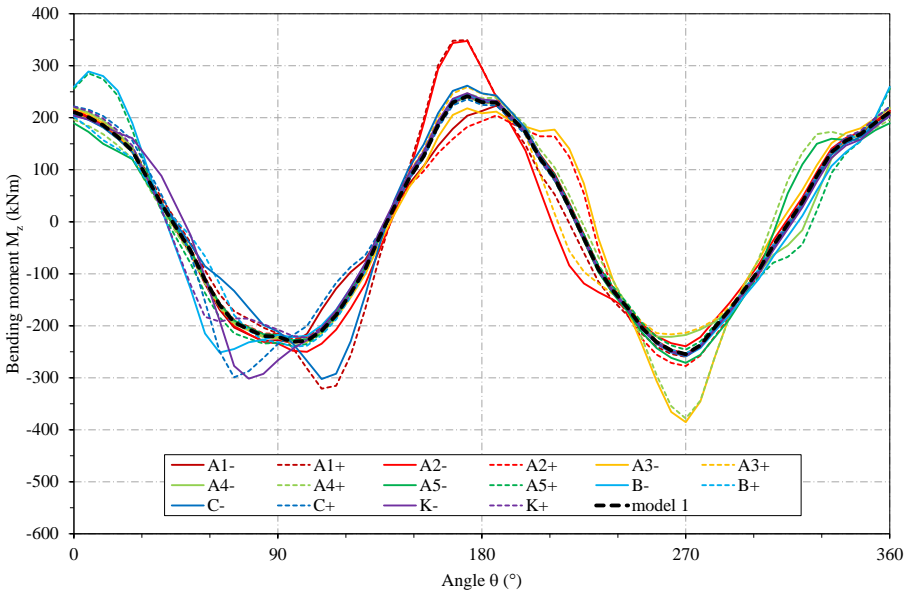


Figure 7.16. Impact of imperfect installation of segments on bending moment M_z in ring -1.

7.3.3 Imperfect installation of 1 joint

In the second type of installation imperfection, an irregularity u in a single joint is considered. It originates when one segment is rotated towards the tunnel exterior and the adjacent segment is rotated inwards, as illustrated in Figure 7.17. An identical irregularity can be obtained by rotating both segments in the opposite direction of Figure 7.17. By convention, a rotation of both segments in counter-clockwise direction, as shown in Figure 7.17, corresponds to a positive joint irregularity. A negative irregularity is caused by a rotation of both segments in clockwise direction. Again, at the same time, all other segments are modelled in accordance with the theoretically perfect geometry.

Such a local imperfection can be modelled for all joints of the tunnel section separately, which are numbered according to their location. Joint 1 is the joint between segments A1 and A2, joint 2 between A2 and A3, etc. Figure 7.18 shows the results of the deformed tunnel section, in case of a positive irregularity in joint 4, located between segments A4 and A5 at the upper left side of the cross-section. Similar to the previous section, it can be observed that the installation imperfection remains perfectly present after deformation of the tunnel section. No corrective behaviour to reverse the initial imperfection is noticed.

Figures 7.19 to 7.22 present the combined results of the normal forces and bending moments for the various locations of the joint imperfection. The results are quite similar to the first type of installation imperfection, concentrated in a single segment. The effect of the joint irregularity on the normal forces in both the middle ring and the adjacent rings is almost identical to the observations discussed in the previous section. However, the impact on the bending moments is less articulated for this type of imperfection. This is mostly due to the symmetry of the joint irregularity around the design profile (see Figure 7.17), as a result of which the eccentricity of the transferred forces in the ring remains slightly smaller. Consequently, the increase in maximum bending moments in the adjacent rings reaches 25%, compared to 50% for the first type of imperfection. Again, the joint irregularity has the most negative impact when it is located close to the top, bottom and sides of the tunnel section, for which the maximum bending moments and deformations are found.

7.3.4 Imperfect installation of multiple segments

Previous sections studied the impact of a local installation imperfection in a single joint or segment. Additionally, it is investigated what happens when

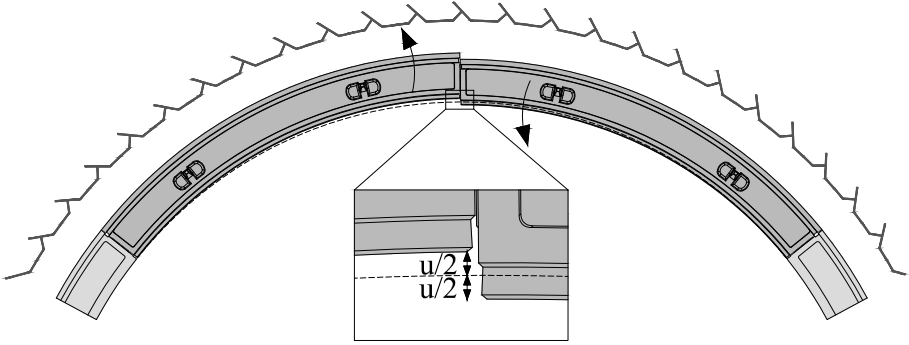


Figure 7.17. Imperfect installation of adjacent segments resulting in a single joint irregularity.

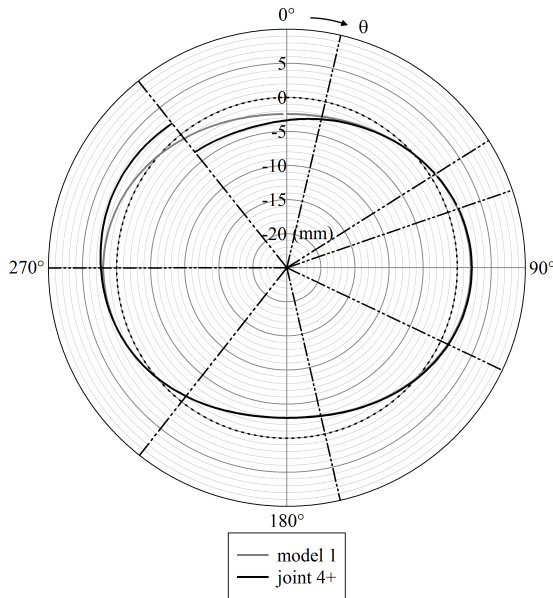


Figure 7.18. Impact of irregularity in joint between segments A4 and A5 on final tunnel profile.

such imperfections occur at more than one location at the same time. For this purpose, combinations are made of the first type of imperfection that was considered, the rotation of a single segment, as this proved to have a larger impact on the bending moments. Dislocated segments can be separated by 'normal' segments, installed according to the perfect design geometry, or can be located next to each other. In the latter case, only those combinations are

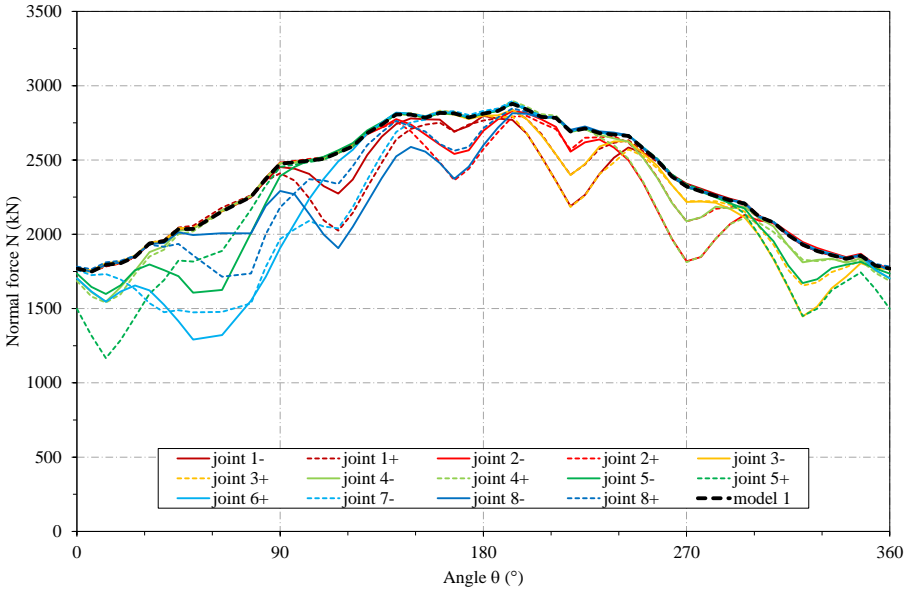


Figure 7.19. Impact of imperfect installation of segments on normal force N in ring 0.

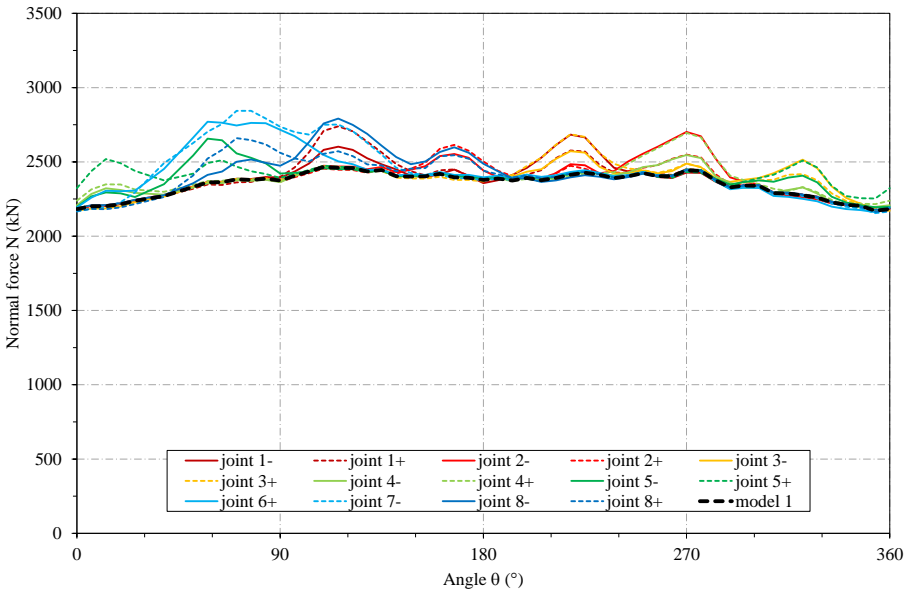


Figure 7.20. Impact of imperfect installation of segments on normal force N in ring -1.

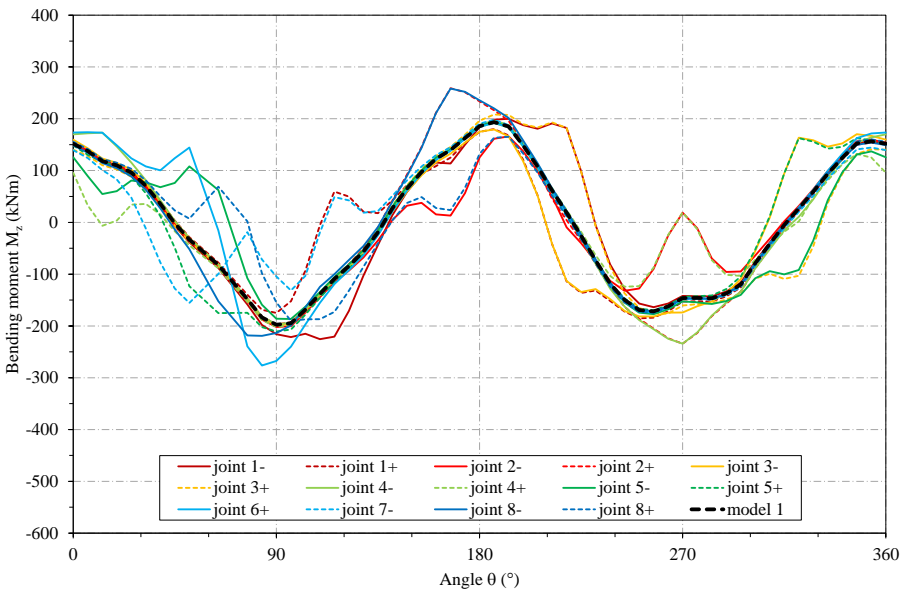


Figure 7.21. Impact of imperfect installation of segments on bending moment M_z in ring 0.

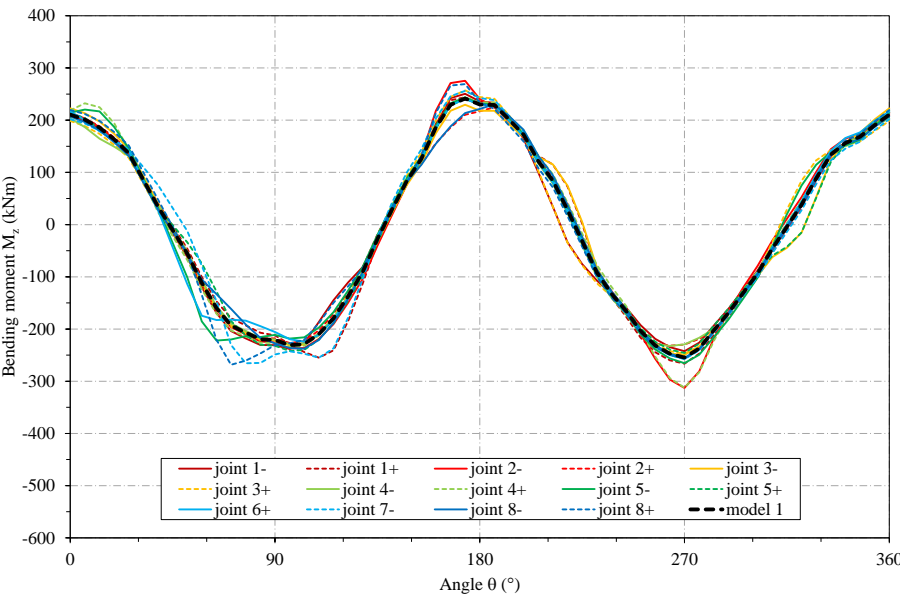


Figure 7.22. Impact of imperfect installation of segments on bending moment M_z in ring -1.

considered that do not result in a larger joint irregularity than the value set forward in section 7.3.1.

Figure 7.23 shows the results for the example of the combined rotation of segments A1 (positive) and A2 (negative), located at the bottom of the tunnel section. The final cross-sectional profile is compared with the deformed tunnel shape as calculated for the separate occurrence of both imperfections. It can be observed that the dislocation of segments A1 and A2 in the combination corresponds almost perfectly to the final position of the segments in the individual cases. Only at the joint between both segments, where no irregularity is present in the combination of both imperfections, a minor reduction of the deviation from the perfect pumpkin shape can be perceived.

Figures 7.24 to 7.27 present the corresponding results for the normal forces and bending moments. From Figures 7.24 and 7.25, it can be concluded that the distribution of the normal forces for the combination of the imperfections in segments A1 and A2 corresponds perfectly to the envelope of the normal forces obtained for the individual imperfections, in the middle ring as well as in the adjacent rings. Consequently, the impact of a combination of segment dislocations on the normal forces is just as negative as for a single segment imperfection. Yet, for the bending moments presented in Figures 7.26 and 7.27, this is not the case. In these graphs, the combined effect of both imperfections results in an amplification of the maximum bending moments at the location of the joint between both segments. This is due to the fact that the eccentricity at this position is larger in this case, compared to the configuration where one dislocated segment is neighboured by a perfect one. For the combined rotation of segments A1 and A2, the increase of maximum bending moments in ring -1 compared to the perfect geometry reaches 60%, which is 15% more than for both of the individual imperfections.

The results for other combinations of imperfections all confirm the previous observations. When dislocated segments are not adjacent to each other, the combined effect corresponds to the envelope of the individual imperfections. When they are located next to each other, the impact on the bending moments is magnified at the location of the common joint between both segments. However, in the latter case, the combined effect is not as large as the sum of the individual cases.

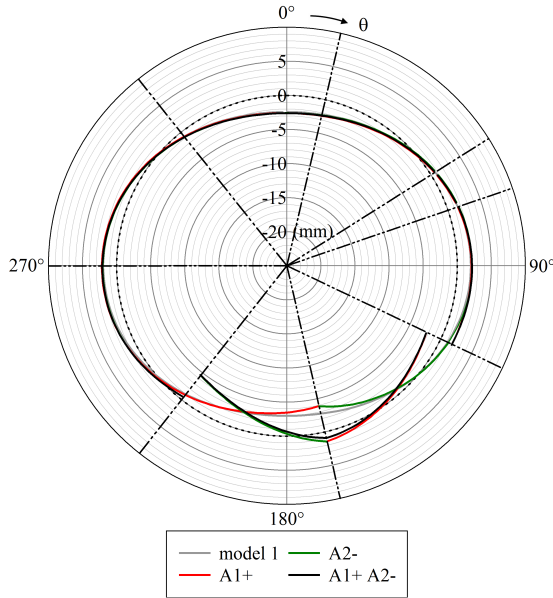


Figure 7.23. Impact of imperfect installation of segments A1 and A2 on final tunnel profile.

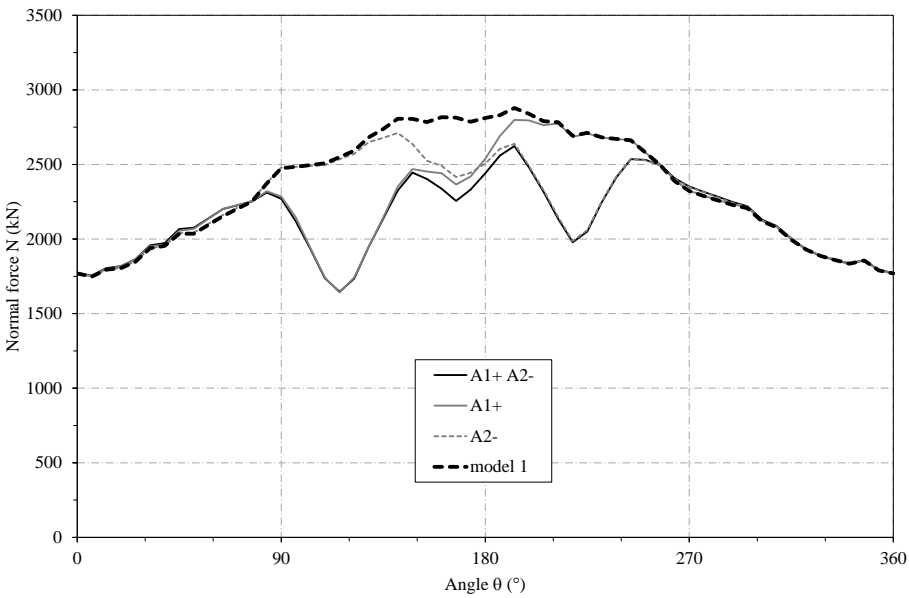


Figure 7.24. Impact of imperfect installation of segments A1 and A2 on normal force N in ring 0.

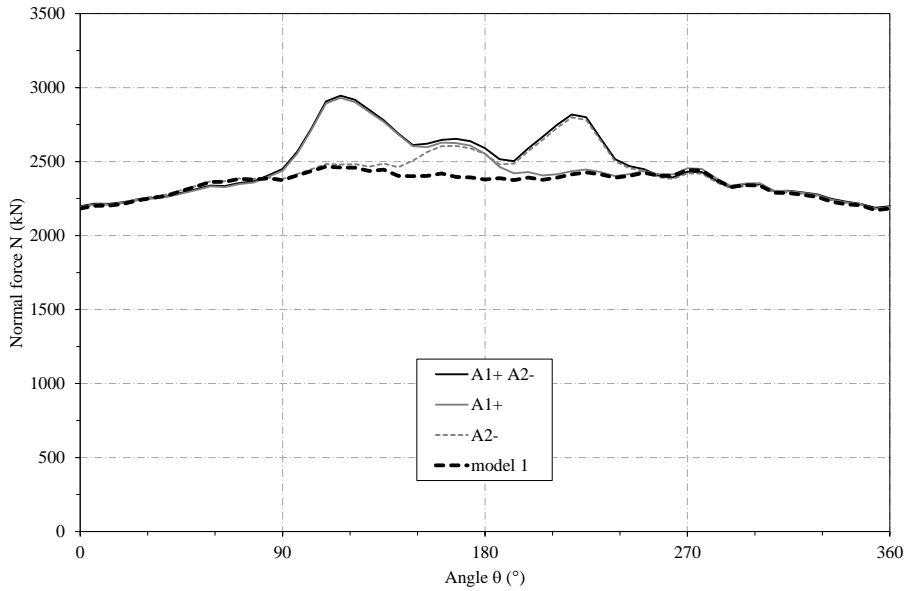


Figure 7.25. Impact of imperfect installation of segments A1 and A2 on normal force N in ring -1.

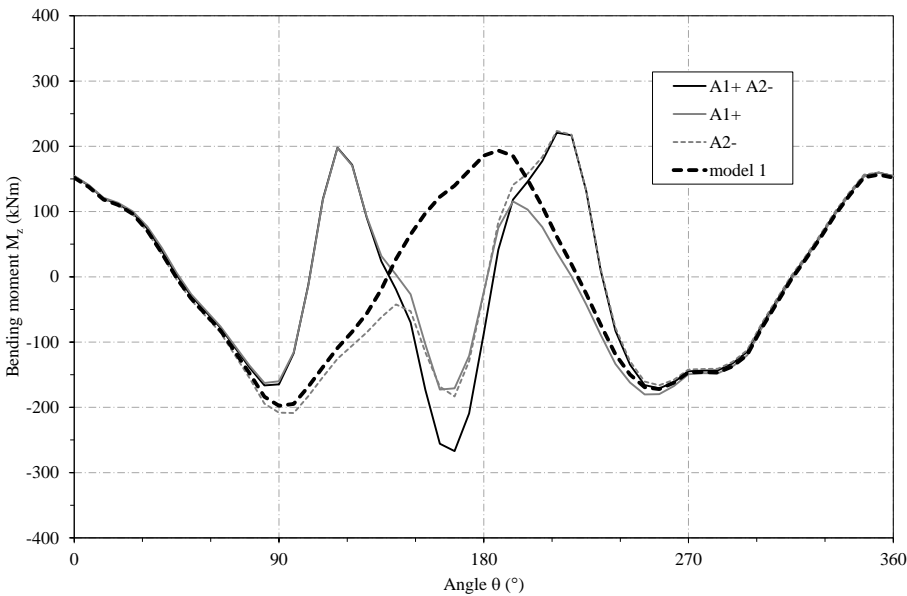


Figure 7.26. Impact of imperfect installation of segments A1 and A2 on bending moment M_z in ring 0.

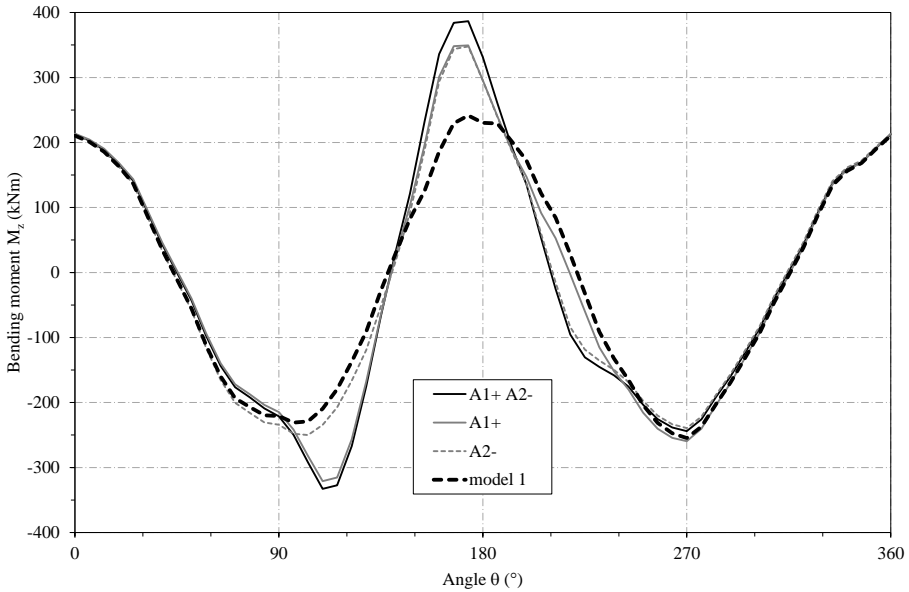


Figure 7.27. Impact of imperfect installation of segments A1 and A2 on bending moment M_z in ring -1.

7.3.5 Conclusion

In the previous sections, the impact of the presence of a local imperfection in an individual joint or segment was investigated, as opposed to the first part of this chapter, where the monitored installation imperfections of an entire tunnel section were implemented. The results have indicated that the inaccurate assembly of just a single joint or segment might already cause a significant deviation of the sectional forces, both in the ring where the imperfection is present and in the adjacent rings. The impact varies with the type of installation imperfection and the location in the tunnel section. The effect is most evident when the joint irregularity is located close to the top or invert and to the sides of the tunnel section. When multiple imperfections are present at the same time, their combined influence is not always larger than for a single imperfection. Only when adjacent segments are inaccurately assembled, a stronger impact might be perceived at the location of the joint between both segments. Nevertheless, all results have proven that virtually every joint imperfection that originates from inaccurate segment installation, remains present in the final deformed tunnel shape, at almost its full original magnitude. This corresponds with the observations of the laser scanning measurements.

In the present study, the implementation of imperfections is limited to one central tunnel ring, flanked by perfectly circular rings. In order to study the combined effect of imperfections in adjoining rings, future research should model such inaccurate installation in multiple neighbouring rings. The magnitude of the imperfections can either be based on future monitoring results, where the installation imperfections of multiple adjoining tunnel sections are measured, or an extensive statistical approach can be applied, combining theoretical imperfections in neighbouring rings.

Chapter 8

Observation of the tidal influence

8.1 Introduction

The trajectory of the Liefkenshoek tunnel crosses River Scheldt, whose water level variation is linked to the tides of the North Sea. This variation has a direct influence on the hydrostatic pressures acting on the tunnel lining. As a result, the impact of the river tide was noticed in various monitoring results after construction. Apart from the constant fluctuation of stresses in the concrete lining, a vertical displacement of the tunnel was observed in response to the river tide. At the centre of the river, levelling measurements showed a decrease of the tunnel level at high tide by a value of about 10 mm with respect to low tide. In literature, only one example was found as the first rail tunnels below the Hudson River in New York City shifted with tide in the silty river bed (Hewett & Brown, 1910; Jacobs, 1910). For an average tide of about 1.50 m, the magnitude of the tunnel oscillation equalled approximately 3 mm. However, no clear explanation of the tidal movements was found, other than the statement that the increased volume of water at high tide pushed the tunnels down, and they would spring back up when the tide receded (MacLowry, 2014). Hence, a detailed investigation of the effect of the river tides on the Liefkenshoek rail tunnel was carried out.

8.2 Tidal characteristics of River Scheldt

In order to assess the response of the tunnel lining to the tidal fluctuations, the detailed characteristics of the river tide need to be determined. Approximately every 12 hours the water level in the river varies between the minimum and maximum values, shifting by three-quarters of an hour per day. The regular variation of the water level is between +6.0 m TAW and -0.5 m TAW, with TAW (“Tweede Algemene Waterpassing”) being the Belgian reference height level. However, a storm surge with an additional water level variation of 2 m had to be considered as well. Figure 8.1 shows the monitored water levels of River Scheldt at the location of the Liefkenshoek crossing for October and November 2012 (Hydrological Information Centre, 2015).

Since more than 50 years these water levels are being monitored at the exact location of the Liefkenshoek crossing. From these data, the common water level variation Δh_w between low and high tide can be studied. Figure 8.2 shows the evolution of the yearly average Δh_w since 1960. Where the average rise of the water level at high tide equalled around 4.70 m in the sixties, this value has clearly increased over the past decades. This change is related to the bathymetric development of the Scheldt estuary, where a second main river channel came into existence after a major storm surge in the fifties (Taverniers *et al.*, 2013). Furthermore, around 1970 the first widening program of the fairway was initiated, to improve the accessibility of the Port of Antwerp. Since 2010, when construction of the Liefkenshoek tunnel began, the yearly average Δh_w exceeds 5.20 m, half a meter more than at the start of the measurements. Therefore it was decided to only use the tidal data obtained from 2010 to 2014 in the current investigation of the tidal effect.

Figure 8.3 shows the histogram of the water level variation Δh_w between low and high tide for the time frame 2010-2014. The magnitude of Δh_w varies with the daily tidal levels due to astronomical parameters, wind effects etc. A minimum value of 2.81 m for Δh_w was monitored during these five years, while the maximum value that was witnessed equals 6.98 m. On average the rise in water level of River Scheldt between low tide and high tide equals $\Delta h_{w,av} = 5.24$ m, with a standard deviation $s = 0.67$ m. The distribution shows a small negative skewness of -0.38, which implies that the tail on the left side is somewhat longer than the right side. Considering the large amount of observations ($n = 7056$) and the rather slight skewness of the distribution, a normal distribution can be assumed with adequate reliability. In that case approximately 99.7% of the observations fall within $3s$ of $\Delta h_{w,av}$, which serves as a perfect range to estimate

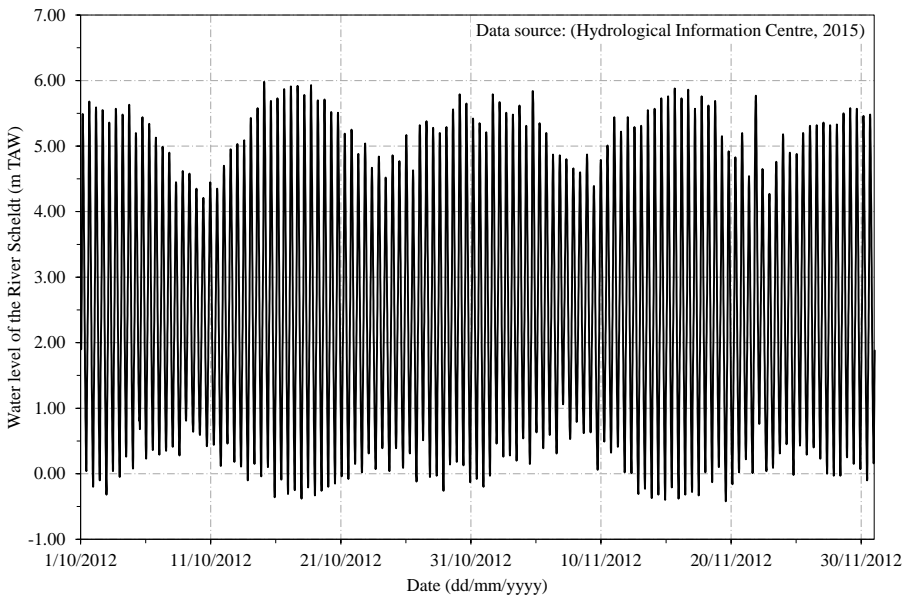


Figure 8.1. Monitored water levels of River Scheldt (data from Hydrological Information Centre (2015)).



Figure 8.2. Yearly average water level variation between low and high tide.

the extreme values of Δh_w (Moore *et al.*, 2009). Therefore, the maximum value $\Delta h_{w,max}$ that is to be expected, equals $\Delta h_{w,av} + 3s = 7.24$ m. The minimum value $\Delta h_{w,min}$ based on the 99.7% interval equals $\Delta h_{w,av} - 3s = 3.23$ m.

Finally, Figure 8.4 shows the histogram of the time between low tide and high tide for the period 2010-2014. It can be observed that the rising tide shows a shorter time interval to reach the maximum water level than the receding tide to reach the low water level. On average, the time between low tide and subsequent high tide equals 5 hours and 39 minutes (5h39'), while an average of 6 hours and 45 minutes (6h45') separates high tide from the following low tide. When no distinction is made between rising and receding tide, an average time difference of 6 hours and 12 minutes (6h12') can be assumed between subsequent low and high tides.

8.3 Description of the measurement set-up

8.3.1 Introduction

To verify the structural behaviour of the newly constructed tunnel lining, several measurement sections were included in the Liefkenshoek project. In particular, two of these cross-sections were located below River Scheldt, as was illustrated in Figure 3.2. At a distance of 2520 m from the entrance shaft, ring number 1400 was monitored both in tunnel north and south (further in the text referred to as N1400 or S1400 respectively). At the exact location below the centre of the river, another measurement section was present in ring number 1497 in tunnel north (N1497) and in ring 1500 in tunnel south (S1500). Again, two main methods were used for the monitoring of the individual tunnel rings: strain measurements and ovalisation measurements using laser scanning. In addition, regular levelling measurements of the tunnel installations were performed by the design office (TUC RAIL Ltd., Brussels, Belgium) along the entire length of the bored tunnel alignment. The three components of the monitoring program assured a clear identification of the structural response of the tunnel lining to the fluctuating water levels in River Scheldt. The following paragraphs give an overview of the main methodology of each measurement technique.

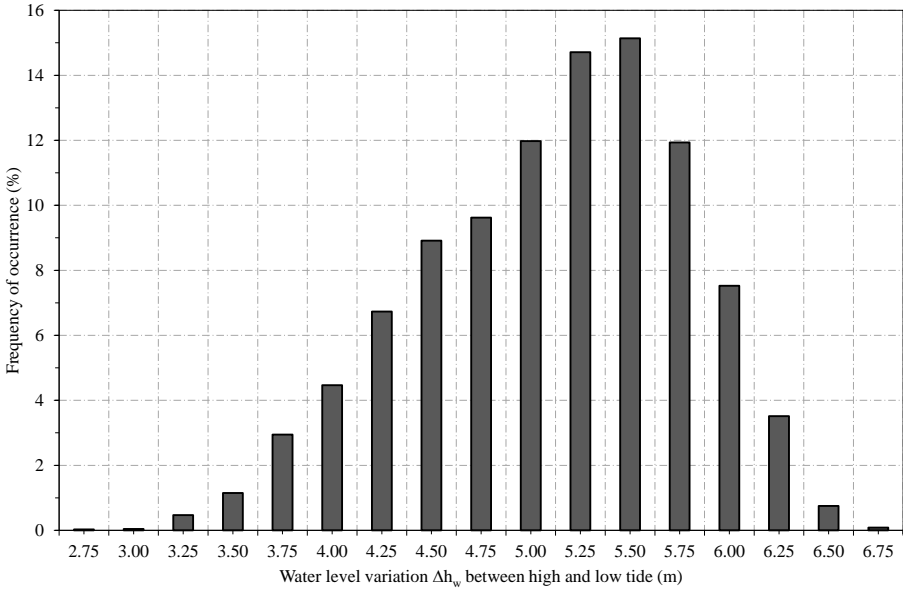


Figure 8.3. Histogram of water level variation between low and high tide for 2010-2014.

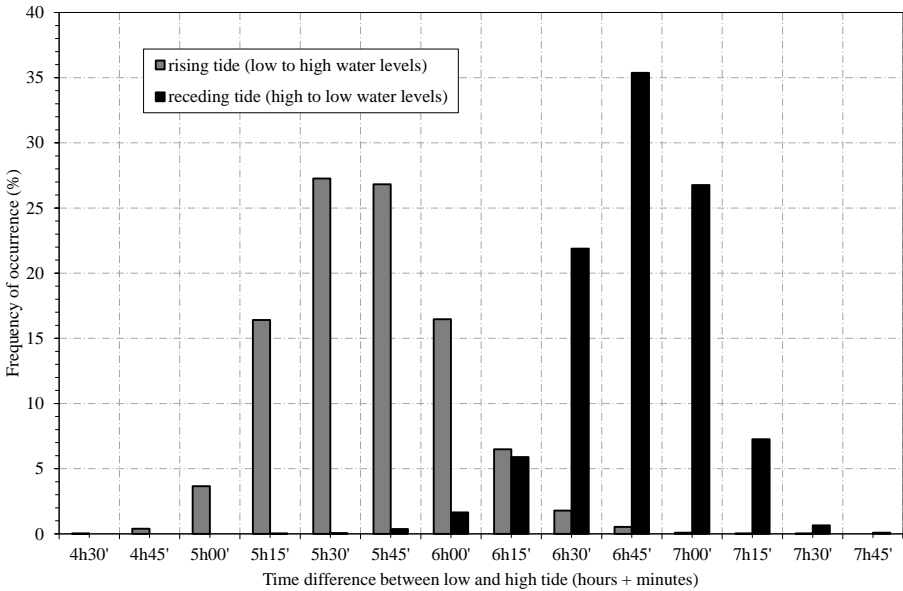


Figure 8.4. Histogram of time difference between low and high tide for 2010-2014.

8.3.2 Strain measurements

The strain measurement set-up was described in detail in Chapter 3. Strains were monitored continuously for several years, starting from the moment immediately after ring assembly. The tidal effect was registered during this entire monitoring period. For a detailed study of the influence of the river tide, a temporary increase of the measurement frequency was applied, as described in section 8.4.3. No further adjustments were made to the strain monitoring set-up or methodology.

8.3.3 Ovalisation measurements

For the investigation of the tidal effect on the tunnel structure, additional control measurements using laser scanning were performed between low and high tide to verify whether the tunnel response incorporates a cross-sectional deformation of the lining as well. For these control measurements, the laser scanner was mounted on a tripod in the invert of tunnel sections N1497 and S1500, as shown in Figure 8.5. The resulting point cloud is shown in Figure 8.6. The applied methodology is identical to the procedure described in section 3.3. However, since the last control measurement at these sections, the concrete rail bed was constructed and the tunnel surface was covered by a fire-resistant spraying. Since the reference targets on the tunnel elements, placed during assembly of the tunnel rings, were now covered at the time of the additional measurements, new reference marks needed to be installed. Therefore, in the vicinity of the measurement sections, six targets were glued on the concrete rail bed, having a much smoother surface compared to the fire-resistant coating.

In addition, new experimental standard deviations were determined for a single laser scanning set-up, in order to quantify the impact of the new surface material and overall tunnel conditions. Using a methodology similar to section 3.3.4, one of the tunnel sections was measured multiple times within a time frame of approximately 20 minutes, assuming that no significant deformations occurred in this short time span. Following this methodology, an experimental standard deviation $s'_c = 0.44$ mm was established for the additional control measurements using one scanning position, taking into account the repositioning of the laser scanner between each measurement (Nuttens *et al.*, 2014).

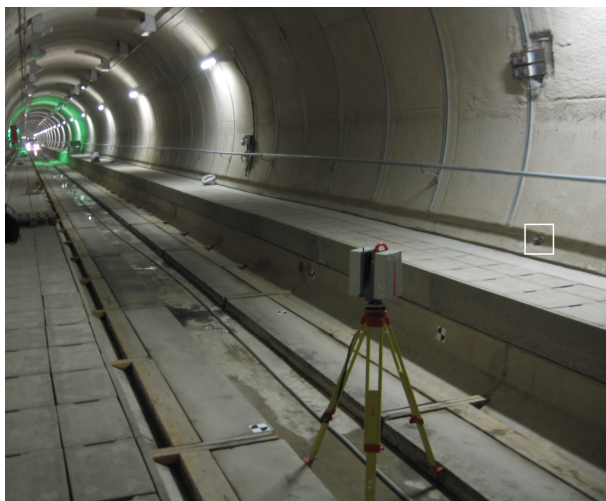


Figure 8.5. Laser scanner set-up during monitoring of tidal fluctuations.

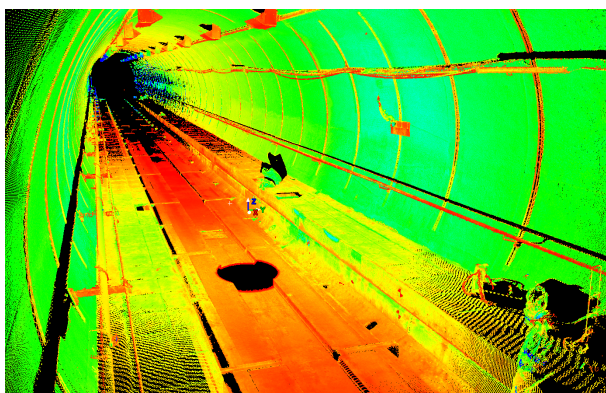


Figure 8.6. Point cloud obtained during a laser scan of the monitored tunnel section.

8.3.4 Levelling measurements

As part of the quality inspection after tunnel construction, several levelling measurements were performed at different points in time to verify the established height level of the newly constructed tunnels. In order to obtain accurate data of the tunnel level, specific topographical bolts were fixed onto the tunnel segments every 25th tunnel ring. Their position is situated at a height of about 2 m above the tunnel invert. On the right side of Figure 8.5, the location of such a bolt is indicated by a square. At specified time intervals, the levels of the bolts are measured using a Leica DNA10 digital level (Leica Geosystems

AG, Heerbrugg, Switzerland) with a standard deviation of 0.9 mm/km double levelling. All measurement series were started from an assumed stable reference point outside the river boundaries, where a link with the surface level could be made through one of the evacuation shafts. Subsequently, the levels of consecutive bolts are measured one by one, until the target location is reached. Finally, in order to reconnect with the reference starting point, the levelling measurement ends with retracing its steps and registering the bolt levels in the opposite direction. In this way, an accurate topographical system can be established that enables to link the tunnel levels with the reference system above ground.

Table 8.1 gives an overview of the five levelling measurements (LM 1 to 5) that were performed below the river and this for both tunnels. The centre of the river was approached either from the left or right riverbank. Furthermore, the time of low and high tide and the corresponding change in water level of River Scheldt is indicated in Table 8.1 for each measurement.

Table 8.1. Overview of levelling measurements.

| Measurement | Date | Tunnel | River bank | High tide ¹ | Low tide ¹ | Δh_w (m) |
|-------------|------------|--------|------------|------------------------|-----------------------|------------------|
| LM 1 | 12/04/2012 | south | right | 8:05 | 15:05 | 5.59 |
| LM 2 | 19/06/2012 | south | left | 4:10 | 10:50 | 5.38 |
| LM 3 | 20/06/2012 | north | left | 4:50 | 11:25 | 5.37 |
| LM 4 | 21/06/2012 | north | right | 5:30 | 12:00 | 5.51 |
| LM 5 | 31/10/2012 | south | left | 16:05 | 10:50 | 5.43 |

Notes: ¹Time in CET.

Data source: (Hydrological Information Centre, 2015)

8.4 Monitoring results of tidal influence

Levelling measurements performed at various points in time showed a discrepancy up to 10 mm in the monitored levels of the tunnel structure below the River Scheldt. As the difference was too large to contribute to errors in the measurement procedure and as it only occurred below the river, further investigation was advised. Since the River Scheldt showed a variation in water level between the different measurements due to tidal fluctuations, the disagreement in levelling results was attributed to the river tides. In order to obtain full confirmation of the correlation between tunnel level and river tides, specific strain, ovalisation, and levelling measurements were combined during a special measurement day on October 31st, 2012. On this occasion, the structural

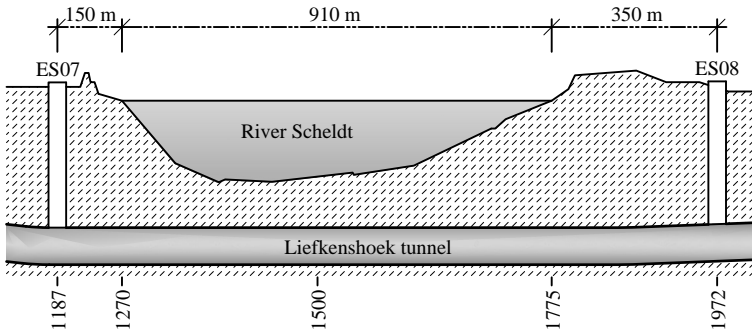


Figure 8.7. Schematic longitudinal profile of the tunnel section below River Scheldt.

response was closely monitored at the location of ring 1500 in tunnel south, situated below the centre of the River Scheldt. In order to observe possible deformations between high and low tide, the combined monitoring session lasted from approximately 8:30 to 18:30. Consequently, the resulting data included the situation at low tide (10:50) and high tide (16:05). The results of this monitoring program are discussed in the following paragraphs.

8.4.1 Levelling measurements

As specified in the description of the measurement set-up, specific levelling bolts were fixed onto the tunnel segments every 25th tunnel ring. In order to allow for multiple measurements in the time interval between low and high tide, only one out of two bolt levels was measured during the special measurement day. Consequently, levelling measurements were performed every 50 rings between an assumed stable reference point at ring 1100 and the centre of the River Scheldt at ring 1500. Figure 8.7 shows the tunnel section below the river with an indication of ring numbers. As ring 1100 is located outside the river boundaries and showed no tidal influence in previous levelling measurements, the assumption as reference point was considered justified.

Over the course of the measurement day, eight levelling measurements were performed, the first at 9:45 (1h05' before low tide) and the final one at 17:30 (1h25' after high tide). The obtained results of the tunnel level, indicated by the bolts fixed to the tunnel lining, are presented in Figure 8.8. Due to the downward slope of the tunnel alignment toward the river, the elevation levels of the first two measurement points are not incorporated within the presented range of the y-axis. Including those data points would significantly increase the range needed on the y-axis, and as a result reduce the graph's

readability, without contributing to the understanding of the tidal influences on the monitored tunnel levels. Nonetheless, a significant fluctuation of the tunnel level can be observed below the River Scheldt over the various time values. The first three curves (9:45, 10:50, 12:05), corresponding to three intervals around low tide, are almost entirely identical. Over the following hours, a stepwise descent of the curves can be observed towards the minimal level measured at 16:25, nearly corresponding to high tide. Afterwards, the measured values at 17:30 show a reverse trend of increasing tunnel level. Consequently, extreme values of the tunnel level below River Scheldt are found at low and high tide.

Figure 8.9 shows the calculated differences in bolt levels between high and low tide, based on the measurement data of Figure 8.8. Since ring 1100 was chosen as fixed reference point, the difference at this location equals zero. It can be observed that the tunnel level remains almost perfectly stable in the vicinity of evacuation shaft 7 (ES07), which is constructed as a rectangular shaft of diaphragm walls between both tunnels. A large shift occurs between measurement points at rings 1250 and 1300, which corresponds to the location of the river bank. From ring 1350 to the centre of the River Scheldt at ring 1500, the difference between low and high tide remains steady at 10 mm.

These results show that the tunnel levels interact with the water level fluctuations of the River Scheldt. The monitored levels reach a maximum value at low tide, while the lowest tunnel levels correspond to high tide, with a maximum difference of 10 mm occurring between high and low tide below the major part of the river. The results show no indication of a time delay between the river tide and the corresponding structural response. Furthermore, the transition between the tunnel section showing none or negligible tidal influence and the affected area below the river appears to be constrained to a relatively small section of about 50 tunnel rings, corresponding to 90 m. A detailed investigation of this area could be performed, with measurement points every couple of rings, to clearly identify the transition zone. The preferred outcome of this analysis would be a gradually increasing difference in tunnel level between high and low tide, rather than a local variation in only a few tunnel rings or joints, most likely situated at the river bank. However, the general slope of the curve in Figure 8.9 tends to confirm the former.

Figure 8.10 displays the calculated differences in tunnel levels between high and low tide for all five levelling measurements. It can be observed that the tunnel level remains almost perfectly stable at a distance of about 100 m outside the riverbanks. At the centre of River Scheldt, the tunnel level decreases at high tide by a value of about 10 mm with respect to low tide.

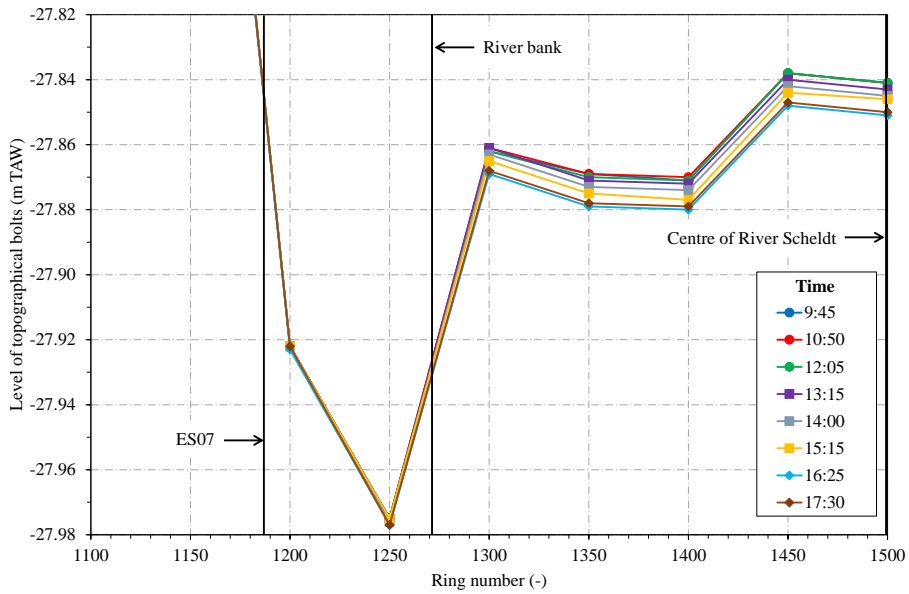


Figure 8.8. Result of levelling measurements of tunnel south below River Scheldt.

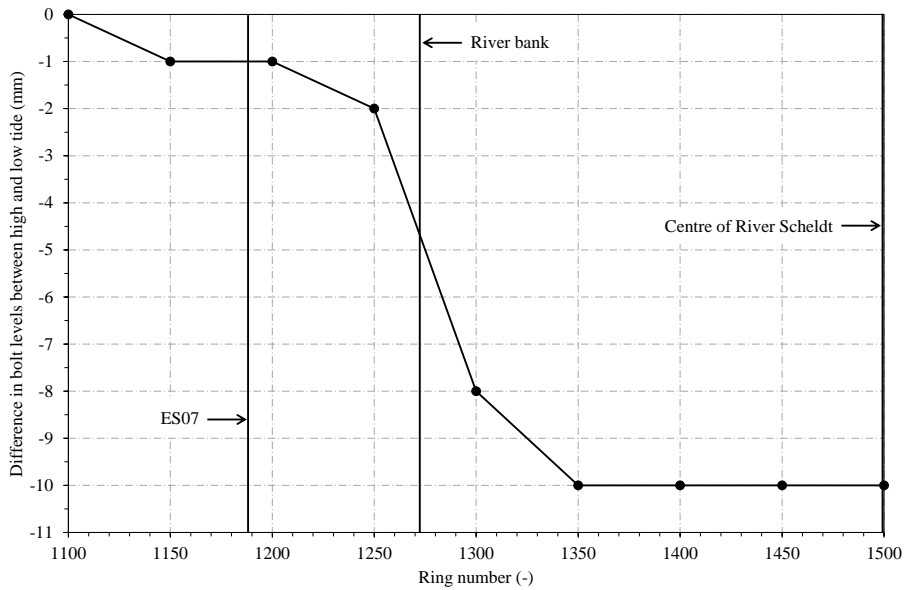


Figure 8.9. Difference in tunnel level between high and low tide below River Scheldt.

8.4.2 Ovalisation measurements

Laser scanning measurements were performed every hour in both tunnels during the scheduled time frame and additionally at the specific instants corresponding with high and low tide. Figure 8.11 shows the comparison of the ovalisation measurements at low tide and high tide for ring 1500 in tunnel south. The difference between both measurements is plotted against the theoretical circular cross section, taking into account that all deviations are 120 times enlarged. It can be observed that for most of the tunnel section, the plotted differences between the measurements at low and high tide show no significant deviations or changes in shape of the tunnel section. The 95% significance levels of $2s'_c\sqrt{2} = 1.24$ mm (shaded area) can be taken as the threshold for this determination. However, the results also show a part with larger deviations located on the left pathway. This side part is covered with individual concrete tiles, which can easily have been displaced between measurements due to people passing by. Furthermore, there are some smaller areas on the rail bed (lower part of the tunnel section) with deviations outside the 1.24 mm boundaries, but these are attributed to the high-water-pressure cleaning of the rail bed that occurred between both measurement times and the loose wooden beams at the bottom of the rail bed for the truck passages.

These results on the cross-sectional deformation of the tunnel section do not show the change in elevation of the levelling bolt, installed at the same tunnel ring. The change in elevation of this bolt is about 10 mm between low and high tide, as previously illustrated in the results of the levelling measurements. The reason for this apparent inconsistency between both monitoring techniques will be explored in section 8.5.

8.4.3 Strain measurements

Strain measurement results

As corresponding measurement sections were installed in both tunnel tubes at approximately identical locations, strain response could be monitored closely in two sections below the River Scheldt: ring 1497 in tunnel north and ring 1500 in tunnel south. As a result of continuing construction works after the installation of the strain monitoring set-up, these two sections unfortunately showed a large amount of erroneous strain results at the time of the special measurement day. This can be caused either by damaged strain gauges, for instance, during concrete casting, or more likely by damaged cables for data

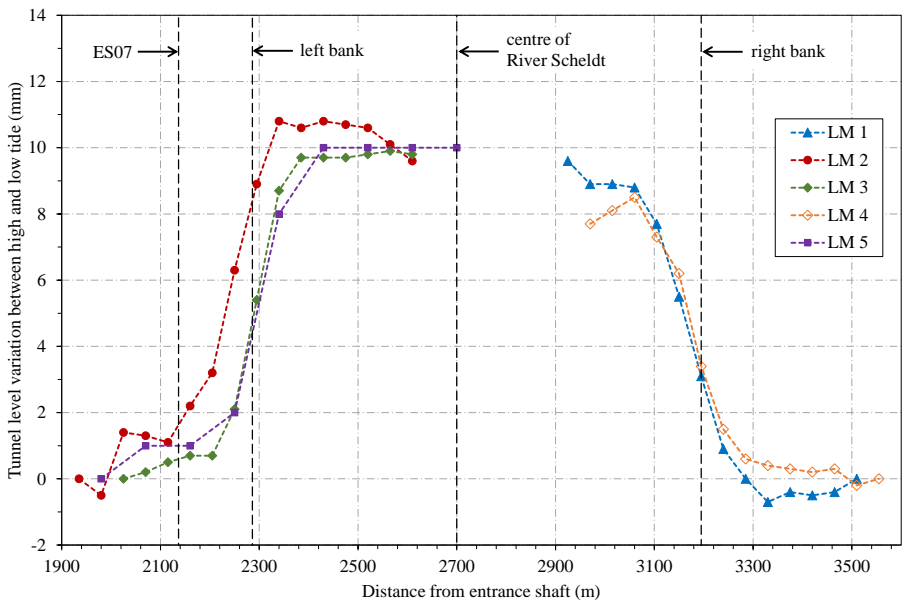


Figure 8.10. Differences in tunnel level between high and low tide below River Scheldt.

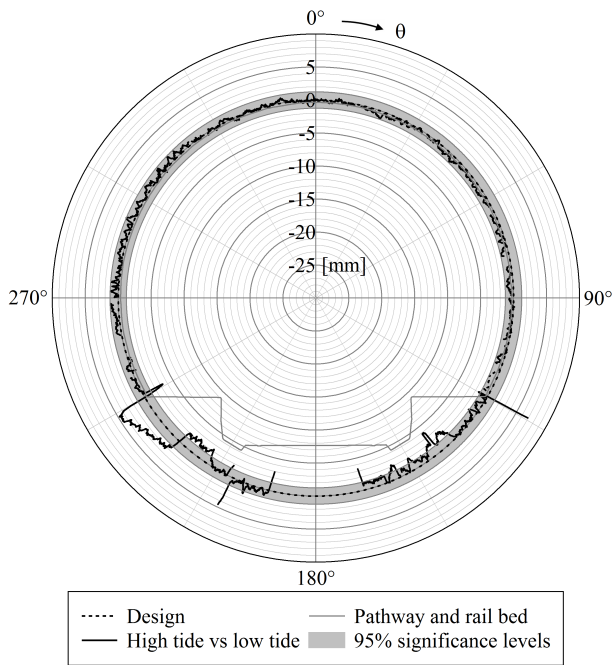


Figure 8.11. Laser scanning results below River Scheldt: comparison of measurements at low and high tide.

transfer. The latter can be the result of the wheels of the TBM backup systems and construction site traffic repeatedly crossing the data cables or can be due to damage during construction of the concrete slab for the railway tracks. In both tunnel sections below the centre of the river, only four out of the original 16 installed strain gauges (25%) were still intact at this time. Figure 8.12 shows the strain results of the active strain gauges in both sections during the scheduled time frame of the special measurement day. At this time after assembly of the tunnel lining, the sampling frequency of the continuous strain measurements was reduced to one sample every two minutes. During the special monitoring session however, this frequency was temporarily increased to one sample every 30 s. In order to clearly illustrate the tidal influence on the obtained strain data, the start of the measurements began around 9:00 and it was set as zero value; strain results are plotted relatively to this initial state.

Figure 8.12 allows a clear observation of the influence of the water level fluctuation of the River Scheldt on the strain results in both tunnel sections. Strains tend to increase at low tide, indicating a relaxation or general decrease in compression of the tunnel rings. A larger head of water at high tide in turn causes a larger uniform compression of the tunnel rings. Notwithstanding a ground cover of about 10 m between the tunnel and the river, which could cause a potential delay of the strain response in correspondence to the rise and fall of the water level, extreme values of the strain curves coincide with low and high tide in the River Scheldt. Consequently, strain results of the tunnel lining show no time shift between the river tides and the structural response.

Figure 8.12 also illustrates that the strain response to the tidal fluctuations is not identical for all strain gauge locations. Although the start of the measurements was set as zero value to clearly show the effect of the tidal influence, the water level fluctuation is only one of many loads acting on the tunnel lining and regular variations in the strain state are still present in the depicted graphs. For example, general results show that the strain gauges attached to the inner concrete surface show more daily fluctuations than the internal gauges attached to the reinforcement (see section 4.1.2). The difference in the strain curves can also be due to unequal supports in the segment joints, as a result of which the pressure distribution over the lining thickness shifts between segments. This may cause an unequal response of strain gauges to a load increase or decrease.

At the end of the special monitoring session, the curves in Figure 8.12 did not exactly return to zero value. This observation is again due to previous considerations regarding diverse strain behaviour. Earlier in the text, Figure 4.12 showed the obtained strain results in measurement section N1497, over the time

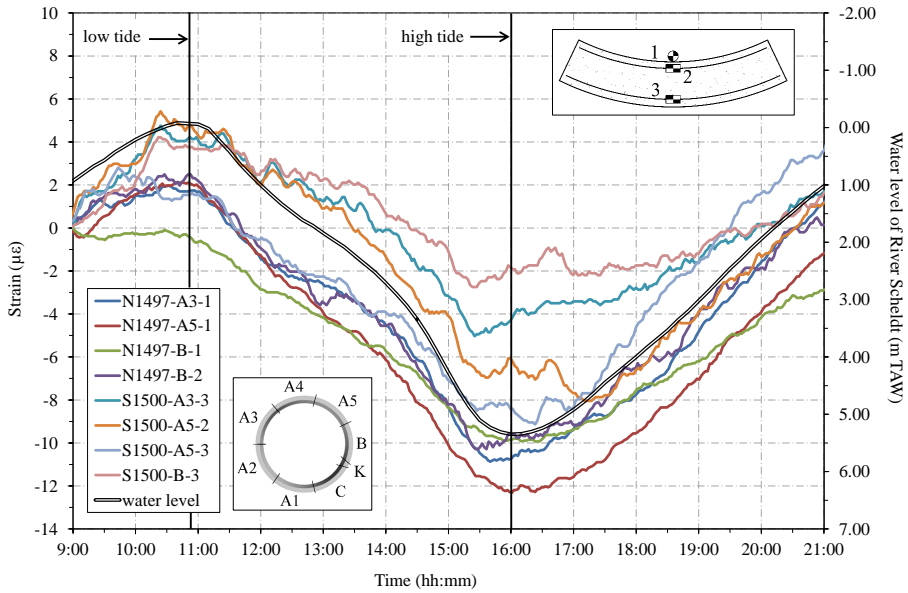


Figure 8.12. Tidal fluctuation of strain results below River Scheldt.

frame of two weeks, around one month after ring assembly. From this graph, it can be observed that periodic half-daily fluctuations occur in the stabilized strain results due to the tidal effects, without the presence of a general secondary drift in the monitored data. Furthermore, identical behaviour is found for every gauge location, as a confirmation of the results depicted in Figure 8.12. Increasing compressive stresses at rising water levels apply for all measurement points, indicating that no significant bending moment is induced in the tunnel lining by the tidal fluctuation. In conclusion, the rise and fall of the water level of the River Scheldt only causes a uniform compression (high tide) or relaxation (low tide) of the tunnel lining below the river, based on the strain measurements. Similar to the results of the levelling measurements, the strain data show no time delay between the tide and the structural response of the segmental lining.

The observation that the rise and fall of the water level of River Scheldt causes a uniform compression (high tide) or relaxation (low tide) of the tunnel lining, can be made for all monitored cross-sections below the river. Figure 4.12 showed results from ring N1497 in tunnel north, an identical response being found for the corresponding section S1500 in tunnel south, as well as for the measurement sections N1400 and S1400 closer to the riverbank.

Correlation between water level variation & monitored strains

The observed strain fluctuations in the concrete segments are caused by the tidal changes in water pressures acting on the tunnel lining. When larger variations in the water level of the river occur between low and high tide, larger strain variations and corresponding stress fluctuations are monitored in the tunnel lining. Since the strain gauges were monitored continuously for several years, sufficient data was available to study the relationship between the water level variation Δh_w and the strain variation $\Delta \epsilon$. An example of an obtained point cloud presenting the monitored absolute values of $\Delta \epsilon$ in relation to Δh_w can be found in Figure 8.13. The displayed results in this figure correspond to the inner rebar of segment A3 of tunnel ring N1497. As mentioned, the strain variations show an increasing trend with the water level variation in the river. However, a significant spread is present in the collection of data points. This is due to the fact that regular variations in the strain state (such as temperature effects) were not filtered from the measurement results. In order to still be able to easily compare the monitored values with the results from finite element calculations in the following paragraphs, the point cloud was fitted with a linear trend line, as depicted in Figure 8.13.

The same method can be applied to determine a linear correlation between Δh_w and $\Delta \epsilon$ for all strain gauges installed below River Scheldt. The linear function can be defined according to equation 8.1, where C_1 is a constant that needs to be determined for each strain gauge. In Table 8.2 the value of C_1 is given for measurement sections N1497 and S1500 below the centre of the river. Table 8.3 presents the same parameters for measurement sections N1400 and S1400, which had strain gauges installed not on the reinforcement bars, but only at the inner concrete surface.

$$\Delta \epsilon = C_1 \Delta h_w \quad (8.1)$$

Tables 8.2 and 8.3 also list the root mean squared error (RMSE) for each trend line, which is an estimate of the standard deviation. Unfortunately, in time several strain gauges in the measurement sections showed erroneous results, for example due to damage as a result of continuing construction works after the installation of the monitoring set-up. As these erroneous results were discarded, Tables 8.2 and 8.3 only present reliable data from strain gauges that remained intact for the entire monitoring period.

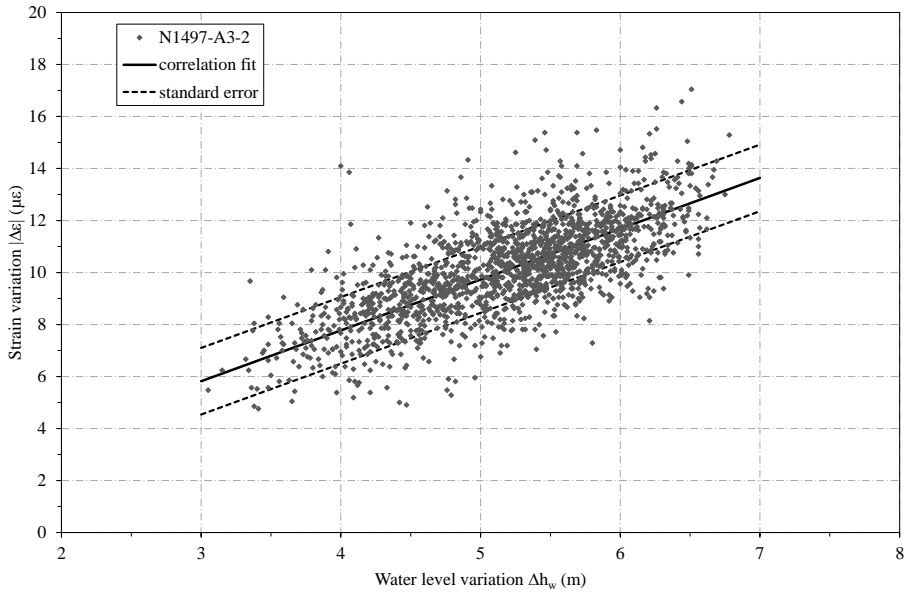


Figure 8.13. Strain variation in monitored strain gauge N1497-A3-2 in relation to water level variations.

8.5 Discussion

Deformations of the tunnel lining corresponding to the stress fluctuations discussed in section 8.4.3 are too small to be perceived by the ovalisation measurements. The change in tangential normal force due to the variation in water level results in deviations of the tunnel radius in the order of magnitude of 0.05 mm. It was not possible to detect such a difference between high and low tide in the results of the ovalisation measurements, as it lies well within the 95% significance levels of those measurements.

For the interpretation of the ovalisation results, it is important to remark that the origin of the coordinate system is determined on a fixed distance from a reference mark on the concrete rail bed (Nuttens, 2014). However, variations may occur in the absolute location of this origin, even without deformations in the shape of the section. This implies that deformations of the tunnel section are plotted to a fixed origin with a possibly variable absolute position. Therefore, absolute displacements of the cross section as a whole, for example a vertical translation, cannot be observed by the ovalisation measurements, since the measurement device and the corresponding local coordinate system are subjected to the same displacement as the tunnel lining.

Table 8.2. Best fit parameters of strain variations in monitored strain gauges in relation to water level variations: tunnel sections N1497 and S1500.

| Strain gauge | Ring N1497 | | Ring S1500 | |
|-----------------|---------------------------|--------------------------|---------------------------|--------------------------|
| | C_1 ($\mu\epsilon/m$) | $RMSE$ ($\mu\epsilon$) | C_1 ($\mu\epsilon/m$) | $RMSE$ ($\mu\epsilon$) |
| A2-1 | 2.267 | 0.46 | 2.003 | 2.38 |
| A2-2 | - | - | 2.887 | 3.16 |
| A2-3 | 1.631 | 1.82 | - | - |
| A3-1 | 1.923 | 1.82 | 2.401 | 1.25 |
| A3-2 | 1.955 | 1.29 | - | - |
| A3-3 | 1.516 | 1.85 | 1.714 | 0.78 |
| A4-1 | 1.744 | 3.12 | 1.268 | 1.80 |
| A4-2 | 1.556 | 2.20 | 1.159 | 1.16 |
| A4-3 | 1.635 | 2.33 | 2.526 | 3.31 |
| A5-1 | 2.182 | 2.31 | 1.427 | 1.44 |
| A5-2 | 2.092 | 1.15 | 1.991 | 1.11 |
| A5-3 | 1.264 | 1.82 | 1.678 | 1.08 |
| B-1 | 1.541 | 2.82 | 2.231 | 2.79 |
| B-2 | 2.136 | 1.47 | - | - |
| B-3 | - | - | 1.396 | 0.99 |
| C-1 | - | - | - | - |
| C-2 | 1.295 | 1.23 | - | - |
| C-3 | 1.897 | 1.26 | - | - |

Table 8.3. Best fit parameters of strain variations in monitored strain gauges in relation to water level variations: tunnel sections N1400 and S1400.

| Strain gauge | Ring N1400 | | Ring S1400 | |
|-----------------|---------------------------|--------------------------|---------------------------|--------------------------|
| | C_1 ($\mu\epsilon/m$) | $RMSE$ ($\mu\epsilon$) | C_1 ($\mu\epsilon/m$) | $RMSE$ ($\mu\epsilon$) |
| A1-1 | 1.286 | 0.37 | 2.452 | 1.32 |
| A2-1 | - | - | 2.741 | 0.98 |
| A3-1 | 2.093 | 1.07 | - | - |
| A5-1 | - | - | 2.513 | 1.58 |
| B-1 | 1.661 | 0.37 | 2.272 | 0.60 |
| C-1 | 1.883 | 0.52 | 2.079 | 0.58 |

Considering the extremely small deformations of the tunnel lining corresponding with the strain data and the absence of significant cross-sectional deformations in the ovalisation results, the monitored difference between low and high tide in the levelling measurements without doubt cannot be assigned to a relative deformation (ovalisation) of the tunnel cross section. As a result, the 10 mm displacement can only be due to a vertical shift of the tunnel lining as a whole, which is not perceptible by the ovalisation measurements. The combined monitoring results leave no room for any other interpretation of the lining deformations than a vertical translation of the complete tunnel section.

Chapter 9

Clarification of the tidal movements

9.1 Introduction

In order to obtain a clear understanding of the tidal response of the Liefkenshoek tunnel, several possible hypotheses are investigated as the causes of the vertical displacements. This chapter presents the outcome of analytical settlement calculations and finite element calculations using both a beam model of the tunnel lining as well as the detailed 3D model. The results are compared to the observations of the monitoring program, discussed in the previous chapter. Consequently, the origin of the tidal oscillation of the Liefkenshoek tunnel is identified and the impact of the water level variation on the segmental lining can be evaluated. Thus the basic understanding of the behaviour of a shield tunnel lining subjected to tidal fluctuations may be improved.

9.2 Impermeability of Boom clay

9.2.1 Influence depth of tidal changes

Due to the tidal fluctuations in River Scheldt, the pore water pressures in the underlying soil layers constantly vary in order to adapt to the new water level. However, the pressure variation in the subsoil can be significantly attenuated, as indicated by field measurements in literature (Bennett & Faris, 1979; Okusa & Uchida, 1980; Zen & Yamazaki, 1991; De Rouck & Van Damme, 1996).

As a result, effective stress variations are introduced in the riverbed (Zen & Yamazaki, 1991). Up to date, various theoretical models have been developed to describe this damping effect for wave-induced pore pressure variations (Mei & Foda, 1981; Okusa, 1985; Jeng, 2003; Liu & Jeng, 2007). Many of them are based on Biot's poro-elastic theory (Biot, 1956a,b), which includes a generalisation to three dimensions of the theory of consolidation developed by Terzaghi (1925).

An analytical model has been developed by De Rouck & Van Damme (1996), based on the Darcy equation and the continuity equation. They found that the pressure variation in the subsoil is attenuated due to a combination of parameters, of which the permeability coefficient appears to be one of the most important. De Rouck & Van Damme (1996) have formulated a differential equation governing the pore water pressure change during one tide as:

$$\frac{\partial^2 u}{\partial z^2} = \frac{\rho_w g}{k E_{oed}} \frac{\partial u}{\partial t} \quad (9.1)$$

In this equation u is the pore water pressure change due to the tide, z is the depth below the riverbed, ρ_w is the specific mass of water, $g = 9.81 \text{ m/s}^2$ is the standard gravity, k is the permeability coefficient of the soil, E_{oed} is the oedometric compression modulus of the soil and t represents time. In the approach leading to equation 9.1, only vertical flow has been considered in the riverbed. As the wavelength of the tidal wave is very large compared to the change in water level, the local water surface can be considered horizontal. Therefore, no pressure variation exists in horizontal direction. Furthermore, as all soil layers are situated below the riverbed, it has been assumed that they are fully saturated. The compressibility of the pore water has been neglected in comparison with the compressibility of the grain skeleton.

Solving differential equation 9.1 is done taking into account the following boundary conditions (De Rouck & Van Damme, 1996):

- a. at the riverbed $z = 0$ and for a fixed horizontal position $x = 0$:

$$u(0, t) = u_0 \cos \frac{2\pi t}{T} = \rho_w g \Delta h_w \cos \frac{2\pi t}{T} \quad (9.2)$$

where T is the period of the tidal wave. According to section 8.2, T equals $5\text{h}39' + 6\text{h}45' = 12\text{h}24'$.

- b. at large depth ($z = \infty$):

$$\lim_{z \rightarrow \infty} u(z, t) = 0 \quad (9.3)$$

This leads to the solution given by equation 9.4.

$$u(z, t) = u_0 e^{-Az} \cos\left(\frac{2\pi x}{L} + \frac{2\pi t}{T} - Az\right) \quad (9.4a)$$

$$u_0 = \rho_w g \Delta h_w \quad (9.4b)$$

$$A = \sqrt{\frac{\rho_w g \pi}{k E_{oed} T}} \quad (9.4c)$$

In equation 9.4a, L represents the real wavelength of the tidal wave. As mentioned before, no influence of the horizontal position x (in the direction of wave propagation) along the riverbed exists for tidal waves. The tidal variation is identical for all positions on the river bottom. Therefore, for simplicity, x can be set to zero.

The influence of the soil characteristics on the variation of the pore water pressures is reflected by the presence of the permeability coefficient k and the oedometric compression modulus E_{oed} in equation 9.4. Laboratory investigation on borehole samples determined the average permeability coefficient to be equal to 2×10^{-11} m/s for the Boom clay layer. According to the theory of De Rouck & Van Damme (1996), the suppression of the river tides is much stronger in the clay layer compared to the sand layers on top, due to the low degree of permeability of the Boom clay and the smaller value of E_{oed} (see Table 2.2). Figure 9.1 gives a visual representation of this principle. The pore water pressures in the permeable layers of tertiary sand are able to closely follow the tidal changes in the river, but the pressure variation decreases rapidly in the impermeable clay layer. Using equation 9.4, the so-called influence depth can be calculated for the Boom clay layer.

The rise in water level between low tide and high tide corresponds to a time interval $t \approx T/2$. Since the pressure variation is studied at the location directly below the occurring water level variation, x equals zero. Figure 9.2 shows the calculated pore water pressure variation $u(z', t = T/2)$ in relation to the depth z' in the Boom clay layer. The pressure variation is plotted as the ratio u/u_0 , with u_0 being the pore water pressure variation at the top of the clay layer. Equation 9.4a yields the envelope for this dimensionless pressure variation as $\exp(-Az')$. Figure 9.2 demonstrates that according to the theory of De Rouck & Van Damme (1996), the river tides with a period $T = 12\text{h}24'$ only influence the pore water pressures in the upper 15 cm of the Boom clay layer. Therefore it is reasonable to state that the Boom clay acts as an impermeable layer, in

which the pore water pressures are not influenced by the tidal fluctuations of the water level in River Scheldt.

However, some remarks have to be made regarding this approach. The differential equation 9.1, formulated by De Rouck & Van Damme (1996), is identical to the solution found by Jacob (1940), using somewhat different notations. The latter was developed for the case of water flow in an elastic artesian aquifer, and serves as a simplification of the more complex theory of three-dimensional consolidation (Biot, 1956a,b). The established theory of Jacob (1940) is based on four main assumptions:

- the total vertical stresses in the soil do not change in time;
- the total soil stresses are the result of effective stresses between individual grains and pore pressures in the water between the grains (Terzaghi, 1925);
- deformations occur only in vertical direction;
- a linear relation exists between vertical effective stresses and vertical strains.

Although several comments can be made regarding the validity of the assumptions, the first one clearly does not apply to the case of the changing tide under investigation, as it implies a constant load on the soil. Nonetheless, the solution of De Rouck & Van Damme (1996) was derived independently from the one of Jacob (1940), for the phenomenon of tidal waves as studied in this research. It was successfully applied to explain monitored values of pore pressures in a seabed, with a similar soil composition as the situation below River Scheldt (sand layers on top of a stiff clay layer at greater depth). Therefore, the results obtained in this section, based on the theory of De Rouck & Van Damme (1996), will be used further in this chapter. However, some caution should still be advised on the applicability of equation 9.1 for this situation. Further research should verify the level of correspondence with other analytical models on wave-induced pore pressures from literature, as cited at the beginning of this section.

9.2.2 Tidal effect on Boom clay

Fluctuating load on the clay layer

The previous section showed that the pore water pressures in the Boom clay layer are not influenced by the river tides. Instead they correspond to the long-

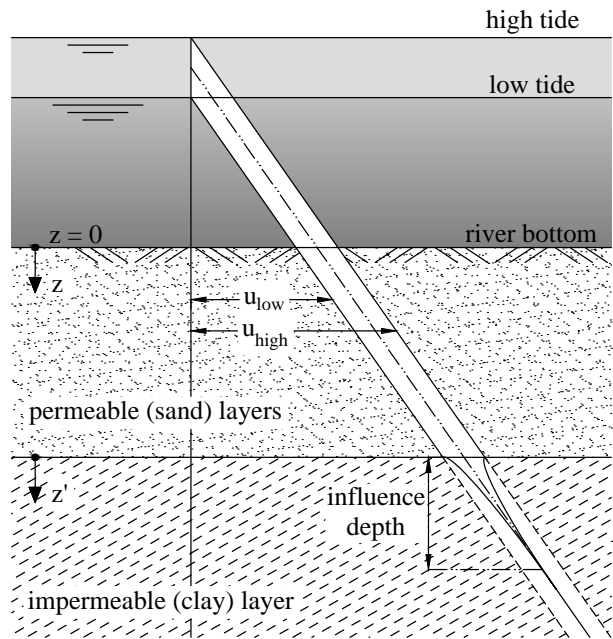


Figure 9.1. Influence depth of pore water pressure variation due to tide action.

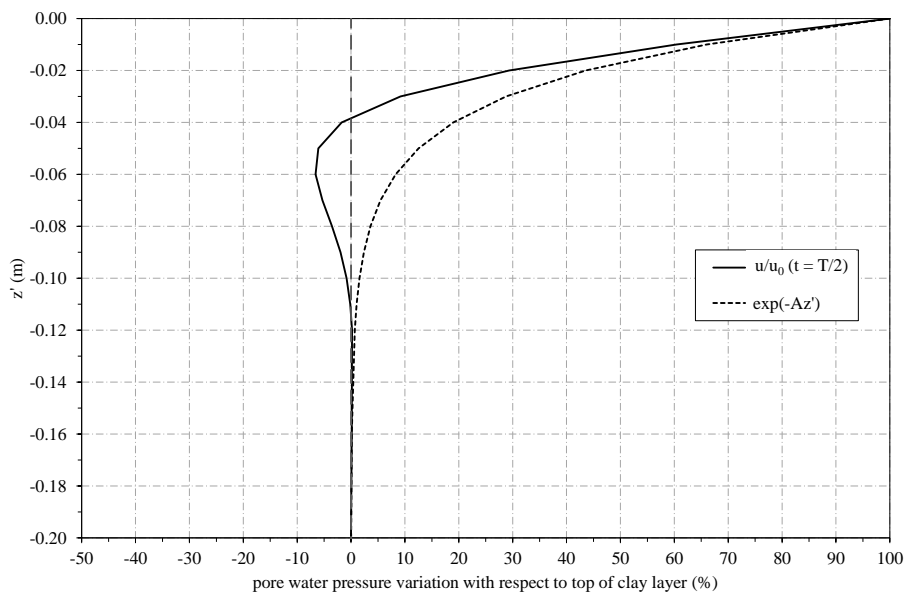


Figure 9.2. Influence depth of pore water pressure variation in clay layer due to tide action.

term mean water level h_{av} in River Scheldt. This leads to ‘overpressures’ in the clay layer at low tide and ‘underpressures’ at high tide. At the same time the impermeability of the Boom clay implies that the rise and fall of the water level in River Scheldt acts as an external surface load on the clay layer. When the mean water level h_{av} in the river is considered as the reference state, the weight of the additional volume of water at high tide constitutes an increase of the vertical load on top of the clay layer. At low tide, the decrease in water level with respect to h_{av} results in a reduction of the vertical load acting on the Boom clay. Consequently, the vertical and horizontal earth pressures in the Boom clay vary accordingly, in order to compensate for the reduced pore water pressure variation.

The implications of the previous paragraph on the degree of impermeability of the Boom clay layer lead to two hypotheses that are examined as a possible explanation of the movement of the Liefkenshoek tunnel in response to the river tides. The validity of both hypotheses is verified by analytical and finite element calculations. It should be mentioned that one hypothesis does not rule out the other.

Hypothesis 1: resulting vertical force on tunnel

As shown in Figure 2.8, the lower part of the tunnel lining is embedded in the Boom clay for a large part of the section below the river. Should the permeability of the grout filling the tail void be limited, then the lower part of the tunnel lining might not encounter the tidal variation of the water pressures. Instead only the fluctuation of the soil pressures will act on the tunnel part in the clay layer. This effect is illustrated in Figures 9.3 and 9.4. Since the coefficient of lateral earth pressure is less than 1, the radial soil pressure variation due to the tides is smaller than the water pressure variation for the case where the tunnel is surrounded by permeable layers. Therefore in hypothesis 1, the lower part of the tunnel lining experiences a reduced pressure variation due to the river tide. Consequently, the combined effect of fluctuating soil and water pressures causes a resulting upward force at low tide and a downward force at high tide compared to the situation where the tunnel is exclusively embedded in permeable layers. As a reaction, a vertical displacement of the tunnel lining might occur in this case.

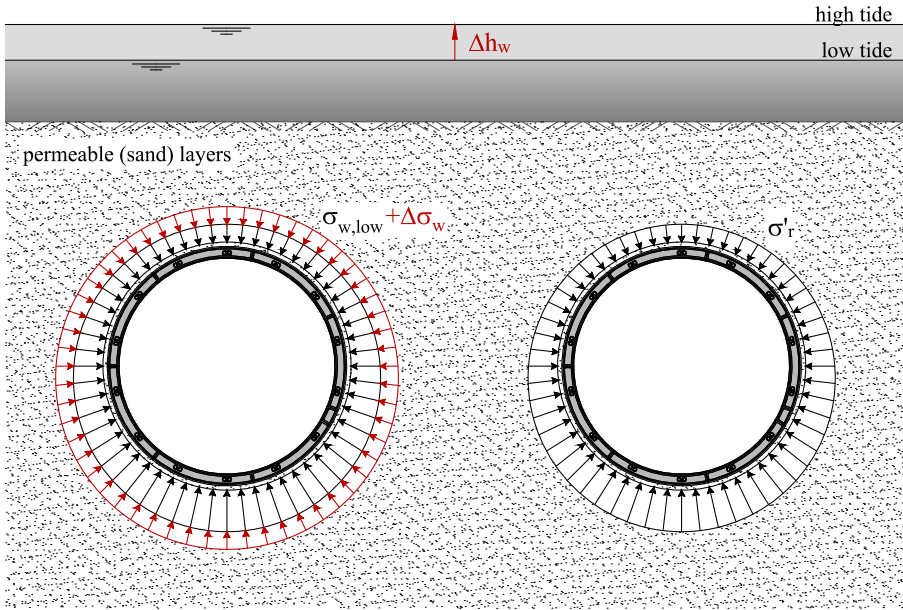


Figure 9.3. Tidal effect on the loads acting on the tunnel lining in permeable soil layers. Left: water pressures; right: effective soil pressures.

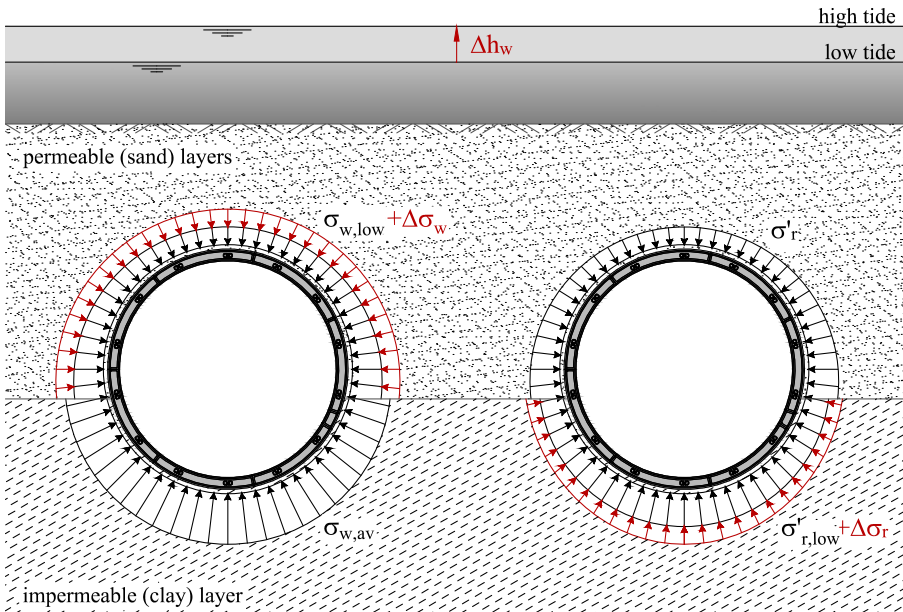


Figure 9.4. Tidal effect on the loads acting on the tunnel lining partly embedded in an impermeable clay layer, according to hypothesis 1. Left: water pressures; right: effective soil pressures.

Hypothesis 2: movement of clay layer below tunnel

It was demonstrated that the water level variation acts as an external load on the clay layer, which might cause consolidation settlements of the Boom clay. Although the time interval between low and high tide seems too restricted to allow significant drainage in the clay layer, a short-term elastic response might still occur. According to this hypothesis, the vertical movement of the tunnel lining might be attributed to the combination of a small settlement of the Boom clay layer at high tide followed by a heave of the same order of magnitude around low tide.

9.3 One-dimensional FE beam model

9.3.1 Characteristics of the beam model

In order to investigate hypothesis 1, a one-dimensional (1D) finite element model was developed, as shown in Figure 9.5. The tunnel lining is modelled as a single beam with a reduced equivalent stiffness, in order to account for the presence of the ring joints. The length of the beam equals 1620 m, which corresponds to the entire tunnel length below River Scheldt ranging from a distance of 1926 m to 3546 m from the entrance shaft. The ground support is implemented as vertical soil springs with varying stiffness in upward and downward direction, in correspondence with the soil layers surrounding the tunnel. At the ends of the beam, vertical supports were modelled as a fixed hinge on one side and as a free hinge at the other end, as illustrated in Figure 9.5.

The equivalent stiffness of the beam was determined according to Lengkeek (1997). The tunnel lining is interpreted as a series connection of concrete segments, ring joints and kaubit strips in the joints. The rotational spring stiffness $K_{rot,eq}$ of the equivalent beam system is defined by equation 9.5, after which the equivalent bending stiffness EI_{eq} can be determined using equation 9.6.

$$\frac{1}{K_{rot,eq}} = \frac{1}{K_{rot,ring}} + \frac{1}{K_{rot,joint}} + \frac{1}{K_{rot,kaubit}} \quad (9.5)$$

$$EI_{eq} = K_{rot,eq}B \quad (9.6)$$

In equation 9.6, B is the combined width of one concrete segment, ring joint and kaubit strip. This results in an equivalent stiffness $EI_{eq} = 8.8 \times 10^{17} \text{ Nmm}^2$, which is about 34% of the bending stiffness of a jointless tunnel tube characterized by the same dimensions.

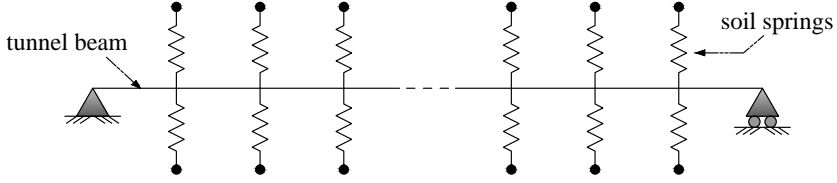


Figure 9.5. Modelling the tunnel lining as a longitudinal beam supported by soil springs.

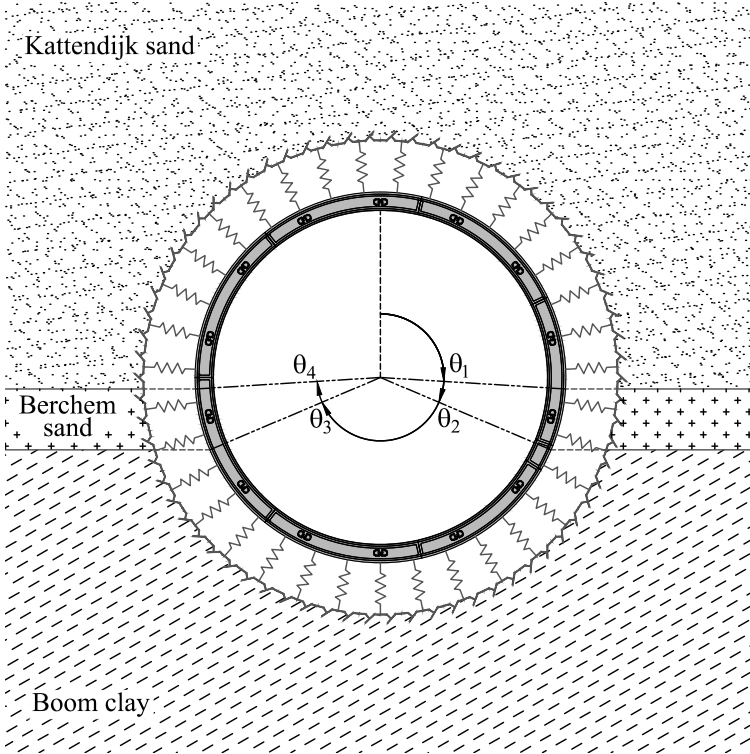


Figure 9.6. Example of a cross-section of the tunnel lining below River Scheldt with radial soil springs.

The determination of the stiffness of the vertical soil springs is based on Duddeck (1980). In his model, the tunnel ring is supported by radial soil springs with a stiffness k_r , as illustrated in Figure 9.6.

$$k_r = \frac{E_{oed}}{R_{out}} \quad (9.7)$$

In equation 9.7, R_{out} is the outer tunnel radius. The vertical component of

the radial spring stiffness is defined by equation 9.8.

$$k_v = k_r \cos^2 \theta \quad (9.8)$$

By integrating the vertical component over half of the tunnel circumference, the total stiffness K_v of the upward and downward soil springs implemented in the beam model can be calculated.

$$K_{v,up} = \int_{-\frac{\pi}{2}}^{\frac{\pi}{2}} k_v R_{out} d\theta = \int_{-\frac{\pi}{2}}^{\frac{\pi}{2}} E_{oed} \cos^2 \theta d\theta \quad (9.9)$$

$$K_{v,down} = \int_{\frac{\pi}{2}}^{\frac{3\pi}{2}} k_v R_{out} d\theta = \int_{\frac{\pi}{2}}^{\frac{3\pi}{2}} E_{oed} \cos^2 \theta d\theta \quad (9.10)$$

Since the soil composition is not uniform along the tunnel lining below River Scheldt, the oedometric compression modulus corresponding to the correct soil layer has to be applied for each portion along the tunnel circumference. For an upward displacement of the tunnel lining, only the upper soil springs with stiffness $K_{v,up}$ are taken into consideration. In case of a downward movement, only the bottom soil springs with stiffness $K_{v,down}$ are active, while $K_{v,up}$ equals zero in this case. This means that both spring types are modelled to only work in compression, not in tension.

Finally the beam model is loaded with an assumed resulting upward force at low tide and downward force at high tide, as discussed for hypothesis 1. Since these forces are caused by the lower part of the tunnel lining being embedded in the impermeable clay layer, their magnitude varies with the embedment depth of the tunnel in the Boom clay. Figure 9.7 shows the location of the soil layers with respect to the tunnel invert for the modelled tunnel section. It can be observed that the part oriented to the left bank encounters the largest fraction of clay, while at the centre of the river (ring 1500 at a distance of 2700 m from the entrance shaft) the clay layer locally does not reach beyond the tunnel invert. In addition to the embedment depth in the clay, the magnitude of the vertical resulting forces on the beam model naturally depends on the water level variation in the river. For the calculations using the beam model, the water levels of Figure 9.8 were considered, which correspond to levelling measurement LM 5. Nevertheless, Table 8.1 shows that the water level variations Δh_w for the other levelling measurements do not differ much from the value for LM 5, which is close to the mean value of Δh_w for all five measurements. Therefore all levelling measurements can be applied appropriately to assess the calculation results of the beam model using $\Delta h_w = 5.43$ m. Finally, Figure 9.9

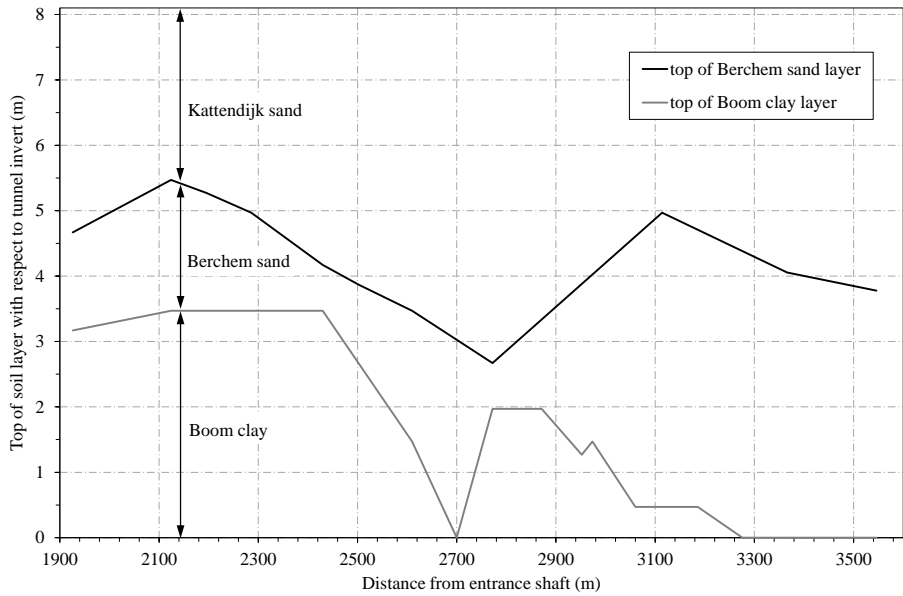


Figure 9.7. Location of various soil layers with respect to the tunnel invert.

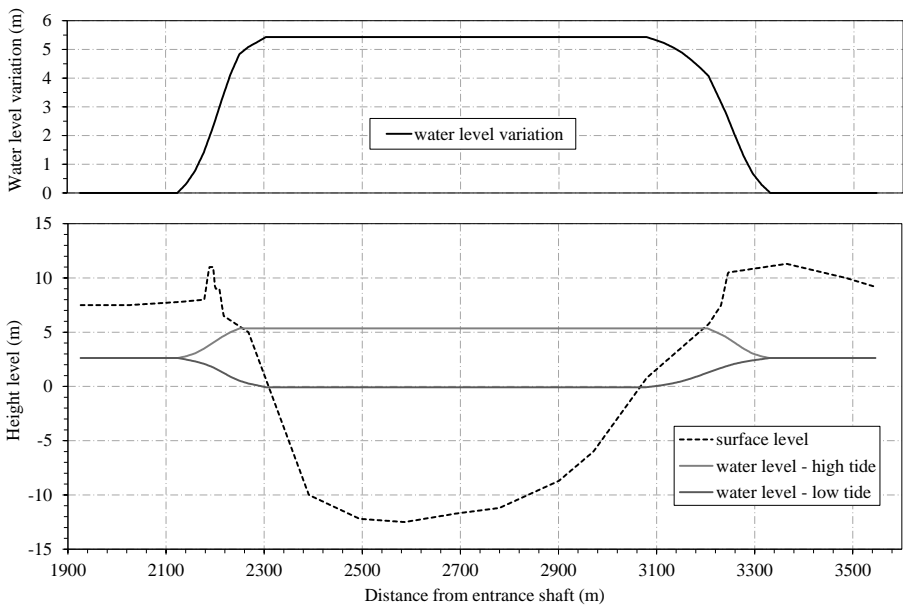


Figure 9.8. Water level fluctuation of River Scheldt between low and high tide on 31/10/2012.

shows the resulting upward (positive) and downward (negative) forces that were implemented as vertical loads on the beam model.

9.3.2 Calculation results of the 1D FE beam model

Results for hypothesis 1 - impermeable Boom clay

Figure 9.10 shows the results of the simulations using the 1D FE-model. Firstly, the influence of the applied bending stiffness for the tunnel beam was investigated. The model was calculated using either the full stiffness of a jointless tunnel tube or the reduced equivalent stiffness as discussed in the previous paragraph. From the results it appears that the beam stiffness has a rather small impact on the calculated vertical displacements of the tunnel lining. Its influence is reflected mostly at locations where a significant gradient in the displacements occurs.

From Figure 9.10 it can be concluded that the calculated vertical tunnel displacements according to hypothesis 1 prove to be significantly smaller than the monitored movements of the tunnel lining, depicted in Figure 8.10. Results of the beam model only show displacements of approximately 1.30 mm at the location of the left riverbank, where actual tunnel displacements up to 11 mm were monitored. At the centre of the river, the calculations result in negligible displacements, due to the small fraction of clay covering the tunnel cross-section at this location.

Results for hypothesis 1 - impermeable Boom clay & Berchem sand

If a larger fraction of clay could possibly exist at the river centre, it would cause a larger resulting force on the tunnel lining. It was already mentioned in Chapter 2 that several of the encountered sand layers along the tunnel alignment contain fractions of clay known as glauconite. These glauconite grains show the ability to shatter easily due to vibrations or repeated mechanical actions (for example caused by the passage of a TBM). As a result of this, the clay fraction locally increases significantly and the permeability of the sand layer is reduced to a large extent (Vancamp, 2012). The Berchem formation can contain a glauconite percentage of over 60% and has shown in the past that it is able to affect the excavation process of a shield-driven tunnel considerably (Van Alboom *et al.*, 2012). As indicated in Figure 9.7, a small layer of Berchem sand covers the Boom clay. If we assume that the tunnel excavation

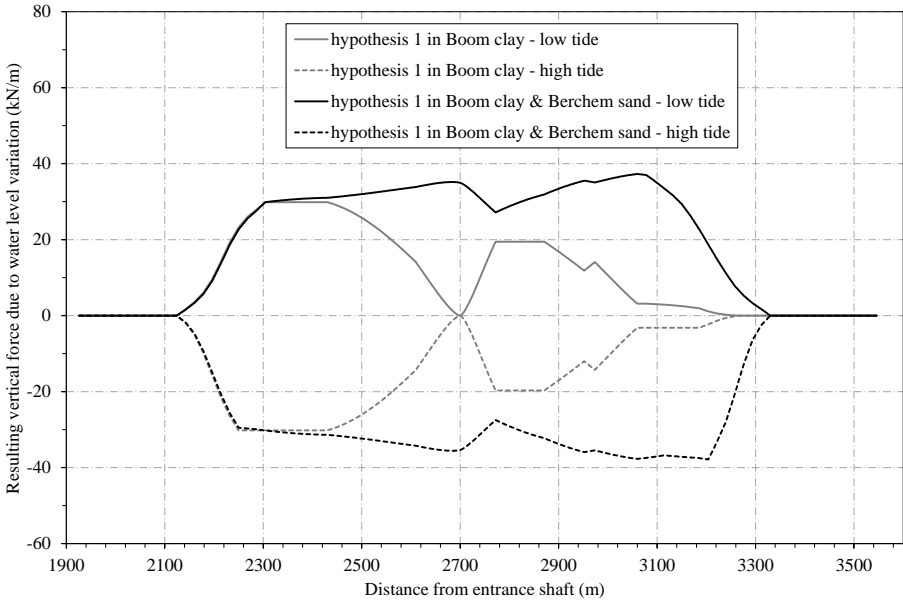


Figure 9.9. Assumed resultant vertical forces on the tunnel lining according to hypothesis 1.

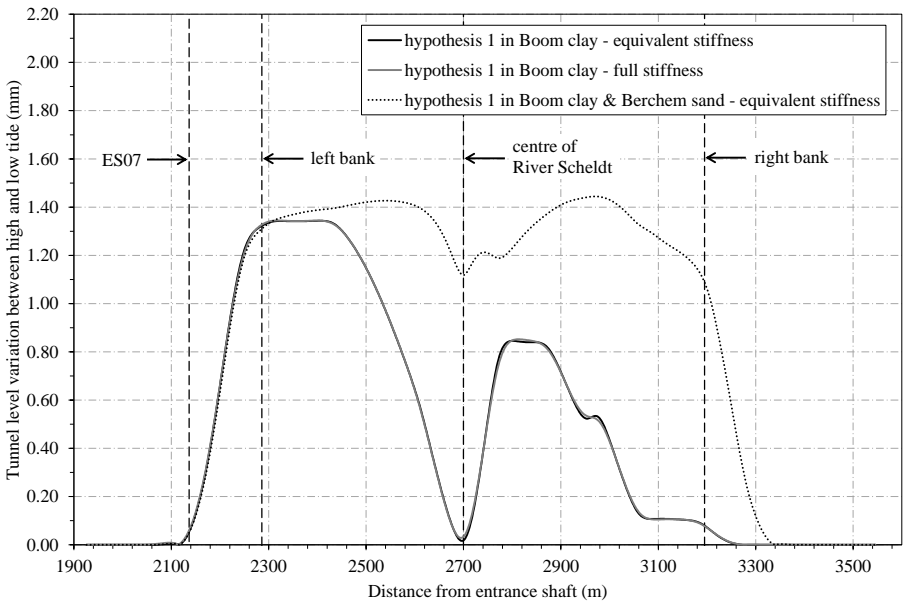


Figure 9.10. Calculated vertical movement of the tunnel lining according to hypothesis 1 using the 1D FE beam model.

alters the behaviour of the Berchem formation from sandy to distinctly clayey, the reasoning of hypothesis 1 might be extended to the Berchem sand. The resulting upward and downward forces acting on the beam model in this case are displayed in Figure 9.9. Figure 9.10 shows the results of the corresponding 1D FE-model calculations, assuming a reduced pressure variation in the Berchem sand layer in addition to the Boom clay layer. For this case, the calculated displacements do not drop to zero at the river centre. Instead they vary between 1.20 and 1.40 mm between both riverbanks. In general, the profile of the calculated displacements corresponds better to the monitored tunnel level variations from Figure 8.10. However, the beam model still fails to accurately predict the order of magnitude of tunnel displacements below the river. Consequently major doubts are raised on the validity of hypothesis 1 as the main cause of the tidal movements.

9.4 Analytical calculation of settlements in Boom clay layer

9.4.1 Hydrodynamic theory of Terzaghi

Solution of differential equation for two-way drainage

In order to verify hypothesis 2, first the short-term settlements of the Boom clay layer in response to the tidal fluctuations are calculated using the hydrodynamic theory of Terzaghi. For saturated soils, Terzaghi & Peck (1948) state that a volume loss can only occur when excess pore water is drained. As a result, the compression of clay in reaction to a load increase proceeds very slowly, due to the low permeability. The differential equation governing one-dimensional consolidation is given by equation 9.11.

$$\frac{\partial u}{\partial t} = c_v \frac{\partial^2 u}{\partial z^2} \quad (9.11)$$

In equation 9.11 c_v represents the coefficient of consolidation:

$$c_v = \frac{k}{\gamma_w m_v} = \frac{kC\sigma'}{\gamma_w} \quad (9.12)$$

where γ_w is the specific weight of water, m_v is the coefficient of volume compressibility, C is the modulus of compressibility and σ' is the effective soil stress (prior to the load increase). The degree of consolidation U for a given time t is defined as:

$$U = \frac{s_t}{s_\infty} = f(T_v) \quad (9.13)$$

where s_t equals the compression at time t and s_∞ the final compression. For a soil layer of thickness $h = 2d$ with two-way drainage from the top and the bottom, the time factor T_v is defined as:

$$T_v = \frac{c_v t}{d^2} \quad (9.14)$$

For $U \leq 60\%$, the solution of differential equation 9.11 is then estimated by equation 9.15 (Budhu, 2000).

$$T_v \approx \frac{\pi}{4} U^2 \quad (9.15)$$

$$\Leftrightarrow U = \sqrt{\frac{4c_v t}{\pi d^2}} = \sqrt{\frac{4kC\sigma' t}{\pi \gamma_w d^2}} \quad (9.16)$$

As the tidal fluctuations cause a continuous loading and unloading of the clay layer, C in previous equations should be substituted with the recompression modulus $A \approx 3C$ (De Beer, 1959).

Calculation of short-term consolidation of Boom clay

As part of the extensive soil investigation program, eight cone penetration tests (CPT's) were performed along the tunnel trajectory below River Scheldt, as shown in Figure 9.11. At four of these locations, borehole samples were extracted from the Boom clay layer. From the laboratory tests on these samples, an average coefficient of permeability $k = 2 \times 10^{-11}$ m/s is determined for the Boom clay. Furthermore, oedometer tests indicate that $C \approx 40$ at the top of the clay layer. A similar value is found from the results of the CPT's, based on the cone resistance q_c ($C = 3/2 \times q_c/\sigma'_v$). An increase of C as a function of the depth z' in the clay is assumed according to the empirical relation of De Beer (1971):

$$C = 40 + 2z' \quad (9.17)$$

The effective stress variations $\Delta\sigma'$ in the clay layer, due to its impermeable behaviour, are calculated using Boussinesq's theory on vertical stress distribution (Boussinesq, 1885) for a water level variation $\Delta h_w = 5.43$ m. Figure 9.12 shows the resulting load increase between low and high tide on the Boom clay

layer. The corresponding final consolidation s_∞ can be calculated using Terzaghi's law on primary consolidation settlements (Terzaghi & Peck, 1948):

$$s_\infty = \frac{h}{C} \ln \frac{\sigma' + \Delta\sigma'}{\sigma'} \quad (9.18)$$

Using equation 9.16, the degree of consolidation U can be determined for $t = 6\text{h}12'$, which corresponds to the average time difference between subsequent low and high tide (see section 8.2). However, the rise in water level Δh_w does not occur instantly, but follows a sinusoidal function. De Beer (1959) presented a solution for the differential equation 9.11 in case of a gradual load increase following a linear behaviour, which serves as an adequate estimation of the actual sinusoidal rise in water level. Comparison showed that in that case U equals about 2/3 of the degree of consolidation calculated for an instant load application.

Figure 9.13 finally shows the determined short-term settlements of the Boom clay layer between low and high tide according to the hydrodynamic theory, assuming a linear load increase. The maximum displacements at the top of the clay layer reach only a small value of 0.40 mm. When comparing this magnitude to the results of the levelling measurements discussed earlier, it is clear that the consolidation theory is not able to explain the vertical movements of the tunnel lining. The time interval between low and high tide proves too restricted to allow significant drainage of the impermeable Boom clay layer, therefore limiting the short-term settlements.

9.4.2 Immediate elastic response calculation using E_0

Small strain properties of Boom clay

The results of the previous section showed that the main explanation of the tunnel level fluctuations matching hypothesis 2 is not found in a short-term drainage of the Boom clay layer. Consequently the immediate elastic response of the Boom clay is investigated for an undrained situation. For this, the small strain soil properties are used, such as the small strain shear modulus G_0 determined by bender element tests. This is widely considered to be an important parameter in earthquake engineering and the prediction of soil-structure interaction (Clayton, 2011; Piriyaikul, 2006). The strains applied in a bender element test are normally less than 0.001%, corresponding to a linear elastic soil response (Karl, 2005). However, the observed tidal deformations of the Boom clay correspond to strains that are about 10 times higher, with an aver-

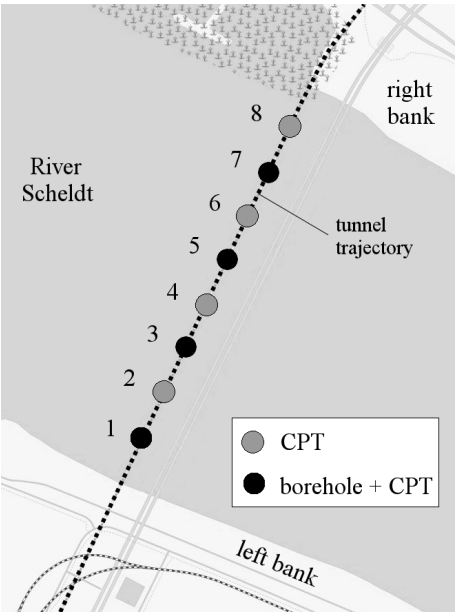


Figure 9.11. Location of boreholes and CPT's below River Scheldt.

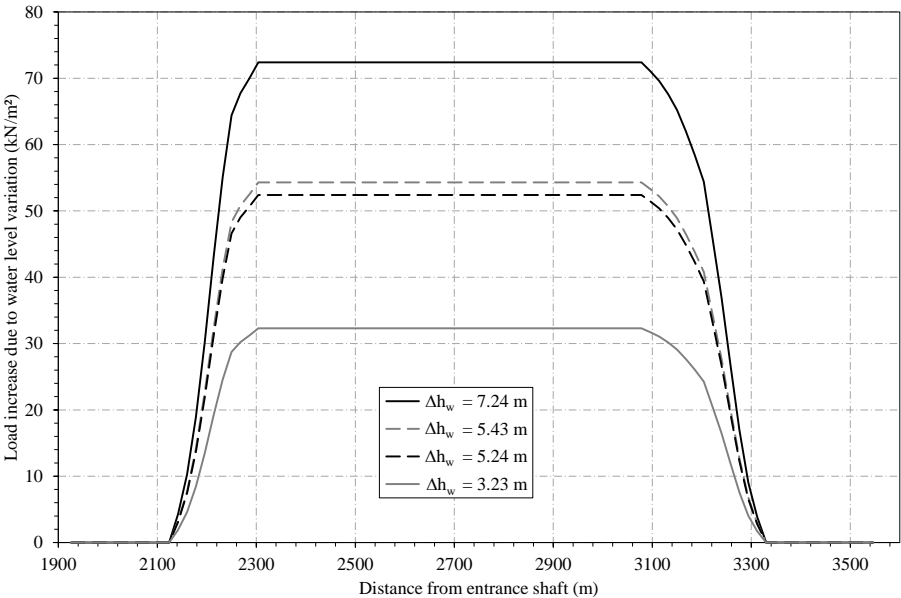


Figure 9.12. Load increase on the Boom clay layer due to various magnitudes of the water level fluctuation.

age around 0.012%. In that case, the stiffness normally varies non-linearly with strain (Atkinson & Salfors, 1991). However, from free torsion pendulum tests on Boom clay samples obtained from another location, it was found that the shear modulus remained almost constant for a strain range between 0.0001% and 0.05% (Karl, 2005). Therefore, it is assumed that the small strain properties such as G_0 may be used to calculate the immediate elastic soil response of the Boom clay layer to the tidal fluctuations.

Determination of G_0 and E_0

The borehole samples (extracted from the locations shown in Figure 9.11) were subjected to a bender element test, in order to determine the small strain shear modulus G_0 . Figure 9.14 shows the corresponding results on a double logarithmic scale. It can be seen that G_0 increases with the consolidation stress σ' . In general, G_0 is expressed by an empirical relation of the following form (Gu *et al.*, 2013; Likitlersuang *et al.*, 2013):

$$G_0 = AF(e)\left(\frac{\sigma'}{p_a}\right)^n \quad (9.19)$$

where A is a constant reflecting soil type, p_a is a reference stress, n is the stress exponent reflecting the effect of the consolidation stress and $F(e)$ is a void ratio function reflecting the effect of soil density. Therefore, in Figure 9.14 the correlation between G_0 and σ' can be fitted with a power function using the least-square curve fitting procedure (Mengé, 2001; Piriyaikul, 2006). The best-fit curve for all data is characterized by a $RMSE$ of 11.12 MPa and a R -square value of 0.85. The latter serves as an indicator of the fit quality, with an R -square value of 1.0 representing a perfect fit.

From the results for G_0 , the corresponding small strain modulus of elasticity E_0 can be determined using equation 9.20 (Gu *et al.*, 2013).

$$G_0 = \frac{E_0}{2(1 + \nu)} \quad (9.20)$$

For the saturated Boom clay layer, where the immediate settlements occur in an undrained situation, Poisson's ratio ν equals 0.5 (Clayton, 2011; De Beer, 1971). This leads to the results displayed in Figure 9.15, where the correlation between E_0 and σ' is again estimated by a best-fit curve with $R^2 = 0.85$ and $RMSE = 33.35$ MPa.

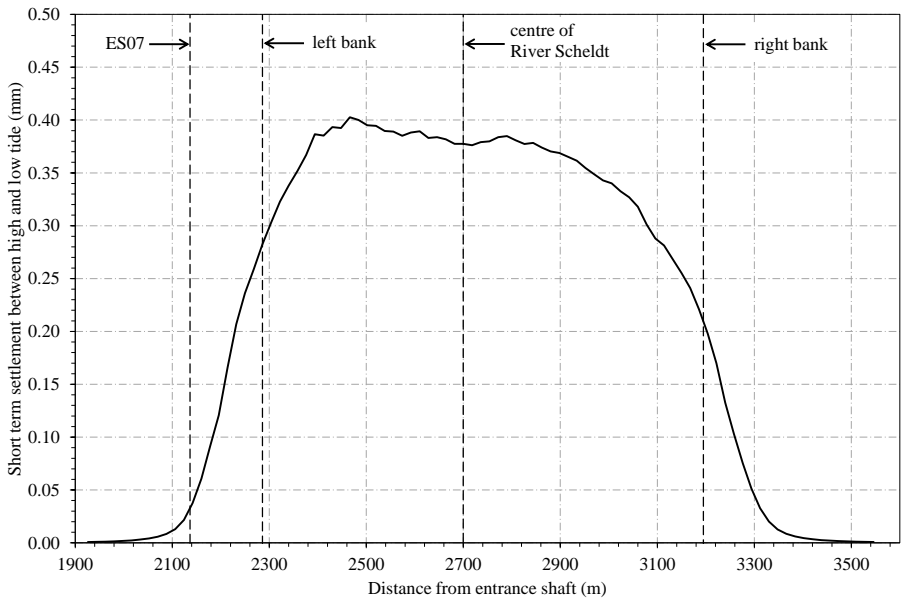


Figure 9.13. Calculated short term settlements of Boom clay due a water level fluctuation $\Delta h_w = 5.43$ m using the hydrodynamic theory of Terzaghi.

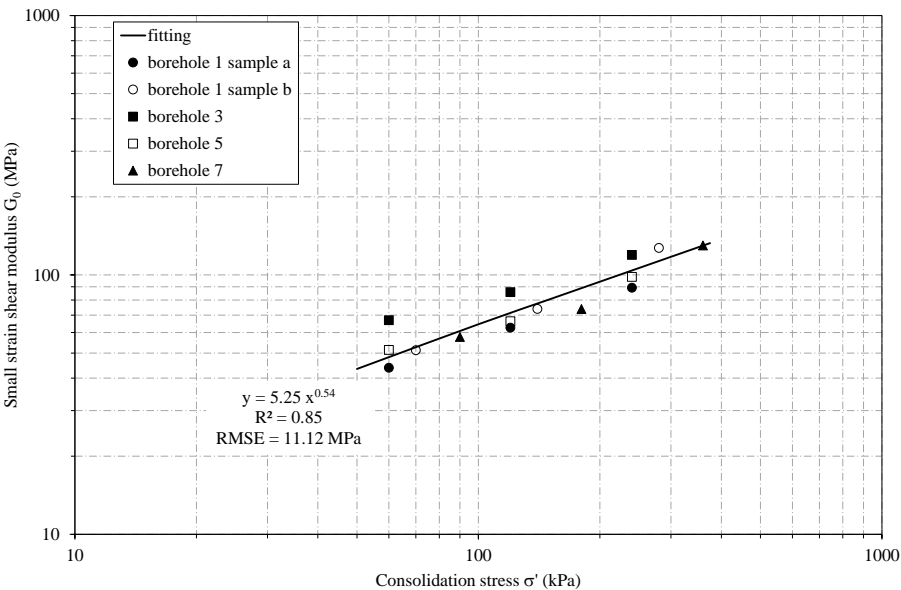


Figure 9.14. Determination of small strain shear modulus G_0 from laboratory tests on borehole samples.

Calculation of elastic response of Boom clay

The best-fit correlation between E_0 and σ' allows to estimate the small strain modulus of elasticity for the entire Boom clay layer. In accordance with hypothesis 2, the elastic deformations of the thick Boom clay in response to the water level variation can then be determined using Hooke's law of elasticity. This time the total stress variations in the clay layer are calculated for four different water level variations Δh_w : the mean, minimum and maximum value of Δh_w as determined in section 8.2, and $\Delta h_w = 5.43$ m. The resulting load increase between low and high tide on the Boom clay layer is also shown in Figure 9.12. By calculating the immediate elastic response for consecutive soil layers of 0.50 m thickness down to the base of the Boom clay layer, the total vertical settlement between low and high tide is determined. Since the Liefkenshoek tunnel is embedded on top of the Boom clay, the tunnel level is assumed to vary by the exact magnitude of these calculated settlements.

Figure 9.16 shows the main results of these calculations. The elastic response of the clay layer varies between 6 and 14 mm, respectively for the minimum and maximum value of Δh_w . For $\Delta h_w = 5.43$ m corresponding to the last levelling measurement, a very good resemblance can be observed between the calculated and monitored variations of the tunnel level between low and high tide. The described calculation method proves to be perfectly suitable to predict the observed movements of the tunnel lining. Finally, Figure 9.17 shows the vertical strains in function of the depth in the Boom clay layer for various distances from the entrance shaft. Settlements and corresponding strains increase from the riverbanks towards the centre of the river. Below the river, strains drop with increasing depth, mainly due to rising values of E_0 .

The results for the elastic settlements have been determined using a one-dimensional approach in vertical direction. However, due to the undrained behaviour of the immediate soil response and the corresponding condition of constant volume, horizontal deformations will occur as well. Therefore, additional insight in the elastic soil response to the river tides might be obtained by considering a two-dimensional approach along the entire cross-section of the river.

Influence of E_0 on calculated deformations

Since G_0 and E_0 were determined with a certain degree of accuracy, the impact of the best fit of these parameters on the calculated elastic response was investigated. The root mean squared error serves as the fit standard error,

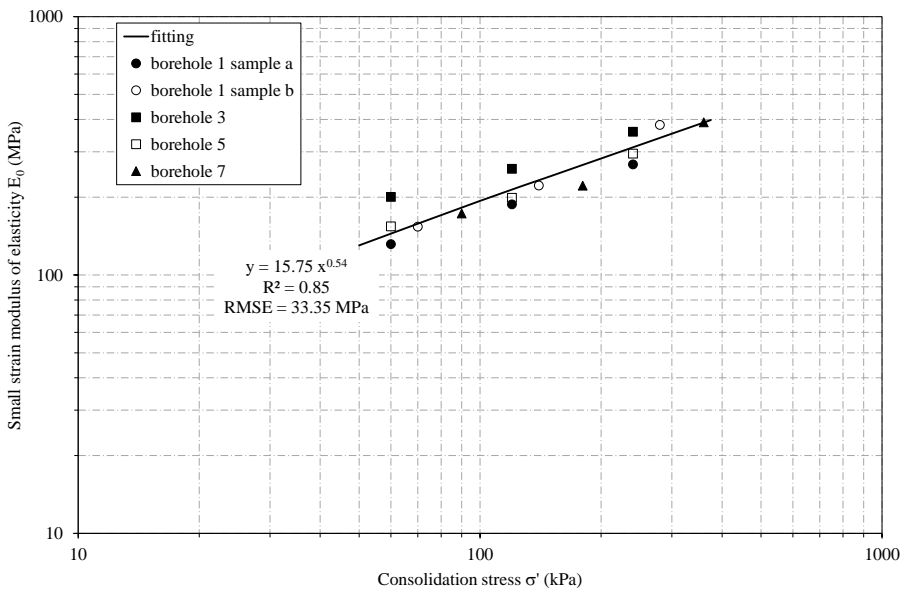


Figure 9.15. Determination of small strain modulus of elasticity E_0 from laboratory tests on borehole samples.

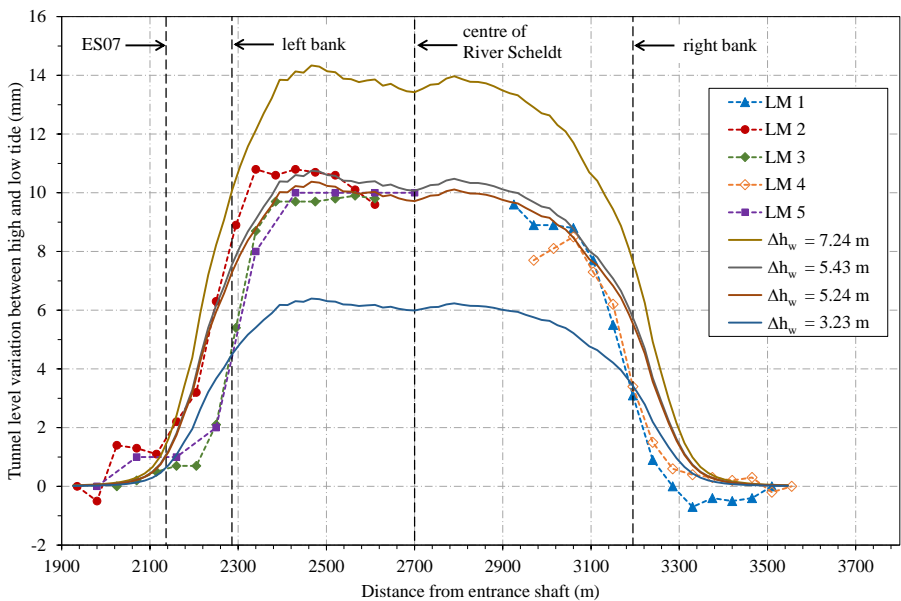


Figure 9.16. Calculated vertical movement of the tunnel lining due to water level fluctuations.

therefore 95% of the data falls within the range of ± 1.96 *RMSE* around the fitted curve. Figure 9.18 shows the calculated tunnel level variations for the boundary values of this 95% confidence interval for E_0 ($\Delta h_w = 5.43$ m). The maximum displacements now range between 9 and 13 mm, still illustrating a good resemblance between calculations and monitoring results.

9.5 Discussion

Two hypotheses are investigated in order to explain the monitored variation of the tunnel level with the river tides. In hypothesis 1, the lower part of the tunnel lining experiences a reduced pressure variation, causing a resulting vertical force on the structure. The corresponding displacements calculated with the 1D FE beam model are much smaller than the observed tidal movements. Even when the large fraction of glauconite in the Berchem sand layer was taken into account, hypothesis 1 was not able to accurately predict the order of magnitude of the tunnel displacements below the river.

In hypothesis 2, it is presumed that the tunnel movement is caused by deformations of the Boom clay. Due to damping of the pore water pressure variation in the impermeable clay layer, the rise and fall of the water level in River Scheldt causes effective stress variations in the Boom clay. According to Terzaghi's theory on one-dimensional consolidation, the consequential deformations of the clay layer equal approximately 0.40 mm. Due to the very slow drainage of the Boom clay, the short-term compression and expansion of the Boom clay remains limited.

While the time interval between low and high tide is too small to allow significant drainage, an immediate elastic response of the clay layer due to the total load variation still occurs. Calculations using the small strain modulus of elasticity E_0 for an undrained situation result in elastic deformations of the thick Boom clay layer that show an almost impeccable resemblance with the monitored variations of the tunnel level. Therefore, hypothesis 2 is accepted as the valid explanation of the vertical movements of the tunnel lining in response to the river tides. The latter can be accurately estimated by calculating the one-dimensional undrained elastic deformations using E_0 , while neglecting the consolidation of the clay layer between low and high tide. Nonetheless, further insight might be obtained by performing a two-dimensional approach for the elastic soil response. Considering the remarks made in section 9.2.1 on the applicability of the theory of De Rouck & Van Damme (1996), these elastic deformations will always occur, regardless of any damping of the pore water

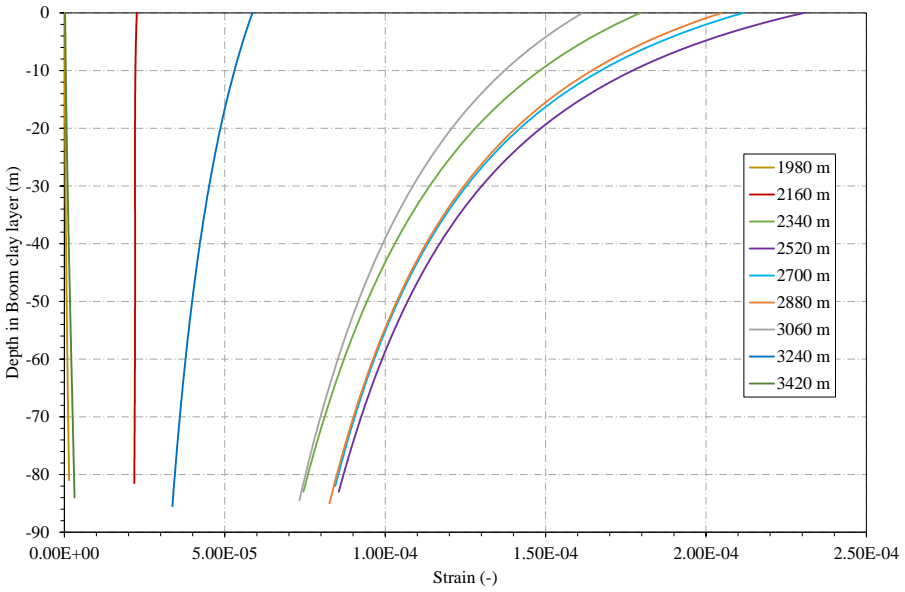


Figure 9.17. Calculated vertical strains in the Boom clay layer due to a water level fluctuation $\Delta h_w = 5.43$ m.

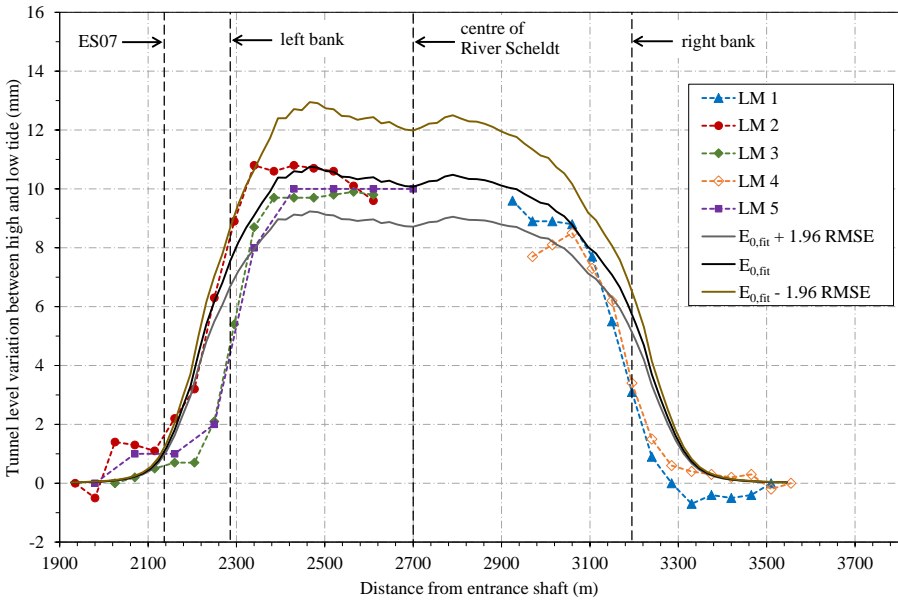


Figure 9.18. Calculated vertical movement of the tunnel lining due to a water level fluctuation $\Delta h_w = 5.43$ m: influence of the small strain modulus of elasticity E_0 .

pressures in the clay layer.

Given the very accurate resemblance between the elastic deformations of the Boom clay and the monitored tunnel movements, it is very unlikely that the tunnel would still experience a resulting vertical force that causes additional displacements, as was suggested in hypothesis 1. Furthermore, the asymmetric loading of the tunnel lining corresponding to hypothesis 1 would result in significant bending moments and cross-sectional deformations of the tunnel section below the river. However, no such observations were made, as mentioned in Chapter 8. This implies that the assumptions of hypothesis 1 are not valid and that the presence of neither the Boom clay nor the Berchem sand prevents the tidal variation of the water pressures from acting on the tunnel lining. This might be attributed to a less pronounced damping of the pore water pressures in the clay layer than determined in section 9.2.1, or the relatively high permeability of the grout filling the tail void, compared to the stiff clay. For the latter, it was already mentioned that $k \approx 2 \times 10^{-11}$ m/s, while in literature permeability values for hardened grout are found ranging between 10^{-7} and 10^{-8} m/s (Bezuijen & Talmon, 2004, 2003; Kasper & Meschke, 2004, 2003; Talmon & Bezuijen, 2009). Consequently, the presence of the annular tail void causes the Liefkenshoek tunnel to experience a load variation corresponding to Figure 9.3 anyway, equal to a tunnel lining that is completely surrounded by permeable sand layers. This behaviour is verified by 3D finite element calculations discussed in the next section.

9.6 3D FE-model of tunnel cross-section

9.6.1 Composition of the 3D FE-model

In order to verify the impact of the river tide on the sectional forces in the tunnel lining, 3D finite element calculations are performed for all measurement sections below River Scheldt. The composition of the applied FE-model is described in detail in Chapter 6. Both the situation at low tide and high tide are considered, again corresponding to the water levels of LM 5 (Figure 9.8). The loads are modelled consistent with Figure 9.3, where the segmental lining experiences the tidal variation of the water pressures along its entire circumference. Results of the verification of the tunnel behaviour according to the assumptions of hypothesis 1 have not been included.

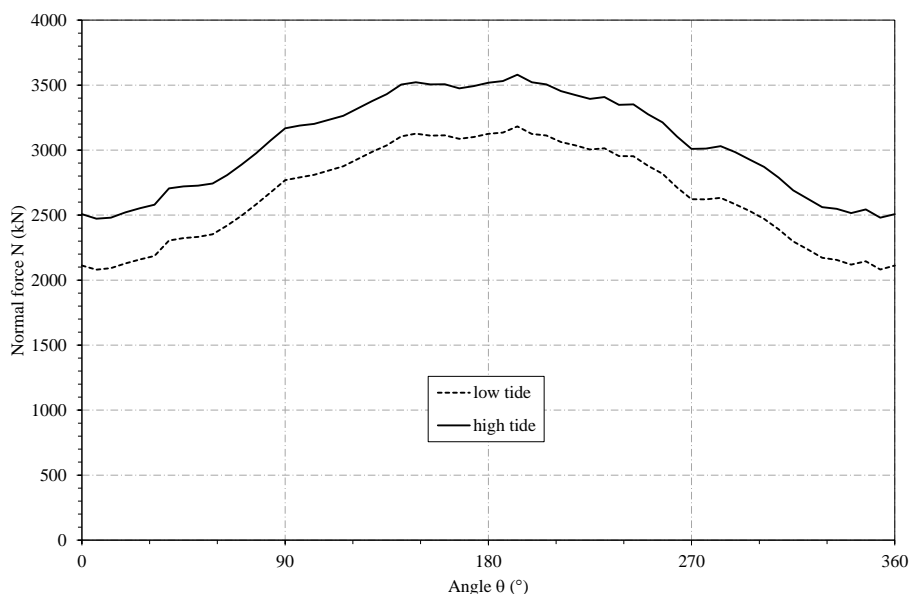


Figure 9.19. Calculated normal forces for tunnel section N1497.

9.6.2 Results of 3D FE-calculations

Tangential normal forces

Figure 9.19 shows the calculated tangential normal forces in tunnel section N1497, located at a distance of 2700 m from the entrance shaft. As section S1500 is located at equal distance and has the same keystone orientation, all calculated results for measurement section S1500 are completely identical to N1497. The graph displays an increase in normal forces between low and high tide due to the larger head of water in the river. Analogue observations can be made for tunnel sections N1400 and S1400 (located at a distance of 2520 m from the entrance shaft).

Bending moments around longitudinal z-axis

Figure 9.20 shows the calculated bending moments in the tunnel lining for section N1497, the results of sections N1400, S1400 and S1500 indicating a similar distribution. In general the resulting curves relate to an ellipsoidal deformation of the corresponding tunnel section, where the horizontal tunnel diameter exceeds the vertical diameter. This so-called horizontal ovalisation of the tunnel cross-section complies with the classical expectations of a “pumpkin”

shaped deformation for circular tunnels in soft soil (Blom, 2002; Duddeck & Erdmann, 1985; Duddeck, 1980; Schulze & Duddeck, 1964). It can be observed that the difference between the bending moments at low and high tide remains very limited.

Strains in concrete and reinforcement bars

The results of the normal forces and bending moments allow to determine the corresponding strains in the tunnel lining, in accordance with CEN/TC 250 (2004). Figure 2.7 showed the arrangement of the rebars in the segment cross-section. Using this information, the variation of steel and concrete strains between low and high tide can be calculated, corresponding to the sectional forces determined with the 3D FE-model. Figures 9.21 to 9.23 display the variation of strains at the intrados and inner and outer reinforcement between low and high tide, for tunnel section N1497, N1400 and S1400 respectively. All calculated results can be compared to the monitored strains at the corresponding locations, as determined using the linear correlations from section 8.4.3. The *RMSE*-values of the monitored results are plotted as error bars in Figures 9.21 to 9.23, as a visualisation of the standard error. Since sections N1400 and S1400 had strain gauges installed only at the inner concrete surface, no monitored data is available for the strains in the rebars.

Figures 9.21 to 9.23 show rather uniform strain variations along the entire tunnel circumference. In general, the variations in the tunnel lining due to the tide remain limited. The corresponding stress changes equal around 0.50 MPa at the concrete surface and 3 MPa in the rebars. An adequate resemblance is found between the calculation results and the monitored strains, especially for section S1400. For the other measurements sections, the monitored strains indicate a somewhat smaller tidal variation compared to the calculated response. This implies that the segmental lining might act a bit stiffer than assumed, or that the tunnel experiences a slightly smaller fluctuation of the water pressures between low and high tide. The latter might be due to a minor damping of the pore water pressure variation between tides in the upper sand layers, similar to the line of reasoning for the Boom clay in section 9.2.1. Nevertheless, all measurement sections indicate a rather uniform increase in compression from low tide to high tide, which would not occur under the asymmetrical loading situation from hypothesis 1.

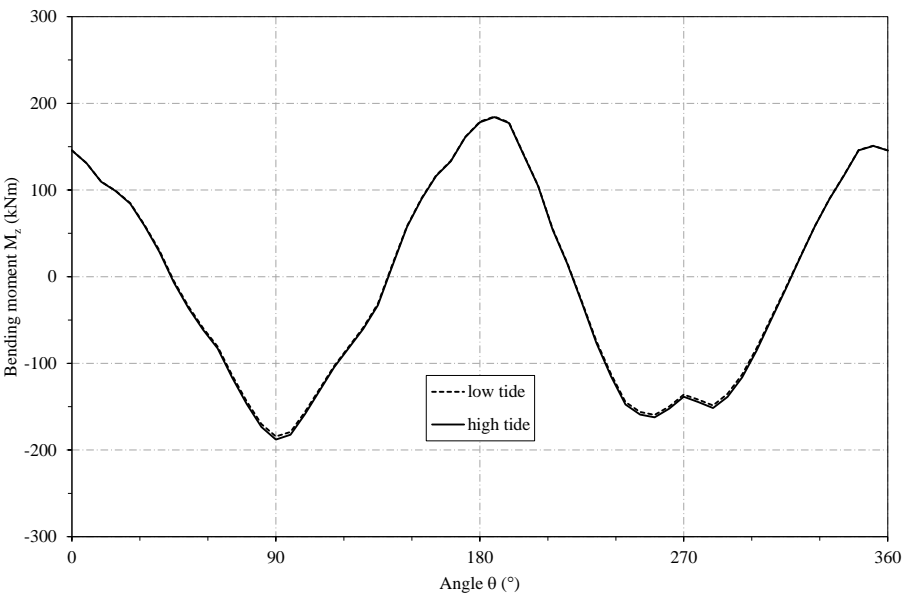


Figure 9.20. Calculated bending moments for tunnel section N1497.

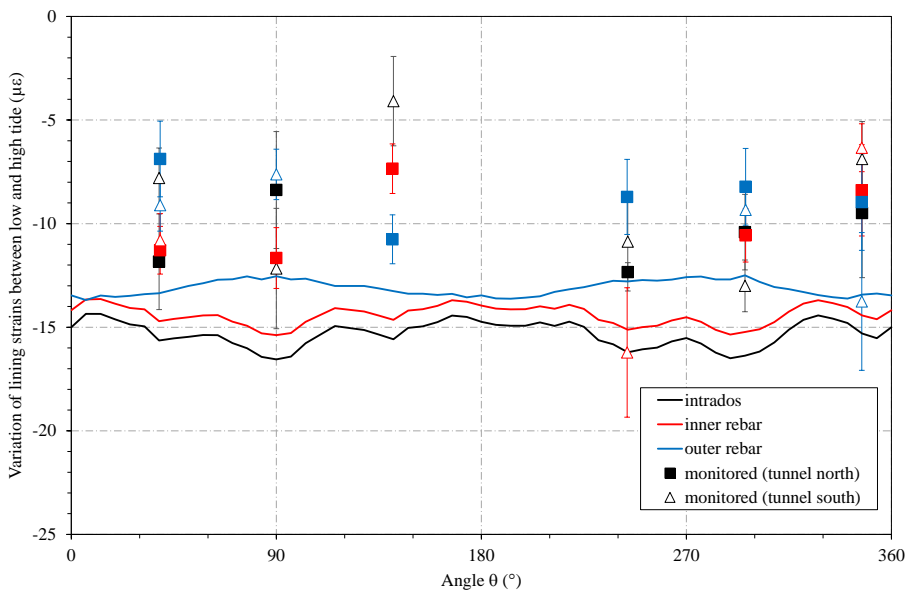


Figure 9.21. Calculated strains for tunnel section N1497.

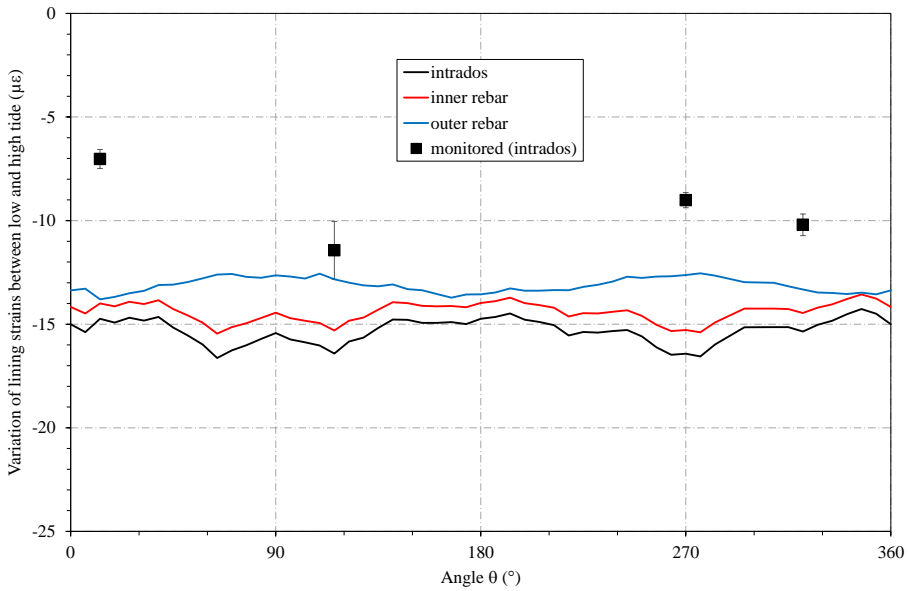


Figure 9.22. Calculated strains for tunnel section N1400.

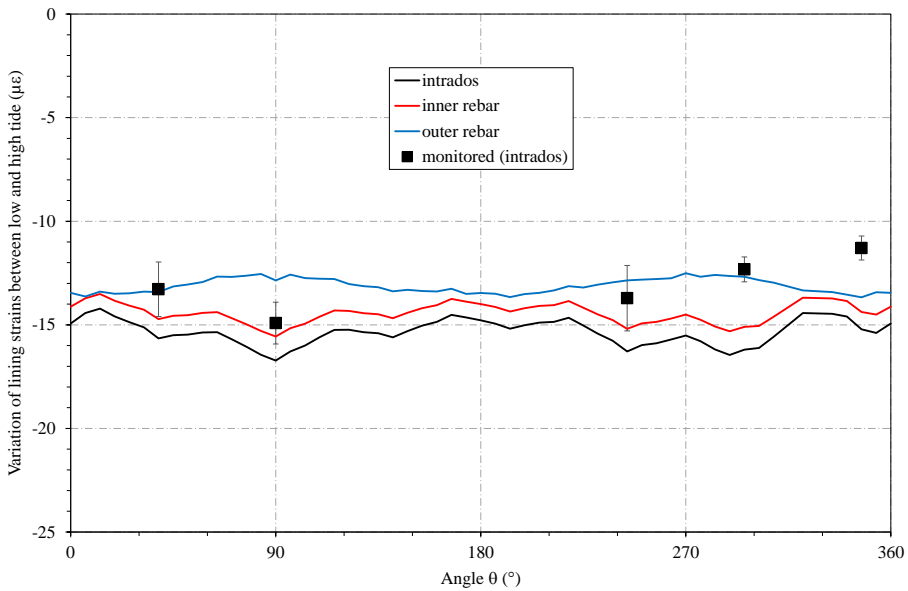


Figure 9.23. Calculated strains for tunnel section S1400.

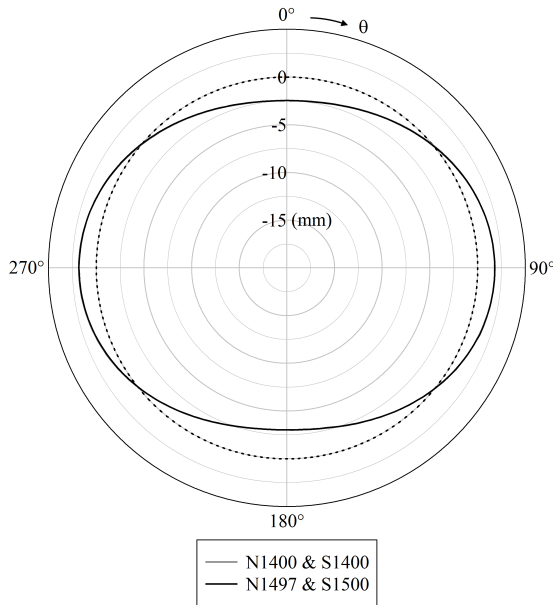


Figure 9.24. Calculated radial displacements for tunnel sections N1400/S1400 and N1497/S1500.

Deformations

Figure 9.24 displays the calculated radial displacements (at high tide) of cross-sections N1400 and N1497 using the 3D FE-model. Due to their locations at equal distances from the entrance shaft, the results for rings S1500 and S1400 are identical to respectively N1497 and N1400. The results for both sections indicate an identical deformation of the tunnel section. In general the tunnel invert rises about 2.5 mm, while the top moves down by about the same magnitude. The sides move outward by approximately 2 mm. These results correspond to the horizontal ovalisation as already observed in the results for the bending moment.

In Figure 9.25 the differences in displacements between tides are plotted. The calculated results are almost identical at low tide and high tide, as a very small difference of only 0.1 mm is observed at the top and bottom of the section. Again, both section N1400 and N1497 show the same behaviour. The very small deformations of the tunnel cross-sections between low and high tide imply that they fall within the 95% significance levels of the ovalisation measurements. Therefore, Figure 9.25 corresponds to the main observation of the ovalisation measurements as discussed in section 8.4.2, where no significant

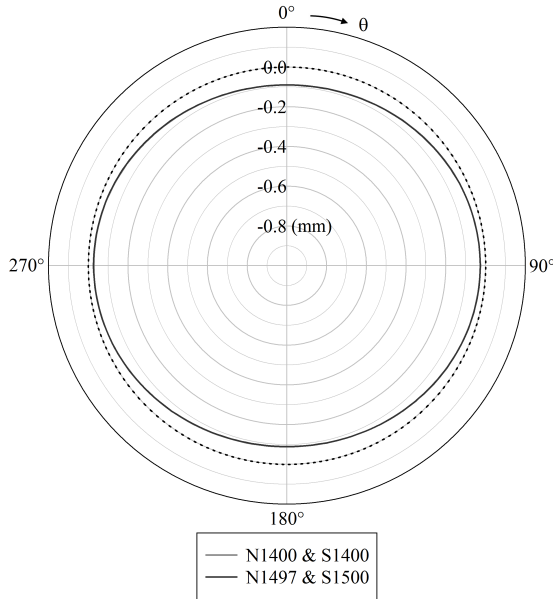


Figure 9.25. Calculated variation in radial displacements between low and high tide for tunnel sections N1400/S1400 and N1497/S1500.

deformations of the cross-section were detected between tides.

9.7 Conclusion

Analytical settlement calculations and finite element calculations using a 1D beam model were performed in order to identify the cause of the tidal movements. Results show that they are mainly due to the elastic response of the thick layer of Boom clay. The Liefkenshoek tunnel is embedded on top of this clay layer, and below the river the clay locally ranges up to 40% of the tunnel section. The variable water level in the river causes a fluctuation of the total load on the Boom clay layer. As a result, the Boom clay experiences a short-term elastic compression at high tide that accounts for the tunnel movement. Once the tide recedes, the short-term settlements are inversed and the tunnel springs back up again. Therefore, no long-term settlements of the Boom clay take place due to the river tide. This behaviour can be accurately estimated by calculating the undrained elastic deformations using the small strain modulus of elasticity.

Levelling measurements prove that the Liefkenshoek tunnel follows the elastic movements of the Boom clay layer by the exact same magnitude. A maximum vertical displacement of 14 mm is to be expected for large variations of the water level in River Scheldt. No noticeable deformations of the cross-section occur during this vertical translation according to 3D FE-calculations, which corresponds with results from ovalisation measurements. Comparison of calculated and monitored strains proves that the segmental lining experiences the tidal variation of the water pressures along its entire circumference. An increase in uniform compression is observed with rising water levels. Neither the clay layer, nor the Berchem sand layer containing large fractions of glauconite, nor the grout layer surrounding the tunnel, is able to shield the tunnel lining from the fluctuating water load.

Chapter 10

Conclusions

10.1 Research conclusions

10.1.1 Combined monitoring of segmental tunnel linings

Despite rough site conditions, accurate strain measurements and ovalisation measurements on the precast concrete lining of shield-driven tunnels under construction have become realistic. However, to have successful monitoring, every detail of the process methodology becomes important, in order to cope with practical complications originating from the construction site conditions and product-specific requirements. If this is assured, combined strain and ovalisation monitoring proves an extremely useful tool to evaluate the on-site behaviour of the tunnel lining under numerous loading conditions during and after tunnel drive works. Both measurement techniques record the impact of the different loading conditions on the tunnel structure, but on a different scale. Strain measurements allow to acquire a thorough understanding of the real-time loads acting on the individual precast concrete segments of the tunnel lining. Laser scanning mainly measures the changes in position of the segments and the influence of these changes on the ovalised shape of the tunnel ring. As a result, in order to obtain a full image of the tunnel behaviour, both techniques need to be applied in order to acquire a complementary set of measurement data. Ultimately, the combined application of strain and ovalisation measurements proves an important advantage in the structural assessment of segmental tunnel linings. The collected measurement results of the Liefkenshoek project hereby served as a perfect illustration.

10.1.2 Early-stage behaviour

The gradual development of strains in the first hours after ring assembly showed that loads acting on the tunnel segments during the construction process can have a substantial influence on the sectional forces in the tunnel lining. The largest stresses in the segments occur in the initial hours after ring erection, rather than at later stages. Once the monitored ring has emerged from the TBM back-up train, no significant changes are observed and the monitored strains often remain smaller than the initial values after ring erection. These conclusions are confirmed by ovalisation measurements, which show deformations of the tunnel structure occurring during the first week after ring assembly. Afterwards, no significant deformations of the tunnel cross-section are observed. The assembly stage is therefore often decisive in the design of the tunnel lining, resulting in a potential economic loss. Without any doubt, the design process of the precast concrete tunnel lining should not focus exclusively to parameters of the surrounding soil, the groundwater situation or loads on the surface level. It should also study the effects of loads during the early construction stages, such as ring erection, advance of the TBM and tail grouting, as obtained measurement results have shown that these construction parameters may constitute a dominant factor in the tunnel lining design.

10.1.3 Presence of installation imperfections

The deformations of 28 cross-sections of the Liefkenshoek tunnel were accurately monitored in the first months after installation using laser scanning. Due to the manually operated installation of the individual lining segments, a tunnel ring is never installed perfectly circular. The reference measurements immediately after erection showed that on average the installed ring profile is egg-shaped, with deviations from the theoretical profile likely to range up to 11 mm. After interaction with the soil and water pressures, the global average deformation of the tunnel lining showed a horizontal ovalisation (pumpkin shape), which complies with the classical expectations for circular tunnels in soft soil. However, it was shown that deformations of individual tunnel sections are likely to differ from the horizontal ellipsoidal shape, due to variable tunnelling parameters and the spreading of the monitored sections along the tunnel axis.

Apart from the global deformation pattern of the tunnel sections, the ovalisation measurements gave insight in the behaviour of the joints between adjacent lining segments. Due to human errors and inaccuracies in the ring building

procedure, small imperfections of the inner tunnel surface are present at the location of the joints. In general, these initial joint imperfections due to installation range between 2.0 and 2.5 mm, with an occasional maximum of about 6 mm. Small movements occur in the joints in the first week after installation, but the average joint irregularity remains almost constant over the monitored period. This is an important observation, as it implies that the initial joint inaccuracies which are present after imperfect installation of the lining segments, remain visible during the rest of the structure's life.

10.1.4 FE-modelling using contact definitions

An advanced 3D finite element model was developed in order to study the behaviour of the segmental tunnel lining under various load conditions. Up to now, all present analytical and finite element models for segmental tunnel linings use a simplified interpretation of the joint behaviour. Consequently, all current models assume a perfectly circular tunnel ring. In order to be able to investigate the effect of geometrical imperfections, this research applied a more realistic approach for the joint behaviour. In the developed FE-model, all joints are modelled using contact conditions with friction between the segments. Although this approach implies a larger computational effort for the FE-analysis, accurate results are found, enabling to simulate a realistic behaviour in the longitudinal and circumferential joints. However, a large influence of the applied coefficient of friction in the contact joints on the results of the simulations including installation imperfections was observed.

10.1.5 Influence of installation imperfections

In general, it is assumed implicitly that the impact of geometrical imperfections is taken care of by the partial safety factors applied in the design. However, the presented research has shown that even small installation inaccuracies have a substantial impact, primarily on the sectional forces in the concrete lining. The FE-model including monitored installation imperfections from laser scanning displayed an irregular deformation pattern which bore very good resemblance to the real deformations of the tunnel section. Due to the imperfect contact in the segment joints in case of an inaccurate installation, sectional forces are transferred to the neighbouring rings via friction in the ring joints. As a result, the maximum tangential normal forces and bending moments around the tunnel axis increase considerably in the adjacent rings. Consequently, the corresponding stresses in the concrete might exceed the allowed safety margins,

both in tension and compression. In this case, undesirable cracks are likely to develop, affecting the durability of the segmental lining. Finally, the lowest normal force in the imperfect ring drops to only a fraction of the original value, possibly influencing the waterproofness of the structure.

The present state of the art of using a manually operated erector to assemble individual precast segments into a tunnel ring is naturally prone to human error. Consequently, small deviations of the theoretical tunnel profile are currently an inevitable part of segmental lining construction. This research demonstrates the important negative impact of these seemingly insignificant imperfections on the tunnel lining. By neglecting the installation imperfections in the design, the stresses in the lining segments are underestimated, affecting the safety and durability of the tunnel structure. The development of an automated segment erection procedure, using precise real-time monitoring of the installation tolerances to reduce initial imperfections, might generate a substantial improvement in the performance of segmental tunnel linings.

10.1.6 Tidal influence

Levelling measurements revealed that the tunnel lining of the Liefkenshoek tunnel moves up and down with the river tide. At high tide, the monitored tunnel level is approximately 10 mm lower compared to the situation at low tide. The monitoring results indicate no time delay between the river tide and the corresponding structural response of the segmental lining. After analysis of all monitoring results, the displacements proved to be due to a vertical rigid body movement of the Liefkenshoek tunnel between tides. Consequently, the impact of the displacements regarding structural damage is considered to be limited. Nonetheless, a detailed investigation of the confined transition zone between the tunnel section showing no tidal influence and the affected area below the river appears necessary. Furthermore, as the railway infrastructure is governed by high accuracy levels and low safety margins for deformations, special attention is required.

Several possible causes for the nature of the tunnel response were identified and investigated. Accordingly, the vertical oscillation of the tunnel lining proves to be the result of the presence of the thick layer of Boom clay below the tunnel alignment. The Liefkenshoek tunnel is embedded on top of this clay layer, and below the river the clay locally ranges up to 40% of the tunnel section. The variable water level in the river causes a fluctuation of the total load on the Boom clay layer. As a result, the Boom clay experiences a short-term elastic

compression at high tide that accounts for the tunnel movement. Once the tide recedes, the short-term settlements are inversed and the tunnel springs back up again. Therefore, no long-term settlements of the Boom clay take place due to the river tide. This behaviour can be accurately estimated by calculating the undrained elastic deformations using the small strain modulus of elasticity.

Levelling measurements prove that the Liefkenshoek tunnel follows the elastic movements of the Boom clay layer by the exact same magnitude. A maximum vertical displacement of 14 mm is to be expected for large variations of the water level in River Scheldt. No noticeable deformations of the cross-section occur during this vertical translation according to 3D FE-calculations, which corresponds with results from ovalisation measurements. Comparison of calculated and monitored strains proves that the segmental lining experiences the tidal variation of the water pressures along its entire circumference. An increase in uniform compression is observed with rising water levels. Neither the clay layer, nor the Berchem sand layer containing large fractions of glauconite, nor the grout layer surrounding the tunnel, is able to shield the tunnel lining from the fluctuating water load. Despite stress variations due to river tides remaining relatively small, they might prove unfavourable for the long-term durability of the tunnel lining.

Thanks to the various components of the extensive monitoring program, consisting of strain, ovalisation and levelling measurements, the structural response of the Liefkenshoek tunnel to the river tide could be accurately assessed. The research results improve the basic understanding of the behaviour of a tunnel embedded on a thick, impermeable clay layer and subjected to tidal fluctuations. However, the observations can be applied to multiple structures in the surrounding region or outside, above ground level as well as below. In addition, the findings presented a perfect example of how the design process of bored tunnel linings requires a thorough understanding of the project surroundings for a correct and utter identification of the loads acting on the tunnel segments, both during and after tunnel drive works.

10.2 Future research prospects

10.2.1 Strain monitoring

Results of the strain monitoring program already gave a detailed insight in the tunnel lining behaviour, during and after construction. Yet due to the absence of the segmental erection phase in the monitoring results, there is a resulting lack of knowledge regarding the assembly stresses present in the concrete elements at the start of the measurements. Therefore, reliable statements on the absolute values of compressive or tensile stresses in the lining segments remain difficult. Future strain measurements of segmental tunnel linings should therefore be initiated before the start of ring assembly, when the tunnel segments are still in a relatively load-free state. This should allow to accurately study the impact of all activities in the early stages of tunnel construction.

Furthermore, the implementation of strain gauges in successive tunnel rings could improve the understanding of the mutual effect of adjoining rings on each other. This effect was only studied theoretically in the presented research, when investigating the impact of the installation imperfections. However, this investigation would benefit significantly from the monitoring of multiple neighbouring tunnel rings, as this would allow to compare the theoretical calculations with the monitored data.

10.2.2 Ovalisation monitoring

The highly detailed and very accurate laser scanning monitoring of tunnel sections in the Diabolo project and Liefkenshoek project resulted in a valuable data set for the evaluation of tunnel structures under real loading conditions. Notwithstanding the achievements of the presented research, the monitoring results still offer several opportunities for further extending the knowledge on early-stage tunnel deformations. At the moment, very few measurement results are available that include information on the deformations of the segmental tunnel lining during the first week after construction. Due to the presence of the TBM installations and back-up train, no intermediate laser scanning measurements can be executed during this period. As a result, the ovalisation measurements are not able to verify critical moments in the construction stage in detail, such as the tunnel section passing the shield tail. The possibility to execute additional laser scanning measurements in the initial hours after ring assembly should therefore be investigated.

Furthermore, some caution was advised with regard to the interpretation of

the ovalisation results. In the applied methodology, the centre of the resulting cross-section of each measurement is based on the axis of the best-fit cylinder. This cylinder is determined for each measurement individually, of which the measured areas are not always equally spread around the inner tunnel surface. As a result, small variations may occur in the orientation of this best-fit cylinder and its centre point, even if there are no deformations in the monitored section. For an accurate evaluation, the ovalisation axis and the deformation pattern should be taken into account in order to compensate for the non-measured areas. In addition, due to the fact that the measurements are not located in an absolute coordinate system, a vertical shift of the whole tunnel structure cannot be detected in the results. Extended research is required in order to solve these issues and improve the accurate interpretation of the deformation results.

Finally, one of the main advantages of laser scanning measurements is the detailed 3D recording of a large part of the tunnel structure, without limiting the measurements to specific points or dimensions of the structure. The segment joints for example are clearly visual in the obtained point clouds. Furthermore, the laser scanning results allow extracting information on the individual segments of a tunnel ring and how their positions change during the different loading stages. Results on the joint displacements and segment rotations in the cross-sectional plane are already available, as discussed in section 5.2. However, to obtain more detailed insights in the complex deformation pattern of these individual segments, a full 3D evaluation of the available laser scanning results is indispensable. That way, displacements and rotations of the individual segments around all three coordinate axes can be identified and the interaction between adjacent segments and tunnel rings can be evaluated. Future research can focus on the development of a methodology for the detection, the quantification and the visualisation of the 3D displacements of tunnel segments. In addition, the interpretation of the laser scanning data should not be limited to a single tunnel ring, but can be expanded to adjacent tunnel sections, included in the point clouds. That way, the installation imperfections could be determined for each of these sections, allowing to further investigate the impact of neighbouring tunnel rings on each other.

10.2.3 Design of segmental tunnel linings

The presented research has demonstrated the opportunity to model all joints using contact definitions between the segments. Using this approach, it was

possible to simulate the complicated three-dimensional deformation state in the initial period after ring assembly and the corresponding stresses in the lining segments. However, the applied FE-model can still be enhanced by taking into account the tangential bedding stiffness and soil loading, which were neglected in this research. Furthermore, realistic tail grouting pressures should be implemented in the FE-analysis, to investigate the behaviour of the tunnel lining when leaving the TBM shield. A more appropriate non-linear behaviour of the reinforced concrete segments could be implemented as well, in order to simulate damage mechanisms in the early stages of construction.

Further research is likely to prove that modelling of contact joints is the next essential step in the evolution of design models for segmental tunnel linings. It will provide the ability to determine to what extent the safety and durability of a segmental tunnel lining can be improved by using contact joints in the design. The influence of geometrical imperfections during ring assembly on the lining behaviour can be quantified, showing their impact on the material safeties that are used in the design procedures. However, in the FE-model presented in this research, the implementation of imperfections was limited to one central tunnel ring, flanked by perfectly circular rings. In order to study the combined effect of imperfections in adjoining rings, future research should model such inaccurate installation in multiple neighbouring rings. The magnitude of the imperfections could either be based on future monitoring results of adjoining tunnel sections, or an extensive statistical approach could be applied, combining theoretical imperfections in neighbouring rings.

The goal should be to obtain a standardised FE-model for segmental tunnel linings including contact joints and installation imperfections. For this purpose, various geometries will have to be investigated in order to quantify the effect of the contact definitions and installation imperfections for a large range of segmental linings. The geometry of the FE-model developed in this dissertation can be adapted by varying the following parameters:

- the inner diameter of the tunnel lining;
- the thickness of the tunnel lining;
- the number of segments in a single tunnel ring;
- the effective contact area between segments (based on joint geometry);
- the width of a tunnel ring.

At the same time, a realistic magnitude of the corresponding installation imperfections at the joints will have to be determined for those additional geometries.

Most certainly the imperfections will differ from the ones obtained for the Liefkenshoek project, as they are likely to depend on project-specific parameters such as lining dimensions and TBM equipment tolerances. Future research should therefore compare current results with available monitoring data from other projects worldwide. The analysis of the collected monitoring results will give an insight in the installation imperfections and provide a basis to determine the magnitude of the inaccuracies that should be modelled for the various tunnel geometries under investigation.

The development of the FE-model using contact joints in Chapter 6 has shown that the information in literature on specific coefficients of friction for tunnelling applications is very limited. The available coefficients of friction μ are characterized by a large range of values and have generally been determined for other types of structures. Due to the particularly small tolerances applied in segment prefabrication resulting in a very smooth concrete surface, it is expected that the friction values currently available in literature deviate significantly from actual tunnel lining behaviour. Results have shown the large influence of the applied value for μ on the results of FE-models including installation imperfections. Therefore, as part of future research, laboratory testing can be performed to determine representative friction coefficients for segmental tunnel linings.

The final goal should be to obtain a full quantification of the impact of installation imperfections (and inevitably also the modelling of contact joints) on the design of segmental tunnel linings. Results will indicate any dependencies with tunnel diameter, number of joints, soil conditions, etc. It will be possible to determine the magnitude of the installation imperfections that can still be tolerated using the current design models. A comparison with the achievable accuracy of the current installation procedures will learn whether or not recommendations need to be given to contractors for enhancing their levels of accuracy during ring assembly. Furthermore, it will be possible to specify the improved safety levels that can be assured when using an updated high-level design model with contact joints. By comparing these safety levels to the ones obtained using the current state-of-the-art design models, it will be possible to present a set of correction factors for the current low-level models to implicitly take into account contact joints and installation imperfections.

10.2.4 Tidal influence

Some remarks were made on the applicability of the theory of De Rouck & Van Damme (1996) for the quantification of the damping effect for wave-induced pore pressure variations. Various other theoretical models have been developed in literature to describe the attenuation of the pore pressures in the subsoil. Further research should check the level of correspondence between these analytical models and verify the validity of the results found in the presented research.

Furthermore, a one-dimensional approach was used in this research to determine the vertical elastic settlements of the Boom clay layer as an immediate response to the river tides. However, due to the undrained soil behaviour preventing a change in volume, horizontal deformations will occur as well. Therefore, additional insight in the elastic soil response to the fluctuating river tides might be obtained by considering a two-dimensional approach along the entire cross-section of the river.

Bibliography

- A. Abellán, J. M. Vilaplana, J. Calvet, D. García-Sellés & E. Asensio (2011). Rockfall monitoring by terrestrial laser scanning - case study of the basaltic rock face at Castellfollit de la Roca (Catalonia, Spain). *Natural hazards and earth system science*, 11(3):829–841.
- H. Ahrens, E. Lindner & K.-H. Lux (1982). Zur dimensionierung von Tunnelausbauten nach den “Empfehlungen zur berechnung von Tunneln im Lockergestein”. *Die Bautechnik*, 59(8):260–273.
- AITES/ITA WG2-Research (2011). ITA Report No. 9 - Monitoring and control in tunnel construction. Technical report.
- M. Alba, L. Fregonese, F. Prandi, M. Scaioni & P. Valgoi (2006). Structural monitoring of a large dam by terrestrial laser scanning. In H.-G. Maas & D. Schneider, editors, *ISPRS Commission V Symposium “Image engineering and vision metrology” (Vol. XXXVI-5)*. Dresden.
- L. Anheuser (1981). Neuzestlicher Tunnelausbau mit Stahlbetonfertigteilen. *Beton- und Stahlbetonbau*, 76(6):145–150.
- R. Argüelles-Fraga, C. Ordonez, S. Garcia-Cortes & J. Roca-Pardinas (2013). Measurement planning for circular cross-section tunnels using terrestrial laser scanning. *Automation in Construction*, 31:1–9.
- O. Arnau & C. Molins (2012). Three dimensional structural response of segmental tunnel linings. *Engineering Structures*, 44:210–221.
- O. Arnau & C. Molins (2015). Theoretical and numerical analysis of the three-dimensional response of segmental tunnel linings subjected to localized loads. *Tunnelling and Underground Space Technology*, 49:384–399.

- J. Atkinson & G. Sallfors (1991). Experimental determination of soil properties. In *Proceedings of the 10th ECSMFE, Vol. 3*, pp. 915–956. Florence.
- M. Bakhshi & V. Nasri (2014). Guidelines and methods on segmental tunnel lining analysis and design - Review and best practice recommendation. In A. Negro, M. Cecílio & W. Bilfinger, editors, *Tunnels for a better life - Proceedings of the World Tunnel Congress 2014: Iguassu Falls, Brazil*, volume XXXVI. CBT/ABMS.
- K. J. Bakker & A. Bezuijen (2009a). Ten years of bored tunnels in The Netherlands: Part I, geotechnical issues. In *Proceedings of the 6th International Symposium on Geotechnical Aspects of Underground Construction in Soft Ground, Shanghai, China*, pp. 243–248.
- K. J. Bakker & A. Bezuijen (2009b). Ten years of bored tunnels in The Netherlands: Part II structural issues. In *Proceedings of the 6th International Symposium on Geotechnical Aspects of Underground Construction in Soft Ground, Shanghai, China*, pp. 249–254.
- R. Bennett & R. Faris (1979). Ambient and dynamic pore pressures in fine-grained submarine sediments: Mississippi delta. *Applied Ocean Research*, 1(3):115–123.
- A. Bezuijen & A. M. Talmon (2003). Grout the foundation of a bored tunnel. In *Tunnelling. A Decade of Progress. GeoDelft 1995-2005*, pp. 95–100. Taylor & Francis.
- A. Bezuijen & A. M. Talmon (2004). Grout pressures around a tunnel lining, influence of grout consolidation and loading on lining. In *Proceedings of the 30th World Tunnel Congress, Singapore*.
- A. Bezuijen, A. M. Talmon, F. J. Kaalberg & R. Plugge (2004). Field measurements of grout pressures during tunnelling of the Sophia Rail Tunnel. *Journal of the Japanese Geotechnical Society of Soils and Foundations*, 44(1):39–48.
- E. Bilotta & G. Russo (2012). Backcalculation of internal forces in the segmental lining of a tunnel: The experience of Line 1 in Naples. In *Proceedings of the 7th International Symposium on Geotechnical Aspects of Underground Construction in Soft Ground, Rome, Italy*, pp. 213–221.

- E. Bilotta, G. Russo & C. Viggiani (2005). Ground movements and strains in the lining of a tunnel in cohesionless soil. In *Proceedings of the 5th International Symposium on Geotechnical Aspects of Underground Construction in Soft Ground, Amsterdam, The Netherlands*, pp. 705–710.
- M. Biot (1956a). Theory of propagation of elastic waves in a fluid-saturated porous solid - Part I: Low-frequency range. *The Journal of the Acoustical Society of America*, 28(2):168–178.
- M. Biot (1956b). Theory of propagation of elastic waves in a fluid-saturated porous solid - Part II: Higher frequency range. *Journal of the Acoustical Society of America*, 28(2):179–191.
- K. Bloemhof (2001). *Geometrisch tunnelmodel - Schade aan tunnelling van gesegmenteerde boortunnels*. masterthesis, TU Delft.
- C. B. M. Blom (2002). *Design philosophy of concrete linings for tunnels in soft soils*. Ph.D. thesis, TU Delft.
- C. B. M. Blom & G. P. C. van Oosterhout (1997). Rapport K100-W-061 Tweede orde evaluatie tunnelconstructie Tweede Heinenoordtunnel - Deel 1. Technical report, CUR/COB, Gouda.
- W. Boehler & A. Marbs (2003). Investigating laser scanner accuracy. Technical report, University of applied sciences, Mainz.
- J. Boussinesq (1885). *Application des potentiels à l'étude de l'équilibre et du mouvement des solides élastiques*. Gauthier-Villars, Paris.
- S. Boxheimer & J. Mignon (2009). Liefkenshoek Railway Tunnel in Antwerp. *Tunnel*, 7:25–31.
- S. Boxheimer & J. Mignon (2011). Half way of construction of the Liefkenshoek rail tunnel. *Tunnel*, 3:41–48.
- British Standards Institution (2008). *BS 5975:2008 Code of practice for temporary works procedures and the permissible stress design of falsework (+A1:2011)*. ISBN 9780580742576.
- G. Brux (2013). Eisenbahntunnel Liefkenshoek in Antwerpen. *Bautechnik*, 90(10):681–684.

- M. Budhu (2000). *Soil mechanics and foundations*. John Wiley & Sons, Inc., New York. ISBN 0-471-25231-X.
- S. Cavalaro, C. Blom, J. Walraven & A. Aguado (2011). Structural analysis of contact deficiencies in segmented lining. *Tunnelling and Underground Space Technology*, 26(6):734–749.
- CEN/TC 250 (2004). Eurocode 2: Design of concrete structures - Part 1-1: General rules and rules for buildings.
- P. Chaipannna, P. Jongpradist & T. Kalasin (2012). 3D FEA of shield tunnel segmental lining with ground spring model. In *Tunnelling and Underground Space for a Global Society: Proceedings of the World Tunnel Congress, Bangkok, Thailand*.
- T. A. Clarke (1996). A review of tunnel profiling methods. Technical report, Optical Metrology Centre.
- C. Clayton (2011). Stiffness at small strain: research and practice. *Géotechnique*, 61(1):5–37.
- E. De Beer (1959). *Grondmechanica, deel I: Inleidende begrippen*. N.V. Standaard Boekhandel, 4th edition.
- E. De Beer (1971). Problèmes posés par la construction du tunnel sous l’escalot a Anvers.
- J. De Rouck & L. Van Damme (1996). Overall slope stability analysis of rubble mound breakwaters. In B. L. Edge, editor, *Proceedings of 25th Conference on Coastal Engineering, Orlando, Florida, Sept. 2-6*, pp. 1603–1616. ASCE, New York.
- D. Delaloye, J. Hutchinson & M. Diederichs (2011). Accuracy issues associated with Lidar scanning for tunnel deformation monitoring. In *2011 Pan-am CGS geotechnical conference*. Toronto.
- N. Della Valle, R. Salas Monge & E. Savin (2014). Adoption of shear keys to provide stability to TBM tunnels segmental lining during cross passages construction: The example of Aked tunnel. In A. Negro, M. Cecílio & W. Bilfinger, editors, *Tunnels for a better life - Proceedings of the World Tunnel Congress 2014: Iguassu Falls, Brazil*, volume XXXVI. CBT/ABMS.

- N. A. Do, D. Dias, P. Oreste & I. Djeran-Maigre (2013). 2D numerical investigation of segmental tunnel lining behavior. *Tunnelling and Underground Space Technology*, 37:115–127.
- DOV (2015). Databank Ondergrond Vlaanderen. URL <http://dov.vlaanderen.be>.
- H. Duddeck (1980). Empfehlungen zur berechnung von Tunneln im Lockergestein. *Die Bautechnik*, 57(10):349–356.
- H. Duddeck & J. Erdmann (1985). On structural design models for tunnels in soft ground. *Underground Space*, 9(5/6):246–259.
- J. Erdmann & H. Duddeck (1983). Statik der Tunnel im Lockergestein - Vergleich der Berechnungsmodelle. *Bauingenieur*, 58(11):407–414.
- Fib (2013). *fib Model code for concrete structures 2010*. Wilhelm Ernst & Sohn, Berlin. ISBN 978-3-433-03061-5.
- T. W. Groeneweg (2007). *Shield driven tunnels in ultra high strength concrete - Reduction of the tunnel lining thickness*. Ph.D. thesis, TU Delft.
- F. Grübl (2006). Modern design aspects of segmental lining. In *International Seminar on Tunnels and Underground Works, Lisbon*.
- F. Grübl (2012). Segmental ring design - New challenges with high tunnel diameters. In *Tunnelling and Underground Space for a Global Society: Proceedings of the World Tunnel Congress, Bangkok, Thailand*, pp. 2–11.
- X. Gu, J. Yang & M. Huang (2013). Laboratory measurements of small strain properties of dry sands by bender element. *Soils and Foundations*, 53(5):735–745.
- A. Harding & M. Chappell (2014). State of the art - Precast linings. *North American Tunneling Journal*, (oct/nov):16–22.
- F. Haring (2002). *Spanningen in de bouwfase en de gebruiksfase van boortunnels*. masterthesis, TU Delft.
- M. J. Henriques & J. Casaca (2006). Uncertainty in tacheometric measurement of convergences in tunnels. In *3rd IAG/12th FIG symposium*. FIG, Baden.

- C. Hesse & H. Stramm (2004). Deformation measurements with laser scanners. Possibilities and challenges. In *International symposium on modern technologies, education and professional practice in geodesy and related fields*, pp. 228–240. Sofia.
- B. H. M. Hewett & W. L. Brown (1910). The New York tunnel extension of the Pennsylvania railroad - The North river tunnels. In *Transactions of the American Society of Civil Engineers, Vol. LXVIII*, pp. 152–302. ASCE, New York.
- K. Hoffmann (2012). *An introduction to stress analysis and transducer design using strain gauges*.
- Hottinger Baldwin Messtechnik GmbH (2016a). Optical fiber sensors. URL <http://www.hbm.com/>.
- Hottinger Baldwin Messtechnik GmbH (2016b). Strain gauges for stress analysis. URL <http://www.hbm.com>.
- A. B. Huang, J. T. Lee, C. C. Wang, Y. T. Ho & T. S. Chuang (2013). Field monitoring of shield tunnel lining using optical fiber bragg grating based sensors. In *Proceedings of the 18th International Conference on Soil Mechanics and Geotechnical Engineering, Paris*, pp. 1719–1722.
- K.-P. Huang, T.-T. Wang, T.-H. Huang & F.-S. Jeng (2010). Profile deformation of a circular tunnel induced by ambient stress changes. *Tunnelling and Underground Space Technology*, 25(3):266–278.
- Hydrological Information Centre (2015). Flanders Hydraulics Research. URL <http://www.waterinfo.be>.
- T. Ishimura, H. Mashimo & S. Morimoto (2013). Influence of construction load for segmental lining by result of in-situ measurement and numerical analysis. In G. Anagnostou & H. Ehrbar, editors, *Underground - The way to the future*, pp. 2372–2379. Taylor & Francis Group, London. ISBN 978-1-315-88727-2.
- ITA Working Group on General Approaches to the Design of Tunnels (1988). Guidelines for the design of tunnels. *Tunnelling and Underground Space Technology*, 3(3):237–249.
- N. Iyer, S. Jayanti, K. Lou, Y. Kalyanaraman & K. Ramani (2005). Three-dimensional shape searching: state-of-the-art review and future trends. *Computer-aided design*, 37:509–530.

- C. E. Jacob (1940). The flow of water in an elastic artesian aquifer. *Transactions of the American Geophysical Union*, 21(2):574–586.
- C. M. Jacobs (1910). The New York tunnel extension of the Pennsylvania railroad - The North river division. In *Transactions of the American Society of Civil Engineers*, Vol. LXVIII, pp. 32–61. ASCE, New York.
- G. Jacobs (2004). High definition surveying - 3D laser scanning: understanding the “useful range” of laser scanners. *Professional Surveyor*, 24(11).
- G. Jacobs (2005). High definition surveying - 3D laser scanning: understanding laser scanning terminology. *Professional Surveyor*, 25(2).
- P. Janssen (1983). *Tragverhalten von Tunnelausbauten mit Gelenktübbings*. masterthesis, Technische Universität Braunschweig, Braunschweig.
- D. Jeng (2003). Wave-induced sea floor dynamics. *Applied Mechanics Reviews*, 56(4):407–429.
- B. Jones (2015a). Segmental lining joints. *Tunnelling Journal*, (Feb/March):38–40.
- B. Jones (2015b). Segmental linings - longitudinal effects. *Tunnelling Journal*, (april/may):17–20.
- JSCE (2007). *Standard specifications for tunneling-2006: Shield tunnels*. ISBN 978-4-8106-0568-6.
- L. Karl (2005). *Dynamic soil properties out of SCPT and bender element tests with emphasis on material damping*. Ph.D. thesis, Ghent University.
- T. Kasper & G. Meschke (2003). Three-dimensional finite element simulations of hydroshield tunneling. In J. Saveur, editor, *(Re)claiming the Underground Space: Proceedings of the ITA World Tunnelling Congress 2003, 12-17 April 2003, Amsterdam, The Netherlands Volume 2*, pp. 779–785. A.A. Balkema Publishers, Amsterdam. ISBN 9058095444.
- T. Kasper & G. Meschke (2004). A 3D finite element simulation model for TBM tunneling in soft ground. *International Journal for Numerical and Analytical Methods in Geomechanics*, 28(14):1441–1460.
- M. J. Kavvadas (2003). Monitoring and modelling ground deformations during tunnelling. In *11th FIG symposium on deformation measurements*. FIG, Santorini.

- V. A. Kontogianni & S. C. Stiros (2005). Induced deformation during tunnel excavation: evidence from geodetic monitoring. *Engineering Geology*, 79(1-2):115–126.
- P. Laga, S. Louwye & S. Geets (2001). Paleogene and Neogene lithostratigraphic units (Belgium). *Geologica Belgica*, 4(1/2):135–152.
- H. M. Lee & H. S. Park (2013). Measurement of maximum strain of steel beam structures based on average strains from vibrating wire strain gages. *Experimental Techniques*, 37(2):23–29.
- Leica Geosystems (2009). Leica HDS6100 datasheet. URL <http://www.leica-geosystems.com/hds>.
- Leica Geosystems (2013a). Leica HDS8810 datasheet. URL <http://www.leica-geosystems.com>.
- Leica Geosystems (2013b). Leica ScanStation P20 datasheet. URL <http://www.leica-geosystems.com/hds>.
- H. J. Lengkeek (1997). *Analyse grond-tunnelinteractie - Analytische en numerieke bepaling van veerstijfheid van de grond voor toepassing in ring- en liggermodel*. masterthesis, TU Delft.
- D. D. Lichti, M. P. Stewart, M. Tsakiri & A. J. Snow (2000). Calibration and testing of a terrestrial laser scanner. In *International archives of photogrammetry and remote sensing (Vol. XXXI-B5)*. Amsterdam.
- S. Likitlersuang, S. Teachavorasinskun, C. Surarak, E. Oh & A. Balasubramaniam (2013). Small strain stiffness and stiffness degradation curve of Bangkok Clays. *Soils and Foundations*, 53(4):498–509.
- C. Lin, S. Wu & T. Xia (2015). Design of shield tunnel lining taking fluctuations of river stage into account. *Tunnelling and Underground Space Technology*, 45:107–127.
- H. Liu & D. Jeng (2007). A semi-analytical solution for random wave-induced soil response and seabed liquefaction in marine sediments. *Ocean Engineering*, 34(8-9):1211–1224.
- A. Luttikholt (2007). *Ultimate Limit State Analysis of a segmented tunnel lining - Results of full-scale tests compared to finite element analysis*. masterthesis, TU Delft.

- R. MacLowry (2014). The Rise and Fall of Penn Station. URL <http://www.thirteen.org/programs/american-experience/hudson-river-tunnel-shifting/>.
- M. Majumder, T. K. Gangopadhyay, A. K. Chakraborty, K. Dasgupta & D. K. Bhattacharya (2008). Fibre Bragg gratings in structural health monitoring - Present status and applications. *Sensors and Actuators, A: Physical*, 147(1):150–164.
- H. Mashimo & T. Ishimura (2006). Numerical modelling of the behavior of shield tunnel lining during assembly of a tunnel ring. In E. Bakker, KJ and Bezuijen, A and Broere, W and Kwast, editor, *Geotechnical Aspects of Underground Construction in Soft Ground*, pp. 587–593. Int Soc Soil Mech & Geotech Engn, TC 28, Taylor & Francis, London. ISBN 0-415-39124-5.
- C. Mei & M. Foda (1981). Wave-induced responses in a fluid-filled poro-elastic solid with a free surface - A boundary layer theory. *Geophysical Journal International*, 66:597–631.
- P. Mengé (2001). Soil investigation results at Sint-Katelijne-Waver (Belgium). In A. Holeyman, editor, *Screw piles - installation and design in stiff clay*, pp. 19–62. A A Balkema Publishers. ISBN 90-5809-192-9.
- S. C. Möller & P. A. Vermeer (2005). Prediction of settlements and structural forces in linings due to tunnelling. In *Proceedings of the 5th International Symposium on Geotechnical Aspects of Underground Construction in Soft Ground, Amsterdam, The Netherlands*, pp. 621–627.
- D. Moore, G. McCabe & B. Craig (2009). *Introduction to the Practice of Statistics*. W. H. Freeman and Company, New York, sixth edition. ISBN 9781429216234.
- A. M. Muir Wood (1975). The circular tunnel in elastic ground. *Géotechnique*, 25(1):115–127.
- National Instruments (2016). FBG optical sensing : a new alternative for challenging strain measurements. URL <http://www.ni.com/white-paper/12338/en/>.
- T. Nuttens (2014). *Tunnel ovalisation monitoring: 3D data acquisition with laser scanning and point cloud processing*. Phd thesis, Ghent University.

- T. Nuttens, C. Stal, H. De Backer, G. Deruyter, K. Schotte, P. Van Bogaert & A. De Wulf (2015). Laser scanning for ovalisation measurements: standard deviations and smoothing levels ('Diabolo' project, Belgium). *ASCE Journal of Surveying Engineering*, In Press.
- T. Nuttens, C. Stal, H. De Backer, K. Schotte, P. Van Bogaert, P. Detry & A. De Wulf (2014). Terrestrial laser scanning as a key element in the integrated monitoring of tidal influences on a twin-tube concrete tunnel. *The Photogrammetric Record*, 29(148):402–416.
- S. Okusa (1985). Wave-induced stresses in unsaturated submarine sediments. *Géotechnique*, 35(4):517–532.
- S. Okusa & A. Uchida (1980). Pore-water pressure change in submarine sediments due to waves. *Marine Geotechnology*, 4(2):145–161.
- N. Pfeifer & C. Briese (2007). Laser scanning - Principles and applications. In *3rd International Exhibition & Scientific Congress on Geodesy, Mapping, Geology, Geophysics, Cadaster GEO-SIBERIA*, pp. 93–112. Nowosibirsk.
- K. Piriyaikul (2006). *Anisotropic stress-strain behaviour of Belgian Boom clay in the small strain region*. Ph.D. thesis, Ghent University.
- Precast/Prestressed Concrete Institute (2010). *PCI design handbook - precast and prestressed concrete*. October. 7th edition. ISBN 978-0-937040-87-4.
- H. Qingwu & Y. Wanlin (2012). Tempo-space deformation detection of subway tunnel based on sequence temporal 3D point cloud. *Disaster Advances*, 5(4).
- M. Rahayem, N. Werghi & J. Kjellander (2012). Best ellipse and cylinder parameters estimation from laser profile scan sections. *Optics and lasers in engineering*, 50(9):1242–1259.
- B. Ring & R. da Fonseca (2014). Design of steel fiber reinforced segmental lining for Line 5, Lot 7 of Metro Sao Paulo. In A. Negro, M. Cecílio & W. Bilfinger, editors, *Tunnels for a better life - Proceedings of the World Tunnel Congress 2014: Iquassu Falls, Brazil*, volume XXXVI. CBT/ABMS.
- M. Rioux (1994). Digital 3-D imaging: theory and applications. In *SPIE proceedings, videometrics III, International symposium on photonic and sensors for controls for commercial applications*, pp. 2–15. Boston.

- P. Rönholm, E. Honkavaara, P. Litkey, H. Hyypä & J. Hyypä (2007). Integration of laser scanning and photogrammetry. In P. Rönholm, H. Hyypä & J. Hyypä, editors, *International archives of photogrammetry, remote sensing and spatial information sciences (Vol. XXXVI-3 / W52)*, pp. 355–362. Espoo.
- K. Rossler, P. Vitek, D. Cyron, J. Vitek, J. Kunak & M. Thewes (2012). Segmental liner behavior during EPBM Advance. In *Tunnelling and Underground Space for a Global Society: Proceedings of the World Tunnel Congress, Bangkok, Thailand*.
- RST Instruments (2016). Vibrating wire strain gauge. URL <http://www.rstinstruments.com/>.
- T. Schäfer, T. Weber, P. Kyrinovic & M. Zamecnikova (2004). Deformation measurement using terrestrial laser scanning at the hydropower station of Gabčíkovo. In *INGEO 2004 and FIG regional Central and Eastern European conference on engineering surveying*. Bratislava, Slovakia.
- H. Schulze & H. Duddeck (1964). Statische berechnung schildvorgetriebener tunnel. *Festschrift Beton- und Monierbau AG 1889-1964*, pp. 87–114.
- V. Sharma, M. Nair & S. Meller (2000). The use of vibrating wire strain gauges in geotechnics. In *Geoshore International Conference on Offshore and Nearshore Geotechnical Engineering*, pp. 201–204. A A Balkema Publishers.
- N. Shirlaw, D. P. Richards, P. Ramond & P. Longchamp (2004). Recent experience in automatic tail void grouting with soft ground tunnel boring machines. In *Proceedings of the 30th World Tunnel Congress, Singapore*.
- Siemens PLM Software (2014). LMS Samtech - Samcef Field, version 16. URL <http://www.plm.automation.siemens.com/en{ }us/products/lms/samtech/index.shtml>.
- H. Sternberg & T. P. Kersten (2007). Comparison of terrestrial laser scanning systems in industrial as-built-documentation applications. In Gruen & Kahmen, editors, *Optical 3-D measurement techniques VIII (Vol. I)*, pp. 389–397. Zurich.
- H. Tajima, M. Kishida, N. Fukai, A. Dan & M. Saito (2006). Study on construction loads during shield tunneling using a three-dimensional FEM model. In

Safety in the Underground Space - Proceedings of the ITA-AITES World Tunnel Congress, Seoul, Korea.

- A. M. Talmon & A. Bezuijen (2005). Grouting the tail void of bored tunnels: the role of hardening and consolidation of grouts. In *Proceedings of the 5th International Symposium on Geotechnical Aspects of Underground Construction in Soft Ground, Amsterdam, The Netherlands*, pp. 319–325.
- A. M. Talmon & A. Bezuijen (2009). Simulating the consolidation of TBM grout at Noordplaspolder. *Tunnelling and Underground Space Technology*, 24(5):493–499.
- E. Taverniers, Y. Plancke & F. Mostaert (2013). MONEOS - jaarboek monitoring WL - Basisboek: Overzicht monitoring hydrodynamiek en fysische parameters zoals door WL in het Zeescheldebekken gemeten - uitleggend basisboek met algemene situering, methodologie en achtergrond. Technical report, Waterbouwkundig Laboratorium, Antwerp, Belgium.
- K. Terzaghi (1925). *Erdbaumechanik auf bodenphysikalischer grundlage*. Deuticke F., Leipzig.
- K. Terzaghi & R. B. Peck (1948). *Soil mechanics in engineering practice*. John Wiley & Sons, Inc., New York; London.
- The British Tunnelling Society and The Institution of Civil Engineers (2004). *Tunnel lining design guide*. Thomas Telford.
- G. Tiberti & G. Plizzari (2014). Structural behavior of precast tunnel segments under TBM thrust actions. In A. Negro, M. Cecilio & W. Bilfinger, editors, *Tunnels for a better life - Proceedings of the World Tunnel Congress 2014: Iguassu Falls, Brazil*, volume XXXVI. CBT/ABMS.
- Trimble (2012). Trimble TX5 scanner datasheet. URL <http://www.trimble.com>.
- Trimble (2013). Trimble TX8 laser scanner datasheet. URL <http://www.trimble.com>.
- R. Ummenthun (2001). *De leegte grouten - het groutproces bij geboorde tunnels*. Ph.D. thesis, TU Delft.
- G. Van Alboom, H. Dupont, J. Maertens & K. Haelterman (2012). Glauconiethoudende zanden. *Geotechniek*, (April):32–37.

- P. Van Bogaert (2008). Le projet Liefkenshoek de liaison ferroviaire sous l'Escaut. *Tunnels et Ouvrages Souterrains*, (205):49–55.
- P. Van Bogaert (2009). Recent and future railway tunnels in Belgium. In P. Kocsonya, editor, *Proceedings ITA-AITES World Tunnel Congress 2009: Safe tunnelling for the city and for the environment*, pp. 689–690. Hungarian Tunnelling Association, Budapest, Hungary.
- P. Van Bogaert & B. De Pauw (2008). New railway connection below Brussels Airport. In *Proceedings of the 17th IABSE Congress Creating and Renewing Urban Structures*, pp. 280–281. IABSE, Chicago, USA. ISBN 978-3-85748-118-5.
- P. Van Bogaert & J. Vereerstraeten (2005). Antwerp North-South railway link for a new urban development Tunnelling and Underground Techniques. In *Receuil du Congrès International de l'AFTES Les Tunnels Clé d'une Europe Durable*, pp. 279–286. A.A. Balkema, Chambéry, France.
- E. J. van der Horst (1998). *Invloed van voegmaterialen op de krachtswerking in gesegmenteerde betonnen boortunnels*. masterthesis, TU Delft.
- E. J. van der Horst (1999). Montagespanningen bij de bouw van geboorde tunnels - Literatuurstudie. Technical report, CUR/COB.
- A. Vancamp (2012). *Grondmechanische herkenning en eigenschappen van glauconietzanden*. masterthesis, Xios Hogeschool Limburg.
- S. B. Walsh, D. J. Borello, B. Guldur & J. F. Hajjar (2013). Data processing of point clouds for object detection for structural engineering applications. *Computer-aided civil and infrastructure engineering*, 00:1–14.
- A. Wehr & U. Lohr (1999). Airborne laser scanning - an introduction and overview. *ISPRS Journal of Photogrammetry & Remote Sensing*, 54(2-3):68–82.
- Working Group No. 2 International Tunnelling Association (2000). Guidelines for the design of shield tunnel lining. *Tunnelling and Underground Space Technology*, 15(3):303–331.
- J.-S. Yoon, M. Sagong, J. S. Lee & K. Lee (2009). Feature extraction of a concrete tunnel liner from 3D laser scanning data. *NDT&E International*, 42:97–105.

- K. Zen & H. Yamazaki (1991). Field observation and analysis of wave-induced liquefaction in seabed. *Soils and Foundations*, 31(4):161–179.
- D.-M. Zhang, H.-W. Huang, Q.-F. Hu & F. Jiang (2015). Influence of multi-layered soil formation on shield tunnel lining behavior. *Tunnelling and Underground Space Technology*, 47:123–135.
- H.-M. Zogg & H. Ingensand (2008). Terrestrial laser scanning for deformation monitoring - load tests on the Felsenau Viaduct (CH). In C. Jun, editor, *XXIst ISPRS Congress - Silk Road for Information from Imagery - Technical Commission V*, pp. 555–562. Beijing, China.

Appendix A

Keystone orientation in the monitored sections

This appendix gives an overview of the orientation of the individual tunnel segments, and specifically the keystone, in each measurement section of the Liefkenshoek project.

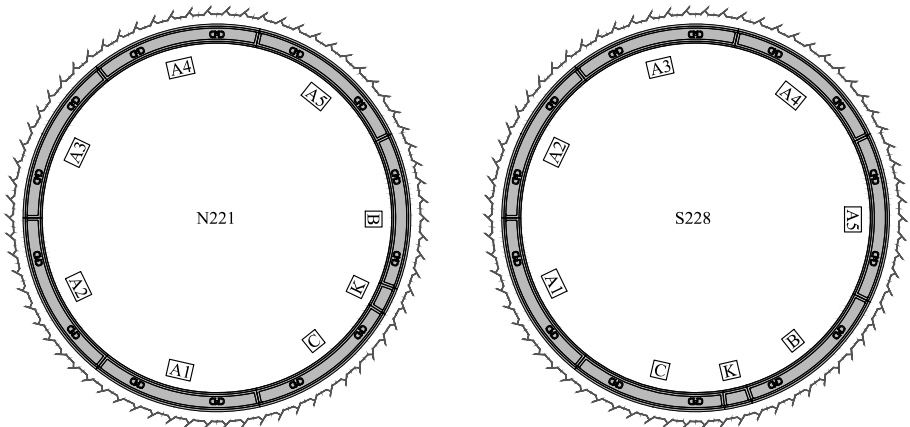


Figure A.1. Segment orientation in tunnel sections N221 and S228.

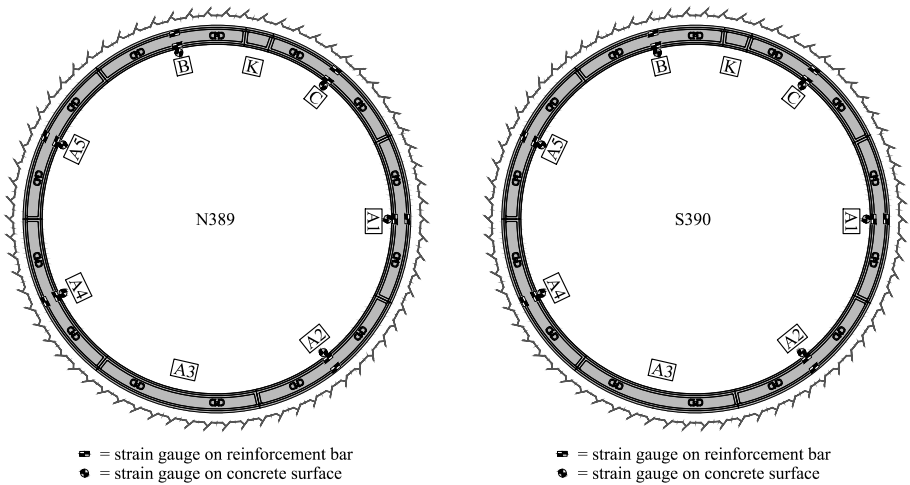


Figure A.2. Segment orientation in tunnel sections N389 and S390.

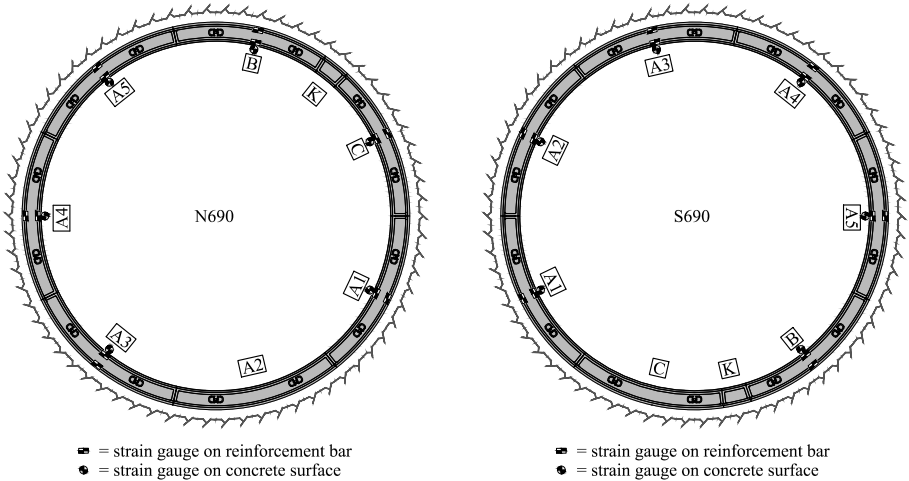


Figure A.3. Segment orientation in tunnel sections N690 and S690.

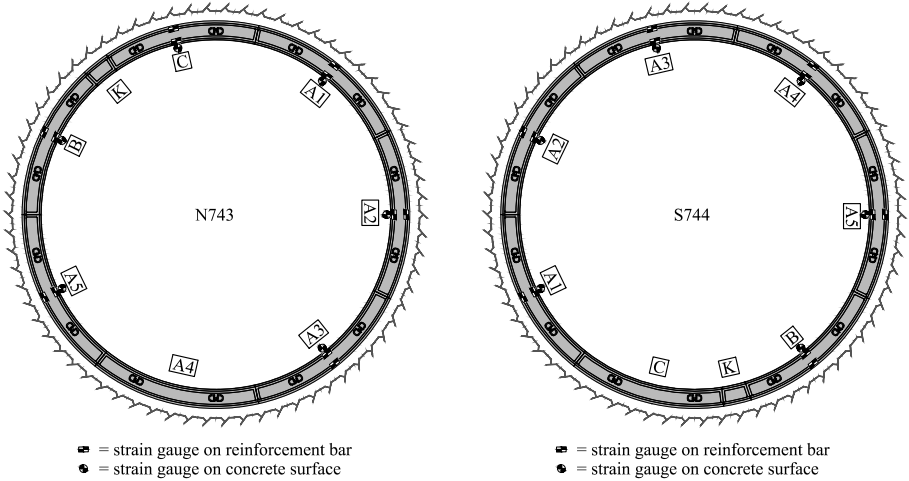


Figure A.4. Segment orientation in tunnel sections N743 and S744.

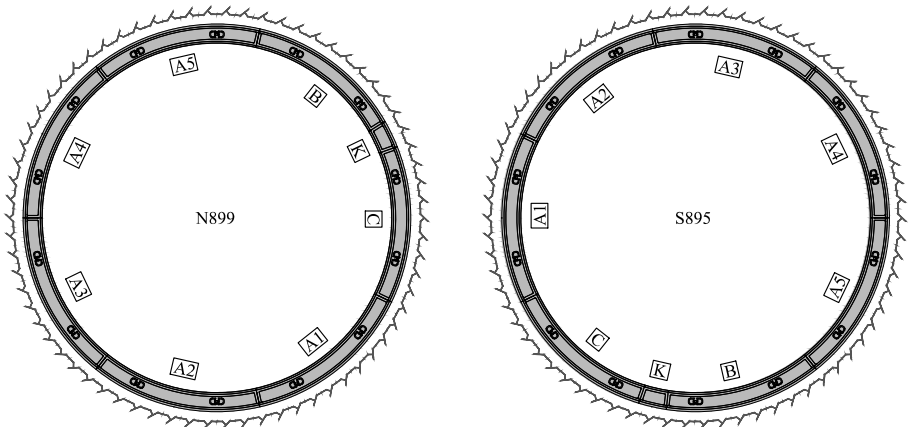


Figure A.5. Segment orientation in tunnel sections N899 and S895.

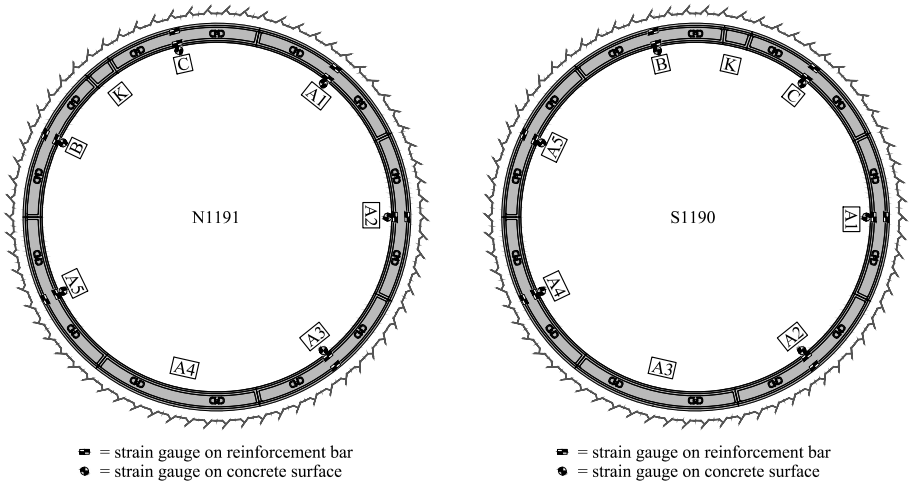


Figure A.6. Segment orientation in tunnel sections N1191 and S1190.

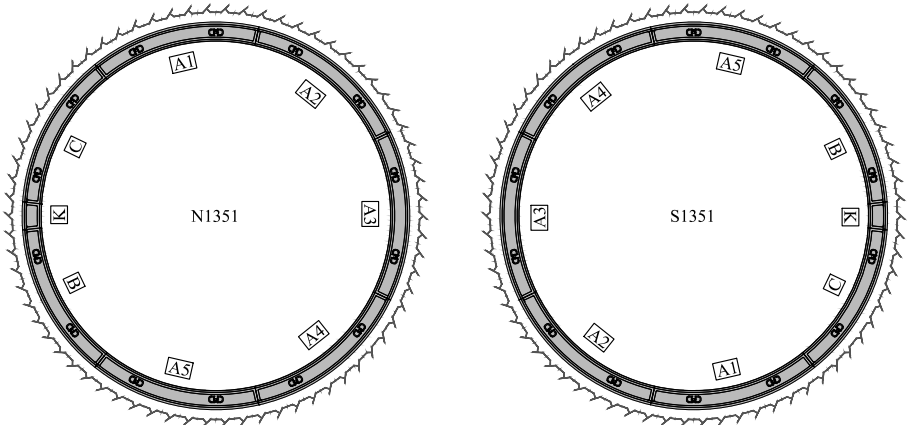


Figure A.7. Segment orientation in tunnel sections N1351 and S1351.

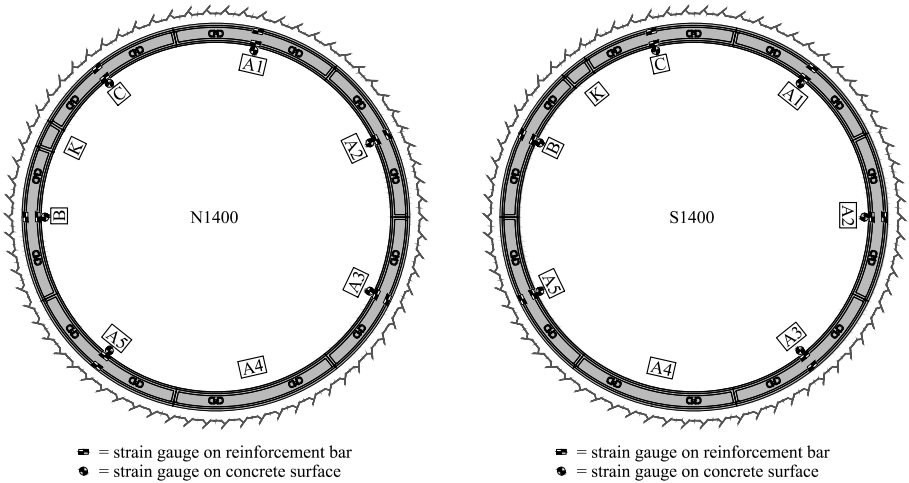


Figure A.8. Segment orientation in tunnel sections N1400 and S1400.

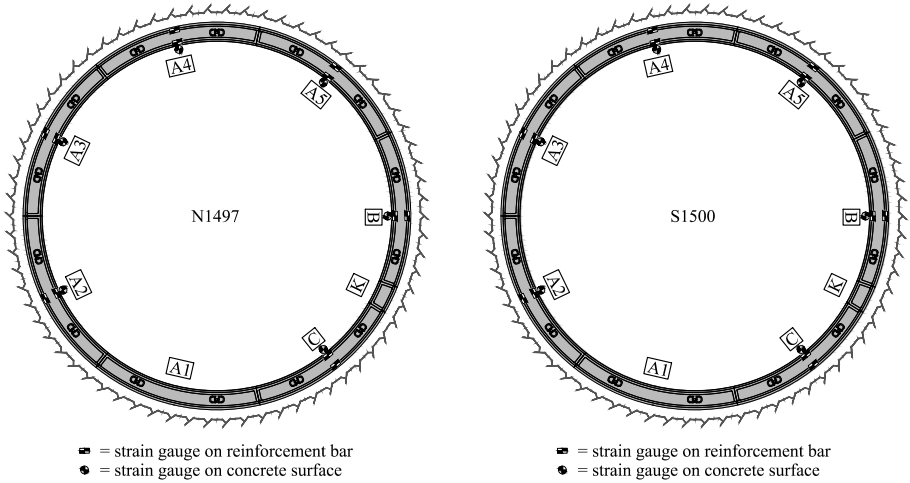


Figure A.9. Segment orientation in tunnel sections N1497 and S1500.

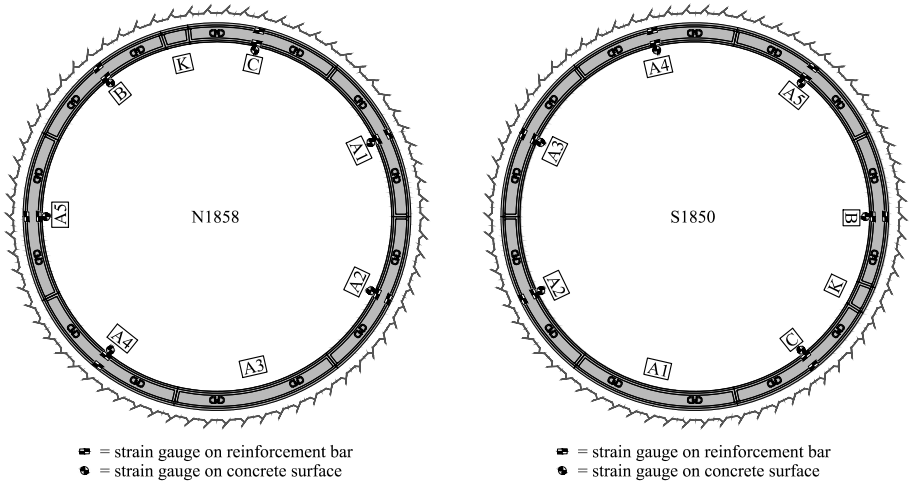


Figure A.10. Segment orientation in tunnel sections N1858 and S1850.

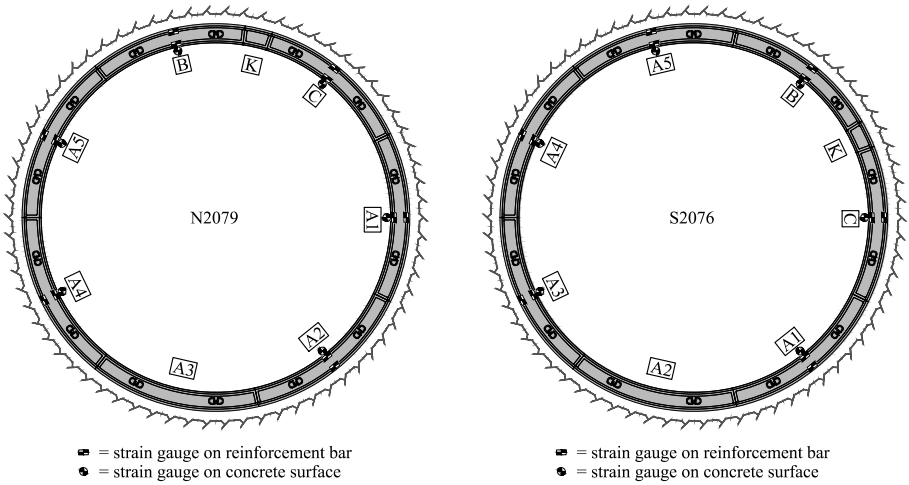


Figure A.11. Segment orientation in tunnel sections N2079 and S2076.

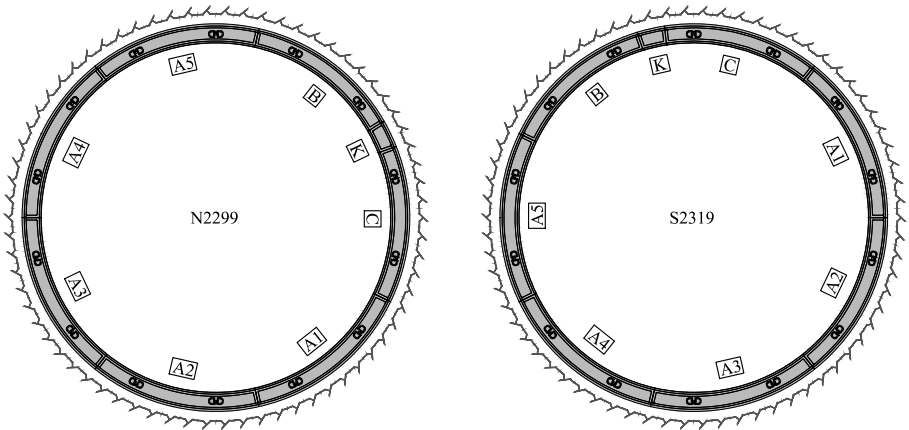


Figure A.12. Segment orientation in tunnel sections N2299 and S2319.

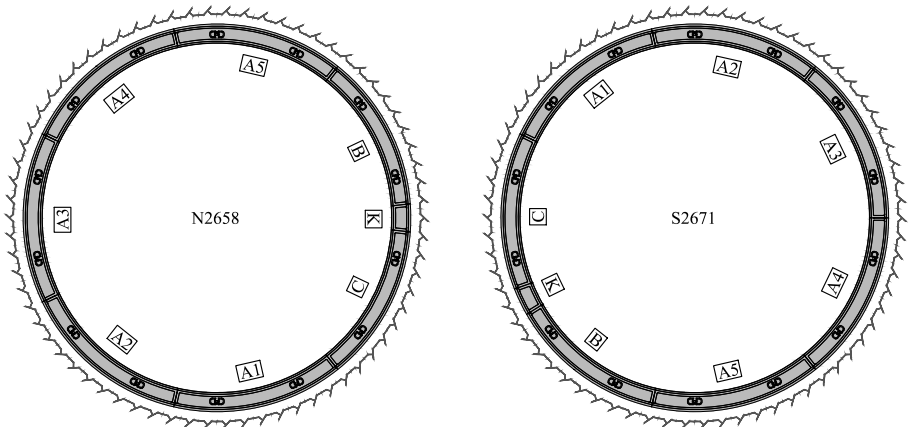


Figure A.13. Segment orientation in tunnel sections N2658 and S2671.

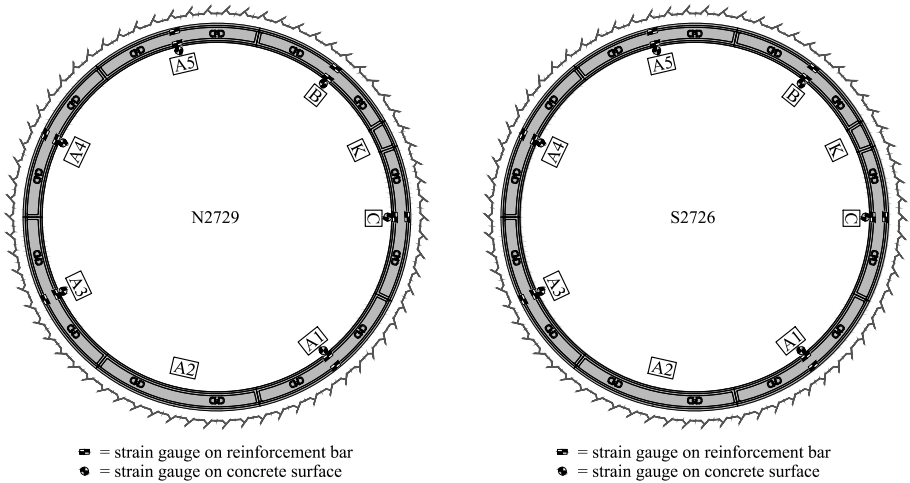


Figure A.14. Segment orientation in tunnel sections N2729 and S2726.

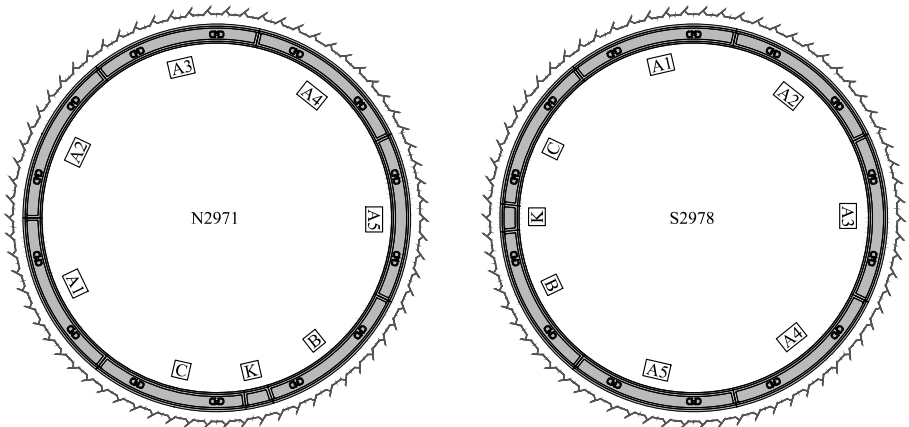


Figure A.15. Segment orientation in tunnel sections N2971 and S2978.

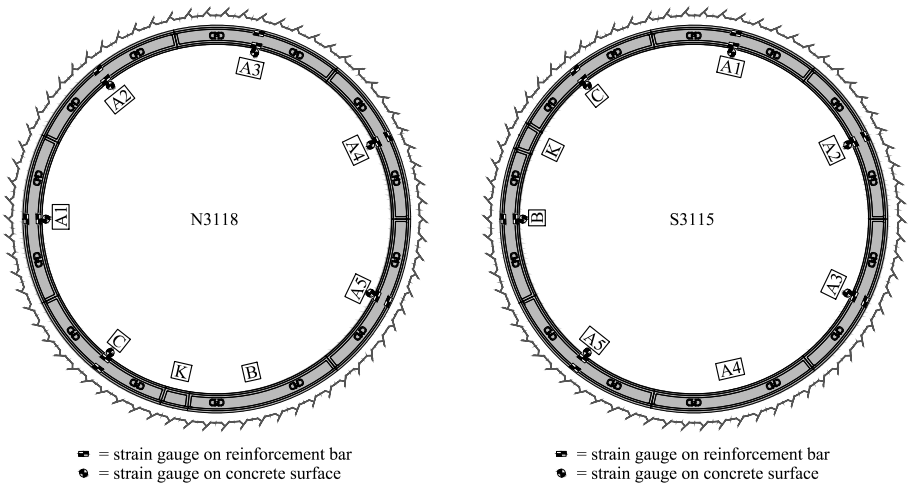


Figure A.16. Segment orientation in tunnel sections N3118 and S3115.

Appendix B

Passage of second tunnel drive: additional results

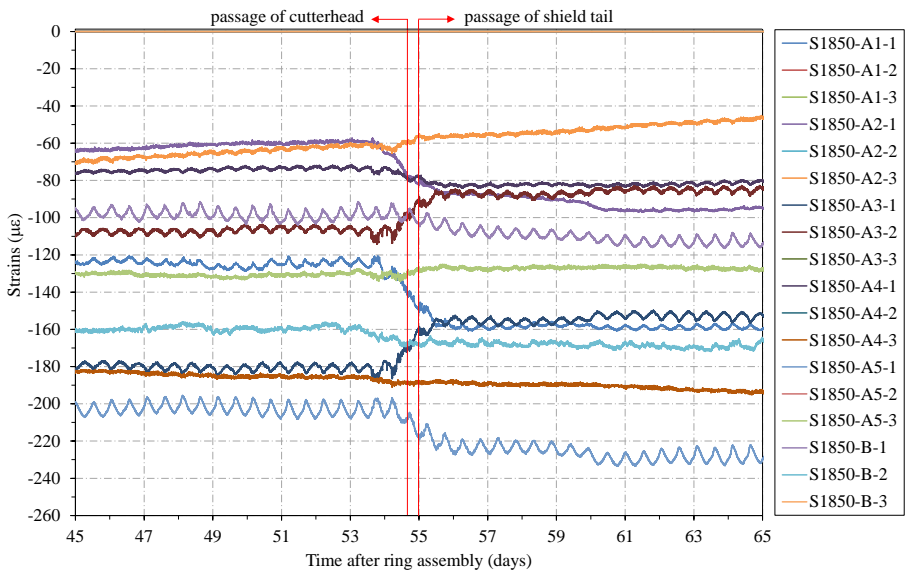


Figure B.1. Strain results in section S1850 during passage of second tunnel drive.

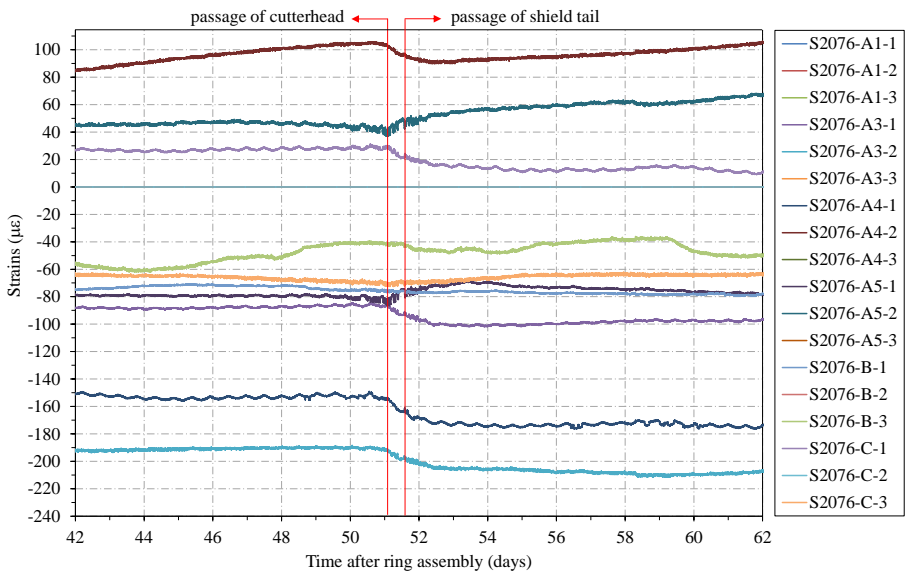


Figure B.2. Strain results in section S2076 during passage of second tunnel drive.

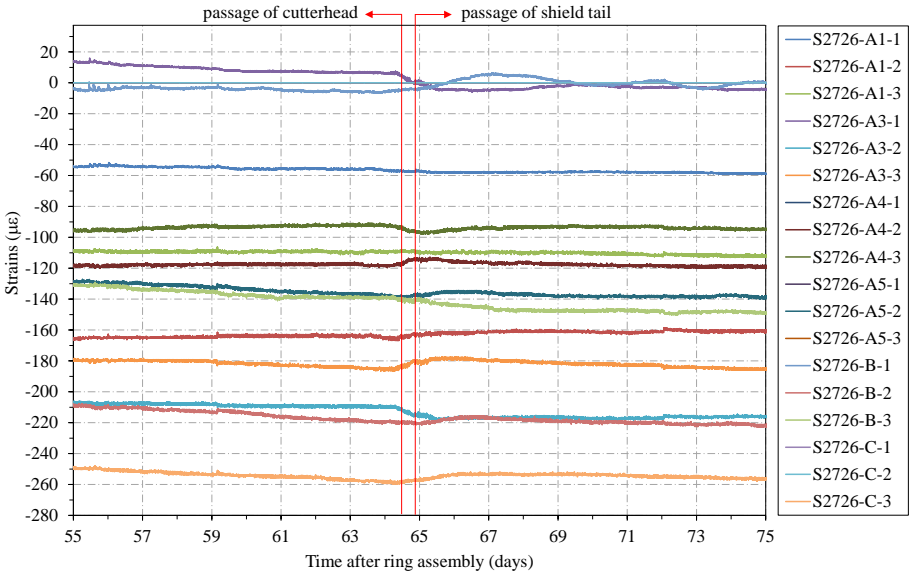


Figure B.3. Strain results in section S2726 during passage of second tunnel drive.

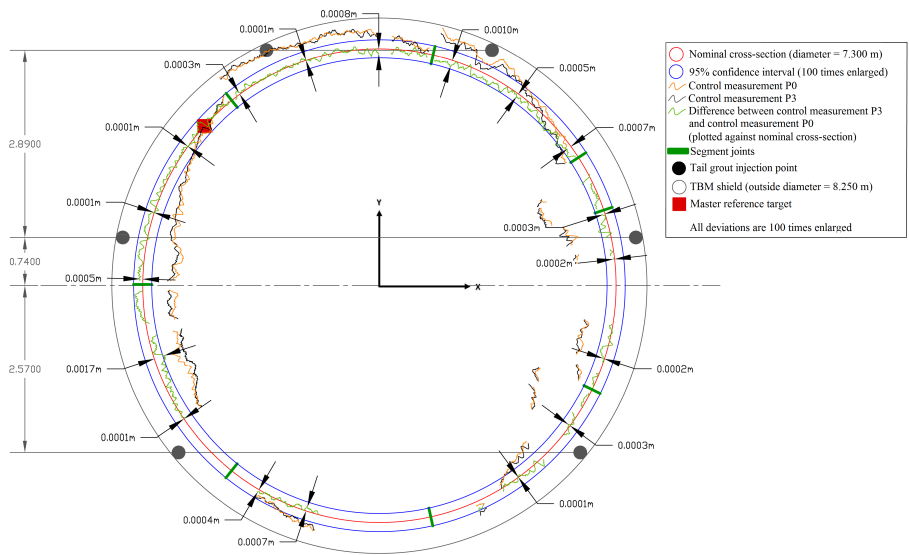


Figure B.4. Ovalisation results after passage of second tunnel drive: measurement CM P3 in comparison with CM P0 for section S2726.

Appendix C

Impact of the mesh size: additional results

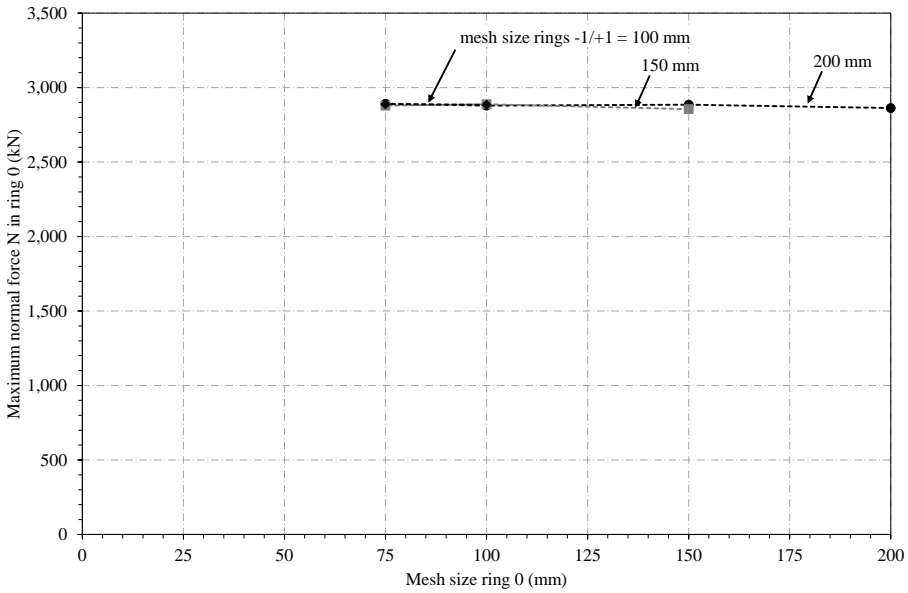


Figure C.1. Impact of the mesh size on the normal forces N in ring 0 for models using design geometry.

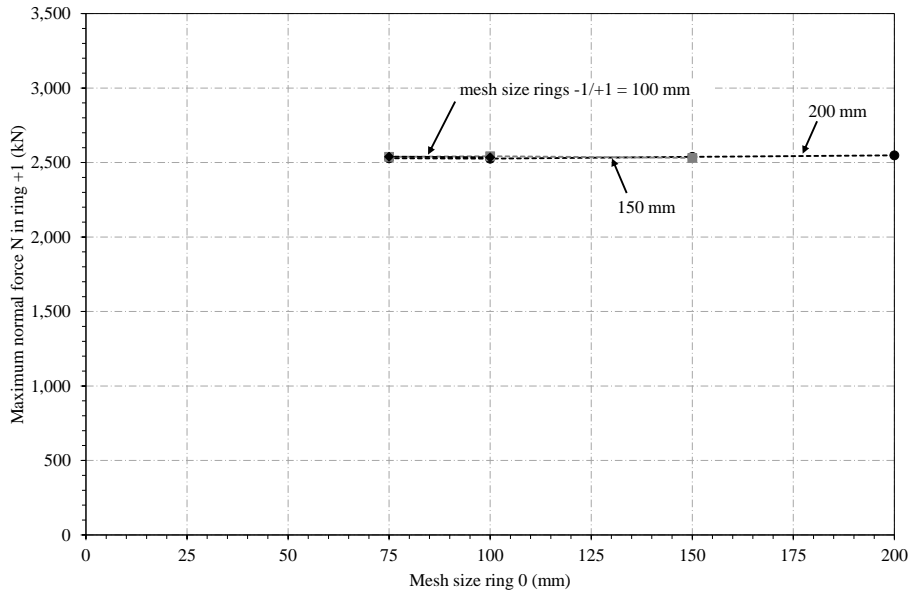


Figure C.2. Impact of the mesh size on the normal forces N in ring +1 for models using design geometry.

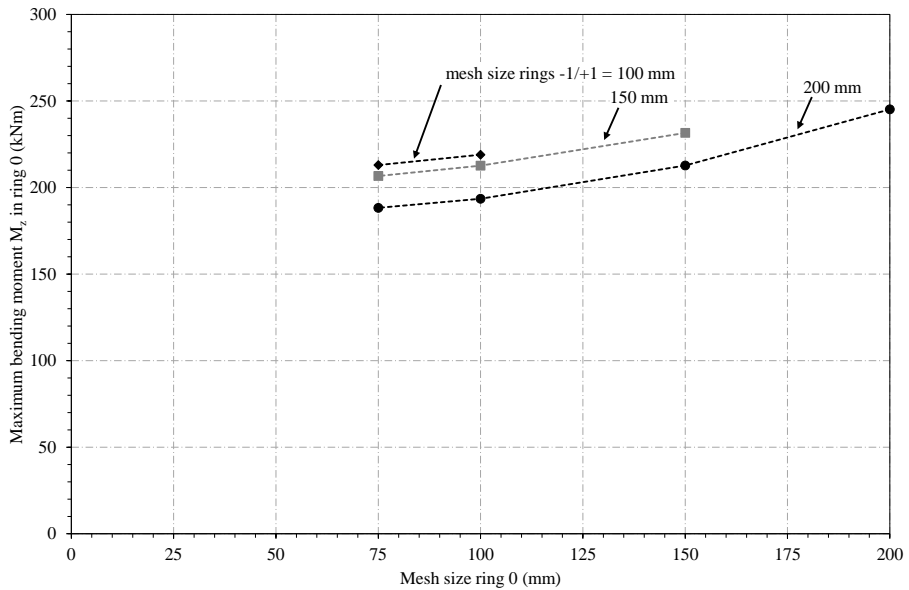


Figure C.3. Impact of the mesh size on the bending moments M_z in ring 0 for models using design geometry.

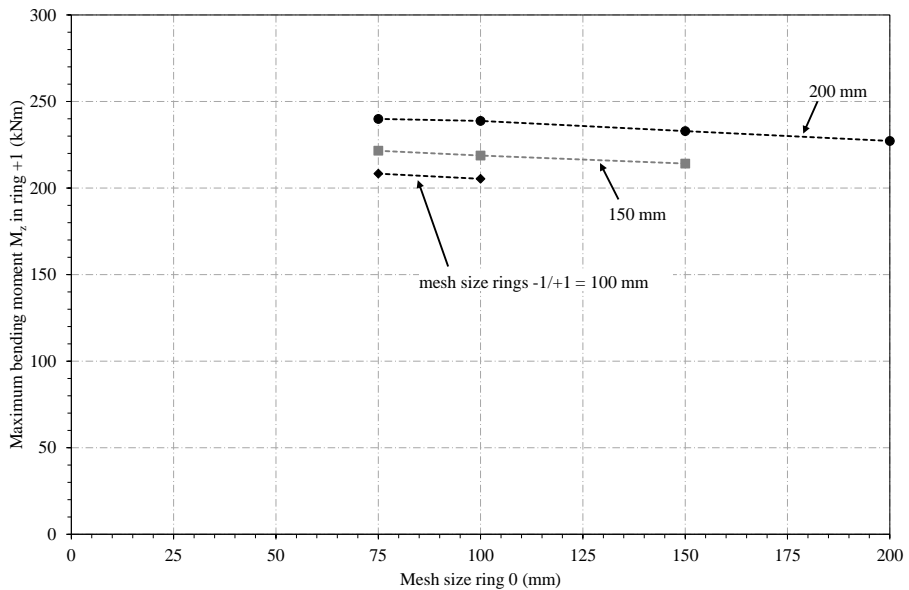


Figure C.4. Impact of the mesh size on the bending moments M_z in ring +1 for models using design geometry.

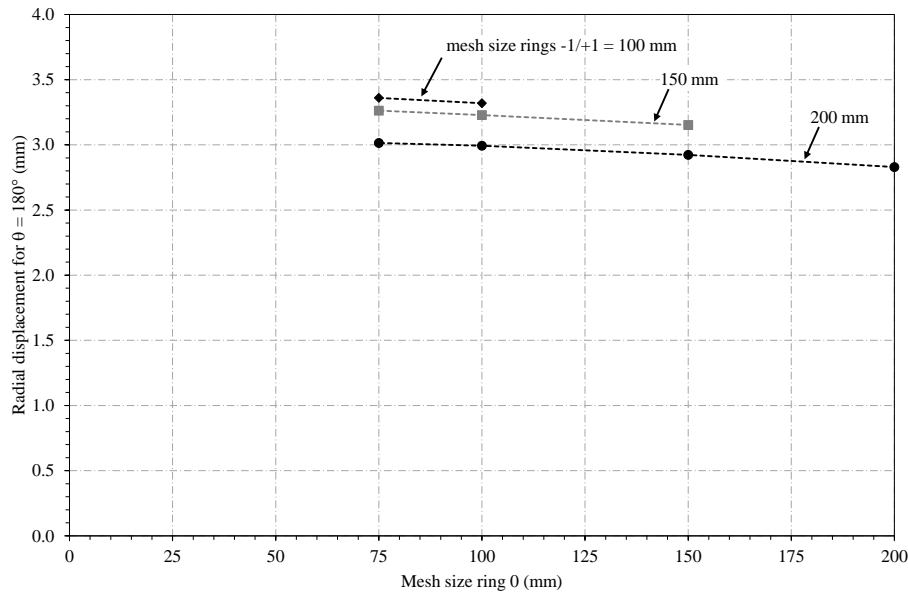


Figure C.5. Impact of the mesh size on the deformations of ring 0 for $\theta = 180^\circ$ for models using design geometry.

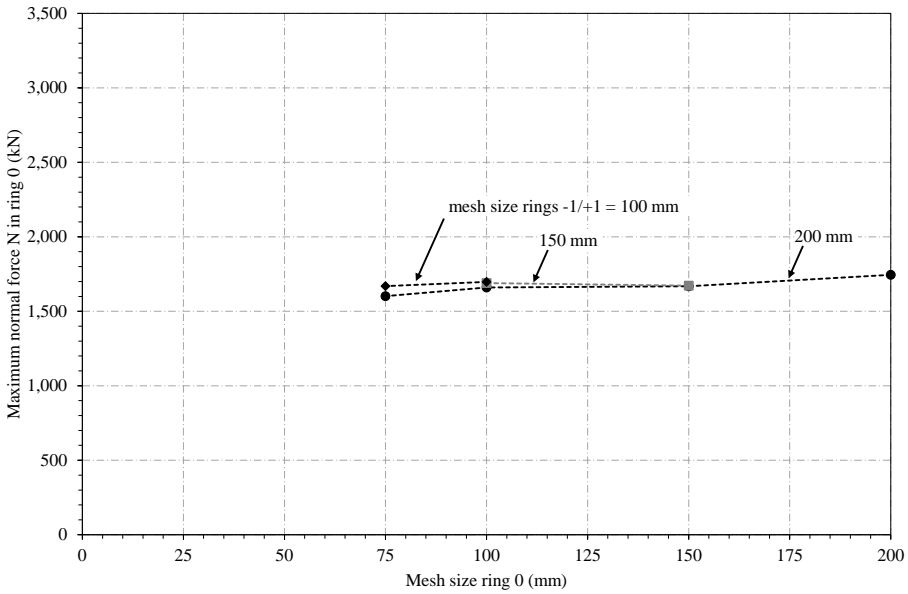


Figure C.6. Impact of the mesh size on the normal forces N in ring 0 for models with installation imperfections.

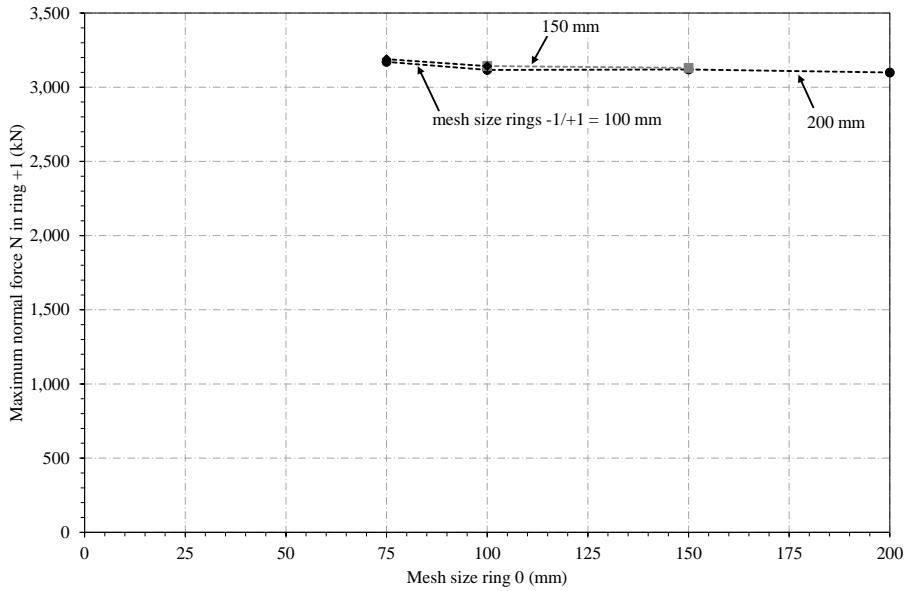


Figure C.7. Impact of the mesh size on the normal forces N in ring +1 for models with installation imperfections.

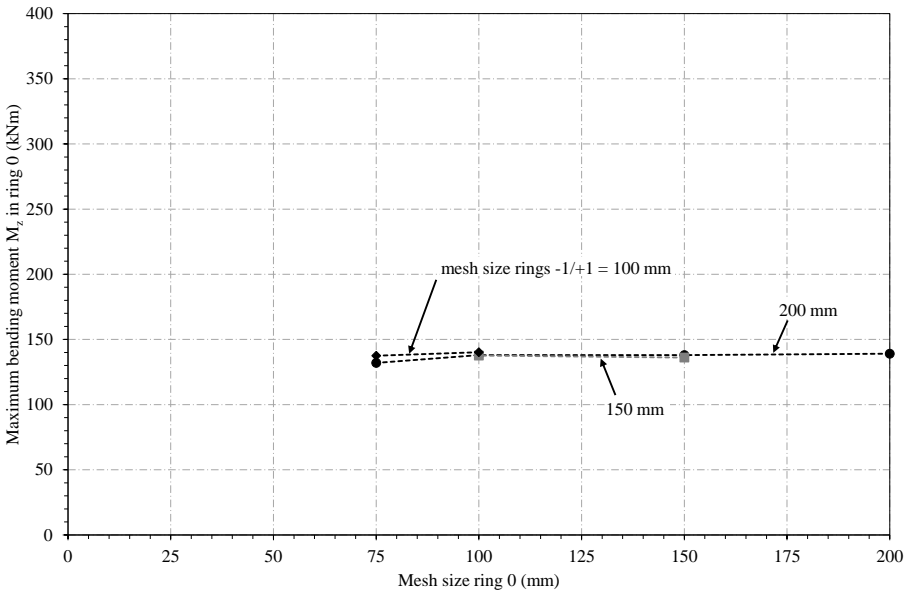


Figure C.8. Impact of the mesh size on the bending moments M_z in ring 0 for models with installation imperfections.

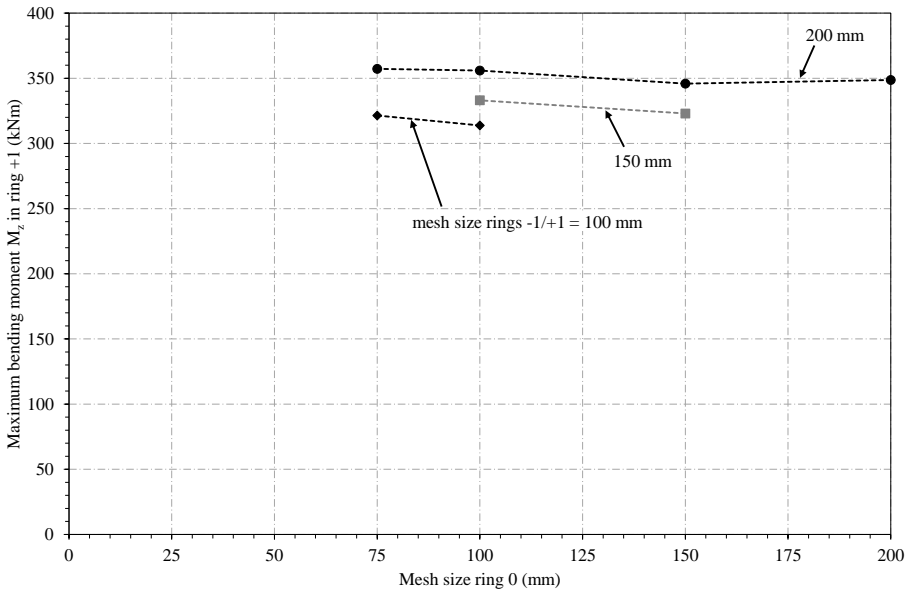


Figure C.9. Impact of the mesh size on the bending moments M_z in ring +1 for models with installation imperfections.

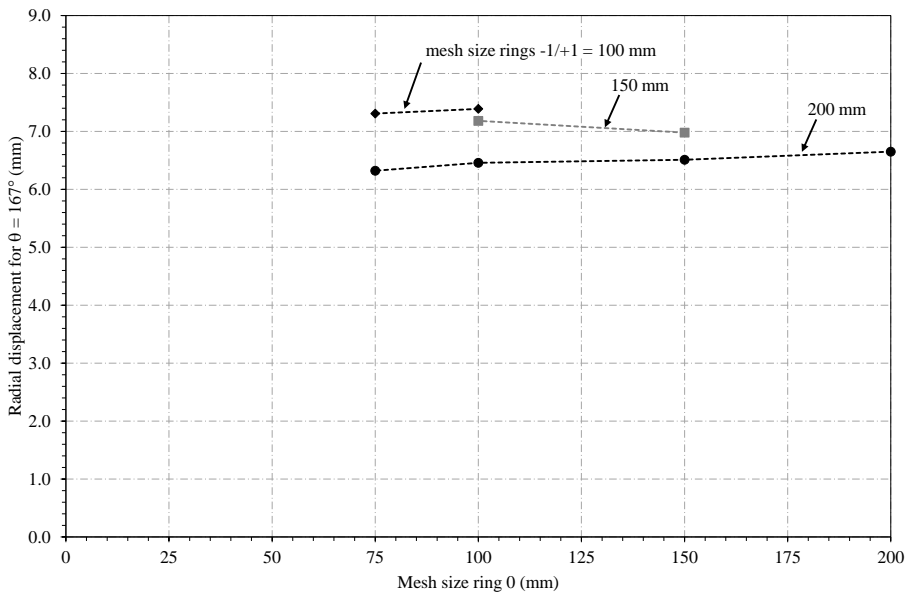


Figure C.10. Impact of the mesh size on the deformations of ring 0 for $\theta = 167^\circ$ for models with installation imperfections.

Appendix D

Impact of the joint friction: additional results

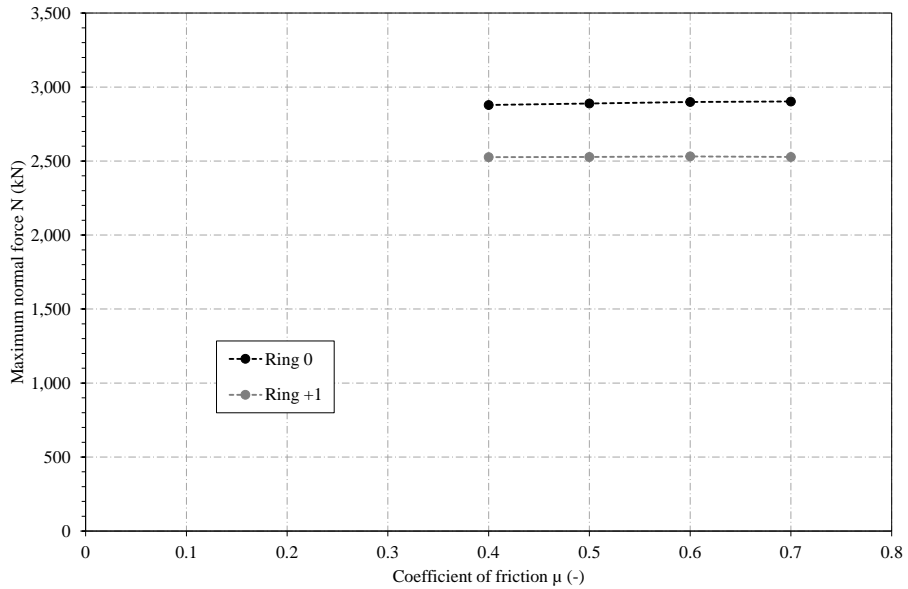


Figure D.1. Impact of the coefficient of friction on the normal forces N in ring 0 and +1 for models using design geometry.

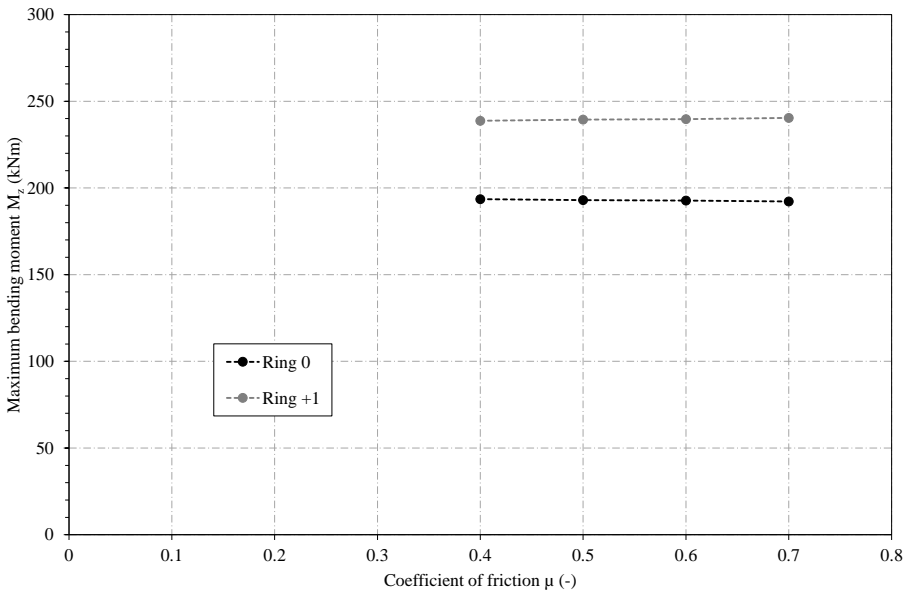


Figure D.2. Impact of the coefficient of friction on the bending moments M_z in ring 0 and +1 for models using design geometry.

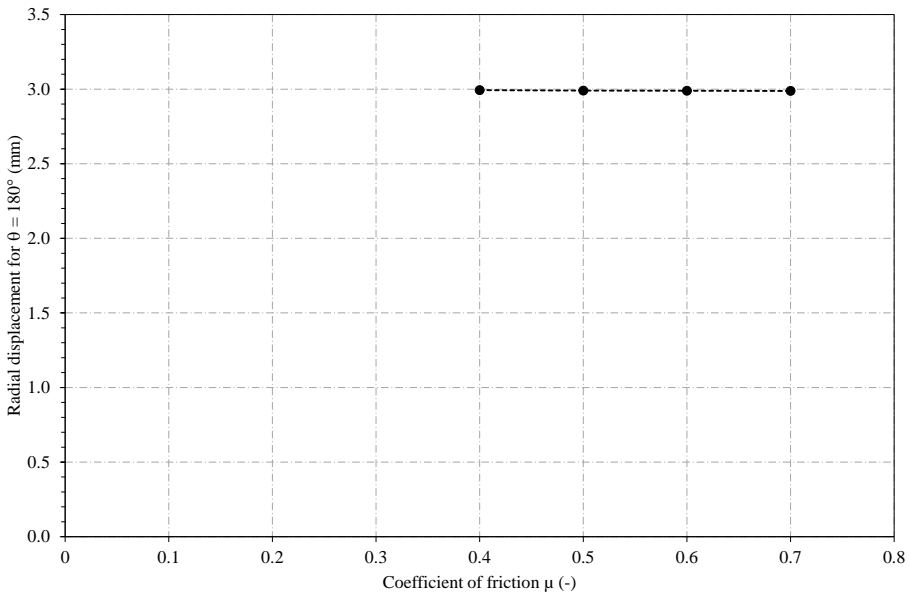


Figure D.3. Impact of the coefficient of friction on the deformations of ring 0 for $\theta = 180^\circ$ for models using design geometry.

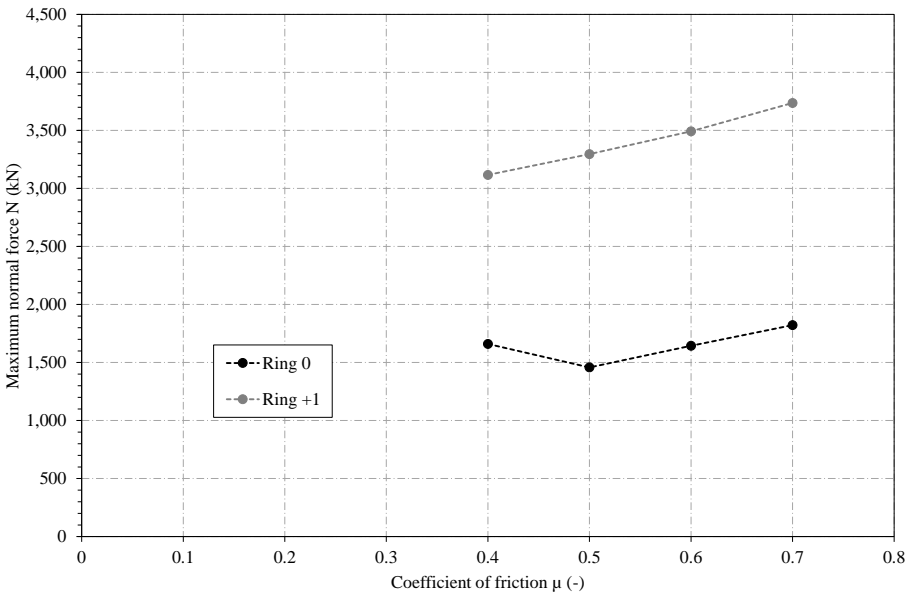


Figure D.4. Impact of the coefficient of friction on the normal forces N in ring 0 and +1 for models with installation imperfections.

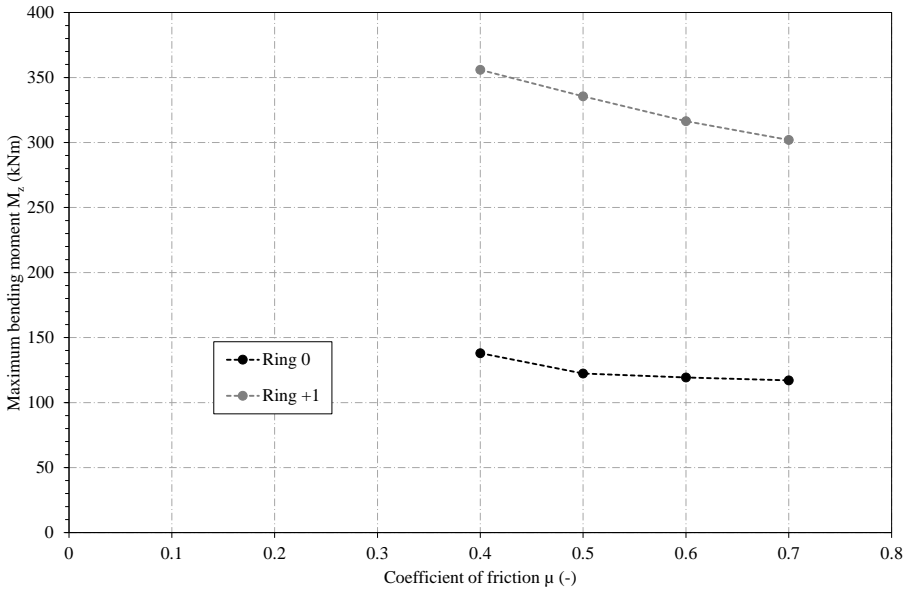


Figure D.5. Impact of the coefficient of friction on the bending moments M_z in ring 0 and +1 for models with installation imperfections.

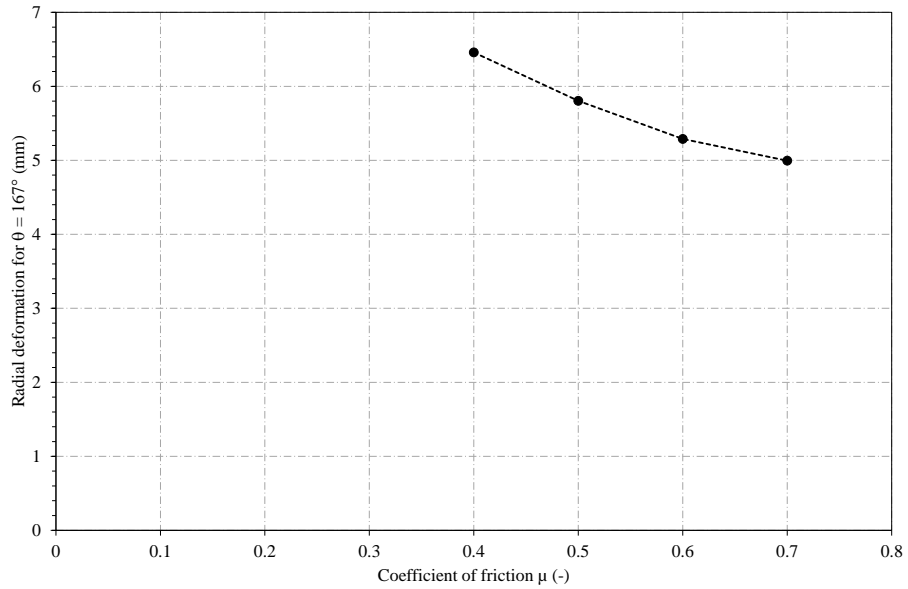


Figure D.6. Impact of the coefficient of friction on the deformations of ring 0 for $\theta = 167^\circ$ for models with installation imperfections.

